



Universidade do Minho
Escola de Engenharia

Ricardo Vieites Salgado Alves Gomes Unified Motor Drive and Battery Charger for Electric Vehicles

Ricardo Vieites Salgado Alves Gomes

Unified Motor Drive and Battery Charger for
Electric Vehicles

UMinho | 2015

outubro de 2015



Universidade do Minho
Escola de Engenharia

Ricardo Vieites Salgado Alves Gomes

Unified Motor Drive and Battery Charger for
Electric Vehicles

Dissertação de Mestrado
Ciclo de Estudos Integrados Conducentes ao Grau de
Mestre em Engenharia Eletrónica Industrial e Computadores

Trabalho efectuado sob a orientação do
Professor Doutor João Luiz Afonso

DECLARAÇÃO

Nome: Ricardo Vieites Salgado Alves Gomes

Endereço eletrónico: a61986@alumni.uminho.pt Telefone: 936902894 / 253251079

Número do Bilhete de Identidade: 14137111

Título dissertação:

Unified Motor Drive and Battery Charger for Electric Vehicles

Orientador: Professor Doutor João Luiz Afonso

Ano de conclusão: 2015

Dissertação submetida na Universidade do Minho para a obtenção do grau de Mestre em Engenharia Eletrónica Industrial e Computadores

É AUTORIZADA A REPRODUÇÃO INTEGRAL DESTA TESE/TRABALHO APENAS PARA EFEITOS DE INVESTIGAÇÃO, MEDIANTE DECLARAÇÃO ESCRITA DO INTERESSADO, QUE A TAL SE COMPROMETE.

Universidade do Minho, ___/___/_____

Assinatura: _____

Às três Marias da minha vida

Acknowledgements

The development of the work presented in this document would not have been possible without the support and contribution of some people, to whom I convey my most sincere thanks.

First of all, I would like to thank Doctor João Luiz Afonso, for believe in my capabilities and providing me the opportunity to work under his supervision.

To all researchers, MSc and PhD students of the Group of Energy and Power Electronics (GEPE), for the respect, friendship and good work environment provided.

A special thanks to the PhD student Delfim Pedrosa, my supervisor in the laboratory of the GEPE, for all the support and collaboration, which resulted in an important contribute to the development of this MSc. Thesis.

To my parents and sister, for the patience and comprehension during this hard-working year and by the fact that I have been more absent and did not always give them the attention that they deserve, especially during the writing of this document.

To my closest friends Dalila Abreu, Paulo Vicente, Rui Saraiva and Ângela Loureiro for all the support and friendship provided, with a special thanks to Paulo Vicente for the help provided in the revision of this document.

I would also like to honor the memory of my colleague Emanuel Ribeiro that, despite no longer being among us, helped motivate me as an example of dedication, especially during the more difficult moments lived in this year.

Unified Motor Drive and Battery Charger for Electric Vehicles

Nowadays, Electric Vehicles are emerging as the most sustainable alternative to support the expected rise in the number of vehicles in circulation around the world, and to reduce the impact of the transportation sector on the environment. However, this is a technology that still has some limitations that restrict its mainstream adoption.

Typically, an Electric Vehicle has a motor drive system and an on-board battery charger that allows charging its battery pack almost anywhere, as long as there is an electrical outlet available. However, this is usually a low-power charger in order to optimize the space and weight on-board the vehicle. As a result, this type of charging typically takes a couple of hours.

The purpose of this MSc. Thesis was the development of a unified power electronics converter, capable of performing the roles of drive the electrical machine of an Electric Vehicle and also charging its battery pack, so as to optimize the space and weight of the power electronics components on-board the vehicle while also providing a faster charging operation.

The first part of this MSc. Thesis consisted in the study of the state of art of the unified hardware solutions proposed, based on the use of the power electronics components of the motor drive system during the battery charging operation, since both operation modes cannot be performed simultaneously, except for regenerative braking. Also the respective control algorithms that allow perform each operation mode, according with the solution proposed, were studied.

The second part consisted in simulating the proposed unified solution and implementing a proof-of-concept prototype. In the proposed solution the battery charger is based on the use of a three-phase Voltage Source Inverter and the windings of a Brushless DC machine. With respect to the control algorithms, for the motor drive mode the Field-Oriented Control was chosen, while for the battery charging mode two control algorithms were chosen (one for single-phase charging and the other for three-phase charging), based on the Model Predictive Control.

The obtained results validate the proposed solution. However, in the case of the electrical machine used in this MSc. Thesis, the values of the inductances of its windings compromise its use as an input filter.

Keywords: Electric Vehicles, On-Board Battery Charger, Unified Solution, Field-Oriented Control, Model Predictive Control

Solução Unificada para Tração e Carregamento das Baterias em Veículos Elétricos

Atualmente os Veículos Elétricos surgem como a alternativa mais sustentável perante o aumento expectável do número de veículos em circulação no mundo e por forma a reduzir o impacto ambiental do sector do transporte. Contudo, esta é ainda uma tecnologia com algumas limitações, que ainda não permitiram a sua aquisição em maior escala.

Tipicamente um Veículo Elétrico possui um sistema de tração e um sistema de carregamento, que permite carregar as suas baterias em praticamente qualquer local, desde que haja disponível uma tomada ligada à rede elétrica. No entanto, este sistema de carregamento tem normalmente uma potência instalada baixa, por forma a otimizar o espaço e peso ocupados no interior do veículo. Como resultado, este tipo de carregamento demora tipicamente algumas horas.

Esta Dissertação de Mestrado teve como objetivo o desenvolvimento de um conversor unificado, capaz de controlar a máquina elétrica usada para a tração de um Veículo Elétrico e de carregar as suas baterias, permitindo otimizar ainda mais o espaço e peso ocupados pelos componentes de eletrónica de potência instalados no veículo e possibilitar ainda carregamentos mais rápidos.

A primeira parte desta Dissertação consistiu num estudo do estado da arte de sistemas de hardware unificados, baseados na utilização dos componentes de eletrónica de potência do sistema de tração durante o modo de carregamento das baterias, tendo em conta que as duas operações não podem ser realizadas em simultâneo, exceto para travagem regenerativa. Também foram estudados os algoritmos de controlo que permitem executar cada uma das operações, de acordo com a topologia proposta.

A segunda parte consistiu na simulação da solução proposta e na implementação de um protótipo para demonstração da funcionalidade. Nesta solução proposta, o sistema de carregamento baseia-se na utilização de um inversor trifásico do tipo *Voltage Source Inverter* e dos enrolamentos de uma máquina elétrica do tipo *Brushless DC*. Em relação aos algoritmos de controlo, para o modo de tração foi selecionado o Controlo por Orientação de Campo (*Field-Oriented Control*), enquanto que para o modo de carregamento foram selecionados dois algoritmos (um para carregamento monofásico e outro para trifásico), baseados no Controlo Preditivo (*Model Predictive Control*).

Os resultados obtidos permitiram validar a solução proposta. Contudo, os baixos valores de indutância da máquina elétrica usada comprometem o seu uso como filtro de entrada.

Palavras-Chave: Veículos Elétricos, Sistema de Carregamento, Sistema Unificado, Controlo por Orientação de Campo, Controlo Preditivo

Contents

Acknowledgements.....	v
List of Figures	xiii
List of Tables.....	xxi
Abbreviations.....	xxiii
Chapter 1 Introduction	1
1.1. General Motivations.....	1
1.2. Electric Vehicle	2
1.2.1. Understanding the Concept of Electric Vehicle	3
1.2.2. Brief History and Actual State.....	3
1.2.3. Motor Drive.....	7
1.2.4. Battery Charger	9
1.3. Problem Statement.....	12
1.4. Main Goals	13
1.5. Relevant Contributions.....	14
1.6. Outline of this MSc. Thesis	16
Chapter 2 Unified Topologies for Motor Drive and Battery Charging.....	17
2.1. Introduction	17
2.2. Non-Isolated Battery Charger.....	19
2.2.1. Level 1 – Using the Power Electronics Converters of the Motor Drive System.....	19
2.2.2. Level 2 – Using the Power Electronics Converters and the Electrical Machine of the Motor Drive System.....	23
2.3. Isolated Battery Charger.....	34
2.4. Proposed Solution.....	37
2.5. Conclusions	38
Chapter 3 Control Algorithms for Motor Drive and Battery Charging	41
3.1. Introduction	41
3.2. Motor Drive.....	41
3.2.1. Field-Oriented Control.....	42
3.2.2. Direct Torque Control.....	52
3.3. Battery Charging.....	54
3.3.1. Direct Current Control Based on Synchronous Reference Frame	55
3.3.2. Direct Power Control Based on Model Predictive Control	62
3.4. Control Algorithms for the Bidirectional DC-DC Converter.....	70
3.4.1. Motor Drive.....	70
3.4.2. Battery Charging	71
3.5. Conclusions	74
Chapter 4 Simulations of the Proposed Solution	75
4.1. Introduction	75
4.2. Electrical Machine	76
4.3. Dynamical Model of a Li-Ion (LiFePO ₄) Battery	80
4.4. Simulations in Motor Drive Mode	84
4.4.1. Proposed Control Algorithm	84
4.4.2. Operating without Load	86
4.4.3. Operating with Nominal Load (80 Nm)	89
4.5. Simulations in the Fast Charging Mode	92
4.5.1. Proposed Control Algorithm	94
4.5.2. Grid-to-Vehicle Operation	97
4.5.3. Grid-to-Vehicle Operation with a Pre-Charge Circuit.....	105
4.5.4. Grid-to-Vehicle Operation with Reactive Power Compensation.....	107
4.5.5. Vehicle-to-Grid Operation	108
4.6. Simulations in the Slow Charging Mode.....	110
4.6.1. Proposed Control Algorithm	111
4.6.2. Phase-Locked Loop System	112
4.6.3. Grid-to-Vehicle Operation	114
4.6.4. Vehicle-to-Grid Operation	117
4.7. Simulations of the Bidirectional DC-DC Converter.....	118
4.7.1. Motor Drive and Battery Charging (Vehicle-to-Grid) Modes.....	118
4.7.2. Battery Charging Mode (Grid-to Vehicle Operation).....	120

4.8. Conclusions.....	121
Chapter 5 Implementation of the Control System and the Power Stage of a Proof-of-Concept Prototype.....	123
5.1. Introduction.....	123
5.2. Control System.....	124
5.2.1. Voltage Sensors.....	127
5.2.2. Current Sensors.....	128
5.2.3. Signal Conditioning.....	129
5.2.4. Digital Signal Controller.....	130
5.2.5. Control Driver of the Insulated Gate Bipolar Transistors.....	131
5.2.6. Control Board for the Pre-Charge Circuit.....	132
5.2.7. Position Sensor.....	132
5.2.8. Interface Board for the Position Sensor.....	133
5.2.9. Torque Reference.....	133
5.2.10. Human–Machine Interface.....	134
5.3. Power Stage.....	134
5.3.1. Three-Phase Voltage Source Inverter.....	135
5.3.2. DC-Bus.....	136
5.3.3. Sources and Auxiliary Loads.....	137
5.3.4. Extra Inductor Filter.....	138
5.3.5. Resistances of the Pre-Charge Circuit.....	138
5.4. Final Result.....	139
5.5. Conclusions.....	140
Chapter 6 Experimental Results.....	141
6.1. Introduction.....	141
6.2. Motor Drive Mode.....	141
6.3. Slow Charging Mode.....	142
6.4. Conclusions.....	145
Chapter 7 Conclusions.....	147
7.1. Main achievements.....	147
7.2. Future Work.....	149
References.....	151
Appendix A Estimative of the Maximum Distortion Value of the Stator Inductances in a Synchronous Machine with Salient Poles.....	163

List of Figures

Figure 1.1 – World population prospects between 2014 and 2050, according to estimates provided by the United Nations [1], considering the scenario of no-change in the behavior of the evolution estimated between 1950 and 2010.....	1
Figure 1.2 – <i>Renault ZOE</i> (gently provided by <i>Renault Portugal</i>).	4
Figure 1.3 – <i>Nissan Leaf</i> (gently provided by <i>Nissan Portugal</i>).	4
Figure 1.4 – <i>Smart Fortwo Electric-Drive</i> (gently provided by <i>Mercedes-Benz Portugal</i>).	5
Figure 1.5 – Statistical data of the market of Electric Vehicles (EV) in Portugal (gently provided by ACAP): (a) Car sales per type of vehicle in Portugal during 2014; (b) Total of Battery Electric Vehicles (BEVs) sold in Portugal during the last years; (c) Light duty BEVs sold in Portugal during 2014.	6
Figure 1.6 – Comparison of the specific energy of the commercially available batteries with the fuel used for propel vehicles with ICE (sources: [16], [24]).	7
Figure 1.7 – Typical electric propulsion system of an EV, using an AC three-phase electrical machine (based on [27]).	8
Figure 1.8 – Ideal performance characteristics for vehicle traction purposes (adapted from [38]).	9
Figure 1.9 – Charging socket and connector used in the <i>Volkswagen e-Up!</i> (gently provided by <i>Volkswagen Portugal – Siva</i>).	9
Figure 1.10 – Public off-board charging stations in Portugal: (a) Slow charging station in Azurém (Guimarães), with an installed power of 3.68 kW [49]; (b) Fast charging station in the service station of the freeway A5 (Oeiras), with an installed power of 55 kW [49] (gently provided by <i>Galp Energia</i> [Manuel Aguiar, <i>Balcão Digital Galp Energia</i>]).	10
Figure 1.11 – Charging of a <i>Renault ZOE</i> , using a dedicated EV supply equipment installed (gently provided by <i>Renault Portugal</i>).	11
Figure 1.12 – Power electronics components typically installed on-board of an EV and some examples of sources for the battery charging operation.	13
Figure 1.13 – <i>Carro Elétrico Plug-In da Universidade do Minho</i> (CEPIUM), the EV developed in the University of Minho: (a) Overview; (b) Power electronics converters and control system implemented under the hood.	14
Figure 1.14 – Potentialities of converting vehicles, using a unified motor drive and battery charger: (a): Considering a vehicle with ICE; (b) Considering an EV with a low-power on-board battery charger; (c) Considering an EV without on-board battery charger.	16
Figure 2.1 – Typical hardware topology of the motor drive system of an EV.	17
Figure 2.2 – Diagram, synthesizing the reported unified topologies studied in this MSc. Thesis.	19
Figure 2.3 – Three-phase three-wire boost AC-DC converter (adapted from [60]).	20
Figure 2.4 – Unified topology with non-isolated battery charger, discussed in [46], based on using three additional filter inductors and three relays contacts.	20
Figure 2.5 – Unified topology with non-isolated battery charger, discussed in [31], combining the features of DC-DC bidirectional converter for motor drive and AC-DC converter for on-board battery charging.	22
Figure 2.6 – Unified topology with non-isolated battery charger, discussed in [66], based on using two stator windings as filter inductors for slow charging.	25
Figure 2.7 – Equivalent circuit for the battery charging mode of the unified topology with non-isolated battery charger, discussed in [19], based on using all the stator windings as filter inductors for fast charging.	26
Figure 2.8 – Unified topology with non-isolated battery charger, discussed in [46], providing fast charging and adapted to electrical machines wye-connected without the neutral point accessible.	28

Figure 2.9 – Unified topology with non-isolated battery charger, discussed in [57], based on using a split-windings Permanent Magnet Synchronous Machine (PMSM): (a) Proposed hardware topology; (b) Equivalent circuit for motor drive; (c) Equivalent circuit for battery charging.	29
Figure 2.10 – Unified topology with non-isolated battery charger, discussed in [45], based on the grid connection through the neutral point of the electrical machine.....	31
Figure 2.11 – Equivalent circuit of the set composed by the windings of the electrical machine and the three-phase Voltage Source Inverter (VSI) during the battery charging mode, corresponding to a Step-Up (Boost) DC-DC converter (adapted from [72]).	31
Figure 2.12 – Unified topology with non-isolated battery charger, discussed in [50], based on the grid connection through the middle points of the stator windings.....	33
Figure 2.13 – Unified topology with isolated battery charger, discussed in [61], based on using a wound-rotor induction machine.	35
Figure 2.14 – Unified topology with isolated battery charger, discussed in [41], based on using a split-windings PMSM: (a) Equivalent circuit for motor drive; (b) Equivalent circuit for battery charging.	36
Figure 2.15 – Unified motor drive and battery charger for EVs proposed in this MSc. Thesis.	38
Figure 3.1 – Block diagram of the Field-Oriented Control (FOC), described by <i>Pedrosa et al.</i> (adapted from [69]).	43
Figure 3.2 – Block diagram of the Proportional Integral (PI) controller, used in this MSc. Thesis (adapted from [52]).	43
Figure 3.3 – Transformation of the stator currents from the $a-b-c$ coordinate system into the $\alpha-\beta$ coordinate system, using the Clarke transform (adapted from [82]).	44
Figure 3.4 – Transformation of the stator currents from the stationary reference frame $\alpha-\beta$ coordinate system into the rotating reference frame $d-q$ coordinate system, using the Park transform (adapted from [82]).	45
Figure 3.5 – Space Vector of V_{ref} in the $\alpha-\beta$ plan (adapted from [69]).	47
Figure 3.6 – Examples of gate signals obtained through the comparison of variables the t_a , t_b and t_c with a triangular-wave: (a) Considering V_{ref} placed in sector I; (a) Considering V_{ref} placed in sector III.	50
Figure 3.7 – Space Vector Pulse Width Modulation (SVPWM) pattern, according to the sector where V_{ref} is placed, known as the hexagon of the SVPWM (adapted from [82]).	50
Figure 3.8 – Gate signals applied to the power semiconductors of the three-phase VSI, considering an ideal switching behavior.	51
Figure 3.9 – Block diagram of the Direct Torque Control (DTC) (adapted from [59], [77], [83]).	52
Figure 3.10 – Equivalent circuit of the first stage of the unified topology proposed in this MSc. Thesis, for the fast charging mode, through an AC three-phase grid supply.	55
Figure 3.11 – Block diagram of the Direct Current Control based on Synchronous Reference Frame (DCC-SRF) (adapted from [39]).	56
Figure 3.12 – Block diagram of the Direct Current Control based on Synchronous Reference Frame (DCC-SRF), changed for attenuate the disturbances due to the use of the windings of a PMSM as filter inductors (adapted from [19]).	58
Figure 3.13 – Block diagram of the typical structure of a Phase-Locked-Loop (PLL) system (adapted from [93]).	59
Figure 3.14 – Block diagram of a basic single-phase PLL system (adapted from [93]).	60
Figure 3.15 – Block diagram of a single-phase Enhanced Phase-Locked-Loop (EPLL) system proposed by <i>Karimi-Ghartemani et al.</i> (adapted from [92], [95]).	60
Figure 3.16 – Diagram block of three-phase PLL system: (a) q-PLL (adapted from [97]); (b) Basic SRF-PLL (adapted from [101]).	61
Figure 3.17 – Block diagram of a direct current control based on Model Predictive Control (MPC), using SVPWM (based on [108]).	62

Figure 3.18 – Operation principle of the Finite Control Set Model Predictive Control (FCS-MPC) (adapted from [104]).....	63
Figure 3.19 – Block diagram of the Direct Power Control based on Model Predictive Control (DPC-MPC) (based on [109]).....	67
Figure 3.20 – Equivalent circuit of the unified topology proposed in this MSc. Thesis, for the slow charging mode, through an AC single-phase grid supply.	68
Figure 3.21 – Block diagram for the reference current, proposed to use in the MPC, for the slow charging mode (adapted from [52]).....	69
Figure 3.22 – Block diagram for the reference current, proposed to use in the MPC, for the Vehicle-to-Grid (V2G) operation during the slow charging mode (based on [52]).....	70
Figure 3.23 – Bidirectional DC-DC converter included in the unified topology proposed in this MSc. Thesis.	70
Figure 3.24 – Equivalent circuit of the bidirectional DC-DC converter operating as a Step-Up (Boost) DC-DC converter.	71
Figure 3.25 – Block diagram of the control algorithm proposed for the bidirectional DC-DC converter, during the motor drive mode (adapted from [52]).....	71
Figure 3.26 – Equivalent circuit of the bidirectional DC-DC converter operating as Step-Down (Buck) DC-DC converter.....	72
Figure 3.27 – Battery charging comprising two steps: constant-current and constant-voltage (adapted from [111]).....	72
Figure 3.28 –Block diagram of the control algorithm proposed for the bidirectional DC-DC converter, during the Vehicle-to-Grid (V2G) mode (adapted from [52]).....	73
Figure 3.29 – Block diagram of the additional control algorithm proposed for the bidirectional DC-DC converter during the Vehicle-to-Grid (V2G), through a single-phase connection to the electrical grid (adapted from [52]).....	73
Figure 4.1 – Brushless DC (BLDC) machine used in this MSc. Thesis (source: <i>Golden Motors</i>).....	76
Figure 4.2 – Configuration of the stator windings and accessible terminals of the BLDC machine <i>HPM-20KW</i>	77
Figure 4.3 – Modified configuration of the stator windings and accessible terminals implemented in the BLDC machine <i>HPM-20KW</i> , for maximizing the values of its inductances.....	77
Figure 4.4 – Setup of the experimental tests performed for obtain the parameters V_{pk} / k_{rpm} and V_{RMS} / k_{rpm} of the BLDC machine used in this MSc. Thesis.....	78
Figure 4.5 – Experimental results of the voltages v_{ab} , v_{bc} and v_{ca} (20 V/div) at the terminals of the BLDC machine, operating as a generator with a rotor speed of 1000 rpm.	79
Figure 4.6 – Dynamical model of a li-ion (LiFePO ₄) battery, proposed by <i>Tremblay et al.</i> in [115].....	80
Figure 4.7 – Simulation model of the model of the battery, developed in the software <i>PSIM</i> : (a) Electrical circuit; (b) Dynamical Model.	82
Figure 4.8 – Block representation of the dynamical model of the battery developed in the software <i>PSIM</i>	83
Figure 4.9 – Simulation results of the voltage at the terminals of the battery pack, connecting the dynamic model of the battery developed to a pure resistive load of 2 Ω, considering that the battery pack is initially full charged.	84
Figure 4.10 – Block diagram of the FOC proposed in this MSc. Thesis.	85
Figure 4.11 – Simulation model of the power electronics circuit, including the mechanical components and the sensor blocks, developed in the software <i>PSIM</i> , for the motor drive mode.	85
Figure 4.12 – Simulation model of the control system responsible for implementing the FOC, developed in the software <i>PSIM</i> , for the motor drive mode.....	86

Figure 4.13 – Simulation results of the torque reference (T_{ref}) and torque (T) produced by the BLDC machine, during the motor drive mode operating without mechanical load.	87
Figure 4.14 – Simulation results of the stator d - q axis reference current i_{q_ref} and the current i_q , during the motor drive mode operating without mechanical load.	88
Figure 4.15 – Simulation results of the speed curve, during the motor drive mode operating without mechanical load.	88
Figure 4.16 – Simulation results of the voltages and currents on the BLDC machine, during the motor drive mode operating without mechanical load: (a) v_{ab} , v_{bc} and v_{ca} ; (b) i_a , i_b and i_c . (The voltages were filtered through a low-pass filter with a cut-off frequency of 500 Hz).	89
Figure 4.17 – Simulation results of the torque reference (T_{ref}) and torque (T) produced by the BLDC machine, during the motor drive mode operating with nominal load.	90
Figure 4.18 – Simulation results of the stator d - q axis reference current i_{q_ref} and the current i_q , during the motor drive mode operating with nominal load.	91
Figure 4.19 – Simulation results of the speed curve, during the motor drive mode operating with nominal load.	91
Figure 4.20 – Simulation results of the voltages and currents on the BLDC machine, during the motor drive mode operating with nominal load: (a) v_{ab} , v_{bc} and v_{ca} ; (b) i_a , i_b and i_c . (The voltages were filtered through a low-pass filter at 500 Hz).	92
Figure 4.21 – Block diagram of the modified DPC-MPC proposed in this MSc. Thesis, for the fast charging mode.	94
Figure 4.22 – Exchange of the p - q powers in an installation where the chargers of the EVs are used as reactive power compensators, a feature provided by the control algorithm of the fast charging mode proposed in this MSc. Thesis.	96
Figure 4.23 – Flowchart of the proposed modified DPC-MPC, for the fast charging mode.	97
Figure 4.24 – Simulation model of the power electronics circuit, developed in the software <i>PSIM</i> , for the fast charging mode.	98
Figure 4.25 – Simulation model of the control system responsible for implementing the DPC-MPC, developed in the software <i>PSIM</i> , for the fast charging mode.	98
Figure 4.26 – Simulation results of the instantaneous p - q powers (in steady-state), during the fast charging mode (G2V operation).	99
Figure 4.27 – Simulation results of the input voltages and currents, during the fast charging mode (G2V operation): (a) v_a , v_b and v_c ; (b) i_a , i_b and i_c	100
Figure 4.28 – Modified simulation model of the power electronics circuit, developed in the software <i>PSIM</i> , for the fast charging mode with an extra input filter.	101
Figure 4.29 – Simulation results of the instantaneous p - q powers (in steady-state), during the fast charging mode (G2V operation) with an extra inductor filter.	102
Figure 4.30 – Simulation results of the input voltages and currents, during the fast charging mode (G2V operation), with an extra inductor filter.	103
Figure 4.31 – Harmonic spectrum of the waveform of the current i_a , obtained in the simulations of the fast charging mode (G2V operation), with an extra inductor filter, in comparison with the limits established by the standard IEC 61000-3-4.	103
Figure 4.32 – Simulation results of the voltage at the terminals of the DC-bus, during the fast charging mode (G2V operation), with an extra inductor filter.	104
Figure 4.33 – Simulation results of the input currents (during the transitory regime), during the fast charging mode (G2V operation), considering that the output filter capacitor is fully discharged.	104
Figure 4.34 – Modified simulation model of the power electronics circuit, developed in the software <i>PSIM</i> , for the fast charging mode with an extra input filter and a pre-charge circuit.	105
Figure 4.35 – Modified simulation model of the control system responsible for implementing the DPC-MPC, developed in the software <i>PSIM</i> , for the fast charging mode with a pre-charge circuit.	106

Figure 4.36 – Simulation results of the input currents, during the fast charging mode (G2V operation), with a pre-charge circuit.....	106
Figure 4.37 – Simulation results of the voltage at the terminals of the DC-bus, during the fast charging mode (G2V operation), with a pre-charge circuit.....	107
Figure 4.38 – Simulation results of the instantaneous $p-q$ powers (in steady-state), during the fast charging mode (G2V operation with reactive power compensation).....	108
Figure 4.39 – Simulation results of the input voltage v_a and current i_a , during the fast charging mode (G2V operation with reactive power compensation).	108
Figure 4.40 – Simulation results of the instantaneous $p-q$ powers (in steady-state), during the fast charging mode (V2G operation).....	109
Figure 4.41 – Simulation results of the input voltage v_a and current i_a , during the fast charging mode (V2G operation).....	109
Figure 4.42 – Harmonic spectrum of the waveform of the injected current i_a , obtained in the simulations of the fast charging mode (V2G operation), with an extra inductor filter.....	110
Figure 4.43 – Block diagram of the Direct Current Control based on Model Predictive Control (DCC-MPC) proposed in this MSc. Thesis, for the slow battery charge mode.....	111
Figure 4.44 – PLL system proposed in this MSc. Thesis, for the slow charging mode.	112
Figure 4.45 – Simulation results of the input voltage v_s and respective pll_{unit} signal, obtained by the PLL system.	113
Figure 4.46 – Harmonic spectrum of the waveform of the pll_{unit} signal, obtained in the simulations of the PLL system, in comparison with the voltage v_s	113
Figure 4.47 – Simulation model of the power electronics circuit, developed in the software <i>PSIM</i> , for the slow charging mode.....	114
Figure 4.48 – Simulation model of the control system responsible for implementing the DCC-MPC, developed in the software <i>PSIM</i> , for the slow charging mode.	114
Figure 4.49 – Simulation results of the input voltage v_s and current i_s , during the slow charging mode (G2V operation), with an extra inductor filter.....	116
Figure 4.50 – Harmonic spectrum of the waveform of the current i_s , obtained in the simulations of the slow charging mode (G2V operation), with an extra inductor filter, in comparison with the limits established by the standard IEC 61000-3-2.....	116
Figure 4.51 – Simulation results of the voltage of the DC-bus V_{DC} , during the slow charging mode (G2V operation), with an extra inductor filter.....	117
Figure 4.52 – Simulation results of the input voltage v_s and current i_s , during the slow charging mode (V2G operation), with an extra inductor filter.....	117
Figure 4.53 – Harmonic spectrum of the waveform of the injected current i_s , obtained in the simulations of the slow charging mode (V2G operation), with an extra inductor filter.....	118
Figure 4.54 – Simulation model of the power electronics circuit, developed in the software <i>PSIM</i> , for the motor drive mode of the bidirectional DC-DC converter of the proposed unified topology.....	119
Figure 4.55 – Simulation results of the DC-bus voltage, during the motor drive mode.	119
Figure 4.56 – Simulation results of the voltage of the battery pack, during the motor drive mode (the <i>PSIM_time_step</i> parameter was adjusted for providing a fast dynamic behavior of the battery pack).....	120
Figure 4.57 – Simulation results of the current flowing through the battery pack, during the constant-current mode of the battery charging.	120
Figure 4.58 – Simulation results of the voltage at the terminals of the battery pack, during the constant-current mode of the battery charging (the <i>PSIM_time_step</i> parameter was adjusted for providing a fast dynamic behavior of the battery pack).....	121
Figure 5.1 – Topology of the proof-of-concept prototype implemented in this MSc. Thesis.	123

Figure 5.2 – Finite-state machine of the control system implemented in this MSc. Thesis.....	125
Figure 5.3 – Diagram describing the proof-of concept prototype and its main components for the implementation of the digital control system proposed in this MSc. Thesis.....	126
Figure 5.4 – Implemented circuit for the measuring the voltage, using the sensor <i>CYHVS5-25A</i> (adapted from [118]).	127
Figure 5.5 – Printed Circuit Board (PCB) developed in the GEPE for the measuring the voltage, using the sensor <i>CYHVS5-25A</i>	127
Figure 5.6 – Implemented circuit for the measuring the current, using the sensor <i>LA 200-P</i> (adapted from [119]).	129
Figure 5.7 – PCB developed in the GEPE for the measuring of the current, using the sensor <i>LA 200-P</i>	129
Figure 5.8 – PCB developed in the GEPE for the signal conditioning.....	130
Figure 5.9 – <i>ControlCARD</i> provided by <i>Texas Instruments</i> to interface with the DSC <i>TMS320F28335</i>	131
Figure 5.10 – <i>Docking station</i> developed in the GEPE providing an easier and more robust interface with the peripherals of the DSC.	131
Figure 5.11 – PCB developed in the GEPE for the control of the drive of the IGBTs.	132
Figure 5.12 – PCB developed in the GEPE for control the actuation of the pre-charge circuit.	132
Figure 5.13 – Position sensor (<i>RMB28SC</i> from <i>RLS</i>), mounted on the electrical machine.	133
Figure 5.14 – PCB developed in the GEPE for interface between the position sensor with the DSC.	133
Figure 5.15 – Electronic accelerator pedal used for setting the torque reference in the motor drive mode.....	134
Figure 5.16 – Human-Machine Interface (HMI), developed in the GEPE, used to provide an easier interface with the control system.....	134
Figure 5.17 – IGBT module <i>SKM300GB126D</i> from <i>Semikron</i> (adapted from [122]): (a) Module; (b) Respective pinout.....	135
Figure 5.18 – PCB developed in the GEPE for the protection of the gates of each module of IGBTs.	136
Figure 5.19 – PCB developed in the GEPE for the driver circuit of the IGBTs.	136
Figure 5.20 – DC-bus implemented, composed by a pack of capacitors resulting in a total capacity of 10 mF and a maximum voltage of 450 V.	137
Figure 5.21 – PCB developed in the GEPE for the protection of the DC-bus.	137
Figure 5.22 – Transformers used to reduce the levels of the voltages supplied by the electrical grid.....	138
Figure 5.23 – Inductor used to implement the extra input filter of proof-of-concept prototype.	138
Figure 5.24 – Resistances used for the pre-charge circuit (each one with a resistance value of 100 Ω \pm 5%, 50 W).....	139
Figure 5.25 – Final result of the implementation of the proof-of-concept prototype.	139
Figure 6.1 – Experimental setup of the proof-of-concept prototype implemented in this MSc. Thesis (for the motor drive mode).....	141
Figure 6.2 – Experimental results of the voltages (20 V/div) and currents (2 A/div) of the BLDC machine, during the motor drive mode, operating without mechanical load.....	142
Figure 6.3 – Experimental results of the voltage (20 V/div) and current (5 A/div) of the DC-bus, during the motor drive mode, operating without mechanical load.	142
Figure 6.4 – Experimental results of the source voltage v_s (20 V/div) and respective obtained PLL signal (1 V/div), obtained during the transitory regime in the slow charging mode.....	143
Figure 6.5 – Experimental results of the source voltage v_s (40 V/div) and respective obtained PLL signal (1 V/div), the current consumed i_s (1 A/div) and its respective reference i_{s_ref} (1 A/div)	

and the voltage at the terminals of the DC-bus (20 V/div), during the slow charging mode with $V_{DC_ref} = 80$ V.....	144
Figure 6.6 – Harmonic spectrum of the current consumed for the slow charging mode with $V_{DC_ref} = 80$ V.....	144
Figure 6.7 – Experimental results of the source voltage v_s (20 V/div) and respective obtained PLL signal (1 V/div), the current consumed i_s (2 A/div) and its respective reference i_{s_ref} (2 A/div) and the voltage at the terminals of the DC-bus (20 V/div), during the slow charging mode with $V_{DC_ref} = 110$ V.....	145
Figure 6.8 – Harmonic spectrum of the current consumed for the slow charging mode with $V_{DC_ref} = 110$ V.....	145
Figure 7.1 – Proposed solution for a unified motor drive and battery charger, considering an EV with the BLDC machine used in this MSc. Thesis.....	150

List of Tables

Table 1.1 – EV charging power levels (adapted from [12]).....	11
Table 2.1 – Allowed switching states for the power semiconductors of a VSI (adapted from [59]).	18
Table 3.1 – Identification of the sector where V_{ref} is placed, according to the value of N	47
Table 3.2 – Attribution of the values of t_1 and t_2 , according to the sector where V_{ref} is placed.....	48
Table 3.3 – Attribution of the t_a , t_b and t_c values, according to the sector where V_{ref} is placed.....	49
Table 3.4 – Typical look-up table used in the DTC (adapted from [77]).....	53
Table 3.5 – Voltage v_{in} , according to the switching states of the three-phase AC-DC converter (adapted from [105]).....	65
Table 3.6 – Voltage v_{in} , according to the switching states of the equivalent single-phase AC-DC converter.....	69
Table 4.1 – Main characteristics of the BLDC machine (<i>HPM-20KW</i>), used in this MSc. Thesis.	76
Table 4.2 – Results of the measurements of the values of inductance and resistance of the windings of the BLDC machine used in this MSc. Thesis (with the proposed modified configuration). The values of the inductances were measured for a frequency of 20 kHz.	78
Table 4.3 – Values of the parameters used in the module of the BLDC machine provided by the software <i>PSIM</i> , for the simulations of the proposed topology.....	79
Table 4.4 – Variables and parameters of the proposed dynamical model of a li-ion (LiFePO_4) battery.	81
Table 4.5 – Parameters of the model of the li-ion battery developed in the software <i>PSIM</i> , used in the simulations of the bidirectional DC-DC converter.....	83
Table 4.6 – Limits for harmonic content emissions for equipment with RMS input current greater than 16 A (per phase) (source: IEC 61000-3-4, for simplified connection of equipment [stage 1]).....	93
Table 4.7 – Parameters used in the simulation of the fast charging operation in the G2V mode.	99
Table 4.8 – Main relevant characteristics of the currents obtained in the simulation of the fast charging operation in the G2V mode.....	100
Table 4.9 –Additional parameters of the simulations for the fast charging mode in the G2V mode with an extra inductor filter.....	102
Table 4.10 – Main relevant characteristics of the currents obtained in the simulations of the fast charging operation in the G2V mode, with an extra inductor filter.	103
Table 4.11 – Limits for emissions of harmonic content for class A equipment with input RMS currents less than 16 A per phase (source: IEC 61000-3-2).	111
Table 4.12 – Parameters used in the simulation of the fast charging operation in the G2V mode.	115
Table 4.13 – Parameters of the circuit used in the simulations of the DC-DC converter for the motor drive mode.	119
Table 5.1 – Flags responsible for the transition of states in the finite-state machine of the control system implemented in this MSc. Thesis.	125
Table 5.2 – Main characteristics of the <i>TMS320F28335</i> (source: [121])	130

Abbreviations

AC	Alternating Current
ACAP	<i>Associação Automóvel de Portugal</i>
ADC	Analog to Digital Converter
BEV	Battery Electric Vehicle
BLDC	Brushless DC
CCS-MPC	Continuous Control Set Model Predictive Control
CEPIUM	<i>Carro Elétrico Plug-In da Universidade do Minho</i>
DC	Direct Current
DCC-SRF	Direct Current Control based on Synchronous Reference Frame
DPC-MPC	Direct Power Control based on Model Predictive Control
DSC	Digital Signal Controller
DTC	Direct Torque Control
EMF	Electromotive Force
EPLL	Enhanced Phase-Locked Loop
ESR	Equivalent Series Resistance
EU	European Union
EV	Electric Vehicle
FCEV	Fuel-Cell Electric Vehicle
FCS-MPC	Finite Control Set Model Predictive Control
FOC	Field-Oriented Control
G2V	Grid-to-Vehicle
GEPE	Group of Energy and Power Electronics
GHG	Greenhouse Gases
HEV	Hybrid Electric Vehicle

ICE	Internal Combustion Engine
IDE	Integrated Development Environment
IEEE	Institute of Electrical and Electronics Engineers
IGBT	Insulated Gate Bipolar Transistor
ISR	Interrupt Service Routine
IWC	Infrastructure Working Council
LF	Loop Filter
MOSFET	Metal Oxide Semiconductor Field Effect Transistor
MPC	Model Predictive Control
PCB	Printed Circuit Board
PD	Phase Detector
PFC	Power Factor Correction
PHEV	Plug-In Hybrid Electric Vehicle
PI	Proportional Integral
PLL	Phase-Locked Loop
PMSM	Permanent Magnet Synchronous Machine
PWM	Pulse Width Modulation
RMS	Root Mean Square
SAE	Society of Automotive Engineers
SPI	Serial Peripheral Interface
SPWM	Sinusoidal Pulse Width Modulation
SRF	Synchronous Reference Frame
SRM	Switched Reluctance Machine
SSI	Synchronous Serial Interface
SVPWM	Space Vector Pulse Width Modulation
THD	Total Harmonic Distortion

USA	United States of America
V2G	Vehicle-to-Grid
VCO	Voltage-Controlled Oscillator
VSI	Voltage Source Inverter

Chapter 1

Introduction

1.1. General Motivations

According to the *World Population Prospects: The 2012 Revision* [1], published by the *United Nations*, at 2050 there should exist about 10.21 billion persons all over the world. This represents an increase of 40.8%, comparatively to the value of 7.25 billion estimated for 2014 (Figure 1.1).

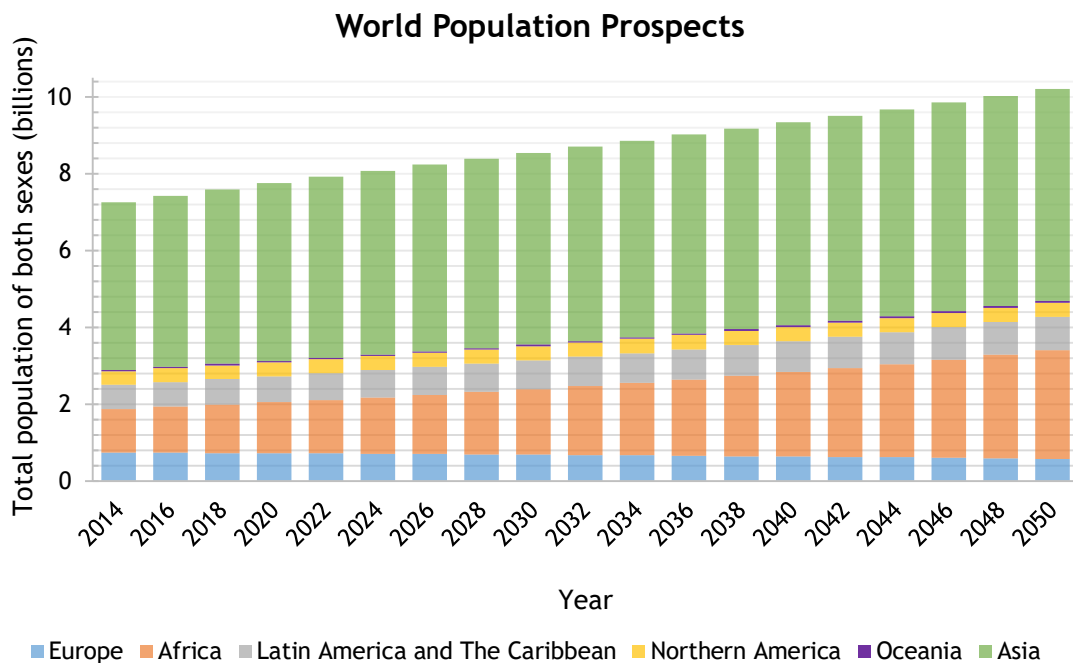


Figure 1.1 – World population prospects between 2014 and 2050, according to estimates provided by the United Nations [1], considering the scenario of no-change in the behavior of the evolution estimated between 1950 and 2010.

Related to this expected world population increase is the number of vehicles in circulation. According to the *Energy Technology Perspectives 2014* [2], published by the *International Energy Agency*, in 2050 the number of light duty vehicles in circulation on the planet will be around 2000 million. This represents an increase of 900 million (81.8%), with respect to nowadays. These predictions are incompatible with the actual scenario of large-scale use of conventional vehicles with Internal Combustion Engine (ICE) [3], [4].

On one hand, the fuel used for propel vehicles with ICE comes from oil resources, constituting a nonrenewable source of energy. Thus, an increase in the number of those vehicles leads to an increase on the fuel consumption and hence its availability can become compromised [3], [5].

On the other hand, the environmental concerns are growing around the world [6]. The vehicles with ICE are contributing to global warming, as result of the greenhouse gases (GHG) emitted (mainly carbon dioxide [CO₂]). Nevertheless, this vehicles also contribute to the degradation of the air quality, especially in densely populated urban areas. This is caused by the exhaust fumes, containing toxic gases to human health, such as nitrogen oxides (NO_x), carbon monoxides (CO), and unburned hydrocarbons (HC) [3], [5], [7], [8].

The fossil fuels dependence of nonproducing countries has also contributed to the search for alternatives to the use of vehicles with ICE [9].

Nowadays, the Electric Vehicle (EV) is emerging as the most sustainable alternative to support this expected rise in the number of vehicles in circulation, and to reduce the impact of the transportation sector on the environment [3], [10].

Despite contribute significantly to reduce the local air and noise pollution, the EVs do not ensure by themselves the reduction of the GHG emissions. Their contribution to that reduction is also dependent on the generation processes used to produce the electricity to charge their battery pack [9], [11]. Thus, it is also necessary promoting an electric energy generation based on energy sources with less impact on the environment, such as renewable energy sources [10], [11].

In [11], *Doucette et al.* concluded that in China and India, unless the power generation changes to processes with less CO₂ impact, the replacement of vehicles with ICE by EVs will not be able to reduce significantly the global pollution levels of those countries [10].

1.2. Electric Vehicle

In this section is introduced the concept of EV and its derivative concepts reported in the literature. Further is presented a brief description of the evolution of the EV from the beginning until nowadays, focusing on its position relatively to the vehicles with ICE. With respect to nowadays, the recent evolution of the market of EVs in Portugal is analyzed. Finally are described the main power electronics components of an EV, comprising the motor drive and the battery charger.

1.2.1. Understanding the Concept of Electric Vehicle

The EV is mentioned in [3] as being a road vehicle with electrical propulsion. Taking into account this assumption, there are currently a wide range of different types of EVs such as Battery Electric Vehicles (BEVs), Hybrid Electric Vehicles (HEVs), Plug-In Hybrid Electric Vehicles (PHEVs) and Fuel-Cell Electric Vehicles (FCEVs) [3], [8].

A BEV, also mentioned as pure EV [8], consists of an EV with only electric propulsion and whose energy is stored in a battery pack that is charged through the electrical grid, using a plug-in connector [8], [12].

A HEV is a vehicle that combines electric and ICE propulsion [3]. The battery pack installed on-board the HEVs is typically recharged by means of the ICE or through regenerative energy (i.e., without interacting with the electrical grid). There is also a different type of HEV known as PHEV, which results from a HEV having more electric range [13], due to the capability of the battery pack be charged from the electrical grid, using a plug-in connection, such as the BEVs [8], [14].

Finally, FCEVs are EVs that use a battery pack [15], but also fuel cells in order to produce electrical energy from hydrogen [14]. This technology has a long-term potential, but is still at an early stage of development [3].

The focus of this MSc. Thesis are the BEVs and thus, from now on in this document, the concept of EV will be referred to BEVs. This, however, does not invalidate that the solution proposed in this MSc. Thesis could it be applied to other types of EVs such as the PHEVs, since they are also charged by means of a connection to the electrical grid.

1.2.2. Brief History and Actual State

The invention of the EV dates from 1834 [8], but it was in the late of the 19th century that it began to be widely used, thanks to the mass production of batteries. The vehicles with ICE at that time were unreliable, since they were usually associated with a bad characteristic odor and the requirement of manual starting of the motor [3], [16].

Later, developments were done in ICEs, such as the arrival of the starter system in 1911. These innovations, along with the limitations of the batteries of EVs and the low oil price at that time, led to a reversal of roles. As a result, in the early 20th century, the vehicles with ICE came to be seen as a better option, leading to the decline of the EVs [16].

Although relegated to a smaller place, the investigation on EVs was never totally ruled out. In the 1970s some countries revived their interest in EVs, motivated by the energy crisis of 1973 [8], [17].

Nowadays, the EVs are emerging again [18]. This occurs after a period of disappointment for their mass-commercialization around the 1990s [18], as result of the still limited state of development of this technology, particularly with regard to the batteries. However, the developments in this technology, make the modern EV a new technology, totally different from the classic EVs [3].

Recently most well-known manufacturers of vehicles with ICE build their own models of EVs [19]. The *Renault ZOE* (Figure 1.2) and the *Nissan Leaf* (Figure 1.3) are some examples. Besides, they also developed EV versions of their well-known ICE-vehicle models, such as the *Smart Fortwo Electric-Drive* (Figure 1.4) and the *Volkswagen e-Golf*.

However, the EVs still have a very low market share comparatively to the ICE ones [18].



Figure 1.2 – *Renault ZOE* (gently provided by *Renault Portugal*).



Figure 1.3 – *Nissan Leaf* (gently provided by *Nissan Portugal*).



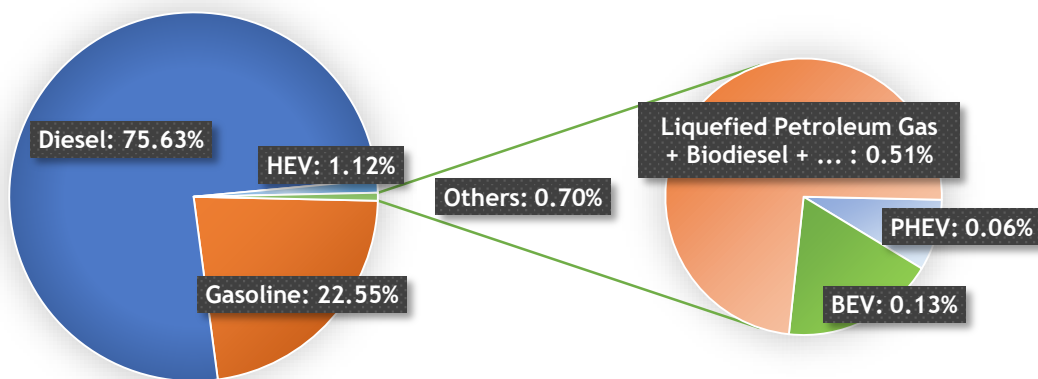
Figure 1.4 – *Smart Fortwo Electric-Drive* (gently provided by *Mercedes-Benz Portugal*).

Analyzing the Portuguese Market of Electric Vehicles

According to statistical data gently provided by the Portuguese Automobile Association (ACAP), the Portuguese market of EVs (considering BEVs, PHEVs and HEVs), represented only 1.31% of the vehicle sales during 2014 [Figure 1.5 (a)].

In 2010 the first BEV was sold in Portugal, while the peak in the sales of BEVs occurred during 2014, with a total of 216 BEVs sold [Figure 1.5 (b)]. This can be considered a good signal, especially after a fall period due to the European economic crisis. The most sold light duty BEVs in Portugal during 2014 are presented in Figure 1.5 (c).

Car Sales Per Type of Vehicle in Portugal During 2014



(a)

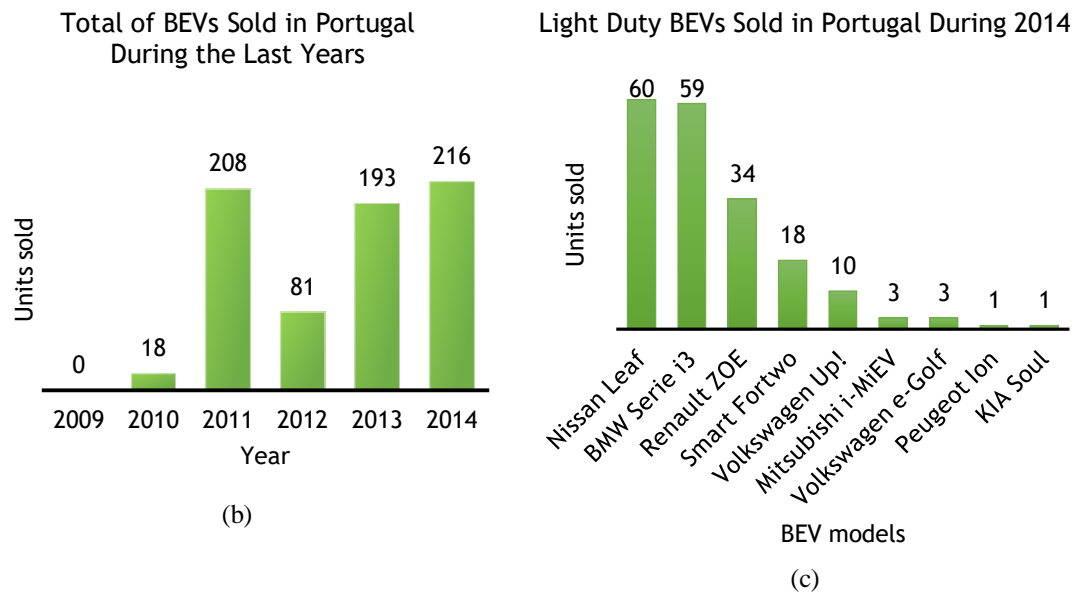


Figure 1.5 – Statistical data of the market of Electric Vehicles (EV) in Portugal (gently provided by ACAP): (a) Car sales per type of vehicle in Portugal during 2014; (b) Total of Battery Electric Vehicles (BEVs) sold in Portugal during the last years; (c) Light duty BEVs sold in Portugal during 2014.

The EVs have to increase their market representation and become widely used in order to have a significant impact on the environment [19]. Thus, there still important developments required in order to make the EV a strong alternative to the vehicles with ICE [20], [21].

The energy storage capacity and the time required for the charging process are, together with the cost of purchasing, the main limitations that contribute to the less attractiveness of the EVs [20], [21].

The energy storage system of an EV represents a significant part of its total cost, comparatively to a vehicle with ICE. Increase the range of an EV entails significant costs, due to the battery pack but also eventually other required changes in the hardware. Contrarily, in a vehicle with ICE the increase of its range typically only requires enlarging the fuel tank, which represents no significant added cost, considering the total cost of the vehicle [22].

The electric propulsion is more efficient than using an ICE, whose set composed by the ICE, gearbox and transmission system has an efficiency typically around 20% [16], [23]. Thus, an EV typically requires less energy stored than a vehicle with ICE. Besides that, an EV requires significantly less maintenance and repair than vehicles with ICE [3], [22].

However, as presented in Figure 1.6, the amount of specific energy (i.e., the energy stored per kilogram), of the fuel used to propel vehicles with ICE is typically around 9000 Wh/kg [16], while the specific energy of the a li-ion battery, a technology widely

used in commercially available BEVs [23], is around 90 Wh/kg [3], [24], representing only 1% of the specific energy of the fuel used in vehicles with ICE.

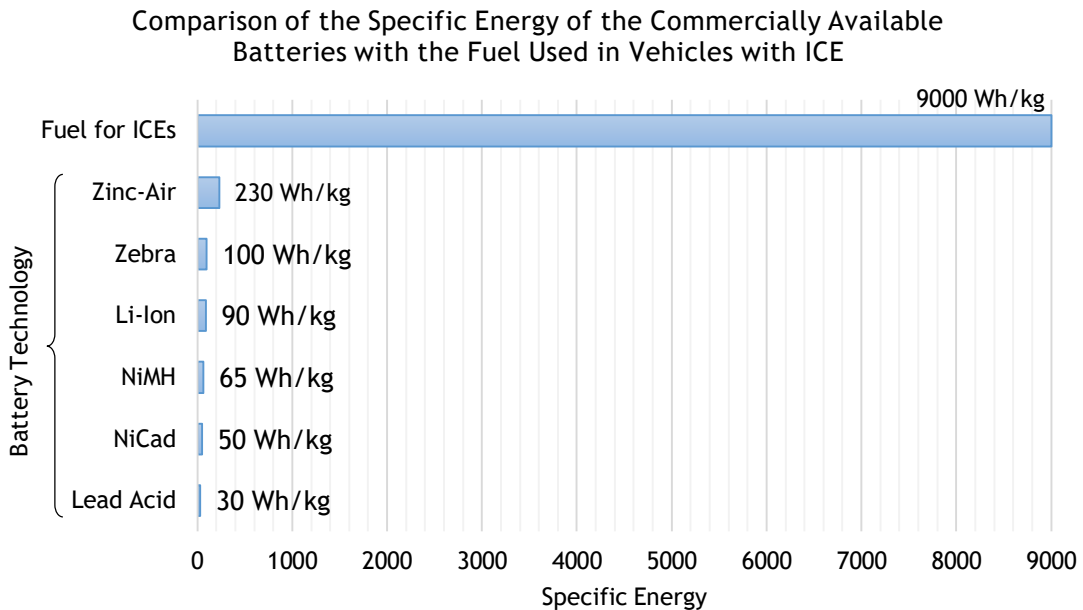


Figure 1.6 – Comparison of the specific energy of the commercially available batteries with the fuel used for propel vehicles with ICE (sources: [16], [24]).

Another drawback in the use of batteries is its limited life cycle [23] and thus they have to be replaced after a time period.

However, new battery technologies continue to be developed, stimulated by the competition for the development and mass commercialization of BEVs [18].

1.2.3. Motor Drive

The motor drive system is the core of the electric propulsion system [3], [5], [25], whose typical configuration is described in Figure 1.7. Its typical configuration comprises a three-phase Voltage Source Inverter (VSI) and a wye-connected three-phase AC electrical machine [20], [26].

An additional power stage comprising a bidirectional DC-DC converter is also considered in some cases [15], [21], [27]–[30]. This converter, placed between the battery pack and the DC-bus of the VSI (Figure 1.7), allows reducing the level of the voltage required at the terminals of the battery pack [31]. The transmission and differential systems can also be considered optional [3], taking into account that the electric propulsion system can be motor-in-wheel, i.e., with electrical machine directly coupled to the traction wheels.

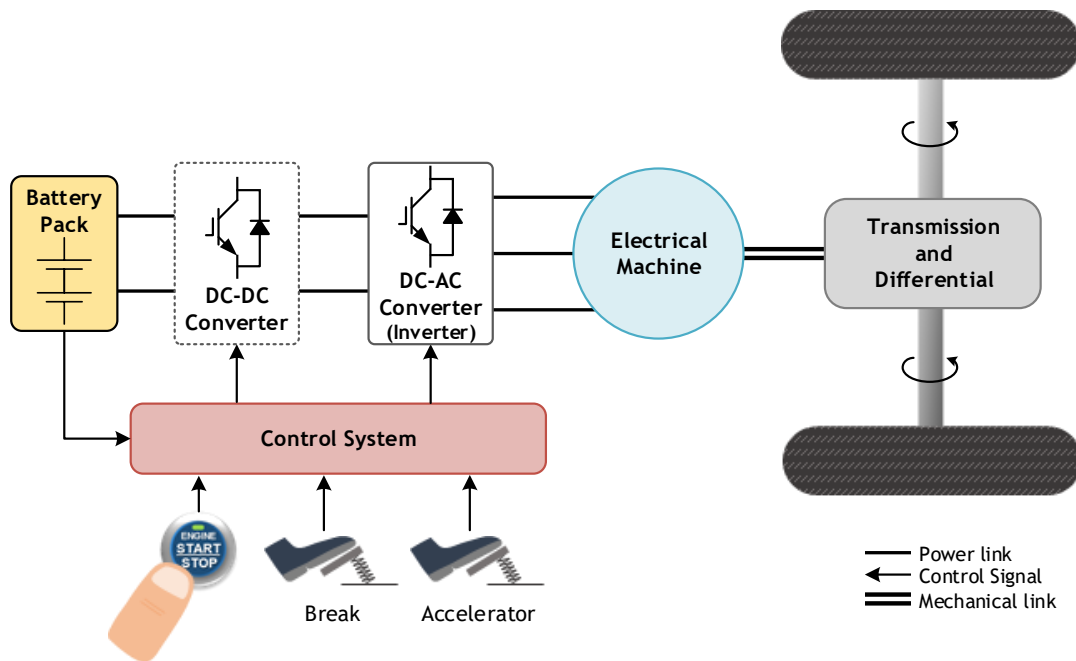


Figure 1.7 – Typical electric propulsion system of an EV, using an AC three-phase electrical machine (based on [27]).

There are motor drive systems with the additional feature of exploiting the energy released during downhill or breaking. This technology is known as regenerative braking [3]. It is responsible for converting kinetic energy, during breaking or downhill driving, to electric energy [32] that is used to recharge the battery pack of the EV, using the electrical machine as a generator [3], [32], [33]. Hence, this feature allows increasing the EV's range (typically between 8% and 25% [34]). For provide more efficient energy recover during those transient moments, the battery of the EV is usually used in conjunction with other energy storage systems, such as flywheels or ultracapacitors [3], [35], [36].

DC machines have been traditionally applied to EVs [3], [25]. They used to be preferred due to their torque-speed characteristic that fits with the ideal performance requirements for traction purposes, presented in Figure 1.8, and their simplicity on the speed control strategies [3], [25]. However, the use of DC machines requires periodic maintenance due to their commutators and brushes [25]. Thus, technological developments have led to commutatorless electrical machines becoming more preferable. Besides their performance, they have typically higher efficiency and reliability, higher power density, lower operating cost and practically a maintenance-free operation [3], [37].

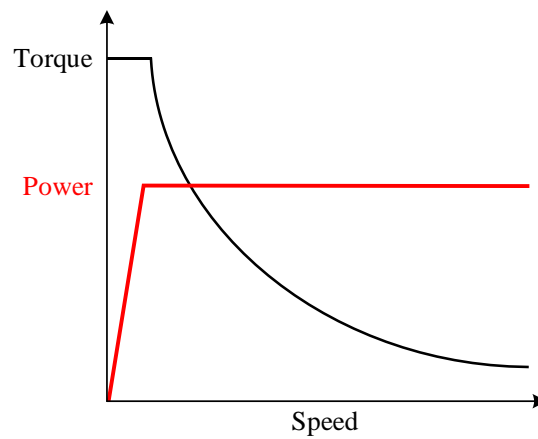


Figure 1.8 – Ideal performance characteristics for vehicle traction purposes (adapted from [38]).

1.2.4. Battery Charger

Batteries are the most common source of energy for EVs [14]. Therefore, were developed charging systems in order to provide the power supply, usually from the electrical grid, to charge its battery pack by means of a charging socket and a connector [39]. In Figure 1.9 is presented an example of a charging socket and connector used in the *Volkswagen e-Up!*.



Figure 1.9 – Charging socket and connector used in the *Volkswagen e-Up!* (gently provided by *Volkswagen Portugal – Siva*).

International organizations such as the Institute of Electrical and Electronics Engineers (IEEE), the Society of Automotive Engineers (SAE) and the Infrastructure Working Council (IWC) are responsible for develop standards and codes for the utility/costumer charger interface [12].

An EV has typically two types of battery charging: on-board and off-board (or standalone) charging system [40]–[42].

The on-board charging system is installed inside the vehicle and thus the cost, weight and space minimization are the main requirements considered [6], [43]. Hence, this system is commonly implemented using low-power converters [6], [43] (typically around 3 kW [26], [41]). Commercially available on-board chargers have a typical power density of approximately 0.6 kW/kg and a weight of 6.2 kg [31]. Hence, the charging has a typical duration of a few hours [44]. Unlike the off-board type, the on-board charging can be done in practically any location, as long as there is an electrical network outlet available [12], [26], [41], for level 1 (slow) charging [40]. Thus, this type of charging contributes to increase acceptance of EVs [45] and to reduce the cost of the infrastructure network for public charging [46], [47].

On the other hand, the off-board charging system uses power electronics converters built-in charging stations, with similar aspect to those used to refuel vehicles with ICEs [30], [46]. This system access directly the DC-bus of the battery pack [48]. Since it is not implemented inside the vehicle, it has lower restrictions than the on-board type. Thus, it is typically composed by higher power electronics converters, allowing thus to perform battery charging with a typically duration of less than 1 hour [44]. In Figure 1.10 two public off-board charging stations in Portugal are presented.



(a)



(b)

Figure 1.10 – Public off-board charging stations in Portugal: (a) Slow charging station in Azurém (Guimarães), with an installed power of 3.68 kW [49]; (b) Fast charging station in the service station of the freeway A5 (Oeiras), with an installed power of 55 kW [49] (gently provided by *Galp Energia* [Manuel Aguiar, *Balcão Digital Galp Energia*]).

There is also a middle-term charging system, provided by some manufactures of EVs that consists of installing a dedicated supply equipment (commercially known as

“wallbox” [50]), that allows for higher charging power using the on-board battery charging system. One example is the supply equipment provided by *Renault* (Figure 1.11) that can be installed in the garage for charging at home the *Renault ZOE*.



Figure 1.11 – Charging of a *Renault ZOE*, using a dedicated EV supply equipment installed (gently provided by *Renault Portugal*).

The main charging power levels, respective charger location and other relevant characteristics, applied to the European Union (EU) and United States of America (USA), are summarized in Table 1.1.

Table 1.1 – EV charging power levels (adapted from [12]).

Power Level Types	Charger Location	Typical Use	Energy Supply Interface	Expected Power Level	Charging Time	Vehicle Technology
Level 1 (Opportunity) \sim 230 V (EU) \sim 120 V (USA)	On-board (single-phase)	Charging at home or office	Convenience outlet	1.4 kW (12 A) 1.9 kW (20 A)	4-11 h 11-36 h	PHEVs (5-15 kWh) EVs (16-50 kWh)
Level 2 (Primary) \sim 400 V (EU) \sim 240 V (USA)	On-board (single-phase or 3-phase)	Charging at private or public outlets	Dedicated EV supply equipment	4 kW (17 A) 8 kW (32 A) 19.2 kW (80 A)	1-4 h 2-6 h 2-3 h	PHEVs (5-15 kWh) EVs (16-30 kWh) EVs (3-50 kWh)
Level 3 (Fast) \sim or \equiv 208-600 V	Off-board (3-phase)	Commercial, like fuel stations for ICE vehicles	Dedicated EV supply equipment	50 kW 100 kW	24 min – 1 h 12-30 min	EVs (20-50 kWh)

Legend: \sim - AC; \equiv - DC

The on-board charging system operates with an alternating current (AC). Thus, the charging system can be conductive or inductive. In a conductive charging system the power is transferred directly through metal contacts between the connectors, while in an

inductive charging system the power is transferred magnetically, offering thus more safety [12], [30]. In this MSc. Thesis only conductive on-board charging systems are considered.

A bidirectional power flow capability is also a relevant feature for a battery charger of an EV, since it provides some additional features [51], [52]. In addition to the normal battery charging process, known as Grid-to-Vehicle (G2V) operation mode, it also supports energy injection back to the electrical grid, known as Vehicle-to-Grid (V2G) operation mode, contributing thus to the development of the Smart Grids [12], [52]. Nevertheless, a bidirectional battery charger can also be used to supply home loads during power outages or to supply loads in places without connection to the power grid, known as Grid-to-Home (G2H) operation mode [52].

The battery charging of an EV is typically done by means of an electrical grid connection. Thus, foreseeing the growth of the popularity of the EVs in the near future [30], it must be considered their impact on the power quality of the electrical grid.

The typical configuration of a battery charger consists of an AC–DC converter [53]. This converter imposes a minimum voltage level for the battery pack, related with the peak of the grid voltage [52]. This restriction can be surpassed by placing a DC-DC converter between the DC-bus of the converter and the battery pack, such as for the motor drive system. On the other hand, using two power-stages helps fulfilling the requirements for a proper battery charging. In the first stage, composed by the AC-DC converter, it is ensured sinusoidal current consumption with unitary power factor, while in the second stage, composed by the DC-DC converter, the current and the voltage applied to the battery pack is controlled, according to the battery charging algorithm [52].

The focus of this MSc. Thesis is the battery charging using the power electronics on-board the vehicle. Thus, only two types of battery charging are considered: fast charging, by means of a three-phase grid connection, and slow charging, by means of a single-phase grid connection.

Typically, the EVs have also a small battery pack for feed auxiliary loads such as lights or air conditioning. Thus, the battery pack responsible for feeding the motor drive of the EV is frequently mentioned in the literature as traction battery [54], [55]. For simplifying, in this MSc. Thesis, the traction battery is simply referred as battery pack.

1.3. Problem Statement

Actually, the battery charger is one of the main technical and economical weaknesses of the EVs [56].

The on-board battery charging system is easier and convenient to use. However, the time required to the battery charging operation is still considerably higher than the time required using an off-board charging system or the time required to refuel the fuel tank of a vehicle with ICE [41], [56].

The typical electric device arrangement in an EV (presented in Figure 1.12) comprises two separate circuits for the motor drive and the on-board charger [30], [31].

During the charging process the vehicle is parked and so it is possible to use some of the hardware components of the motor drive system for the on-board battery charging. This is what is referred in this MSc. Thesis as a unified motor drive and battery charger. As a result, this integration process allows reducing the cost, weight and space occupied by the power electronics components inside the vehicle [6], [43].

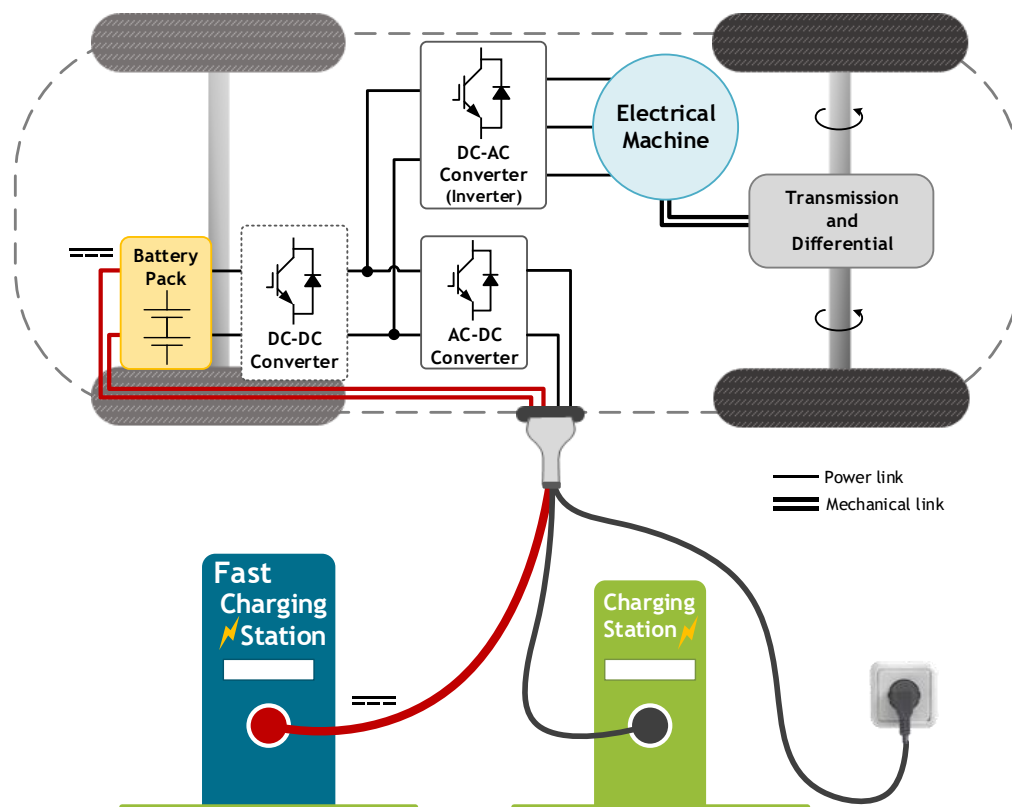


Figure 1.12 – Power electronics components typically installed on-board of an EV and some examples of sources for the battery charging operation.

1.4. Main Goals

The purpose of this MSc. Thesis is the development of a unified power electronics converter, capable of performing the roles of drive the electrical machine of an EV and also charging its battery pack, so as to optimize the space and weight of the power electronics components on-board the vehicle.

The unified converter has to be capable of drive the electrical machine of the vehicle and respond appropriately to the control actions performed by the user.

On the other hand, the battery charger should operate efficiently, with unity power factor and consuming currents with low harmonic content, in order to promote the power quality of the electrical grid. It also has to be capable of deliver back the energy stored in the battery pack to the electrical grid, operating in the V2G mode.

1.5. Relevant Contributions

This MSc. Thesis was developed in the Group of Energy and Power Electronics (GEPE), in the University of Minho. This is a research group whose main field of action is the application of power electronics to energy systems.

The electric mobility is one of the main research themes that the GEPE has been working during the last years, developing electronic power systems for EVs. An example is the project CEPIUM (Plug-In EV of the University of Minho, from the Portuguese *Carro Elétrico Plug-In da Universidade do Minho*), presented in Figure 1.13. It consisted in the conversion of a vehicle with ICE (a Volkswagen Polo 1.0L) into an EV.

Hence, first of all, this MSc. Thesis contributes to enhance the know-how of the GEPE, regarding to the electric mobility, potentiating the development of new solutions in this area.



Figure 1.13 – *Carro Elétrico Plug-In da Universidade do Minho* (CEPIUM), the EV developed in the University of Minho: (a) Overview; (b) Power electronics converters and control system implemented under the hood.

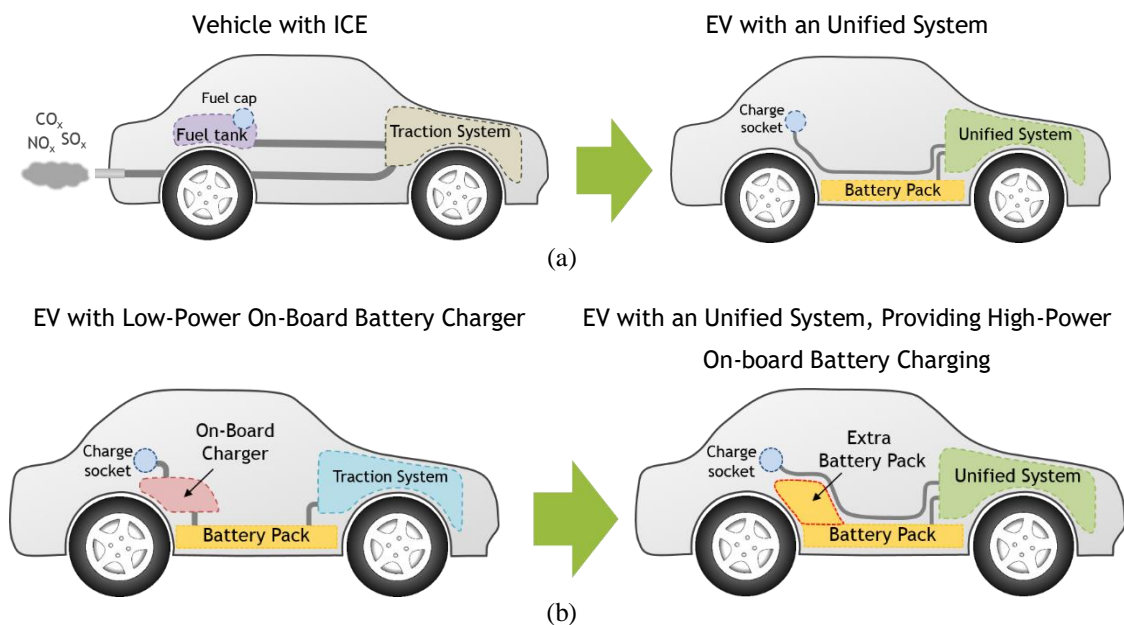
A unified solution based on the use of the power electronics components typically installed on the motor drive system of an EV contributes to potentiate a widely adoption of this solution.

Using the high power electronics components installed on the motor drive system for the battery charging operation allows for faster charging times, by means of a three-phase grid connection. Hence companies or even individuals having three-phase installations could charge their fleet of electric vehicles fast, in their own facilities and without the need of extra equipment.

One concern in this MSc. Thesis was to develop a solution that contributes to potentiate the conversion of vehicles with ICE [Figure 1.14 (a)]. A unified hardware could it simplify the conversion process, offering more advantages to their users such as less space required for the power electronics and a high-power battery charger.

On the other hand, a unified solution potentiates that an EV with a low power on-board charger installed could it be converted into an EV with a high-power on-board charger that occupies less space [Figure 1.14 (b)]. Such free space could it be used to install more battery cells, allowing for an increase of the vehicles' range.

Also the case of having an EV with no on-board charger installed can be considered. This vehicle can only be charged by means of a fast charging station. Thus, converting it into an EV with a unified hardware [Figure 1.14 (c)] provides on-board battery charging without requiring practically no extra space (e.g., the case of a HEV converted into a PHEV, providing thus more electric range).



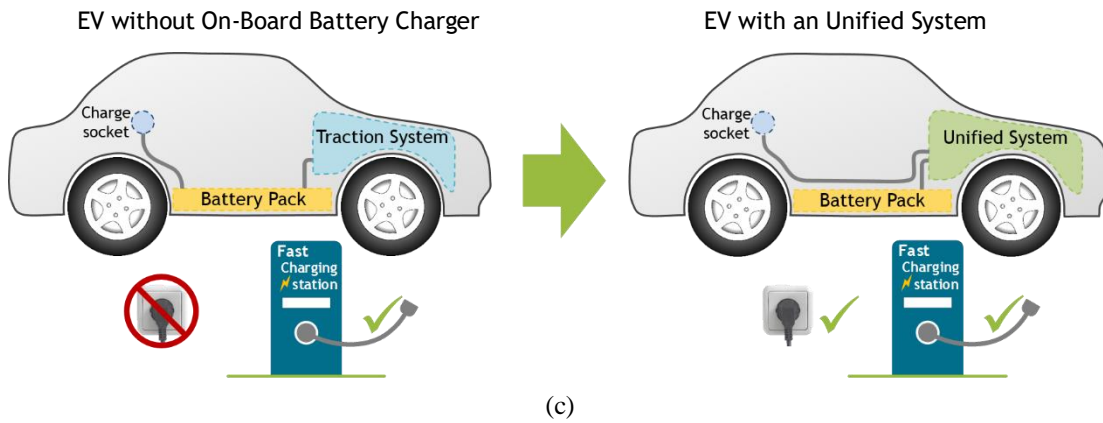


Figure 1.14 – Potentials of converting vehicles, using a unified motor drive and battery charger: (a): Considering a vehicle with ICE; (b) Considering an EV with a low-power on-board battery charger; (c) Considering an EV without on-board battery charger.

1.6. Outline of this MSc. Thesis

The other chapters of this MSc. Thesis are structured as follows:

- In **Chapter 2** the main relevant unified hardware topologies reported in the literature that integrate the functions of motor drive and battery charging are presented and discussed, as well as the unified solution proposed in this MSc. Thesis.
- In **Chapter 3** the main reported control algorithms for the battery charging and the motor drive modes that are compatible with the unified solution proposed are presented and discussed.
- In **Chapter 4** the main obtained simulation results of the proposed unified solution are described. There are also presented the proposed control algorithms for the battery charging and the motor drive modes.
- In **Chapter 5** the implementation of the power stage and the control system of a proof-of-concept prototype of the proposed unified solution is described.
- In **Chapter 6** the main obtained experimental results from the proof-of-concept prototype implemented are presented.
- Finally, in **Chapter 7** the main achievements of this MSc. Thesis are summarized and presented the suggestions of future work to be developed.

Chapter 2

Unified Topologies for Motor Drive and Battery Charging

2.1. Introduction

In this chapter the more relevant reported unified hardware topologies for battery charging and motor drive of an Electric Vehicle (EV) are reviewed and compared. This integration process allow to overcome the on-board battery charger issues, discussed in the previous chapter, by means of a total or partial use of the power electronics components of the motor drive system. Ideally, the goal is to have an on-board battery charger without requiring any extra hardware in addition to the components of the motor drive system. This results in what is typically mentioned in the literature as an integrated motor drive and battery charger or simply as an integrated charger [30], [57]. It is important to note that this is only possible considering that the motor drive and the battery charging operations cannot be performed simultaneously, except for regenerative braking [30].

The hardware typically implemented for the motor drive system of an EV is presented in Figure 2.1. It is based on an AC electrical machine, a three-phase Voltage Source Inverter (VSI) and also an optional DC-DC converter [58], as discussed in the previous chapter.

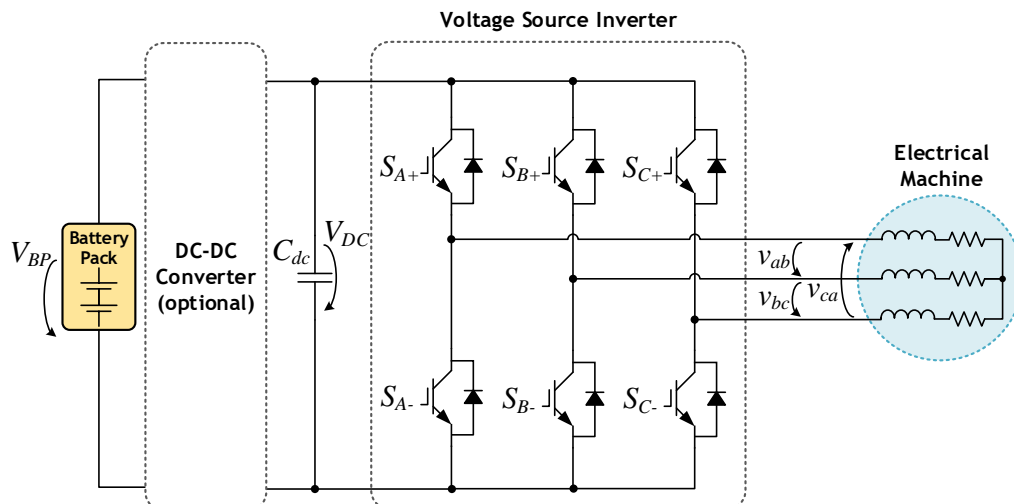


Figure 2.1 – Typical hardware topology of the motor drive system of an EV.

In a three-phase VSI only one power semiconductor of each leg can be active at each instant. This prevents the occurrence of a short circuit with the DC-bus, where the capacitor C_{dc} is placed (Figure 2.1). Thus, there is a limited number of allowed switching states that are presented in Table 2.1.

Table 2.1 – Allowed switching states for the power semiconductors of a VSI (adapted from [59]).

S_{A+}	S_{B+}	S_{C+}	S_{A-}	S_{B-}	S_{C-}	v_{ab}	v_{bc}	v_{ca}
OFF	OFF	OFF	ON	ON	ON	0	0	0
ON	OFF	OFF	OFF	ON	ON	$+V_{DC}$	0	$-V_{DC}$
ON	ON	OFF	OFF	OFF	ON	0	$+V_{DC}$	$-V_{DC}$
OFF	ON	OFF	ON	OFF	ON	$-V_{DC}$	$+V_{DC}$	0
OFF	ON	ON	ON	OFF	OFF	$-V_{DC}$	0	$+V_{DC}$
OFF	OFF	ON	ON	ON	OFF	0	$-V_{DC}$	$+V_{DC}$
ON	OFF	ON	OFF	ON	OFF	$+V_{DC}$	$-V_{DC}$	0
ON	ON	ON	OFF	OFF	OFF	0	0	0

There is a wide range of proposed unified hardware topologies for motor drive and battery charging of EVs [28], [30], [40], [47], [54]. In order to avoid digressing from the focus of this MSc. Thesis, in this chapter are only presented and discussed the main relevant solutions based on the use of the power electronics components typically already installed for the motor drive system of an EV, i.e., one AC electrical machine and a three-phase VSI (Figure 2.1). Thus, unified topologies developed for motor-in-wheel EVs or that require more than one electrical machine are not considered, since it would result in a significant increase of cost and weight for the typical configuration considered.

A first approach into the solutions that have been reported allow to distinguish them into two categories: solutions providing an isolated battery charger and solutions providing a non-isolated battery charger [47]. These solutions can also be categorized in terms of “integration levels”, which are related with the amount (total or partial) of the power electronics components of the motor drive system that are also used for the battery charging. In this MSc. Thesis two integration levels are considered, regarding to non-isolated battery charging solutions. The level 1 refers to topologies in which the power electronics converter of the motor drive system (typically the three-phase VSI) is used for the battery charging. Besides the power electronics converter, the topologies of level 2 also include the use of the electrical machine, more specifically its windings to operate as inductors during the battery charging operation.

The reported unified solutions providing isolated battery charging typically use both the power electronics converter and the electrical machine of the motor drive system.

These solutions typically consist of using a special kind of electrical machine, such as a wound-rotor induction machine or a split-windings Permanent Magnet Synchronous Machine (PMSM).

Taking into account the last presented considerations, the unified hardware topologies that are presented and discussed in this chapter were grouped and categorized according to Figure 2.2.

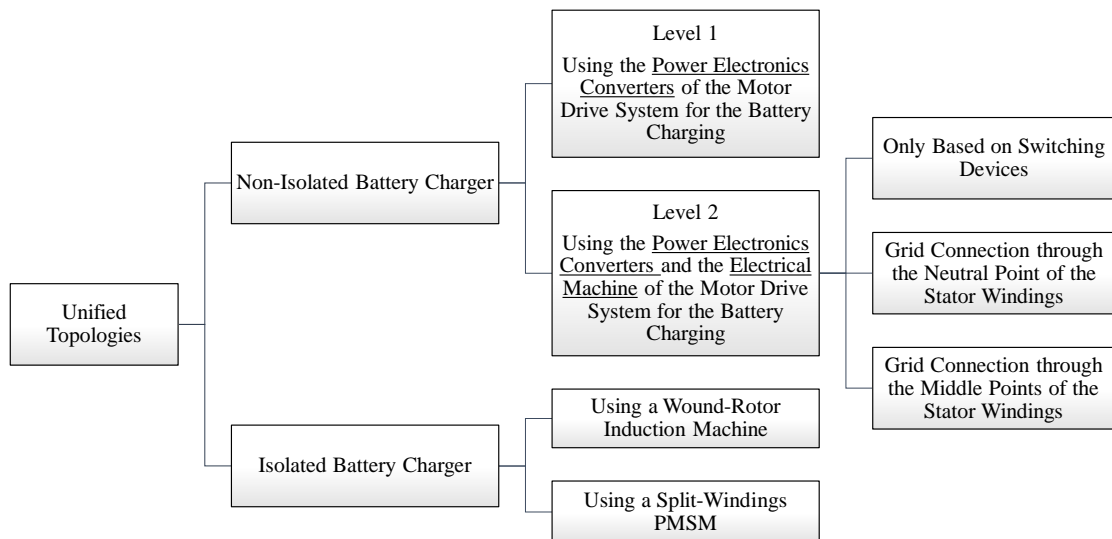


Figure 2.2 – Diagram, synthesizing the reported unified topologies studied in this MSc. Thesis.

2.2. Non-Isolated Battery Charger

The isolation is one of the most important aspects regarding to the battery charging. A battery charger can operate isolated or non-isolated from the electrical grid. Isolated chargers are preferred for safety reasons but due to its impact on the vehicles' cost and weight they are usually avoided. Thus, most of the reported integrated chargers are non-isolated [41], [43].

All the following discussed topologies that allow for fast charging, through an AC three-phase grid supply, are also compatible with slow charging, through an AC single-phase grid supply. Typically for slow charging only some modifications in the control algorithm are required and less amount of power electronics components are used.

2.2.1. Level 1 – Using the Power Electronics Converters of the Motor Drive System

A review of three-phase AC-DC converters with improved power quality is presented in [60]. These converters can be implemented for the battery charging operation. One of the presented converters is a three-phase three-wire boost AC-DC converter, which is shown in Figure 2.3. This converter is very similar to the three-phase

VSI, typically installed in the motor drive system (Figure 2.1). The majority of the unified hardware topologies discussed in this MSc. Thesis are based on this fact, considering the use of the VSI of the motor drive system to act as an active rectifier during the battery charging mode.

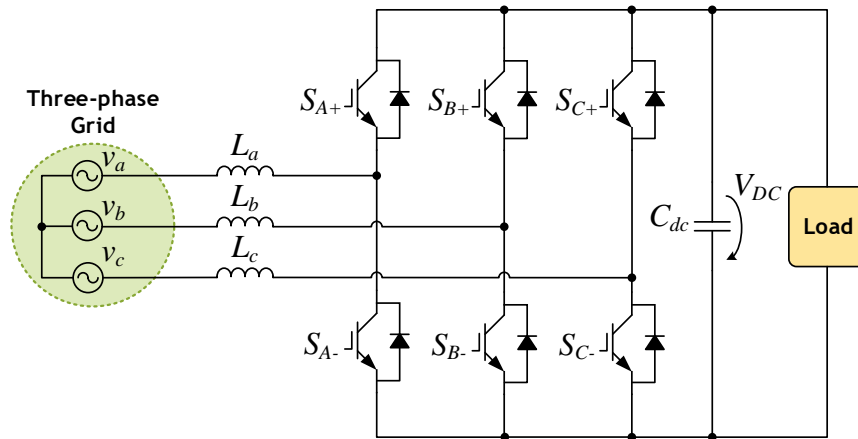


Figure 2.3 – Three-phase three-wire boost AC-DC converter (adapted from [60]).

A simple topology that concretizes this principle is discussed in [46] and presented in Figure 2.4. This topology is compatible with fast charging, through an AC three-phase grid supply. In order to prevent the injection of high magnitude harmonics in the electrical grid and to achieve unity power factor operation [46] it requires the addition of an input filter, composed by three high-current inductances, representing a significant amount of space and weight occupied [54], [61].

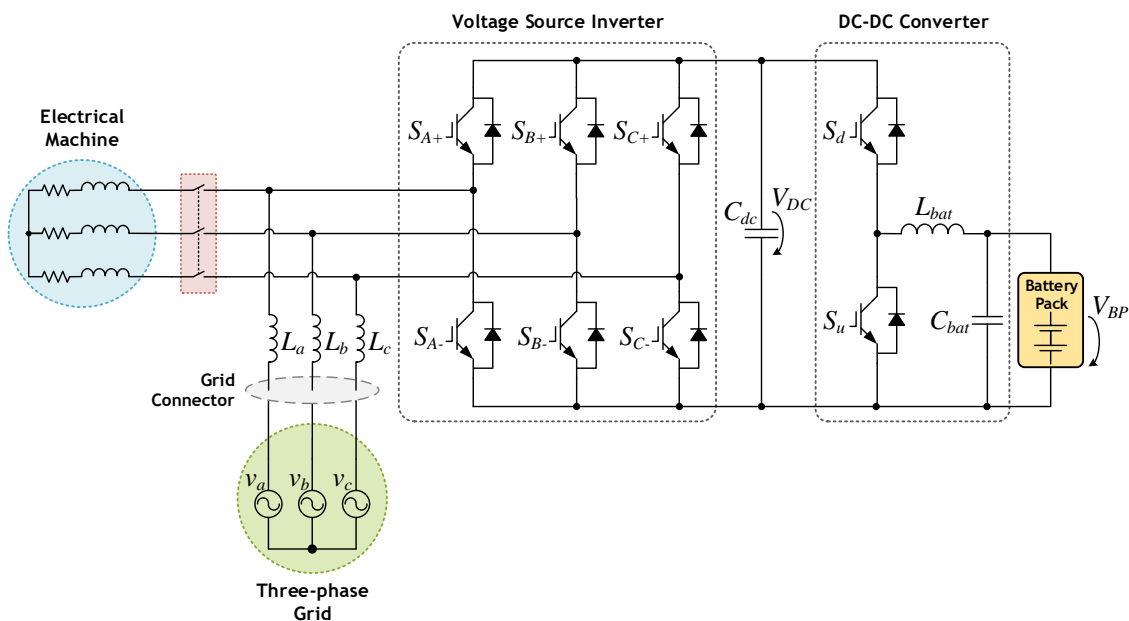


Figure 2.4 – Unified topology with non-isolated battery charger, discussed in [46], based on using three additional filter inductors and three relays contacts.

This solution requires three relays contacts, for disconnecting the electrical machine during the battery charging. On the other hand, it has bidirectional power compatibility, supporting energy injection back to the electrical grid. One interesting feature is that it is compatible with electrical machines wye-connected without the neutral point accessible, i.e., it is compatible with electrical machines without all terminals of the windings accessible.

The issue of the weight and space occupied by the on-board inductor filter is solved in [58], by placing it in a dedicated EV supply equipment. *Rodrigues et al.* propose to use only two legs of the VSI of the motor drive system, operating as a single-phase active rectifier for the battery charging. Hence, it only allows for slow charging. However, the proposed topology can be easily adapted for fast charging, by using all the three legs of the VSI and installing three high-current inductances in the EV supply equipment, instead of only one. This solution has the drawback of limiting the available sources for the battery charging operation, since it can only be performed in places where the proposed supply equipment is installed.

The generally of the reported level-1 topologies consists of using the three-phase VSI of the motor drive system, operating as a single-phase or three-phase active rectifier. However, there are other types of solutions, such as in [31], [62], in which the shared power electronics converter is not the VSI but the bidirectional DC-DC converter, placed between the DC-bus and the battery pack.

Dusmez et al. propose in [31] a multi-purpose converter, combining on-board battery charger and a DC-DC converter for the motor drive. In this case, the inductor typically installed at the DC-DC converter is used for the battery charging operation. However, as a result, this solution only allows for slow charging, through an AC single-phase grid supply. On the other hand, this topology is only applicable if a DC-DC converter is required, which is dependent on the battery pack characteristics. Also does not support bidirectional power flow and fast charging. This solution is also characterized by a poor exploitation of the motor drive hardware, since it does not uses the VSI and it requires to change or replace the typical DC-DC converter already installed into a new combined topology, presented in Figure 2.5.

The proposed multi-purpose converter operates as a DC-DC converter for the motor drive operation and as an AC-DC converter for the battery charging [31]. Hence, during the battery charging a DC-DC converter is not available and so it requires that the voltage of the battery pack has to be higher than the peak value of the AC single-phase grid voltage [31]. This issue is solved in [62], by adding an on-board transformer between the

grid and the converter, in order to reduce the input AC voltage level. However, although providing isolation for the battery charging, resulting in a different type of topology, this solution is not considered, since it results in a significant increase of the weight on-board the vehicle.

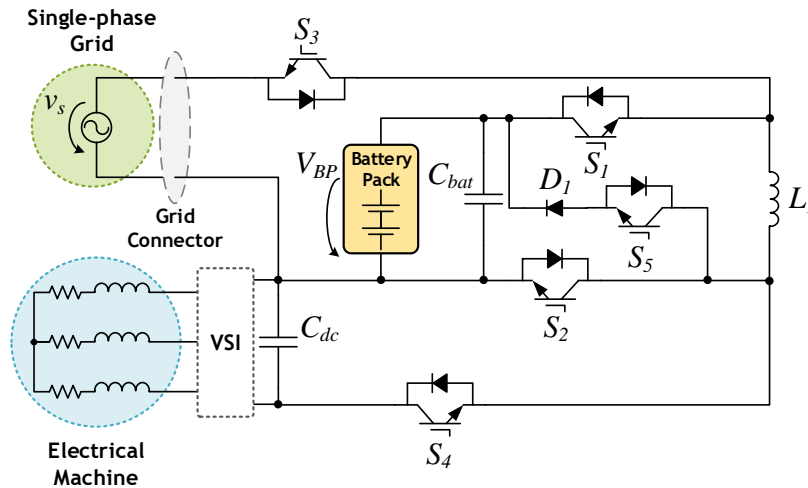


Figure 2.5 – Unified topology with non-isolated battery charger, discussed in [31], combining the features of DC-DC bidirectional converter for motor drive and AC-DC converter for on-board battery charging.

There are other types of solutions that involve modifications on the available motor drive hardware for integrating the battery charging operation. An example is presented in [27], in which the VSI of the motor drive system is incorporated into a new topology that encapsulates the VSI, the bidirectional DC-DC converter and the on-board charger into a single module. This solution does not allow taking advantage of the already installed hardware, if a DC-DC converter already exists. However, if a DC-DC converter is not already present in the vehicle it has the advantage of allowing reduce the voltage level of the battery pack [31]. As drawbacks this solution requires a higher number of power semiconductors that are conducting simultaneously, comparatively to the other already presented solutions, which leads to more power losses. Despite, it also requires an input filter, composed by a single inductor for a battery charging with high power factor and consuming currents with low harmonic content. This topology does not allow for fast charging but it provides bidirectional power capability, allowing Vehicle-to-Grid (V2G) and Vehicle-to-Home (V2H) operation modes.

In [42] it is proposed to adding two more power semiconductors upper the three-phase VSI (one at each leg, for the two rightmost legs of the VSI), resulting in an eight-switch inverter. Like the last discussed topology it has bidirectional power flow capability but it requires an input filter, composed by a single inductor. Also only allows for slow charging mode and has a higher number of power semiconductors conducting

simultaneously, comparatively to the other analyzed solutions, leading to higher power losses.

2.2.2. Level 2 – Using the Power Electronics Converters and the Electrical Machine of the Motor Drive System

The level-2 topologies have the potentiality of maximizing the unifying process, since more components of the motor drive system are used for the battery charging operation. Thus, practically no space is required for implementing the on-board battery charging system.

The major issue of level-1 solutions is concerned with the filter inductors. These are required for a battery charging operation with unity power factor and consuming currents with low harmonic content, contributing to the power quality of the electrical grid. Thus, they need to be installed on-board the vehicle or eventually in a dedicated supply equipment. In level-2 solutions this issue is proposed to be solved by using the stator windings of the electrical machine to operate as inductors, during the battery charging operation [28]. The high-current inductors are large components, comparatively to the other power electronics components required, such as the power semiconductors [28], [30]. Thus, this type of solutions allows saving the space occupied by the filter inductances, contributing to reduce the weight and space occupied by the power electronics components on-board the vehicle.

The use of the stator windings of the electrical machine in the battery charging operation has associated some concerns. The magnetic fields generated by the currents flowing through the windings of the stator interact with the magnets of the rotor. The result of such interactions can range from simple vibrations to the rotation of the machine, depending on the type of electrical machine used, leading to security issues [50], [57]. Thus, the main challenge is to ensure the magnetic decoupling between the stator and the rotor, so that the vehicle does not move during the battery charging [57]. There are cases in which that condition is not possible to ensure, requiring a mechanical system, typically a clutch system, to operate during the battery charging, disconnecting the rotor from the transmission system of the vehicle [28].

The reliability of using the electrical machine in the battery charging operation can lead to an increase of the complexity of the control algorithms. This results from the fact that there is a magnetic coupling between the inductances of the electrical machine, described in terms of mutual inductances [63]. The leakage inductances, also known as self-inductances [57], represent the part of the inductances that has no coupling to the other inductances [54]. Thus, the performance of the charging operation will be affected

by the all inductance matrix, comprising leakage and mutual inductances [57], [63]. Due to this coupling, the control of the current flowing through one winding can influence on the currents flowing through the other windings [63]. In the case of using electrical machines having salient poles, the values of the inductances (leakage and mutual) can have small variations, according to the rotor position, due to effects of saliency [63], [64].

Ideally, the purpose of this level of unified topologies is to eliminate all the input filter inductors required. However, this goal is dependent on the inductances' values of the electrical machine. If the values of the inductances of the windings were are not sufficiently high it can result in a battery charging operation with an input current with high ripple [57]. When that occurs, this type of solutions cannot replace the total input filter, only allowing reduce its size [65]. Nevertheless, in some situations, this issue can be overcome depending on the characteristics of the electrical machine, by using a special winding arrangement [20], as it will be discussed further in this chapter.

In the last discussed topologies, the power of the charger was only dependent on the capability of the power electronics components of the VSI. However, since the electrical machine is also used, the power of the battery charger would it be also limited by the characteristics of the electrical machine, such as its thermal limits. [28], [47].

The majority of the reported level-2 solutions can be distinguish into three different categories: (i) Only Based on Switching Devices; (ii) Grid Connection through the Neutral Point of the Stator Windings; (iii) Grid Connection through the Middle Points of the Stator Windings.

Level-2 Solutions Only Based on Switching Devices

In 1994, *AC Propulsion Inc.* patented a solution [66], which is currently in use in the car industry, based on the use of the windings of an induction machine. This solution, shown in Figure 2.6, proposes the use of relays contacts in order to reconfigure the windings of the electrical machine. For the battery charging operation, through an AC single-phase grid supply, two windings of the electrical machine are used as inductances [54], indicated in Figure 2.6 as L_{sa} and L_{sb} .

In order to guarantee unity power factor operation, it is mentioned in [54] that the voltage of the battery pack must be higher than the peak value of the voltage of the AC supply. However, as discussed before, this restriction can be easily surpassed by adding an additional stage between the VSI and the battery pack, consisting of a DC-DC converter, which is already presented in Figure 2.6.

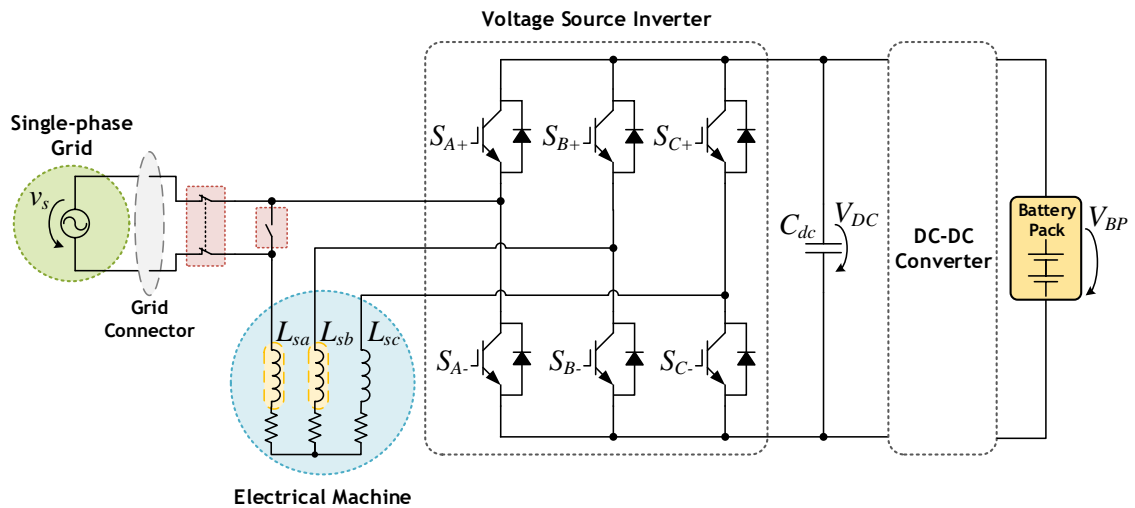


Figure 2.6 – Unified topology with non-isolated battery charger, discussed in [66], based on using two stator windings as filter inductors for slow charging.

The relays contacts, presented in Figure 2.6, are required for security issues. They avoid the occurrence of a short circuit due to a grid connection when the relay contact between the inductance L_{sa} and the leg of the VSI is accidentally closed.

The proposed solution has bidirectional power flow capability, allowing V2G and V2H operation modes. However, it is not compatible with fast charging, through an AC three-phase grid supply. Nevertheless, it can be adapted for fast charging, resulting in the solution discussed by *Zaja et al.* in [19], whose equivalent circuit for the battery charging mode is presented in Figure 2.7.

The proposed alternative topology for fast charging has some restrictions. If using an asynchronous machine, such as an induction machine, the grid connection of all three windings of the stator will lead to the creation of a rotating magnetic field that will develop such a torque that will force the machine to rotate [19]. Thus, it will require a mechanic clutch system to disconnect the rotor of the electrical machine from the transmission system of the vehicle, during the battery charging operation. On the other hand, this topology can be implemented without requiring practically any extra hardware, by using for instance a PMSM [19], since a synchronous machine is not capable of rotating when directly connected to the grid (i.e., without the synchronism process), from the stationary state. Thus, the electrical machine would not be capable of rotating during the battery charging operation [19].

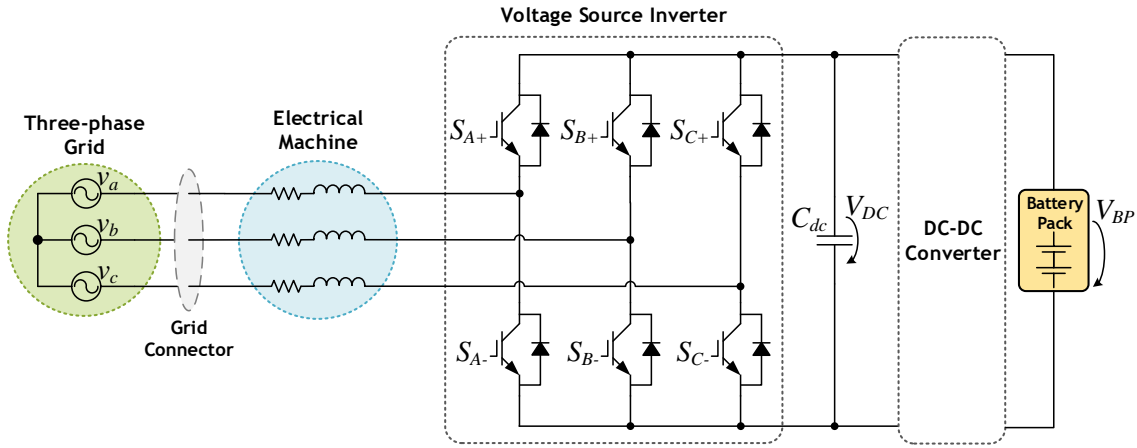


Figure 2.7 – Equivalent circuit for the battery charging mode of the unified topology with non-isolated battery charger, discussed in [19], based on using all the stator windings as filter inductors for fast charging.

It is important to note that, even using a PMSM, the currents flowing through the windings results in the creation of magnetic fields in the stator that can induce undesirable vibrations at the rotor of the machine. Those vibrations typically do not correspond to the development of any significant torque, besides, taking into account that the rotor will be loaded by the weight of the vehicle, they will be attenuated and therefore no additional mechanical blockade should be required [19], [50].

As mentioned before, the values of the inductances of the windings can vary according to the rotor position [19] in the case of using a synchronous machine with salient poles [63], [64]. This issue is verified in [63] using a synchronous machine constituted by buried magnets (i.e., whose magnets are placed inside the rotor [67]). In [19] this issue is discussed for a PMSM, where this variation is defined using the d -axis and q -axis stator inductances that are defined in terms of inductance mean, described in (2.1), and inductance variation, described in (2.2).

$$\bar{L} = \frac{L_d + L_q}{2} \quad (2.1)$$

$$\tilde{L} = \frac{L_d - L_q}{2} \quad (2.2)$$

The defined variables allows establishing, in a simplified method [19], each inductance value per phase, according to (2.3), (2.4) and (2.5), where p represents the number of poles of the electrical machine and θ_r the rotor angle (in radians).

$$L_u = \bar{L} + \tilde{L} \cos(p \theta_r) \quad (2.3)$$

$$L_b = \bar{L} + \tilde{L} \cos\left(p \theta_r - \frac{2\pi}{3}\right) \quad (2.4)$$

$$L_c = \bar{L} + \tilde{L} \cos\left(p \theta_r + \frac{2\pi}{3}\right) \quad (2.5)$$

For charging the battery pack of the EV, the rotor of the electrical machine can be stopped at any position. *Zaja et al.* analyze the worst possible scenario for a PMSM, i.e., the situation where the inductances values are more dispersed. For that purpose, a vector \vec{L}_0 is defined in [19] according to (2.6).

$$\vec{L}_0 = L_d + L_b e^{j\frac{2\pi}{3}} + L_c e^{-j\frac{2\pi}{3}} \quad (2.6)$$

Consequently, the rotor position having the highest inductances differences is obtained calculating the absolute value of \vec{L}_0 , which represent the amount of system unbalance [19], using (2.3), (2.4), (2.5) and (2.6). The final obtained result is presented in (2.7) and its demonstration is described in Appendix A.

$$|\vec{L}_0| = \frac{3}{4}(L_d - L_q) \quad (2.7)$$

The obtained result demonstrates that although the inductances values varies, its maximum unbalance is not dependent on the rotor position and remains the same, according to the L_q and L_d values.

However, the performance of the control algorithm for the battery charging can be affected by the individual variation of the values of the inductances. This variation can result in unbalances in the current consumed, since the electrical grid acts like a voltage source [19].

Although allowing fast charging, this topology requires access to all the terminals of the windings of the electrical machine. However, there are electrical machines that do not comply with that requirement. One example of that is the electrical machine used by our research lab GEPE in the project CEPIUM, whose characteristics are described in [35], [68], [69], consisting of a wye-connected PMSM whose neutral point is not accessible. This fact makes the presented solution infeasible. Considering this issue, a solution is proposed in [46] and presented in Figure 2.8. It consists of a “middle-term” topology, between the last discussed topology (using all three windings) and the level-1 solution presented requiring three extra high-current inductors. In this case, instead of

require three extra high-current inductors, it only requires two of them. The accessible two end-points of the windings of the electrical machine allows using the electrical machine as the third inductor [46]. This solution is also very similar to the first-presented level-2 solution. However, this topology allows fast charging, through an AC three-phase grid supply.

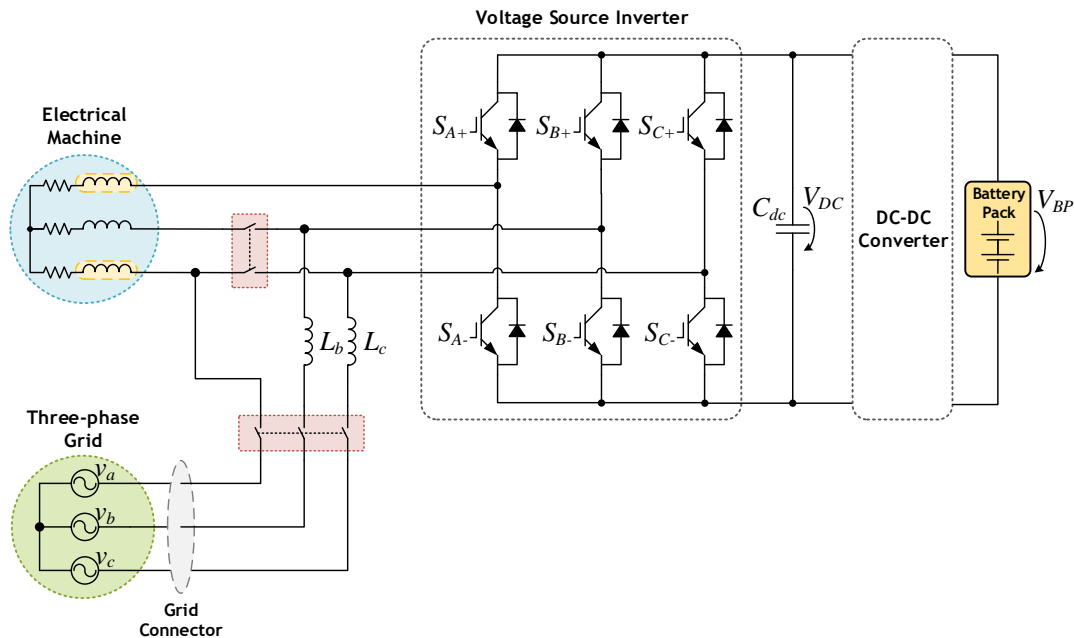


Figure 2.8 – Unified topology with non-isolated battery charger, discussed in [46], providing fast charging and adapted to electrical machines wye-connected without the neutral point accessible.

In [57], *Hagbin et al.* propose a solution based on the use of a slip-windings PMSM. It consists of an electrical machine having the double of stator windings per phase (e.g., having two windings per each phase instead of one, considering a two-pole three-phase machine). This solution is compatible with any phase-shift between each set of the windings of the same phase and it has bidirectional power flow capability.

The proposed hardware topology is presented in Figure 2.9 (a). It is composed by a more complex switch-based mechanism that reconfigures the windings of the electrical machine, according to the operation mode (motor drive or battery charging). Thus, for a better understanding, the equivalent circuits for motor drive and battery charging are presented respectively in Figure 2.9 (b) and (c).

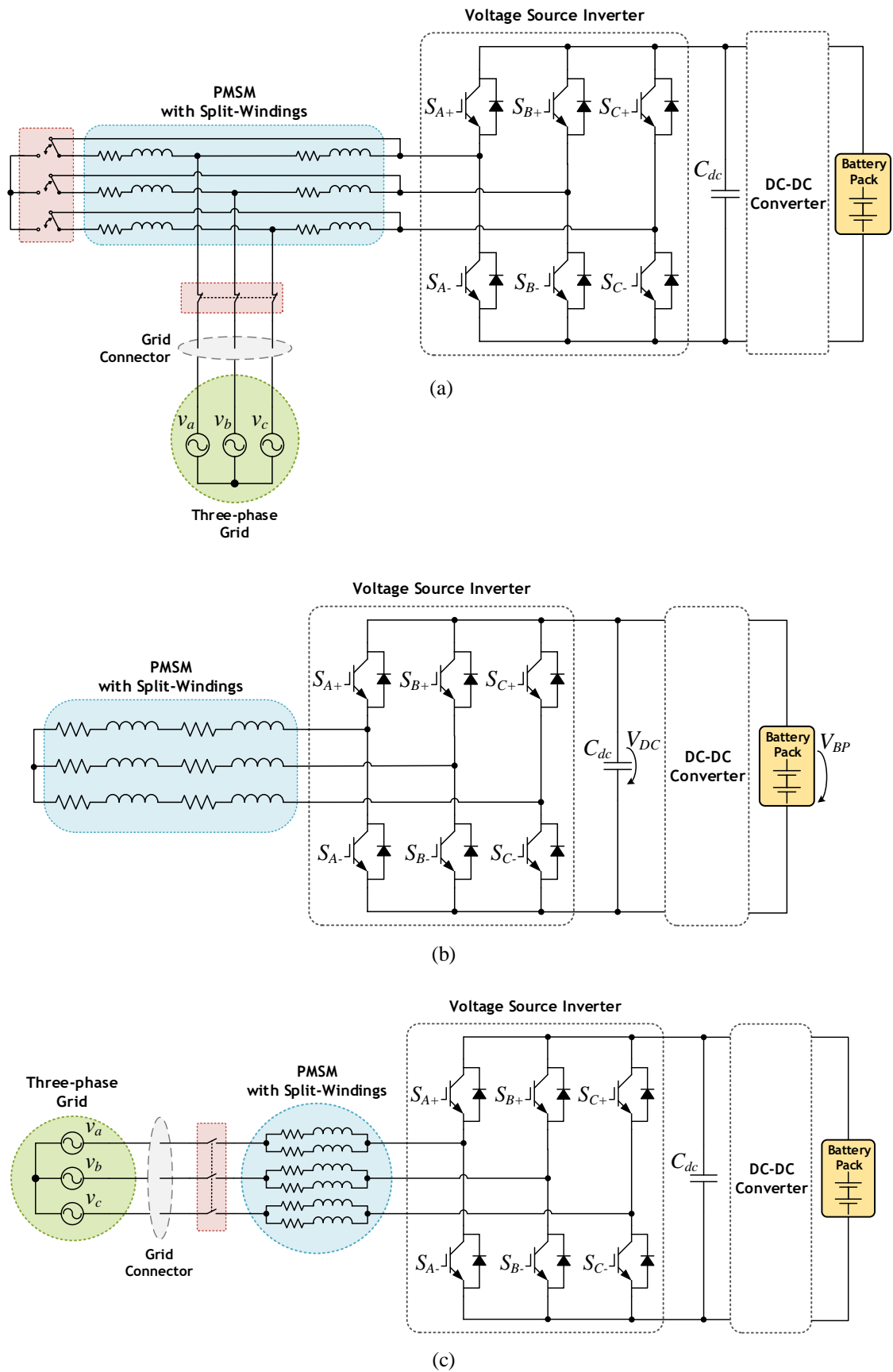


Figure 2.9 – Unified topology with non-isolated battery charger, discussed in [57], based on using a split-windings Permanent Magnet Synchronous Machine (PMSM): (a) Proposed hardware topology; (b) Equivalent circuit for motor drive; (c) Equivalent circuit for battery charging.

For the battery charging operation mode, the split-stator windings of each phase can be connected in a series or a parallel configuration. A parallel configuration allows increasing the power of the battery charger (considering that the power electronics components of the VSI can handle it), since it supports twice of the rated current of the electrical machine. However, the equivalent leakage inductance is half of the leakage inductance of each split-winding, and thus the ripple of the input current is expected to be higher (for the same switching frequency) [28], [57]. On the other hand, connecting the split-windings of each phase in a series configuration allows to duplicate the value of the leakage inductance per phase, corresponding to four times the equivalent leakage inductance of the parallel configuration and thus resulting in less ripple of the input current. However, in opposition, the maximum power of the charger is lower [28], [57]. This choice constitutes a special winding arrangement that allows improving the battery charging operation. In this case [57], a parallel configuration of the windings was chosen.

Nevertheless, the performance of the battery charging operation is not only compromised by having low values of inductances. Also too high values of inductances can lead to control and power transfer problems due to the large voltage drop that occurs in the inductances [57].

It is important to note that the values of the leakages inductances used for the battery charging are not the only condition required to ensure the proper operation of the battery charger. For instance, the higher the switching frequency of the power semiconductors, the smaller the values of the leakage inductances can be, for achieve the same results. That occurs due to the fact that the inductive reactance X_L , defined by (2.8), depends not only on the value of the inductance, but also on the switching frequency. However, it is important to note that increasing the switching frequency leads to an increase of the power losses during the switching of the power semiconductors.

$$X_L = 2\pi f_s \quad (2.8)$$

The use of relays contacts has typically advantages in the cost, since they have a lower price than the switches based on power semiconductors, despite having a shorter life time [28].

Level-2 Solutions Based on the Grid Connection through the Neutral Point of the Stator Windings

Another type of level-2 solution is based on the grid connection through the neutral point of the electrical machine. Some example are discussed in [29], [45], [70], [71]. The

typical hardware topology using a single electrical machine is discussed in [45] and presented in Figure 2.10.

Naturally, the access to the neutral point of the stator windings of the electrical machine is the mandatory criterion for implementing this kind of solutions.

For the battery charging operation, the three-phase VSI together with the windings of the electrical machine act as a Step-Up (Boost) DC-DC converter, resulting in the equivalent circuit presented in Figure 2.11. The VSI operates as a single switch, i.e., the lower power semiconductors S_{A-} , S_{B-} and S_{C-} are controlled with the same gate control signal, while the upper power semiconductors S_{A+} , S_{B+} and S_{C+} remain disconnected, acting as simple diodes [45]. The stator windings of the electrical machine are used as three parallel-connected inductors for the DC-DC converter.

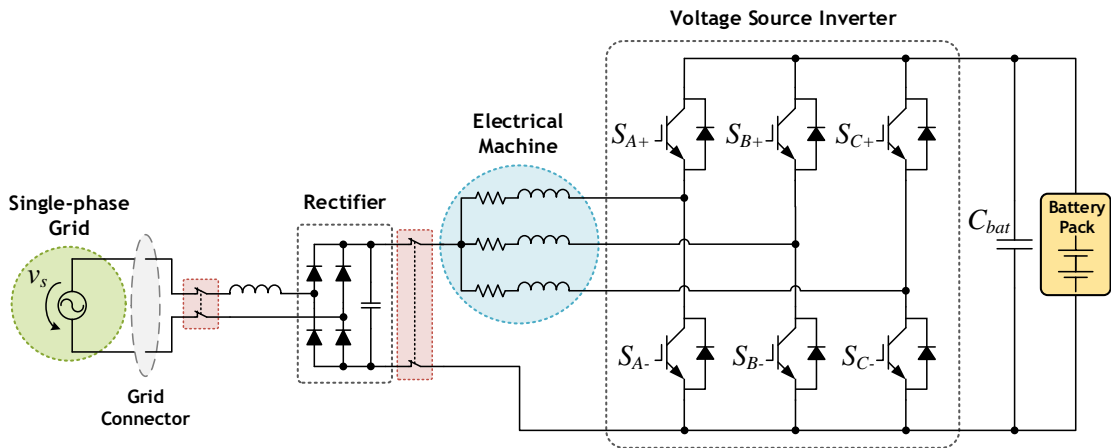


Figure 2.10 – Unified topology with non-isolated battery charger, discussed in [45], based on the grid connection through the neutral point of the electrical machine.

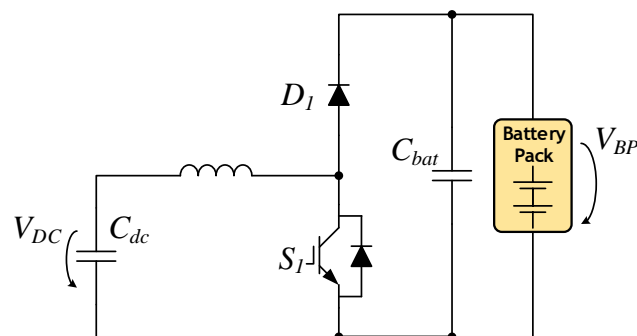


Figure 2.11 – Equivalent circuit of the set composed by the windings of the electrical machine and the three-phase Voltage Source Inverter (VSI) during the battery charging mode, corresponding to a Step-Up (Boost) DC-DC converter (adapted from [72]).

Typically, the DC-bus voltage outside the rectifier is higher than the voltage of the battery pack [52] and this is why in the already presented topologies the DC-DC converter operates as a Step-Down (Buck) DC-DC converter, during the battery charging mode. In the case of this topology, the equivalent DC-DC converter operates as a Step-Up (Boost)

converter and as result it will force to have a battery pack with a voltage level higher than the peak value of the voltage of the electrical grid. This is justified due to the fact that in [45], this topology operates under an electrical grid with a Root Mean Square (RMS) voltage value of 110 V, while the battery pack is rated with 180 V (i.e., the battery pack has a higher voltage level than the voltage RMS value of the electrical grid). However, this does not correspond to the typical situation, since it leads to constraints when using other levels of grid voltages available around the world. As example, if this topology was used in the European Union (EU), in which the electrical grid has a typically a RMS voltage value of 230 V, the battery pack would have to be rated with a voltage of at least 325.27 V, considering that the electrical grid delivers a pure-sinusoidal-wave voltage.

It is also important to note that for the motor drive mode, this topology does not provide a DC-DC converter.

The positive thermal coefficient of the Insulated-Gate Bipolar Transistors (IGBTs) ensures that the current flow is equally distributed among the power semiconductors. Thus, ideally only one third of the total current flows per each one of the three IGBTs allowing less power losses, comparatively to the case of using a single IGBT [45].

This topology is one of the presented solutions that least achieves the main goals established for this MSc. Thesis, since is the level-2 solution that requires more extra hardware (a diode-based rectifier and an input filter), it only allows for unidirectional power flow, it is only compatible with slow charging and it requires a battery pack with a high voltage level. There is no torque developed during the battery charging [45], and thus an extra mechanical system is not required.

It is important to note that in contrast to the other topologies analyzed, in this case, the values of the inductances of the windings of electrical machine do not affect directly the characteristics of the current consumed. However, since the electric machine is used as part of the DC-DC converter, the values of the inductances should ensure the continuous conduction mode of the converter, for providing less power losses.

There are also other similar topologies presented in [70], [73], that use two electrical machines and two VSIs. The grid connection is done at the neutral points of the stator wye-connected windings of each electrical machine. The VSIs of the motor drive system are used as a single-phase AC-DC active rectifier [47], and thus the extra diode rectifier is not required. However, as discussed in the introduction of this chapter, this solution is not considered, since for a typical EV it would require installing an extra electrical machine and an extra power electronics converter. *Hagbin et al.* propose a similar type

of solution in [74], but instead of using two electrical machines it is based on the use of a split-windings PMSM, using also two VSIs.

Level-2 Solutions Based on Grid Connection through the Middle Points of the Stator Windings

Another type of unified converter, using the electrical machine as inductor filter, is presented and discussed in [20], [26], [50], [56], [63]. This solution is based on a three-phase grid connection done through the middle points of the windings of the same phase. The proposed topology (presented in Figure 2.12) is based on a 6-leg VSI, but it can also be seen as two 3-leg VSIs or even as three H-bridges [26], [50]. In this topology, the windings of the same phase of the stator have a dedicated H-bridge, allowing elevate the voltage applied to the stator windings, for the motor drive operation [20], [50].

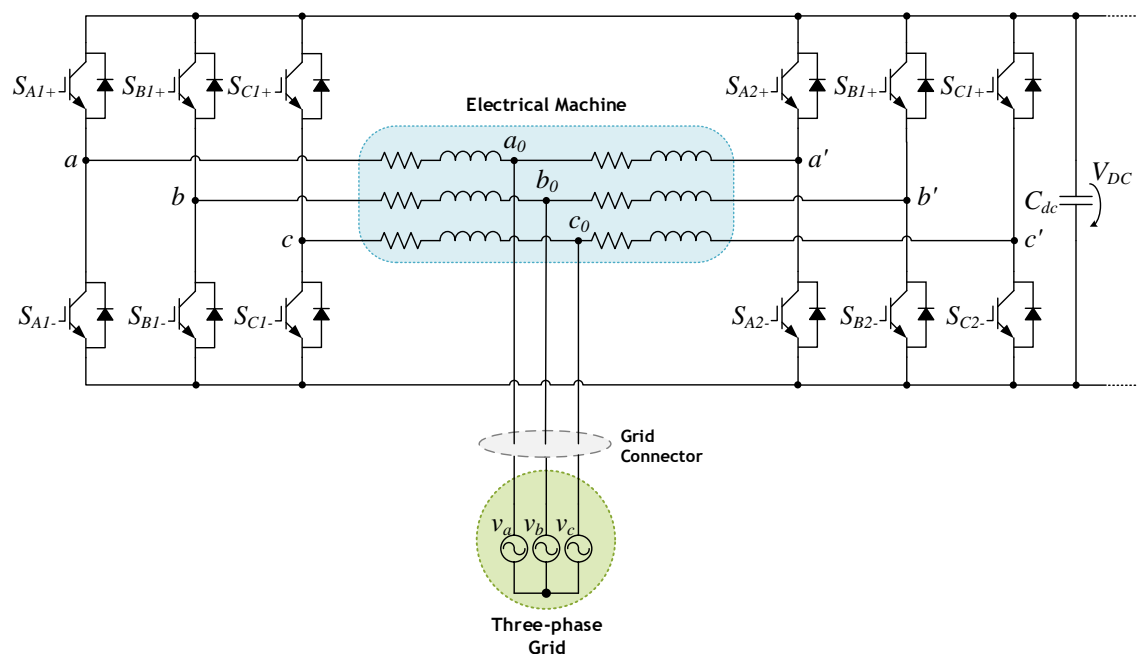


Figure 2.12 – Unified topology with non-isolated battery charger, discussed in [50], based on the grid connection through the middle points of the stator windings.

The major advantage of this topology is that no relay contacts are required, since the AC plug does not disturb the system, during the motor drive operation mode [20], [28].

This solution requires an electrical machine that provides access to the middle-points of the stator windings. Thus, it can be considered a split-windings machine, with a null phase shift between the two sets of the windings of the same phase [57] or even a dual-stator machine.

It is important to note that the control algorithm leads to be more complex using this topology [63], since it has to be guaranteed the current balancing in each winding.

The grid connection through the middle-points a_0 , b_0 and c_0 (Figure 2.12), has to be controlled in order that at each half windings of a given phase it flows opposite and equals currents. Thus, the current of each side of the split-phase windings will cancel the effect of the other [20]. This ensures that the rotating magnetic field components developed in the stator are eliminated, and thus the resultant induced magnetic force is zero and the vehicle remains stationary, even using an induction machine [63]. However, in practice, some insignificant vibrations can be detected, due to unbalanced distribution of the currents or constructive aspects such as unbalanced rotor mass [20].

The already presented unified topologies use a wye-connection of the stator windings of the electrical machine, in the motor drive mode. As a result, the zero-sequence currents are canceled at the neutral point, since the sum of the balanced three-phase currents is null [20]. However, in this topology, the windings of the stator are not electrically connected between them. Hence, the open windings connection proposed by this topology is not able to prevent the zero-sequence currents from flowing in the stator windings, resulting in extra power losses and torque ripple disturbances [20], [50]. Thus, the control algorithm for the motor drive mode requires considering the presence of zero-sequence currents, increasing its complexity [20].

Another issue that can be pointed out in this solution is the fact that it requires one more VSI than the conventional solution for motor drive, doubling the number of power semiconductors and increasing the cost of the solution [28]. Despite this, it is possible to have the identical silicone area of a single VSI, since the current flowing per each VSI can be half of the one that flows through a single VSI, for the same value of power [50].

This solution provides an alternative operation mode, in case a failure occurs in one of the power semiconductors, since it does not compromise the DC-bus. This mode consists in using just one of the VSIs [50]. Further, it provides fast charging and bidirectional power flow. For the slow charging mode, only four legs of each VSI and the windings of two phases are used, corresponding to two H-bridges, one for each phase [50], [54].

2.3. Isolated Battery Charger

There are some special types of electrical machines that can be used to operate as a transformer/generator, during the battery charging operation, with the advantage of providing galvanic isolation without requiring practically any extra equipment [75].

All the unified topologies with isolated battery charger presented in this MSc. Thesis have bidirectional power flow and fast charging capability.

Isolated Battery Charger using a Wound-Rotor Induction Machine

In [61] one of the most reported unified converters providing isolated battery charging is described [30], [40], [47], [54]. Its topology is presented in Figure 2.13, consisting in an induction machine with a special wound rotor type, implemented in an industrial truck.

For the battery charging operation, the electrical machine is used as a low-frequency step-down transformer [28], providing thus galvanic isolation. The rotor windings are connected to the three-phase electrical grid, operating as the primary side of the transformer. On the other hand, the stator windings constitute the secondary side of the transformer, being connected to the VSI. The battery charging with improved quality power is ensured using the stator and the rotor leakage inductances, operating as filter inductors [54], [61].

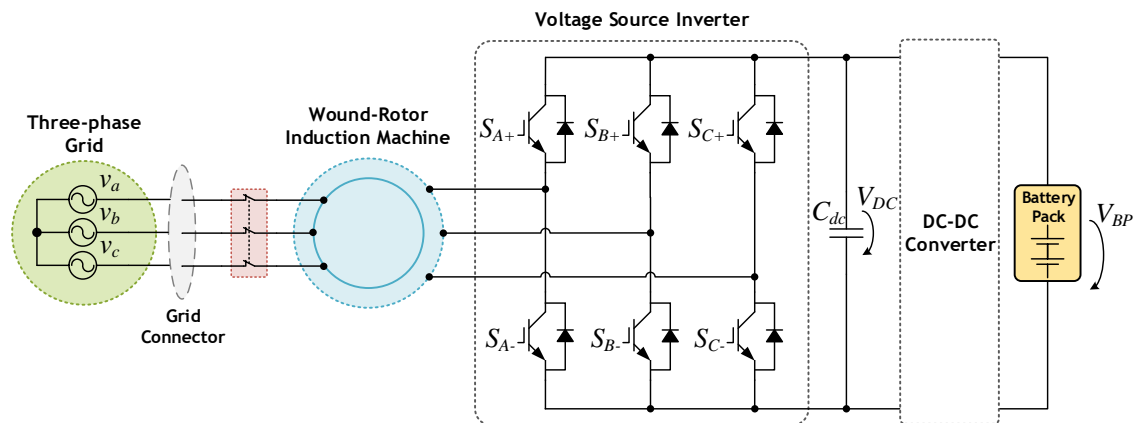


Figure 2.13 – Unified topology with isolated battery charger, discussed in [61], based on using a wound-rotor induction machine.

The main drawbacks of this topology are the need for a mechanical lock, since it is an asynchronous machine, the need of relays contacts and the fact that it requires a wound-rotor type of induction motor, which is more expensive than a squirrel cage induction machine and whose windings have to be adapted for support the required voltages of the charging operation (further increasing its cost) [28], [30].

The battery charging efficiency is depend on the air-gap of the electrical machine, causing losses due to the need for high magnetization currents [28], [47].

Isolated Battery Charger using a Split-Windings PMSM

Isolated topologies are also possible using synchronous machines like PMSMs. However, they also require a special type of electrical machine. In [41], [43], [54], [75], *Hagbin et al.* discuss an unified topology providing isolated battery charging based on

the use of a PMSM with split-windings. In this case the battery charging is performed using the electrical machine operating as a rotating transformer, providing a three-phase isolated voltage source for the VSI. Thus, despite using a PMSM, an extra clutch is needed.

The proposed solution requires relays contacts for the windings reconfiguration and for the three-phase grid connection [41]. The equivalent circuits for motor drive and battery charging operation modes are presented, respectively, in Figure 2.14 (a) and (b). In the motor drive mode, the half windings of each phase are connected in series between them while are connected in a wye configuration with the windings of the other phases.

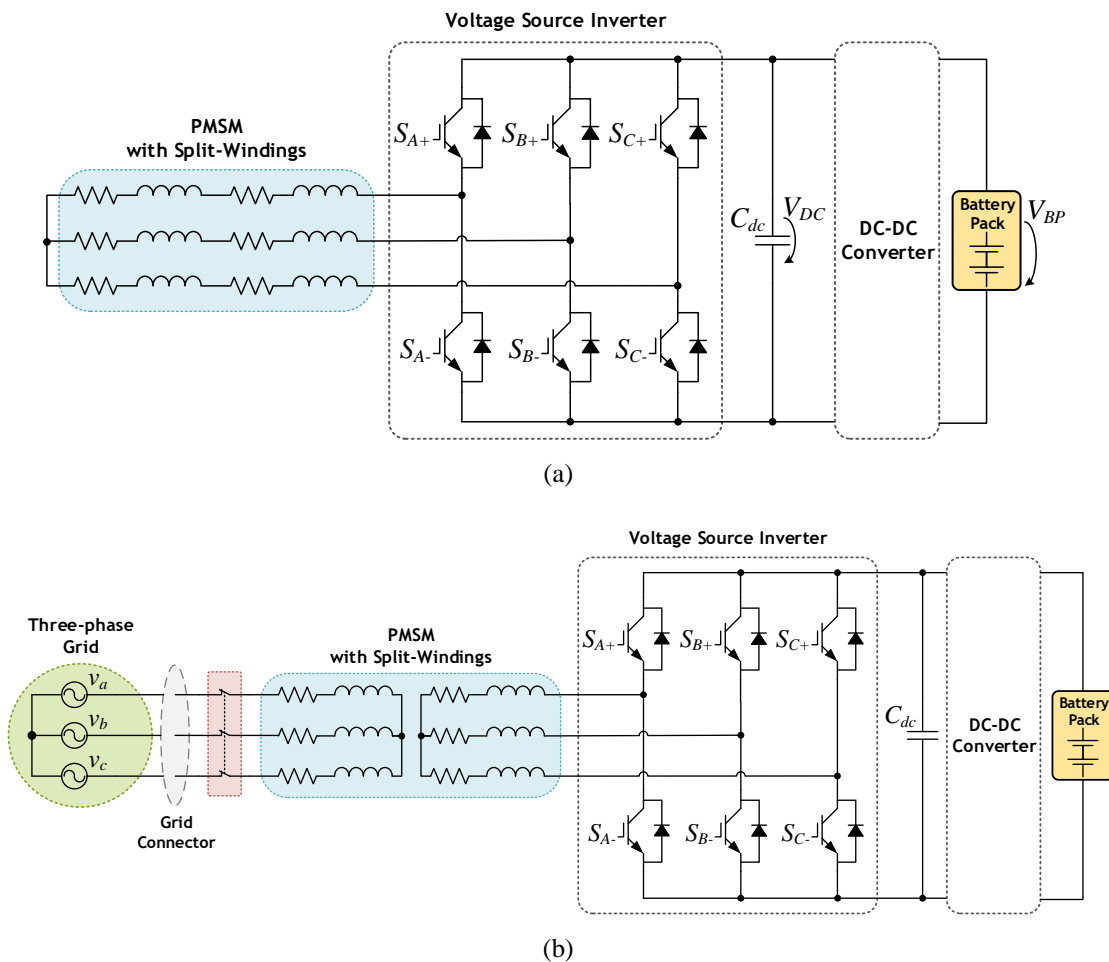


Figure 2.14 – Unified topology with isolated battery charger, discussed in [41], based on using a split-windings PMSM: (a) Equivalent circuit for motor drive; (b) Equivalent circuit for battery charging.

In this topology, for a proper battery charging operation it requires an initial step known as grid synchronization, i.e., the electrical machine has firstly to be synchronized with the electrical grid [41]. Initially, the grid contactors are open and the control system actuates in order for the electrical machine rotates at the synchronous speed (that is equal to $2\pi f$ rad/sec, considering f the supply grid frequency [75]), and produce the same voltages as the grid (in terms of amplitude and phase) at the inverter-side windings

[Figure 2.14 (b)]. This is done using the energy stored in the battery pack. As soon as the error values, obtained from the comparison between the voltages (in amplitude and phase) of the electrical grid and the induced voltages at the inverter-side, are considered low, the relays contacts are closed and the charging operation can proceed.

Hence, for the grid synchronization process, the battery pack has to have stored energy enough for the VSI to generate the grid voltage levels required for the synchronization process. Thus, this topology requires a minimum of energy stored in the battery pack, for properly ensuring the reliability of the charging operation, which is an important issue, since it can be seen as a decrease of the vehicle's range.

The fact of the electrical machine be forced to rotate during the battery charging operation, for the grid synchronization process, solves the issue of the system efficiency related to the large air-gap since, in this case, the high magnetization currents are, thereby, eliminated [75].

Like the last presented topologies, the use of the leakage inductances of the electrical machine provides unity power factor operation with low harmonic content of the currents consumed.

2.4. Proposed Solution

In Figure 2.15 is presented the unified topology proposed for this MSc. Thesis.

This solution is based on the level-2 topology analyzed by *Zaja et al.* in [19]. It provides non-isolated battery charging, using the power electronics converters and the electrical machine of the motor drive system. It is composed by two power stages. The first is the set composed by the three-phase VSI and the electrical machine operating as an active boost AC-DC rectifier during the battery charging, being responsible for interface with the electrical grid. The second stage is composed by a bidirectional DC-DC converter, responsible for interface with the battery pack (for both operation modes).

This solution was chosen because it has a considerable potential, since it provides a high integration level, without requiring practically any extra hardware.

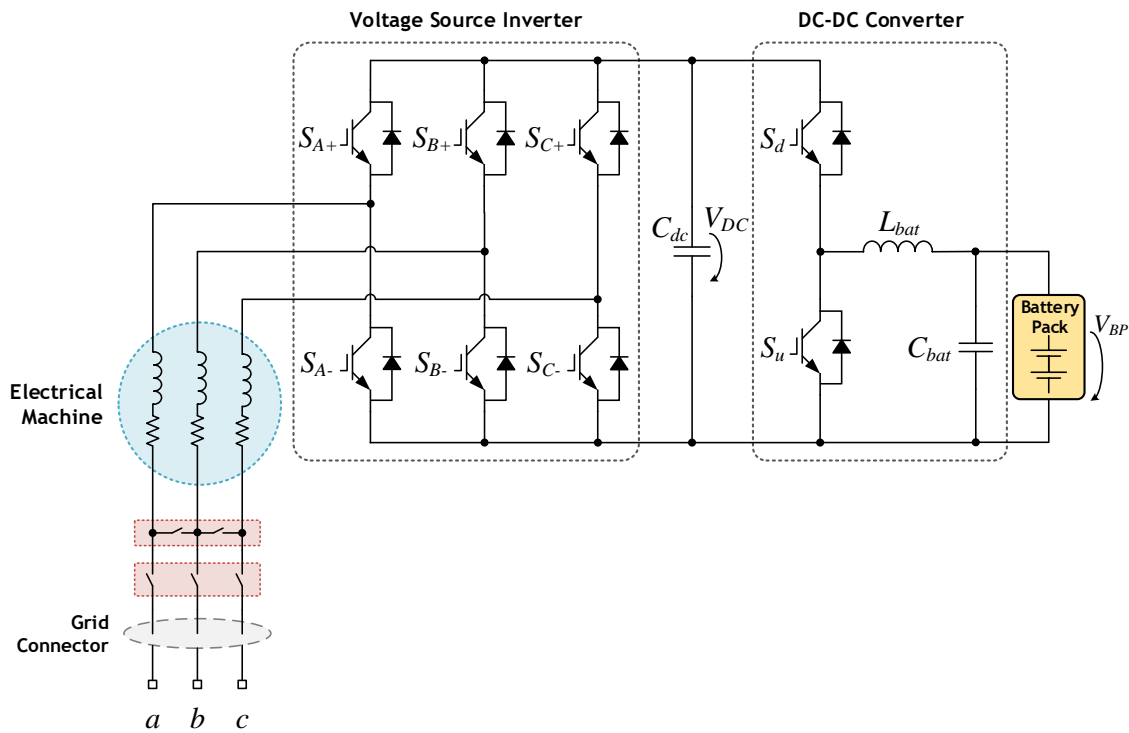


Figure 2.15 – Unified motor drive and battery charger for EVs proposed in this MSc. Thesis.

2.5. Conclusions

There is a wide range of reported unified hardware topologies for motor drive and battery charging applied to EVs. Thus, only the solutions that meet the requirements of this MSc. Thesis are analyzed.

Initially, non-isolated battery charging solutions are discussed. Two kinds of topologies are distinguish: the ones that use the power electronics converters of the motor drive system (defined as level-1 solutions) and the ones that, besides the power electronics converters, also employ the electrical machine of the motor drive system (defined as level-2 solutions).

Level-1 solutions are manly based on using the VSI of the motor drive system as an active AC-DC rectifier. Nevertheless, there are also solutions that involve modifications in the available motor drive hardware for integrating the battery charging operation. However, these solutions typically lead to more power losses, since more power semiconductors are acting simultaneously. The major issue of level-1 solutions is related to the inductor filter, required for a battery charging operation with unity power factor and consuming currents with low harmonic content, contributing to the power quality of the electrical grid. Even so, these solutions have the added-value of not being restricted to the type of electrical machine installed inside the vehicle, since it is not used during the battery charging operation.

In level-2 solutions the issue of the input filter is solved by using the stator windings of the electrical machine as inductors, during the battery charging. However, using the electrical machine typically results in more complex control algorithms. These kinds of solutions were categorized in three different types: (i) Only Based on Switching Devices; (ii) Grid Connection through the Neutral Point of the Stator Windings; (iii) Grid Connection through the Middle Points of the Stator Windings.

The main reported unified topologies providing isolated battery charger are the more limited solutions, since they are only applicable for specific types of electrical machines and mandatorily require a mechanical system for disconnecting the rotor from the transmission system of the vehicle, during the battery charging operation.

There are other types of solutions that are based on the use of Switched Reluctance Machines (SRMs) [30], [40], [47], [54]. However, topologies based on this type of electrical machine are not considered in this MSc. Thesis since these machines are still in an early development stage for vehicle traction and are not widely used by the car industry [28].

It is important to note that, despite providing fast charging, the available power is dependent on the power electronics components of the motor drive system. Eventually, the available power can also be dependent on the electrical machine characteristics, if it is used in the unified topology considered. However, high-power charging is normally achieved since the power devices of the motor drive system are typically oversized, with respect to the technical specifications for the battery charging [45].

Chapter 3

Control Algorithms for Motor Drive and Battery Charging

3.1. Introduction

This chapter is dedicated to the main reported control algorithms that are possible to implement in the unified hardware topology proposed in this MSc. Thesis, presented in Section 2.4.

Initially, the main reported control algorithms applied to the motor drive of an Electric Vehicle (EV), using a three-phase Voltage Source Inverter (VSI) and an electrical machine, operating as a motor, are presented and discussed.

Afterwards, the main reported control algorithms used for battery charging operation are analyzed. These are based on the use of a three-phase VSI and an input inductor filter, which in this case is composed by the windings of the electrical machine, whose set operates as a boost active rectifier.

Finally the control algorithms for the bidirectional DC-DC converter of the proposed topology, responsible for interface with the battery pack, are presented and discussed.

3.2. Motor Drive

In this section the control algorithms typically implemented for motor drive an EV, using a three-phase VSI topology and a single AC electrical machine, are described.

The expression that defines the synchronous speed n_s in an AC electrical machine is presented in (3.1), representing the rotor speed for a synchronous machine. Thus, the rotation speed can change by modifying the construction parameters, such as the number of poles p , or changing the frequency f of the voltages that are applied at its terminals.

$$n_s = \frac{120f}{p} \quad (3.1)$$

The option of varying the frequency of the voltages supplied to the electrical machine is the most preferable method, enhancing the development of what is mentioned in the literature as variable-frequency drive control methods [76].

The variable-frequency drive control is categorized in terms of scalar control and vector control. The vector control allows for easier control of AC electrical machines [77]. There are different vector control algorithms reported in the literature. The Field-Oriented Control (FOC) and the Direct Torque Control (DTC) are the most widely used [78].

3.2.1. Field-Oriented Control

The purpose of the Field-Oriented Control (FOC) is providing a decoupled control of the stator flux and the torque of the electrical machine. This control method is based on the transformation of the equations that define the dynamic behavior of the electrical machine into a coordinate system that rotates, synchronized with the rotation of the electrical machine [59], [69].

Using coordinate transformations, the stator currents are represented in a two-phase rotating coordinate system, known as Synchronous Reference Frame (SRF) or d - q coordinate system. This allows for the simplification of the control equations, removing dependencies such as time or the rotor position and, thereby, approximating it to the control of a DC machine [69], [78]–[81].

Typically, the speed of the electrical machine is used as control variable in the FOC. However, for controlling the motor drive of an EV it is more suitable to use the torque as the control variable, whose value is defined by the position of the accelerator pedal [69].

In [69], *Pedrosa et al.* describe a FOC applied to an EV, using an Axial Flux Permanent Magnet Synchronous Machine (PMSM), whose block diagram is presented in Figure 3.1.

In the decoupled control proposed by the FOC, the d -axis current (I_d) is responsible for adjusting the stator flux, while the q -axis current (I_q) adjusts the torque [69]. Each one of these variables are measured and compared with their respective reference value. The error obtained for each control variable feeds a Proportional Integral (PI) controller, whose block diagram is described in Figure 3.2, where e represents the error, u the command signal obtained from the PI controller, K_p the proportional gain and K_i the integral gain.

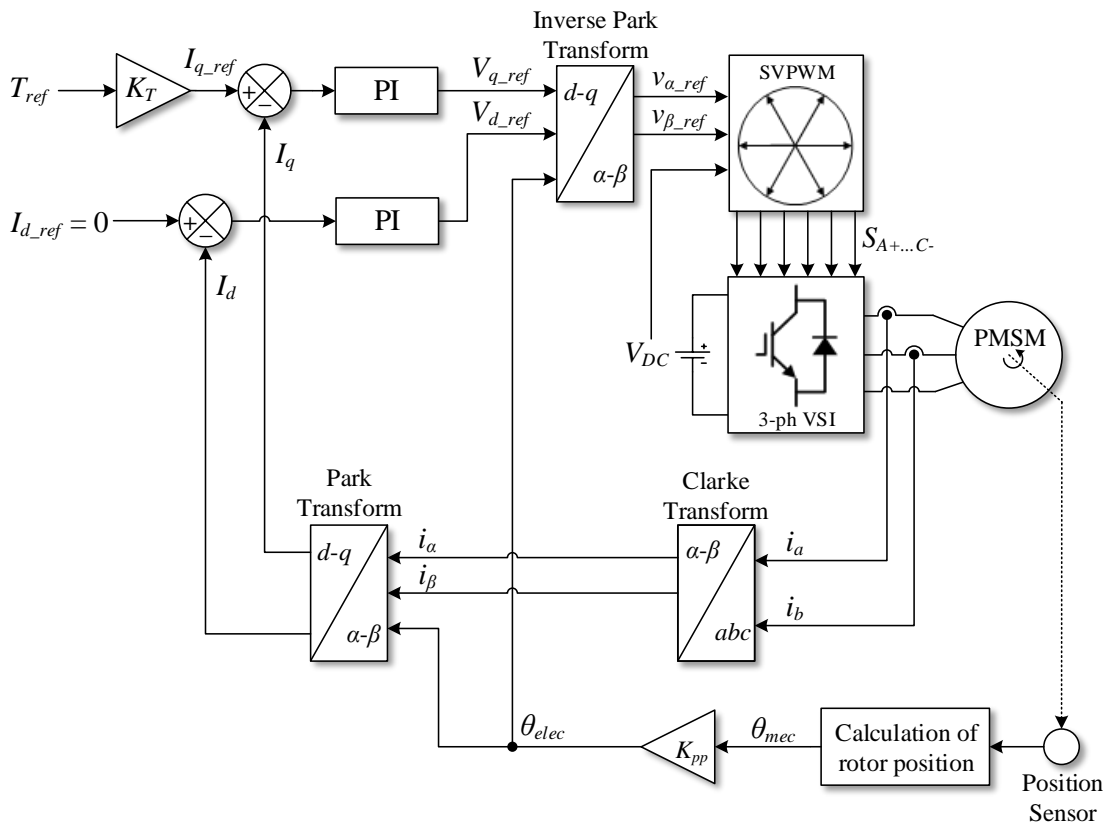


Figure 3.1 – Block diagram of the Field-Oriented Control (FOC), described by *Pedrosa et al.* (adapted from [69]).

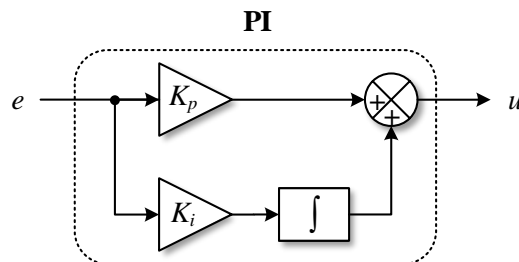


Figure 3.2 – Block diagram of the Proportional Integral (PI) controller, used in this MSc. Thesis (adapted from [52]).

The “Clarke Transform”, “Park Transform” and “Inverse Park Transform” blocks presented in Figure 3.1 are responsible for the coordinate transformations. Each one of these blocks is described below.

Clarke Transform

The Clarke transform consists in a coordinate transformation from a typical three-phase system into a two-phase system, defined by α and β axes, as shown in Figure 3.3. Both systems have a stationary reference frame.

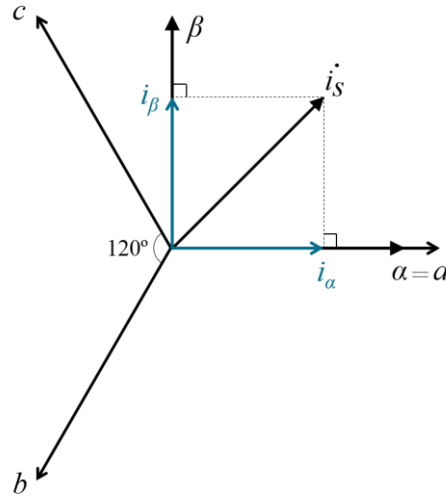


Figure 3.3 – Transformation of the stator currents from the a - b - c coordinate system into the α - β coordinate system, using the Clarke transform (adapted from [82]).

In (3.2) the Clarke transform is defined, in which the matrix containing the i_α and i_β values is obtained by applying a transformation matrix to the matrix containing the three-phase currents i_a , i_b and i_c .

$$\begin{bmatrix} i_\alpha \\ i_\beta \end{bmatrix} = \frac{2}{3} \begin{bmatrix} 1 & -\frac{1}{2} & -\frac{1}{2} \\ 0 & \frac{\sqrt{3}}{2} & -\frac{\sqrt{3}}{2} \end{bmatrix} \begin{bmatrix} i_a \\ i_b \\ i_c \end{bmatrix} \quad (3.2)$$

For balanced systems, in which the condition presented in (3.3) is verified, the Clarke transform described in (3.2) can be simplified into (3.4), resulting in a sensor-less option, since it only requires measuring two currents.

$$i_a(t) + i_b(t) + i_c(t) = 0, \forall t \in \mathbb{R}_0^+ \quad (3.3)$$

$$\begin{bmatrix} i_\alpha \\ i_\beta \end{bmatrix} = \begin{bmatrix} 1 & 0 \\ \frac{1}{\sqrt{3}} & \frac{2}{\sqrt{3}} \end{bmatrix} \begin{bmatrix} i_a \\ i_b \end{bmatrix} \quad (3.4)$$

Park Transform

The Park transform consists in a coordinate transformation from the stationary reference frame two-phase system, defined by α and β axes and obtained previously using the Clarke transform, into a rotating reference frame two-phase system, defined by the axes d and q , as is shown in Figure 3.4.

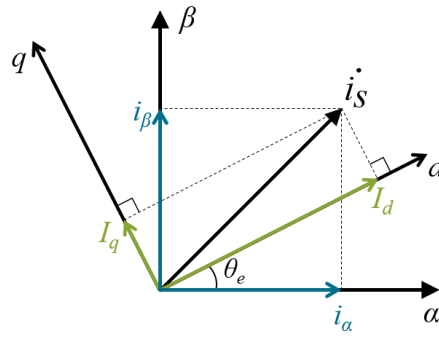


Figure 3.4 – Transformation of the stator currents from the stationary reference frame α - β coordinate system into the rotating reference frame d - q coordinate system, using the Park transform (adapted from [82]).

As mentioned before, the d - q coordinate system has the particularity of having a rotating reference frame. Its rotation is defined according to the variable θ_e , as is shown in Figure 3.4.

In the FOC, the stator currents represented in the d - q coordinate system must be synchronized with the angle of the rotor position. As is shown in Figure 3.1, this is done attributing to θ_e the value of the electric angle of the rotor θ_{elec} . This value is obtained by applying the gain K_{pp} (which is the number of poles pairs of the electrical machine), to the mechanical rotor angle θ_{mec} , obtained from the position sensor.

The Park transform is described in (3.5). The matrix containing the I_d and I_q values is obtained by applying a transformation matrix (which depends on the value of θ_e), to the matrix containing the two-phase currents i_α and i_β .

$$\begin{bmatrix} I_d \\ I_q \end{bmatrix} = \begin{bmatrix} \cos(\theta_e) & \sin(\theta_e) \\ -\sin(\theta_e) & \cos(\theta_e) \end{bmatrix} \begin{bmatrix} i_\alpha \\ i_\beta \end{bmatrix} \quad (3.5)$$

As shown in Figure 3.1, the FOC produces two voltage references (V_{q_ref} and V_{d_ref}) that represent the voltages that must be applied to the stator windings of the electrical machine. Thus, the next step consists in translating these reference values into gate signals for apply to the power semiconductors of the VSI. This is done using the inverse Park transform and the Space Vector Pulse Width Modulation (SVPWM) technique.

Inverse Park Transform

The inverse Park transformation is used in the proposed FOC with the purpose of translate the voltage reference values into the α - β coordinate system.

The already presented transformation matrixes used for Clarke and Park transformations are the same for both current and voltage values. Knowing the transformation matrix between two coordinate systems, its inverse transformation

consists in computing the inverse of the transformation matrix. Thus, the inverse Park transform is defined according to (3.6).

$$\begin{bmatrix} v_\alpha \\ v_\beta \end{bmatrix} = \begin{bmatrix} \cos(\theta_e) & -\sin(\theta_e) \\ \sin(\theta_e) & \cos(\theta_e) \end{bmatrix} \begin{bmatrix} V_d \\ V_q \end{bmatrix} \quad (3.6)$$

Space Vector Pulse Width Modulation

The next step consists in obtaining the gate pulses to apply to the power semiconductors of the VSI. For that purpose, the Space Vector Pulse Width Modulation (SVPWM) technique is used.

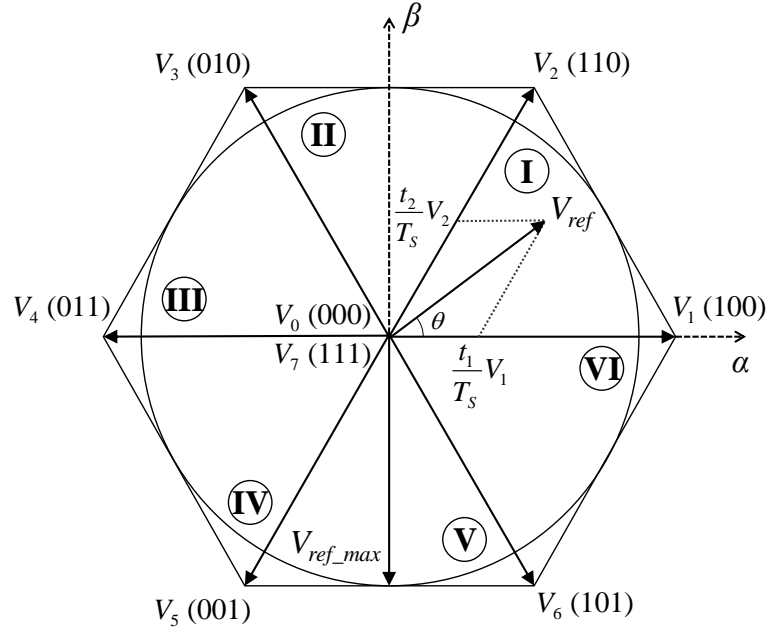
The SVPWM is a modulation technique with high performance and good accuracy, developed for vector references. It is considered the best modulation technique for minimizing the harmonic contents, comparatively to other well-known techniques such as the Sinusoidal Pulse Width Modulation (SPWM) or the delta modulation [46], [69], [82].

As discussed in the introduction of the previous chapter, in a three-phase VSI there are eight possible switching states, remembering that both power semiconductors of the same leg cannot have the same state. However, only six of them produce voltage values different from zero, since there are two redundant states (all the upper power semiconductors ON or all the lower power semiconductors ON), in which the output voltage produced is zero.

In the SVPWM the six non-null possible voltages are mapped into the α - β plan, where the vector V_{ref} is placed, dividing it into six sectors, as presented in Figure 3.5. Each value of V_{ref} (defined by the V_{α_ref} and V_{β_ref} components), can be decomposed into two adjacent vectors that define the sector where it is placed. For each V_{ref} these adjacent vectors are time weighted for a switching period T_s , in order to produce the desired voltage.

As presented in Figure 3.5, the binary representation for each consecutive voltage vector only differs in one bit. This ensures that between two adjacent sectors only one leg of the VSI switches state [82].

The first step consists in determining the sector where the vector V_{ref} is placed. This is done by first verifying the condition presented in (3.7). Since the voltage values are represented under the α - β coordinate system, this condition is evaluated using the inverse Clarke transformation expressed in (3.8), resulting in (3.9). Then the sector is determined by means of (3.10) and Table 3.1.


 Figure 3.5 – Space Vector of V_{ref} in the α - β plan (adapted from [69]).

$$\left\{ \begin{array}{l} \text{If } v_a > 0 \quad \text{Then } A = 1, \text{ Else } A = 0 \\ \text{If } v_b > 0 \quad \text{Then } B = 1, \text{ Else } B = 0 \\ \text{If } v_c > 0 \quad \text{Then } C = 1, \text{ Else } C = 0 \end{array} \right. \quad (3.7)$$

$$\left\{ \begin{array}{l} v_a = v_\beta \\ v_b = \frac{\sqrt{3}}{2} v_\alpha - \frac{1}{2} v_\beta \\ v_c = -\frac{\sqrt{3}}{2} v_\alpha - \frac{1}{2} v_\beta \end{array} \right. \quad (3.8)$$

$$\left\{ \begin{array}{l} \text{If } v_\beta > 0 \quad \text{Then } A = 1, \text{ Else } A = 0 \\ \text{If } (v_\alpha \sqrt{3} - v_\beta) > 0 \quad \text{Then } B = 1, \text{ Else } B = 0 \\ \text{If } (-v_\alpha \sqrt{3} - v_\beta) > 0 \quad \text{Then } C = 1, \text{ Else } C = 0 \end{array} \right. \quad (3.9)$$

$$N = A + 2B + 4C \quad (3.10)$$

 Table 3.1 – Identification of the sector where V_{ref} is placed, according to the value of N .

N	1	2	3	4	5	6
Sector	II	VI	I	IV	III	V

Considering that the vector V_{ref} is placed in sector i (represented by its corresponding value, instead of its Roman numeral representation), the adjacent vectors

are time weighted for a switching period T_s (Figure 3.5), according to (3.11). The variable t_1 represents the time during which the adjacent vector V_i is applied and t_2 the time during which the adjacent vector V_{i+1} is applied. As example, in Figure 3.5 the vector V_{ref} is placed in sector 1 (I), and so V_{ref} is defined as (3.12).

$$V_{ref} = \frac{t_1}{T_s} V_i + \frac{t_2}{T_s} V_{i+1} \quad (3.11)$$

$$V_{ref} = \frac{t_1}{T_s} V_1 + \frac{t_2}{T_s} V_2, \quad \text{for } i=1 \quad (3.12)$$

The t_1 and t_2 values are attributed using (3.13) and Table 3.2, where V_{DC} is the voltage of the DC-bus.

$$\begin{cases} X = \frac{v_\beta \sqrt{3}}{V_{DC}} T_s \\ Y = \frac{(v_\beta \sqrt{3} + 3v_\alpha)}{2V_{DC}} T_s \\ Z = \frac{(v_\beta \sqrt{3} - 3v_\alpha)}{2V_{DC}} T_s \end{cases} \quad (3.13)$$

Table 3.2 – Attribution of the values of t_1 and t_2 , according to the sector where V_{ref} is placed.

	Sector					
	I	II	III	IV	V	VI
t_1	-Z	Z	X	-X	-Y	Y
t_2	X	Y	-Y	Z	-Z	-X

The last presented considerations allow concluding that the sum of t_1 and t_2 values has to be lower or equal to the switching period T_s i.e., the condition expressed in (3.14) must be verified. If this condition is not satisfied, the values attributed to t_1 and t_2 are recalculated, using (3.15) by means of a proportional attribution, based on the weight of their last values and the switching period T_s .

$$t_1 + t_2 \leq T_s \quad (3.14)$$

$$\begin{cases} t_1 = \frac{t_1}{t_1 + t_2} T_s \\ t_2 = \frac{t_2}{t_1 + t_2} T_s \end{cases} \quad (3.15)$$

On the other hand, if the sum of t_1 and t_2 values is lower than the switching period T_s , three time intervals t_1 , t_2 and t_0 are considered. The time interval t_0 corresponds to the deference between T_s and the sum of t_1 and t_2 . This is the time during which the null voltage vectors V_0 and V_7 are applied.

Following with the algorithm, the time intervals t_1 and t_2 are then translated in terms of three different variables t_a , t_b and t_c , (in which the time interval t_0 is determined), in order to obtain the gate switching Pulse-Width Modulation (PWM) signals. This is done using (3.16) and the Table 3.3.

$$\begin{cases} t_{aON} = \frac{T_s - (t_1 + t_2)}{4} \\ t_{bON} = t_{aON} + \frac{t_1}{2} \\ t_{cON} = t_{bON} + \frac{t_2}{2} \end{cases} \quad (3.16)$$

Table 3.3 – Attribution of the t_a , t_b and t_c values, according to the sector where V_{ref} is placed.

		Sector					
		I	II	III	IV	V	VI
t_a	t_{aON}	t_{bON}	t_{cON}	t_{cON}	t_{bON}	t_{aON}	
t_b	t_{bON}	t_{aON}	t_{aON}	t_{bON}	t_{cON}	t_{cON}	
t_c	t_{cON}	t_{cON}	t_{bON}	t_{aON}	t_{aON}	t_{bON}	

The next step consists in generating the gate signals for the power semiconductors, by comparing the obtained t_a , t_b and t_c values with a triangular-wave with period T_s . In Figure 3.6 some examples of the obtained results are presented. Figure 3.6 (a) shows a case where V_{ref} is placed in sector I and Figure 3.6 (b) a case where V_{ref} is placed in sector III.

It is possible to conclude that the obtained signals have different pulse-widths between them, according to V_{ref} . However, with a careful analysis it is possible to define a pattern in terms of comparison of the pulse-width between the three generated signals, according to the sector where V_{ref} is placed. This pattern is shown in Figure 3.7.

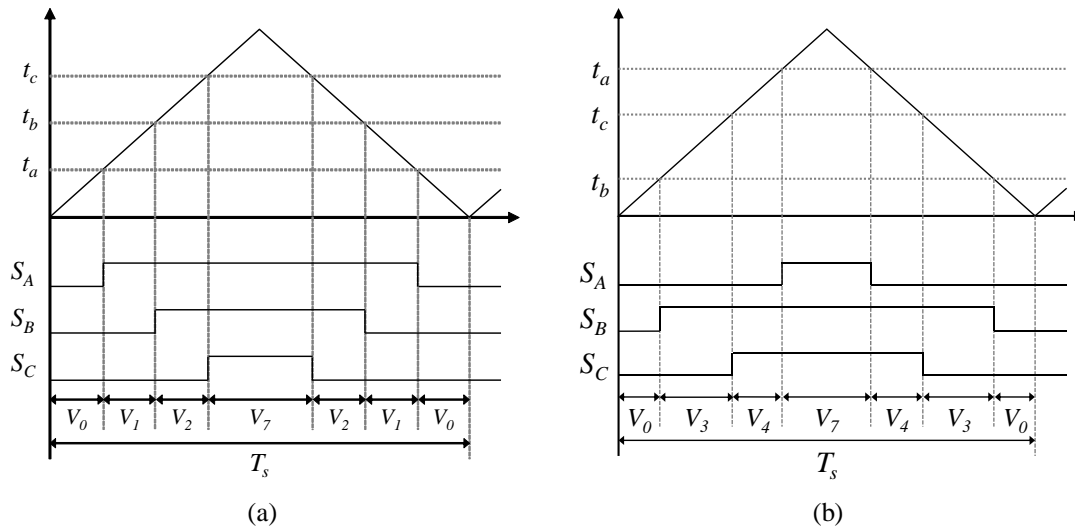


Figure 3.6 – Examples of gate signals obtained through the comparison of variables the t_a , t_b and t_c with a triangular-wave: (a) Considering V_{ref} placed in sector I; (a) Considering V_{ref} placed in sector III.

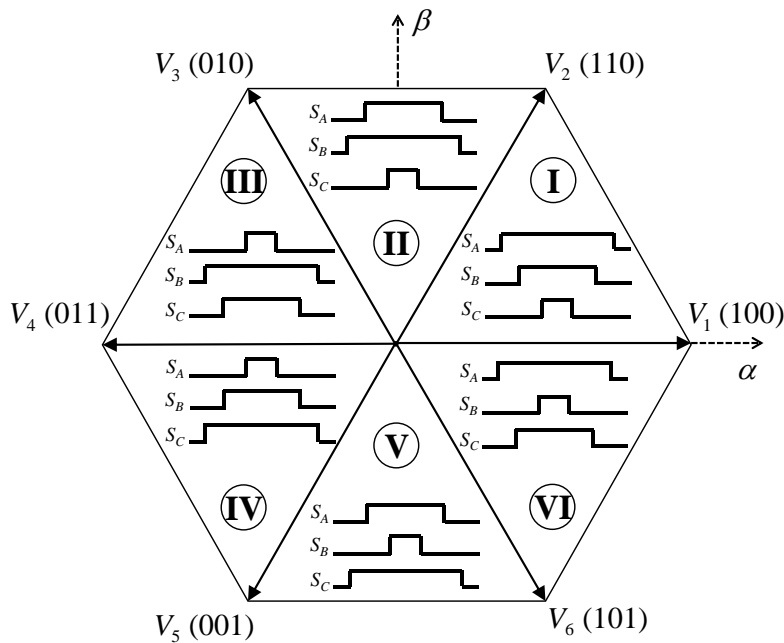


Figure 3.7 – Space Vector Pulse Width Modulation (SVPWM) pattern, according to the sector where V_{ref} is placed, known as the hexagon of the SVPWM (adapted from [82]).

Finally, the three gate signals obtained S_A , S_B and S_C have to be translated into the six gate signals to be applied to each power semiconductor of the VSI, which is done according to the Figure 3.8. However, this attribution considers an ideal behavior of the power semiconductors. Thus, in a real implementation, the gate signals applied should consider the real behavior of the power semiconductors, such as the fact of they do not change its state instantaneously, typically taking more time to turn-off. Thus, a dead time has to be considered, for ensuring the integrity of the power electronics components.

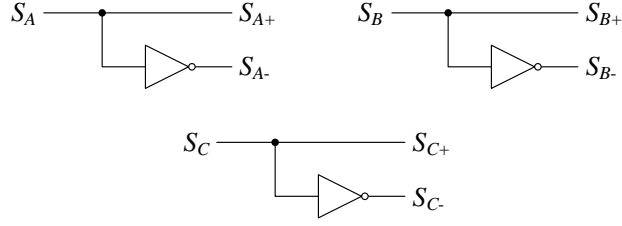


Figure 3.8 – Gate signals applied to the power semiconductors of the three-phase VSI, considering an ideal switching behavior.

According to [69], in the d - q coordinate system the equations that define the voltage and the flux linkage of a PMSM are described respectively in (3.17) and (3.18), where R_s represents the armature resistance, I_d and I_q the stator d - q axis currents, p_p the number of poles pairs, ω_e the electrical angular speed, L_d and L_q the d - q axis inductances, and ψ_r the permanent magnets flux linkage.

$$\begin{cases} V_d = R_s I_d + p_p \psi_d - \omega_e \psi_q \\ V_q = R_s I_q + p_p \psi_q + \omega_e \psi_d \end{cases} \quad (3.17)$$

$$\begin{cases} \psi_d = L_d I_d + \psi_r \\ \psi_q = L_q I_q \end{cases} \quad (3.18)$$

The torque developed on a PMSM is defined, according to [69], by (3.19).

$$T_e = p_p (I_q \psi_d - I_d \psi_q) \quad (3.19)$$

Typically, using a PMSM the d -axis reference current is set to zero, obtaining the maximum torque. Nevertheless, when a speed above the nominal speed of the electrical machine is wanted, this reference current is set to be negative, operating in a region known as “field-weakening”, that reduces the effective flux of the permanent magnets. As a result, the machine will produce less torque, since it will be limited according to the condition expressed in (3.20) that needs to be guaranteed. However, this operation mode is not recommended, since it creates fluxes in opposition to the natural flux produced by the permanent magnets. During long periods, this condition can lead to the demagnetization of the permanent magnets. Consequently, the produced torque is reduced and causes excessive overheating of the machine [59], [69].

$$I_s = \sqrt{I_d^2 + I_q^2} \leq I_{s_max} \quad (3.20)$$

The main advantages of implementing the FOC are the low ripple and distortion in steady-state for the torque. This control method has fixed switch frequency, allowing the

use of an extra current filter for improving the waveform of the currents consumed [59], [77].

On the other hand, the FOC has the disadvantage of having a slower dynamic response to torque variations, in comparison with other control technics such as the Direct Torque Control (DTC) [59], [69].

3.2.2. Direct Torque Control

The Direct Torque Control (DTC) is a more recent vector control technique than the FOC that also achieves decoupled control of torque and flux. Nevertheless, the DTC has a faster response to variations of the torque, despite presenting typically higher ripple in steady-state [77]. A diagram block of the conventional DTC is presented in Figure 3.9.

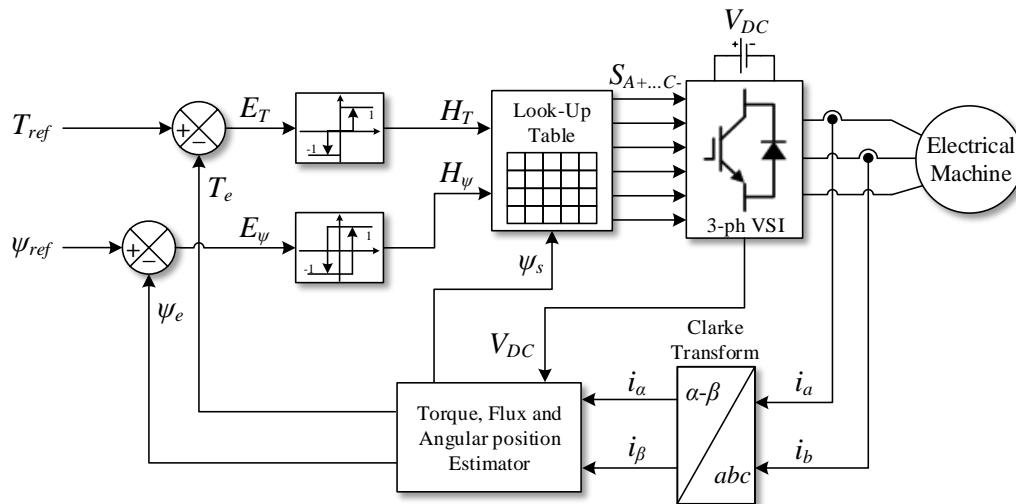


Figure 3.9 – Block diagram of the Direct Torque Control (DTC) (adapted from [59], [77], [83]).

The DTC only uses the Clarke transformation and so the calculations are based on the stationary α - β coordinate system. This control algorithm consists of estimating the values of the controlled variables (the torque and the flux stator linkage), and comparing them with their reference values by means of hysteresis controllers. The use of this type of controllers, instead of PI controllers, allows for faster response, improving its dynamic behavior. Based on the obtained torque error, stator flux linkage error and angular position of the stator flux linkage vector, an appropriate switching signal is generated by means of a look-up table and applied to the three-phase VSI [59], [83].

The expressions that compute the estimated values for the control variables are naturally dependent on the type of electrical machine used. As examples, *Bian et al.* study in [84] the case of using PMSM, while *Ozturk et al.* in [85] consider the case of using a Brushless DC (BLDC) machine with non-sinusoidal back-Electromotive Force (EMF).

Despite a hysteresis controller being applied to both controlled variables, their respective control block is represented differently in Figure 3.9. That is because they have a different number of output levels. According to [59], the hysteresis controller for the stator flux linkage is defined by (3.21), while for the torque it is defined by (3.22).

$$\begin{cases} H_{\psi} = 1 & \text{if } E_{\psi} > LB_{\psi} \\ H_{\psi} = -1 & \text{if } E_{\psi} < -LB_{\psi} \end{cases} \quad (3.21)$$

$$\begin{cases} H_T = 1 & \text{if } E_T > LB_T \\ H_T = 0 & \text{if } -LB_T < E_T < LB_T \\ H_T = -1 & \text{if } E_T < -LB_T \end{cases} \quad (3.22)$$

Thus, the hysteresis controller of the flux linkage has two output levels and a width-band of $2LB_{\psi}$. On the other hand, the hysteresis controller applied to the torque has three output levels and a width-band of $2LB_T$.

Similarly to the SVPWM technique used for the FOC, in the DTC the α - β plan is divided into six sectors, (from I to VI), where also eight vectors are mapped, corresponding to the switch state possibilities of the three-phase VSI. The applied switching state is determined through a look-up table, using the values obtained from the hysteresis controllers and the estimated angular position of the stator flux linkage vector [59]. The typical look-up table used for the DTC implementation is shown in Table 3.4.

Table 3.4 – Typical look-up table used in the DTC (adapted from [77]).

H_{ψ}	H_T	Sector(ψ_s)					
		I	II	III	IV	V	VI
1	1	V_2	V_3	V_4	V_5	V_6	V_1
	0	V_7	V_0	V_7	V_0	V_7	V_0
	-1	V_6	V_1	V_2	V_3	V_4	V_5
-1	1	V_3	V_4	V_5	V_6	V_1	V_2
	0	V_0	V_7	V_0	V_7	V_0	V_7
	-1	V_5	V_6	V_1	V_2	V_3	V_4

This control algorithm provides a better dynamic performance and does not require measuring the rotor position [59], [77].

On the other hand, the DTC has a variable switch frequency, which does not allow for the use of passive filters tuned at the switching frequency for improve the waveform of the currents consumed. However, there is a DTC-based technique known as DTC-

SVPWM, that uses the SVPWM such as the FOC, providing a fixed switching frequency [59], [77].

The windings of the electrical machines applied to EVs have typically low values of inductances. Hence, since the typical DTC strategies are based on hysteresis comparators, it may result in a significant torque ripple [83]. For improving the torque response in those cases, *Gupta et al.* propose in [83] to develop a neural network controller to replace the hysteresis controllers and the look-up table. However, this solution represents a huge increase of complexity, requiring more computation effort than the FOC.

3.3. Battery Charging

In this section the most relevant control algorithms for charging the battery pack of the EV are described, based on the use of the first stage of the proposed topology, comprising the three-phase VSI and the windings of the electrical machine, whose set operates as a three-phase boost AC-DC converter, providing Power Factor Correction (PFC).

As discussed in the previous chapter, one of the main concerns regarding the battery charging operation is its influence on the power quality of the electrical grid. Thus, the battery charging operation should be performed with unity power factor and consuming sinusoidal currents, i.e., with low harmonic content [30], [36].

Operating with unity power factor allows reducing the electrical power delivered by the transmission network, reducing the power losses. On the other hand, the consumption of currents with considerable harmonic content leads to power losses but also voltage distortions, compromising the performance of more sensitive equipment [36].

Initially in this section the Direct Current Control based on Synchronous Reference Frame (DCC-SRF), a widely adopted control algorithm for three-phase boost AC-DC converters [86], is presented and discussed. It is also presented a brief analysis of the main reported Phase-Locked Loop (PLL) systems, required for a proper synchronization of the converter with the electrical grid, using this type of control algorithms.

Then a different type of control algorithm is presented and discussed. It consists of a controller based on predicting the future behavior of the control variables of the system, known as Model Predictive Control (MPC).

3.3.1. Direct Current Control Based on Synchronous Reference Frame

The equivalent circuit of the first stage of the proposed topology, for fast charging mode, is presented in Figure 3.10. Assuming a balanced three-phase supply and an ideal behavior of the power semiconductors, the dynamic behavior of the circuit presented in Figure 3.10 was modeled in [87] under a d - q coordinate system, resulting in (3.23). The variable ω represents the angular frequency (i.e., $\omega = 2\pi f$, where f is the fundamental frequency of the voltages supplied by the electrical grid).

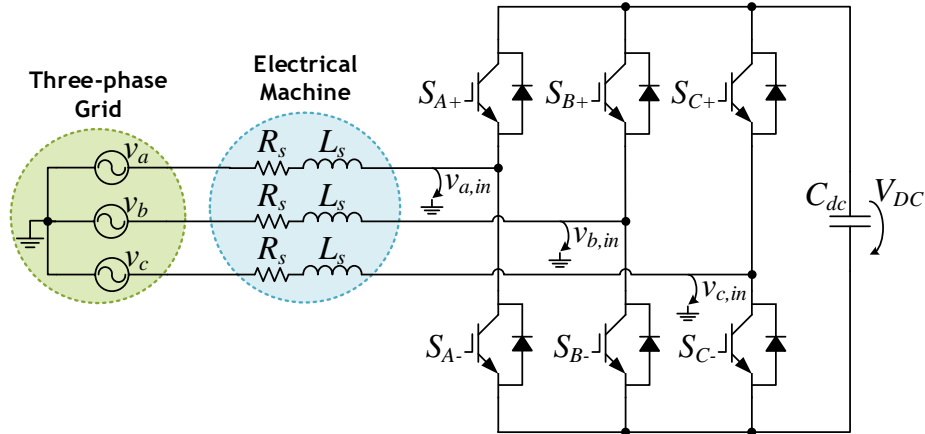


Figure 3.10 – Equivalent circuit of the first stage of the unified topology proposed in this MSc. Thesis, for the fast charging mode, through an AC three-phase grid supply.

$$\begin{cases} L_s \frac{dI_d}{dt} = V_d - I_d R_s + \omega L_s I_q - V_{d,in} \\ L_s \frac{dI_q}{dt} = V_q - I_q R_s - \omega L_s I_d - V_{q,in} \end{cases} \quad (3.23)$$

The Direct Current Control based on Synchronous Reference Frame (DCC-SRF) is based on this obtained model, resulting in the block diagram presented in Figure 3.11.

It is possible to infer that the DCC-SRF has some similarities with the already presented FOC for the motor drive mode. Both are based on the regulation of the current by means of a SRF [86].

For improve the obtained results, in [39], [75], [86], [88] the coupling component presented in (3.23) is added to the DCC-SRF. This component is the feedforward compensation, represented by the $\omega L_s I_q$ and $\omega L_s I_d$ components, presented in Figure 3.11.

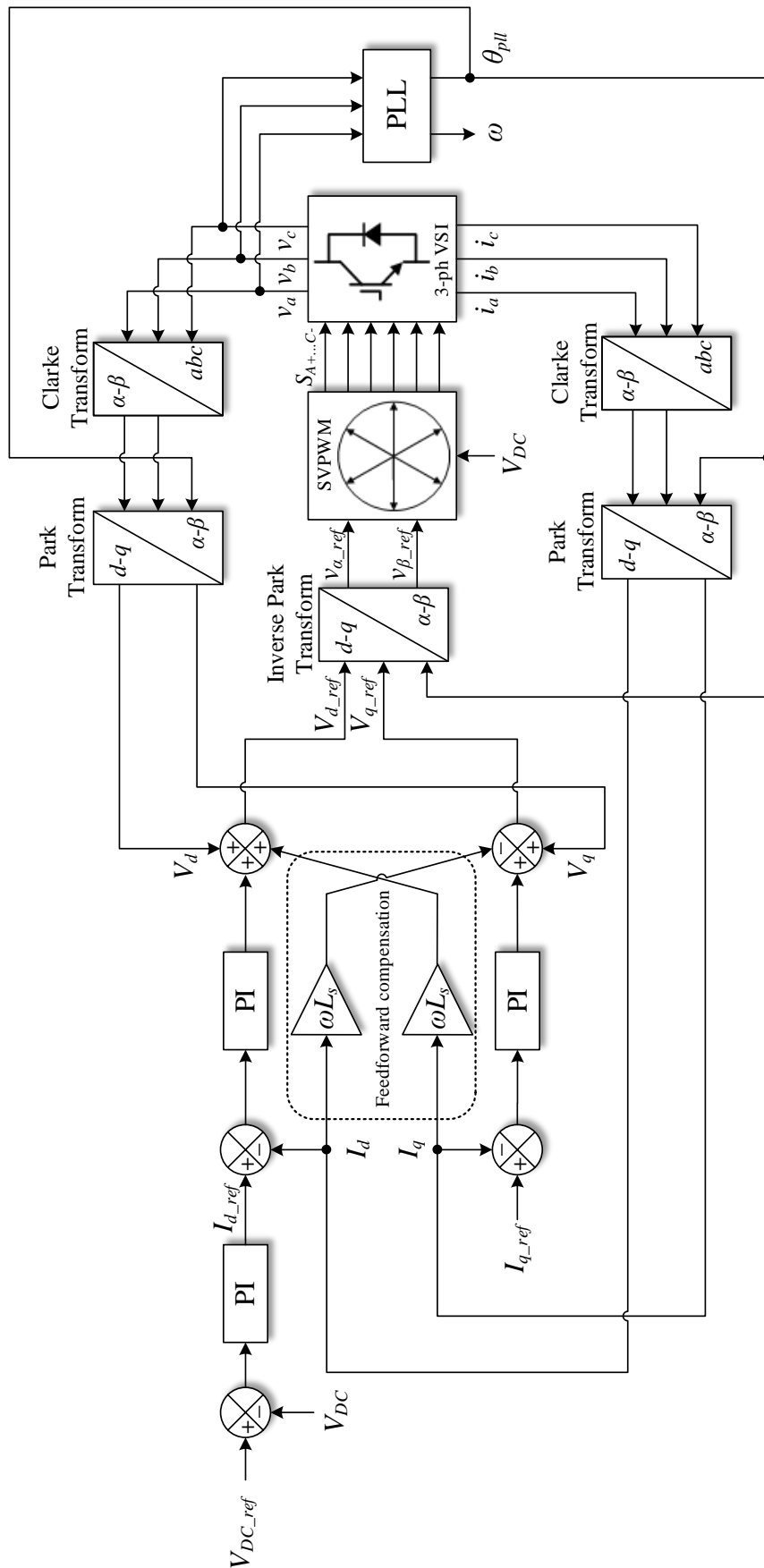


Figure 3.11 – Block diagram of the Direct Current Control based on Synchronous Reference Frame (DCC-SRF) (adapted from [39]).

In the DCC-SRF, the d -axis component of the current is responsible for adjusting the voltage reference for the DC-bus, while the q -axis component of the current adjusts the power flow. Thus, a positive value of I_{q_ref} establishes that the electrical power flows from the electrical grid to the vehicle, i.e., the controller operates in the Grid-to-Vehicle (G2V) mode, while a negative value establishes that the electrical power flows from the vehicle to the electrical grid, i.e., the controller operates in the Vehicle-to-Grid (V2G) mode [39].

Reported solutions using this control algorithm mention the fast dynamic current response, good accuracy and fixed switching frequency as its main advantages [39], [86].

Such as the FOC, the switching signals for the power semiconductors are modulated using the SVPWM. However, the angle θ applied to the Park transform has to be obtained using a Phase-Locked-Loop (PLL) system, to ensure a proper synchronization with the electrical grid.

In the unified topology, proposed in this MSc. Thesis, the input filter consists of using the windings of the electrical machine. Thus, there are associated disturbances that may compromise the performance of the control system.

In [19], the variation of the values of the inductances is discussed, using a PMSM. This issue will cause a system unbalance, the currents I_q and I_d will not be pure DC and an inverse sequence component with twice the grid frequency will appear at the output current. As solution, *Zaja et al.* propose adding a sine wave of adjustable amplitude and phase to the d -axis voltage [19]. The proposed control block is described in Figure 3.12.

The feedforward compensation is not included in [19]. However, as mentioned before, its inclusion provides improved results [39], [75], [86], [88]. In this case, only for simplifying the comprehension of the control block diagram this component is not included in Figure 3.12.

The compensation wave is generated according to the measured and the reference values of the voltage of the DC-bus. A good dynamic performance can be achieved determining the optimal values, according to the obtained errors and implementing them in a look-up table [19]. However, for battery charging operation, fast dynamic response is not generally required and thus, *Zaja et al.* propose another type of method. First, the error ripple is determined and then its RMS value. After that, a wave optimizer produce two parameters, corresponding to the amplitude and phase for the compensation wave, using the bisection method until the convergence criteria is fulfilled. Finally, the amplitude and phase parameters are fed to the wave generator, producing the compensation signal with twice of the grid frequency [19].

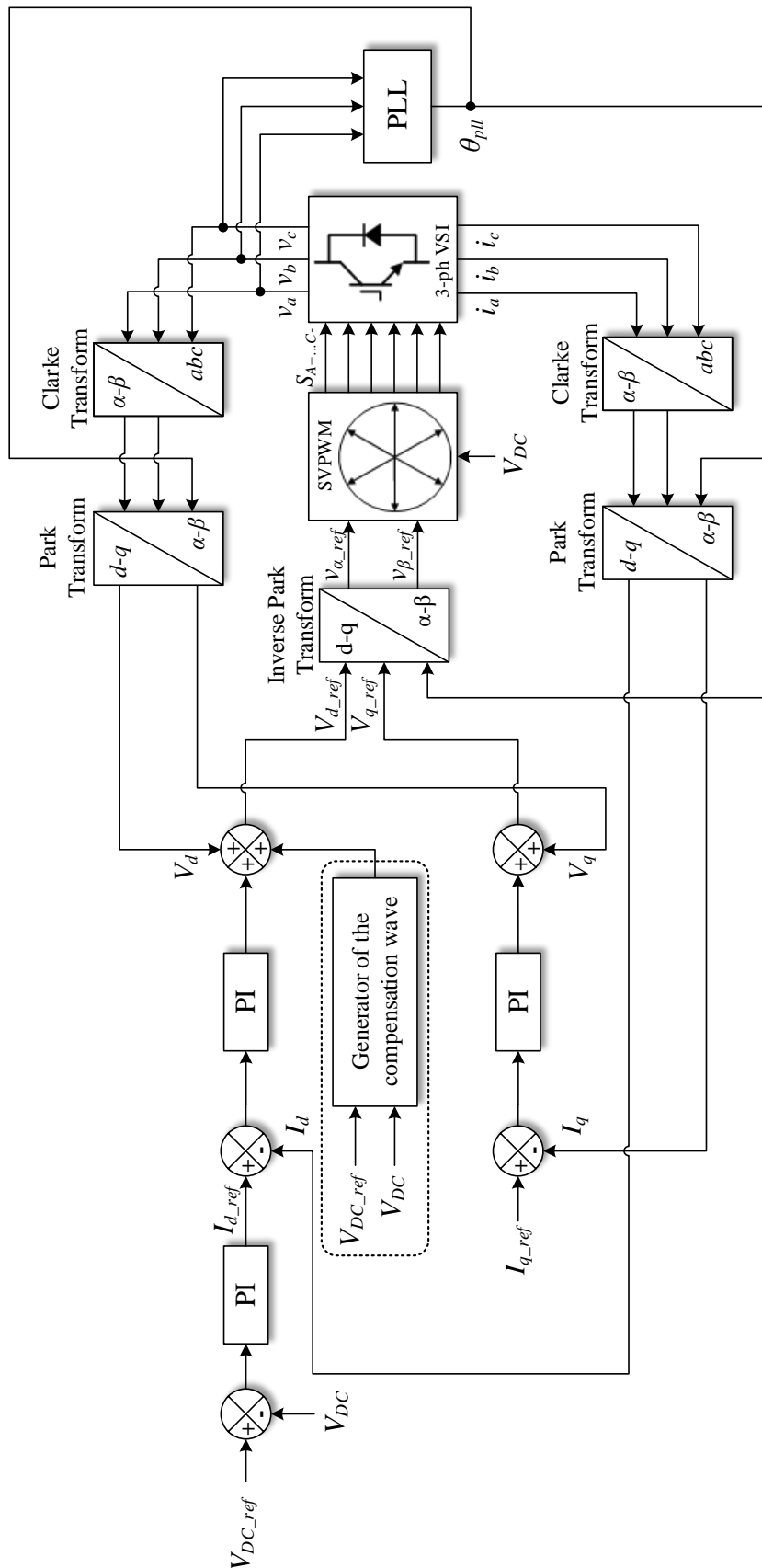


Figure 3.12 – Block diagram of the Direct Current Control based on Synchronous Reference Frame (DCC-SRF), changed for attenuate the disturbances due to the use of the windings of a PMSM as filter inductors (adapted from [19]).

Phase-Locked-Loop

For synchronizing the d - q coordinate system of the DCC-SRF with the electrical grid, the phase angle of the grid voltages has to be provided to the Park transform. However, the grid voltage is frequently contaminated with harmonic content or unbalances, compromising the quality and precision of the obtained information. Thus, a synchronizing system immune to those type of disturbances is required, for a proper synchronization of the power electronics converter with the electrical grid [89], [90].

The most widely accepted solution consists of using a Phase-Locked Loop (PLL) system [91]. This system must be capable of generating a sinusoidal signal whose phase is equal to the one of the fundamental component of the input signal [89], [90], [92].

The typical structure of a PLL system is described in Figure 3.13. The Phase Detector (PD) computes the phase difference between the input and output signals, the Loop Filter (LF) is responsible for adjusting the loop dynamic performance and to generate the signal for feed the Voltage-Controlled Oscillator (VCO), which is responsible for generate the synchronized output signal [92], [93].

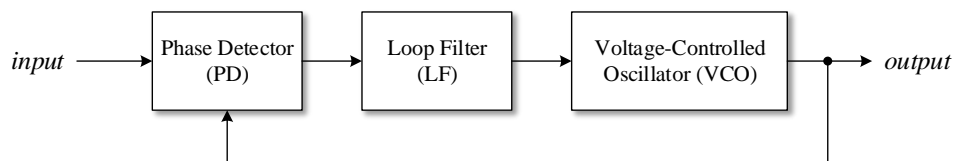


Figure 3.13 – Block diagram of the typical structure of a Phase-Locked-Loop (PLL) system (adapted from [93]).

A basic single-phase PLL system is described in Figure 3.14. The PD is realized by means of a multiplier, generating a signal whose phase is corresponds to the phase difference between the two signals [92]. The LP is realized using a PI controller, while the VCO is realized using an integrator, generating the synchronized angle signal, and a cosine function to generate the synchronized sinusoidal signal pll_{unit} , whose amplitude is normalized to the unity [93]. The parameter ω_o is the central frequency of the VCO, while the parameters of the PI controller are represented as K_{p_LP} and K_{i_LP} . The variable θ_{pll} is the obtained synchronized angle of the PLL system and v_s the input voltage of the source.

Karimi-Ghartemani et al. propose in [92], [94], an Enhanced Phase-Locked Loop (EPLL) system, described in Figure 3.15, based on an alternative method for the PD [92].

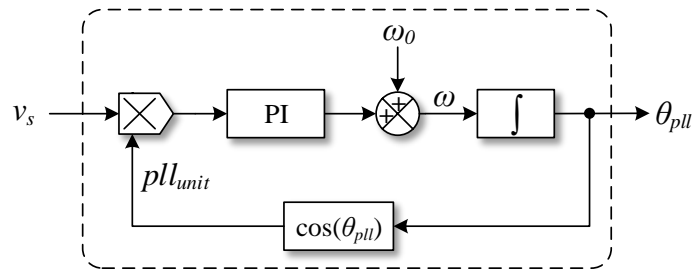
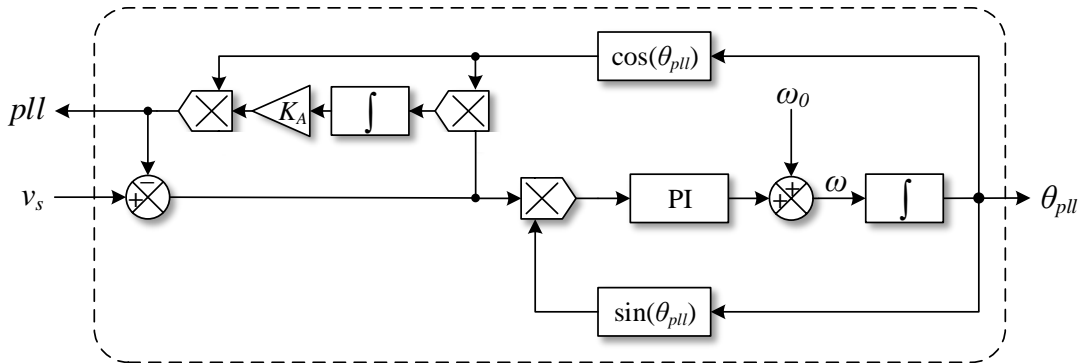


Figure 3.14 – Block diagram of a basic single-phase PLL system (adapted from [93]).

Figure 3.15 – Block diagram of a single-phase Enhanced Phase-Locked-Loop (EPLL) system proposed by Karimi-Ghartemani *et al.* (adapted from [92], [95]).

The modified PD of the EPLL results in a PLL system operating as a nonlinear notch filter. This PLL system provides direct estimation of the phase and amplitude of the main component of the input signal. Thus, besides the output obtained signal be locked in phase it is also locked in amplitude, enhance other applications for this PLL system [94].

The main advantages of this PLL system are its structure simplicity and performance robustness, since that small variations on values of the parameters K_A , K_{p_LP} , K_{i_LP} and ω_o are tolerated without affect significantly its performance [92].

The parameter K_A adjusts the convergence rate of the amplitude, while K_{p_LP} and K_{i_LP} adjusts the dynamic of the loop. It is important to note that the tuning of the parameters is compromised between the dynamic speed and the filtering performance [93].

In the proposed EPLL it is assumed that the fundamental frequency of the input signal is fixed. Hence, the performance of this PLL system is compromised when variations occurs in the frequency value of the fundamental component. However, according to [96], this system is capable of follow small variations in the frequency of the fundamental component.

However, for fast charging operation it is required a three-phase grid connection and, hence, the proposed DCC-SRF requires a three-phase PLL system.

In [97], *Sasso et al.* propose two PLL configurations based on the p-q theory [98], [99], where the instantaneous real power p and imaginary power q are defined according to (3.24). One of those configurations is the q-PLL that is described in the Figure 3.16 (a).

$$\begin{cases} p = v_{\alpha} i_{\alpha} + v_{\beta} i_{\beta} \\ q = v_{\beta} i_{\alpha} - v_{\alpha} i_{\beta} \end{cases} \quad (3.24)$$

The synchronized signal obtained by the q-PLL results from computing fictitious currents $i_{\alpha f}$ and $i_{\beta f}$, in order to obtain a correspondent fictitious imaginary power q_f , which is compared with a reference value (set to zero, in this case) and submitted to a PI controller. When appropriately tuned, the q-PLL configuration can become almost insensitive to harmonics in the input voltage [97].

In [100]–[102] a different type of three-phase PLL system is discussed, based on using the Park transform, known as SRF-PLL. It is one of the most used PLL techniques [100], [103] and its basic configuration is presented in Figure 3.16 (b). This basic configuration presented has some problems of performance, in the presence of distorted and unbalanced supply voltages. However, taking advantage of its structure simplicity, there is a wide range of reported PLL configurations described in [103], that are based on the SRF-PLL, but providing improved immunity to those issues.

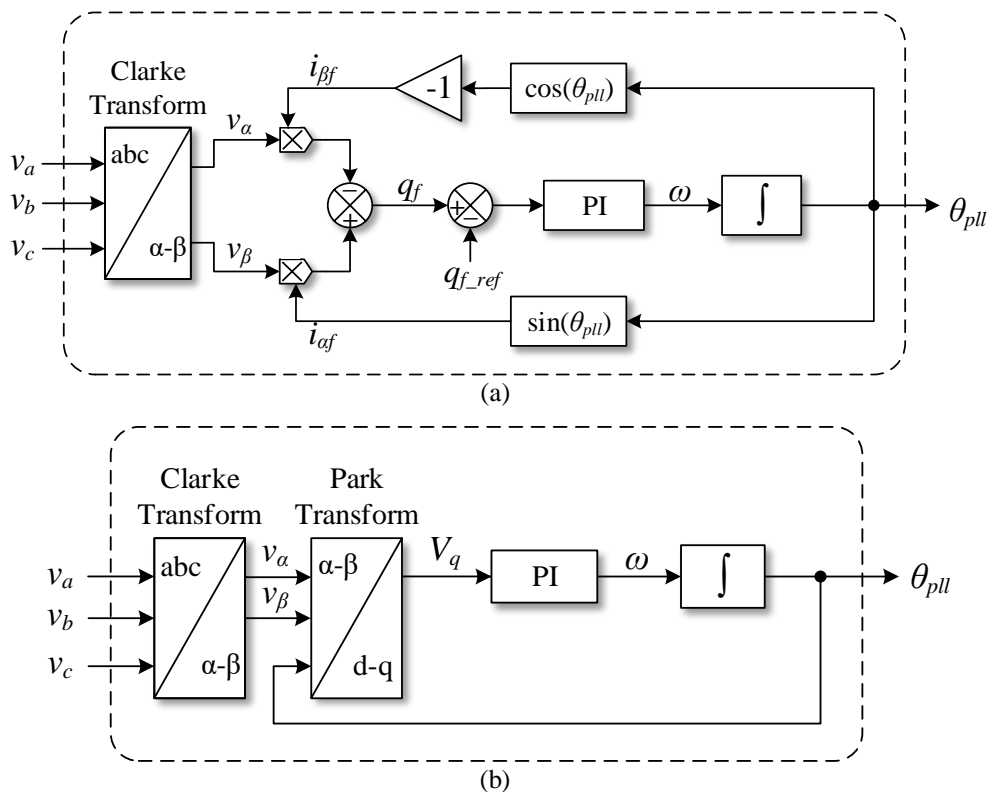


Figure 3.16 – Diagram block of three-phase PLL system: (a) q-PLL (adapted from [97]); (b) Basic SRF-PLL (adapted from [101]).

3.3.2. Direct Power Control Based on Model Predictive Control

Classic linear controllers with modulation techniques and nonlinear controllers based on hysteresis comparators are the most widely used control algorithms. However, the developments achieved over the years in digital electronics, including on Digital Signal Controllers (DSCs), offer more computational power, potentiating the development of new and more effective and complex control techniques, such as the Model Predictive Control (MPC) [104]–[106].

Using a dynamical model of the system, the MPC predicts the future behavior of its control variables. Then it selects the most appropriate control action, based on an optimal criterion, typically a cost function whose result has to be minimized. The MPC is considered a very attractive alternative control technique for three-phase grid-connected power converters due to its simple and intuitive concept, its effectiveness, flexibility and its fast dynamic response. However, since the MPC is based on predicting the system behavior, it typically requires a higher amount of calculations comparatively to classic controllers [104]–[106].

A direct current control based on MPC, using SVPWM and applied to a three-phase boost AC-DC converter is discussed in [107], [108] and its typical configuration is shown in Figure 3.17. This type of MPC is known as Continuous Control Set MPC (CCS-MPC) [106]

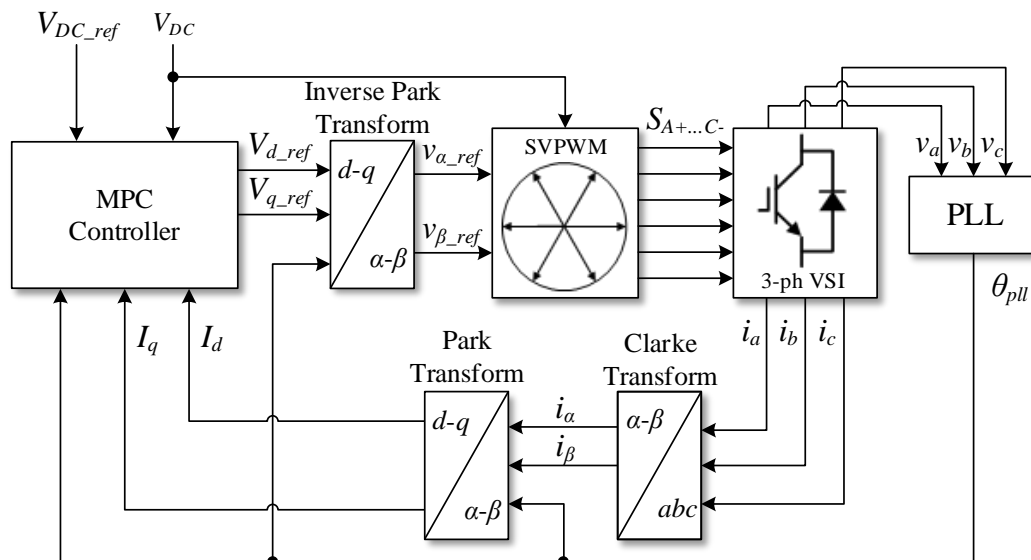


Figure 3.17 – Block diagram of a direct current control based on Model Predictive Control (MPC), using SVPWM (based on [108]).

However, as discussed in the previous chapter, power converters such as three-phase VSIs have a limited number of switching states. Thus, the control action is limited to eight possible actions, considering the allowed switching states of the VSI. This

condition allows for the optimization of the MPC, reducing its computation effort, since the prediction of the system behavior can be done considering only the possible switching states. This approach is known in literature as Finite Control Set Model Predictive Control (FCS-MPC) [104], [106].

Contrarily to the CCS-MPC, the FCS-MPC does not require a modulation stage to generate the switching states, since the control action is directly evaluated in terms of the allowed switching states of the converter [106].

An example illustrating the operating principle of the FCS-MPC is presented in Figure 3.18. Supposing that x is a control variable and that is intended that this variable follow the behavior of another called x_{ref} , i.e., the cost function, in this case, is defined as the difference between x_{ref} and x , corresponding to the traditional concept of error. Supposing that in the power electronics converter used there are only n possible control actions. Thus, at each sampling instant t_{k+i} the MPC make a prediction of the values that x can take, depending on the control action applied (from x_{p1} to x_{pn}). Then, the algorithm chooses the control action that minimizes the cost function, i.e., the control action that minimizes the error and approaches x from x_{ref} .

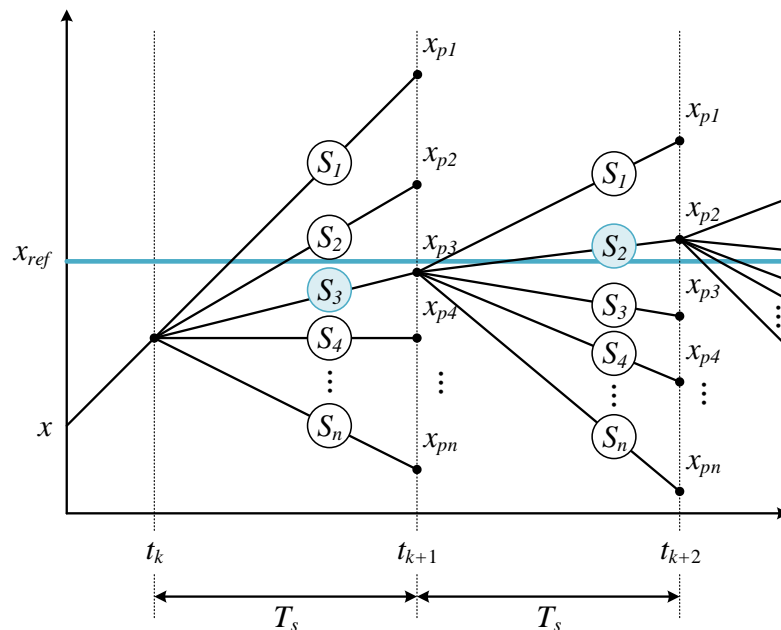


Figure 3.18 – Operation principle of the Finite Control Set Model Predictive Control (FCS-MPC) (adapted from [104]).

In [109], *Cortés et al.* propose a type of FCS-MPC, mentioned as Direct Power Control based on Model Predictive Control (DPC-MPC), for controlling a boost AC-DC converter.

The dynamical model of the three-phase boost AC-DC converter is obtained analyzing the already presented Figure 3.10, obtaining (3.25) and resulting in (3.26).

$$v_s(t) = v_R(t) + v_L(t) + v_{in}(t) = R_s i_s(t) + L_s \frac{di_s(t)}{dt} + v_{in}(t) \quad (3.25)$$

$$\frac{di_s(t)}{dt} = \frac{1}{L_s} [v_s(t) - R_s i_s(t) - v_{in}(t)] \quad (3.26)$$

Using the Euler approximation, the derivative of the current is approximated to (3.27), and thus the input predicted current i_s is discretized for a sample period T_s , resulting in (3.28).

$$\frac{di_s(t)}{dt} = \frac{i_s(k+1) - i_s(k)}{T_s} \quad (3.27)$$

$$i_s(k+1) = \left(1 - \frac{R_s T_s}{L_s}\right) i_s(k) + \frac{T_s}{L_s} [v_s(k) - v_{in}(k)] \quad (3.28)$$

To accommodate all three-phase components of the system, the input currents and voltages are defined as space vectors, according to (3.29) and (3.30) respectively, where $a = e^{j(2\pi/3)}$.

$$i_s = \frac{2}{3} (i_a + a i_b + a^2 i_c) \quad (3.29)$$

$$v_s = \frac{2}{3} (v_a + a v_b + a^2 v_c) \quad (3.30)$$

The voltage v_{in} is dependent on the switching state of the power electronics converter and the voltage of the DC-bus. In this case, *Cortés et al.* propose define v_{in} as a space vector according to (3.31). The value of S is defined according to (3.32), where S_a , S_b and S_c are the switching states of each leg of the converter, according to Figure 3.8 already presented, where if S_x is OFF then $S_x = 0$ and if S_x is ON then $S_x = 1$ ($x = \{A, B, C\}$).

$$v_{in} = S V_{DC} \quad (3.31)$$

$$S = \frac{2}{3} (S_A + a S_B + a^2 S_C) \quad (3.32)$$

The possible values of v_{in} , according to (3.31) and (3.32) are presented in Table 3.5. There are two switching states (both S_A , S_B and S_C ON and both S_A , S_B and S_C OFF), in which the obtained value of v_{in} is exactly the same (zero). Thus, only seven switching states can produce different results and hence only seven predictions of the input current are required.

Table 3.5 – Voltage v_{in} , according to the switching states of the three-phase AC-DC converter (adapted from [105]).

Switching states			Voltage space vector of v_{in}
S_A	S_B	S_C	
0	0	0	$v_{in,1} = 0$
0	0	1	$v_{in,2} = -\frac{1}{3}V_{DC} - j\frac{\sqrt{3}}{3}V_{DC}$
0	1	0	$v_{in,3} = -\frac{1}{3}V_{DC} + j\frac{\sqrt{3}}{3}V_{DC}$
0	1	1	$v_{in,4} = -\frac{2}{3}V_{DC}$
1	0	0	$v_{in,5} = \frac{2}{3}V_{DC}$
1	0	1	$v_{in,6} = \frac{1}{3}V_{DC} - j\frac{\sqrt{3}}{3}V_{DC}$
1	1	0	$v_{in,7} = \frac{1}{3}V_{DC} + j\frac{\sqrt{3}}{3}V_{DC}$
1	1	1	$v_{in,8} = 0$

Considering the space vector definitions used for the voltage and current values, the predicted values for the instantaneous real power p and imaginary power q are defined, respectively, according to (3.33) and (3.34).

$$p(k+1) = v_{s\alpha} i_{s\alpha} + v_{s\beta} i_{s\beta} = \Re \left\{ v_s(k+1) \bar{i}_s(k+1) \right\} \quad (3.33)$$

$$q(k+1) = v_{s\beta} i_{s\alpha} - v_{s\alpha} i_{s\beta} = \Im \left\{ v_s(k+1) \bar{i}_s(k+1) \right\} \quad (3.34)$$

Using a high sampling frequency, the condition (3.35) is verified and thus, the measured values of the input voltages can be used to predict the future p and q values.

$$v_s(k+1) \approx v_s(k) \quad (3.35)$$

The DPC-MPC is based in the control of the instantaneous powers p and q and thus, *Cortés et al.* propose a cost function g defined according to (3.36).

$$g = |q(k+1)| + |p_{ref} - p(k+1)| \quad (3.36)$$

The minimization of the result obtained by the cost function is achieved considering two assumptions. On one hand, the instantaneous imaginary power q has to be as close as possible to zero, resulting in a battery charging operation with unity power factor. On the other hand, the real power p has to be as close as possible from p_{ref} , which represents

the desired voltage for the DC-bus by means of a PI controller. Both of the two criteria have the same weight. Defining a constant value for the reference p_{ref} provides a charging operation consuming currents with low harmonic content. It is also possible to deliver back the energy stored in the battery pack to the electrical grid (i.e., operating in the V2G mode), by defining a negative value for the reference instantaneous real power p_{ref} .

However, there is an important issue that compromises the practical implementation of the presented control algorithm. In real-time applications is not possible to measure variables, predict their future values and apply the respective control action at the same instant. Thus, it is not correct to determine the predicted values considering that it is possible to apply the desired switching state at the same instant. Hence, to avoiding errors with the predictions, a delay in the predictive model has to be considered, resulting in a two-step-ahead prediction [104], [109].

Since the selected voltage can only be applied at the next step ($k + 1$), it is necessary to predict the current obtained as consequence of the select switching state, i.e., the current at $k + 2$. This current is obtained by shifting (3.28) one step forward, resulting in (3.37).

$$i_s(k+2) = \left(1 - \frac{R_s T_s}{L_s}\right) i_s(k+1) + \frac{T_s}{L_s} [v_s(k+1) - v_{in}(k+1)] \quad (3.37)$$

Thus, first $i_s(k+1)$ is calculated using (3.28), considering the current and voltage measured and the value of v_{in} obtained as consequence of the switching state selected in the previous sampling. Then, the obtained predicted current is used in (3.37) as well as the voltage measured, in order to obtain the seven predicted currents. Similarly, the cost function g is modified, resulting in (3.38).

$$g = |q(k+2)| + |p_{ref} - p(k+2)| \quad (3.38)$$

The block diagram of the proposed DPC-MPC is presented in Figure 3.19.

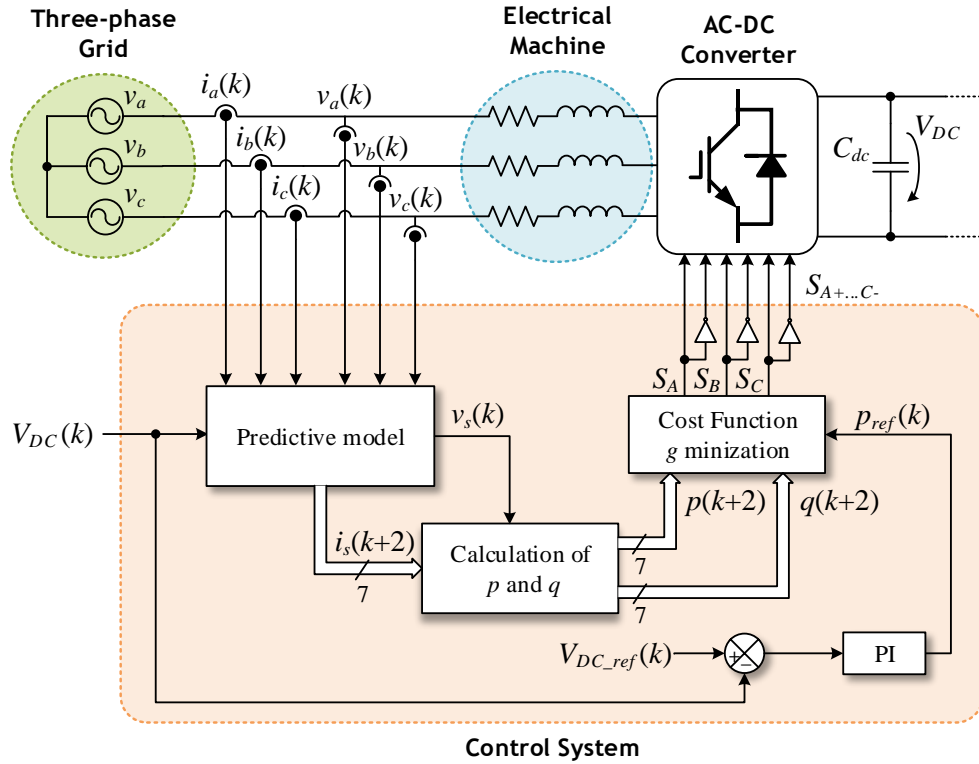


Figure 3.19 – Block diagram of the Direct Power Control based on Model Predictive Control (DPC-MPC) (based on [109]).

Since the presented FCS-MPC uses Direct Power Control, it does not require a PLL system for synchronizing the power converter with the electrical grid. As drawback, this control algorithm does not impose a fixed switching frequency, since the power semiconductors of the AC-DC converter only commute according to the results obtained from the cost function [104]. Hence, it makes unfeasible the use of extra current filters for improve the waveform of the currents consumed. However, this issue can be easily overcome by including in the cost function a condition that ensures a certain number of commutations during a certain time period, to obtain thus a fixed switching frequency. An example of such condition is presented in [104], resulting in a new cost function defined in (3.39). The variable $\overline{f_{sw}^*}$ is the reference for the average switching frequency, defined as $\overline{f_{sw}^*} = C^*/\Delta t$, where C^* is the number of the desired commutations, during the time period Δt .

$$g' = g + \lambda \left| \overline{f_{sw}^*} - \frac{1}{\Delta t} \sum_{i=0}^{\frac{\Delta t}{T_s}-1} C(t_{k-i}) \right| \quad (3.39)$$

The proposed control algorithm has also other drawbacks such as the high complexity level, since it requires calculations using complex numbers and, hence, a significant computational effort is required.

A FCS-MPC used for battery charging of an EV, operating in V2G and G2V modes is reported in [105], but using direct current control.

The immunity of the proposed DPC-MPC to the variations of the input filter inductances' values, comparatively to the values defined in the predictive model, is discussed in [109], but considering that both three inductances vary equally from the value defined in the model. The results obtained concluded that the proposed algorithm has proved to be robust when errors in the inductance values are present (establishing an inductance value of 10 mH and range their real value between 5 mH and 20 mH) [109]. However, only an analysis on the results obtained using this control algorithm in the unified topology proposed in this MSc. Thesis can assess the effective need of changes in the control algorithm. These may involve considering the inductances matrix and the possible range of the values of the individual inductances, according to the rotor position.

Nevertheless, any constraint can generally be included in the predictive model and the cost function of the MPC, since it can be mathematically modeled and measured [104]. Thus, this control algorithm seems to offer greater ease in solving the possible disturbances that may occur, due to the use of the windings of the electrical machine, in a simplest way than using the DCC-SRF.

The unified topology proposed in this MSc. Thesis is easily adapted for the slow charging mode, through a single-phase grid connection and using only two windings of the electrical machine and two legs of the three-phase VSI, as presented in Figure 3.20.

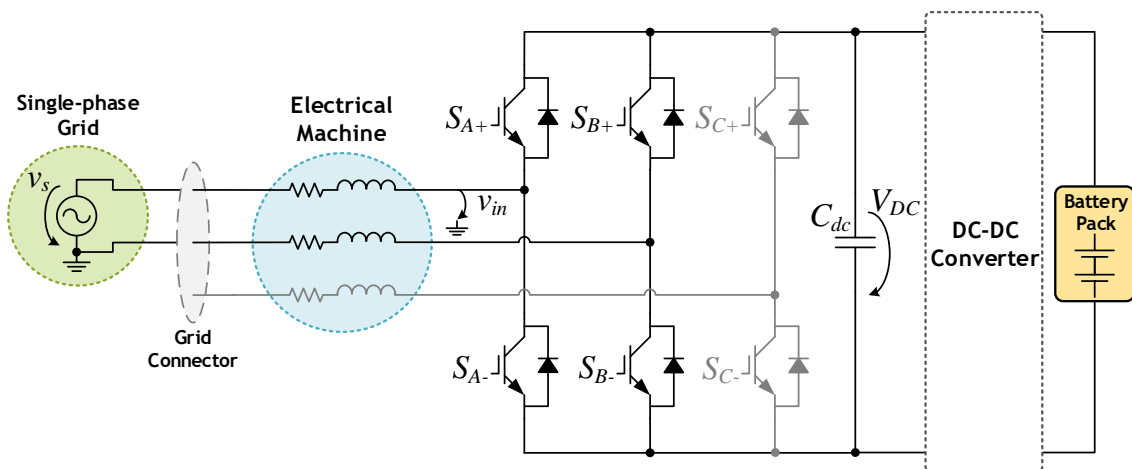


Figure 3.20 – Equivalent circuit of the unified topology proposed in this MSc. Thesis, for the slow charging mode, through an AC single-phase grid supply.

The proposed DPC-MPC is also easily adapted for the slow charging mode. In this case, the expression defined for the predicted current is the same, except the fact that the current i_s and voltages v_s and v_{in} are not required to be mapped into space vectors.

Since only two legs of the converter are used, the possible switching states are reduced to four possibilities. Similarly, according to Table 3.6, two of them are redundant, and thus only three different possibilities are considered

Table 3.6 – Voltage v_{in} , according to the switching states of the equivalent single-phase AC-DC converter.

S_A	S_B	v_{in}
0	0	0
0	1	$-V_{DC}$
1	0	V_{DC}
1	1	0

Since it is a single-phase system, the cost function has to be modified. In this case it will be used another type of cost function widely used [105], [110], presented in (3.40), which is based on the input current value. Hence the MPC is now a direct current control.

$$g = |i_{s_ref} - i_s(k+2)| \quad (3.40)$$

In [52], *Pinto et al.* propose a bidirectional single-phase battery charger for an EV, in which the reference current is generated according to Figure 3.21. The variable pll_{unit} is the unitary synchronized signal obtained by the single-phase PLL system, P_{ref} the active power reference and I_{s_ref} the RMS value of the reference current.

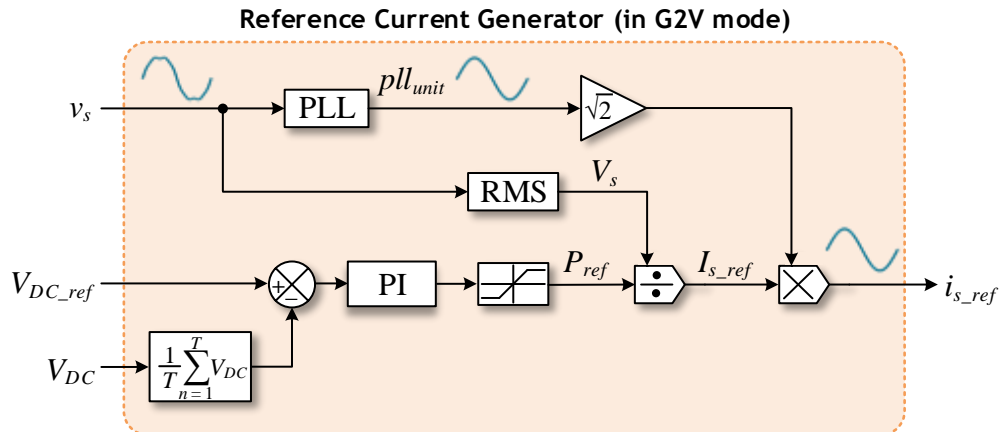


Figure 3.21 – Block diagram for the reference current, proposed to use in the MPC, for the slow charging mode (adapted from [52]).

For deliver back the energy stored to the electrical grid (operating in the V2G mode), the reference power P_{ref} has to be negative. Hence, the last presented control block

for generate the input reference current in the G2V mode could be adapted for the V2G mode, resulting in the block diagram presented in Figure 3.22.

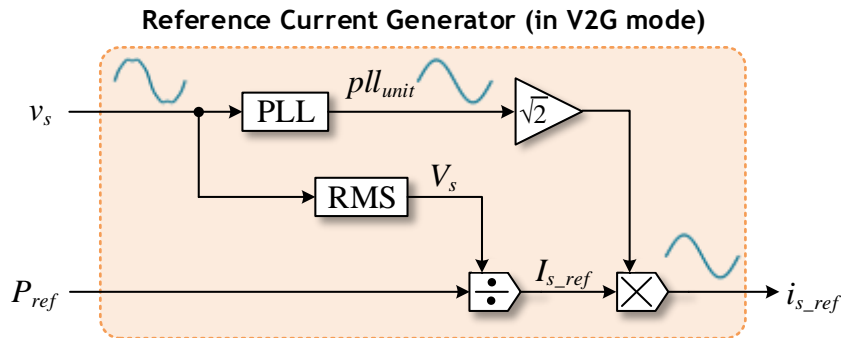


Figure 3.22 – Block diagram for the reference current, proposed to use in the MPC, for the Vehicle-to-Grid (V2G) operation during the slow charging mode (based on [52]).

3.4. Control Algorithms for the Bidirectional DC-DC Converter

In this section the control algorithms for the bidirectional DC-DC converter, comprising the second stage of the proposed unified topology, are presented and discussed. This converter is used to interface the battery pack with the DC-bus of the VSI and should operate in three different modes: motor drive and battery charging (G2V and V2G) modes.

The topology of the proposed DC-DC converter is presented in Figure 3.23.

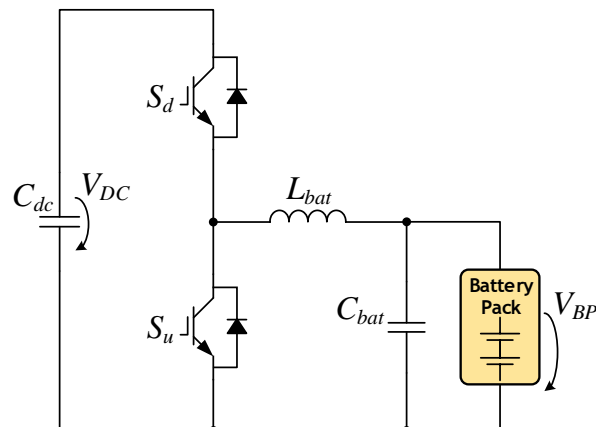


Figure 3.23 – Bidirectional DC-DC converter included in the unified topology proposed in this MSc. Thesis.

3.4.1. Motor Drive

The voltage of the battery pack is typically lower than voltage of the DC-bus [52]. Hence, for the motor drive operation, the bidirectional DC-DC converter has to elevate the voltage of the battery pack to ensure the proper operation of the VSI. Thus, the DC-DC converter has to act as a Step-Up (Boost) DC-DC converter. This corresponds to

applying a control gate signal to the power semiconductor S_u (Figure 3.23), leaving the power semiconductor S_d disconnected, corresponding to the equivalent circuit presented in Figure 3.24.

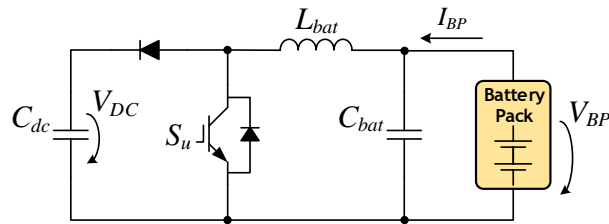


Figure 3.24 – Equivalent circuit of the bidirectional DC-DC converter operating as a Step-Up (Boost) DC-DC converter.

In [52], *Pinto et al.* propose a control algorithm for implementing the Vehicle-to-Home (V2H) mode in a battery charger, comprising a single-phase AC-DC boost converter and a bidirectional DC-DC converter, whose topology is equal to the one that is presented in Figure 3.23. The proposed control algorithm for the bidirectional DC-DC converter provides the required voltage regulation for the motor drive purpose. Thus, the proposed control algorithm, whose block diagram is presented in Figure 3.25, is used for the motor drive mode.

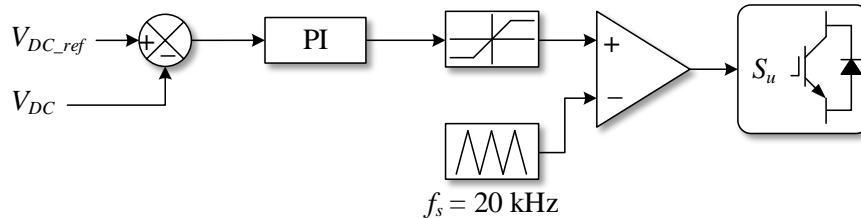


Figure 3.25 – Block diagram of the control algorithm proposed for the bidirectional DC-DC converter, during the motor drive mode (adapted from [52]).

3.4.2. Battery Charging

The control algorithms for the bidirectional DC-DC converter operating in the battery charging mode are described in this section for the Grid-to-Vehicle (G2V) and the Vehicle-to-Grid (V2G) modes.

Grid-to-Vehicle Mode

For the typical battery charging operation, i.e. in the Grid-to-Vehicle (G2V) mode, the bidirectional DC-DC converter has to act as a Step-Down (Buck) DC-DC converter, since the voltage of the DC-bus is typically higher than the voltage of the battery pack [52]. This corresponds to apply a control gate signal to the power semiconductor S_d

(Figure 3.23), leaving the power semiconductor S_u disconnected, corresponding to the equivalent circuit presented in Figure 3.26.

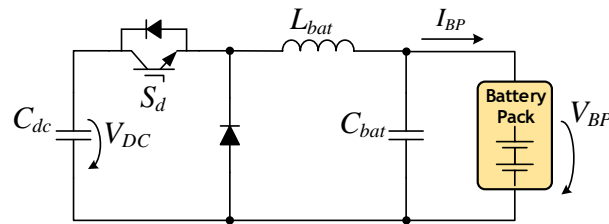


Figure 3.26 – Equivalent circuit of the bidirectional DC-DC converter operating as Step-Down (Buck) DC-DC converter.

Most of the battery manufactures recommend a battery charging process comprising two steps [52]: constant current followed by constant voltage, according to Figure 3.27. First, the battery pack is charged with constant current, until the voltage across the battery pack reaches a recommended maximum value V_{B_MAX} . Then, a constant voltage is applied to the terminals of the battery pack. As soon as the current flowing to the battery pack reaches a residual value I_{B_MIN} , the control system stops acting and the battery charging operation is complete [52], [111].

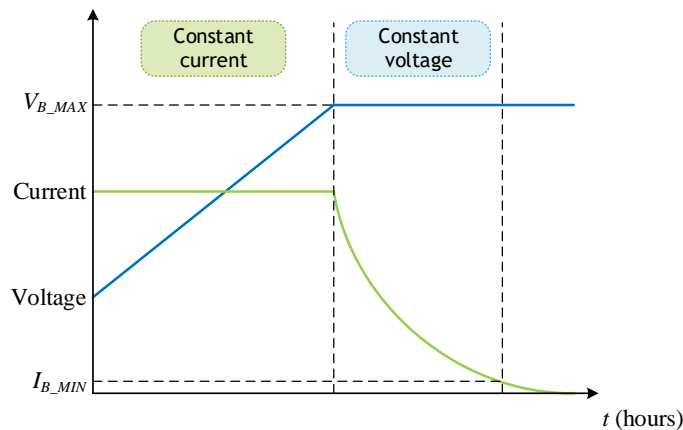


Figure 3.27 – Battery charging comprising two steps: constant-current and constant-voltage (adapted from [111]).

In [52], *Pinto et al.* propose a control algorithm for implementing this battery charging process. The proposed control algorithm is presented in Figure 3.28, comprising voltage regulation and current regulation modes.

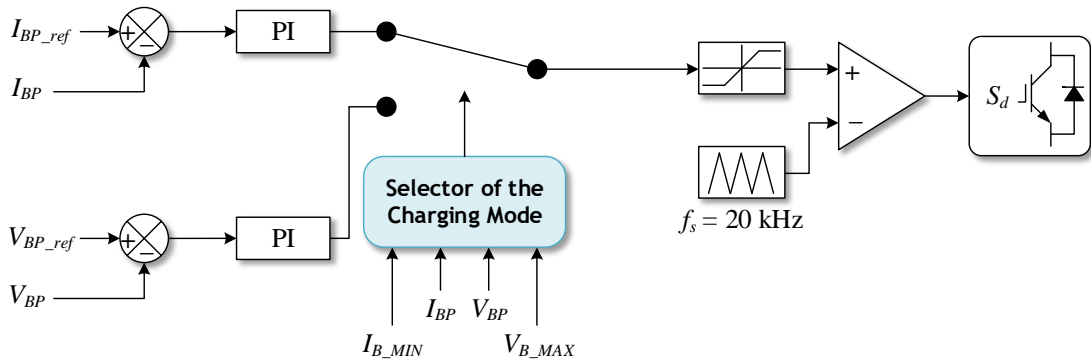


Figure 3.28 –Block diagram of the control algorithm proposed for the bidirectional DC-DC converter, during the Vehicle-to-Grid (V2G) mode (adapted from [52]).

Vehicle-to-Grid Mode

Besides the normal battery charging operation, the DC-DC converter also plays an important role supporting the Vehicle-to-Grid (V2G) operation mode. For a proper operation of the VSI in this mode, the voltage of the DC-bus has to be slightly greater than the peak of the voltage of the electrical grid [52]. Thus, such as in the motor drive mode, the bidirectional DC-DC converter has to act as a Step-Up (Boost) DC-DC converter, corresponding to the equivalent circuit already presented in Figure 3.24.

The control algorithm already presented in Figure 3.25 for the motor drive mode can be used for control the DC-DC converter in the V2G mode, adjusting the reference for the DC-bus voltage according to the required power to deliver back to the electrical grid and the voltage peak value of the electrical grid, or even for the V2H mode.

In addition, when the EV is operating in the V2G mode by means of a single-phase connection to the electrical grid, it can be used the control algorithm for the V2G mode proposed by *Pinto et al.* in [52], which is presented in Figure 3.29, using the same value for the P_{ref} defined in the reference current generator block applied to the VSI (Figure 3.22).

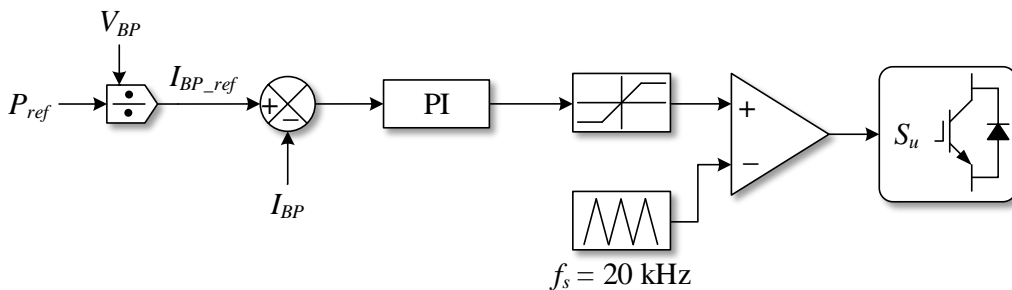


Figure 3.29 – Block diagram of the additional control algorithm proposed for the bidirectional DC-DC converter during the Vehicle-to-Grid (V2G), through a single-phase connection to the electrical grid (adapted from [52]).

3.5. Conclusions

The most relevant control algorithms that allow for the implementation of the motor drive and the battery charging of an Electric Vehicle (EV), using the unified topology proposed in this MSc. Thesis, are presented and discussed in this chapter.

Two different types of vector control algorithms for the motor drive operation mode are analyzed: the Field-Oriented Control (FOC) and the Direct Torque Control (DTC).

The FOC allows for a low torque in steady-state, while the DTC provides a better dynamic response. However, electrical machines applied to EVs have typically low values of inductances and thus a traditional DTC by means of hysteresis controllers can lead to a considerable high torque ripple in steady-state.

For the battery charging operation two control algorithms are analyzed: the Direct Current Control based on Synchronous Reference Frame (DCC-SRF) and the Direct Power Control based on Model Predictive Control (DPC-MPC).

The DCC-SRF has various similarities with the FOC. The synchronism with the electrical grid is done by means of a Phase-Locked Loop (PLL) system. The case of using the proposed unified topology using a PMSM is analyzed. Since the values of the inductances vary according to the rotor position, the inclusion of a wave compensator is proposed for improve the obtained results.

The DPC-MPC allows for control the instantaneous real power p and imaginary power q exchanged between the electrical grid and the unified topology, based on using a dynamical model of the system in order to predict its future behavior. Besides the good results reported, it allows for an easily adaptation for slow charging and a simplest addition of constraints to the control algorithm than the DCC-SRF, since they could it be mathematically modeled and measured. An alternative approach for slow charging, through a single-phase connection to the electrical grid, is analyzed. A direct current control is used and a PLL system is required for generate the input current reference.

Finally the proposed algorithms for controlling the bidirectional DC-DC converter, for the motor drive and battery charging (considering Grid-to-Vehicle (G2V) and Vehicle-to-Grid (V2G) modes), by means of a single-phase or three-phase connection to the electrical grid are presented.

Chapter 4

Simulations of the Proposed Solution

4.1. Introduction

In this chapter the computational simulations performed for the proposed solution, comprising the unified hardware topology and the control algorithms chosen to perform the functions of motor drive and battery charger, are presented and discussed.

The simulation stage is a process of great importance, since it allows for the anticipation of some problems that might occur in a real implementation. Hence, it contributes to the optimization of the time required for the development as well as the financial resources required.

All the simulation results presented in this chapter were developed using the electronic-circuit simulation software package *PSIM*.

Initially the main characteristics of the electrical machine used in this MSc. Thesis for testing the proposed topology are presented, as well as the laboratory experiments performed to obtain some of their parameters, required by the software *PSIM*.

Afterwards it is presented the dynamical model developed in the software *PSIM* for simulating the behavior of a li-ion (LiFePO_4) battery pack, in order to validate the control algorithms described in Sections 3.4.1 and 3.4.2 for the bidirectional DC-DC converter.

In the simulations of the motor drive mode the chosen control algorithm is firstly presented, followed by the simulation results obtained for two different conditions: operating without load and operating with nominal load.

The simulations for the battery charging mode are separated into fast charging, through an AC three-phase grid supply, and slow charging, through an AC single-phase grid supply. For each one the respective control algorithm chosen is presented as well as the main simulation results obtained for the Grid-to-Vehicle (G2V) and Vehicle-to-Grid (V2G) modes. In the fast charging mode the simulation results of the unified system operating as a reactive power compensator are also presented.

The last simulation results presented in this chapter are the ones performed for the bidirectional DC-DC converter.

4.2. Electrical Machine

The electrical machine used in this MSc. Thesis for testing the proposed unified topology is the *HPM-20KW* model from *Golden Motors*, presented in Figure 4.1. This is a dual-stator Brushless DC (BLDC) machine with a nominal power of 20 kW and whose main characteristics are described in Table 4.1.



Figure 4.1 – Brushless DC (BLDC) machine used in this MSc. Thesis (source: *Golden Motors*).

Table 4.1 – Main characteristics of the BLDC machine (*HPM-20KW*), used in this MSc. Thesis.

Characteristics	Value	Unit
Nominal Power	20	kW
Rated Speed	3500	rpm
Nominal DC Voltage	120	V
Nominal Torque	80	Nm
Peak Torque	160	Nm
Number of poles	8	poles
Dimensions	30x30x25	cm
Weight	39	kg

The dual-stator configuration of the electrical machine allows for an improved efficiency, since, for the same amount of power, the currents can be divided between the two stators, reducing the heat losses. The configuration of their stator windings as well as the accessible terminals are presented in Figure 4.2.

As discussed in Section 2.2.2, one of the concerns about the use of the electrical machine in the battery charging operation is the values of the inductances of their windings. If the values of the inductances were not sufficiently high, the battery charging operation might consume input currents with high harmonic content.

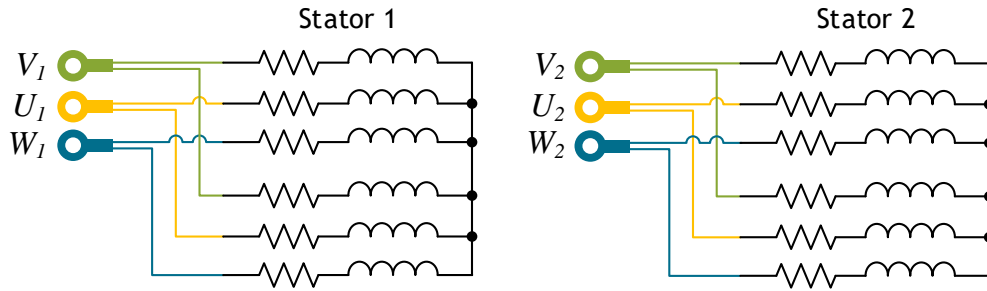


Figure 4.2 – Configuration of the stator windings and accessible terminals of the BLDC machine *HPM-20KW*.

Thus, in this case, it was chosen to modify the windings' arrangement, for maximizing the values of the inductances. In this arrangement the windings corresponding to the same phase of each stator are connected in series, resulting in the configuration presented in Figure 4.3. As a result, the electrical machine has now the same configuration as a single-stator machine. This winding arrangement is applied to both the motor drive and battery charging modes, in order to avoid the need of switching devices for reconfiguring the windings.

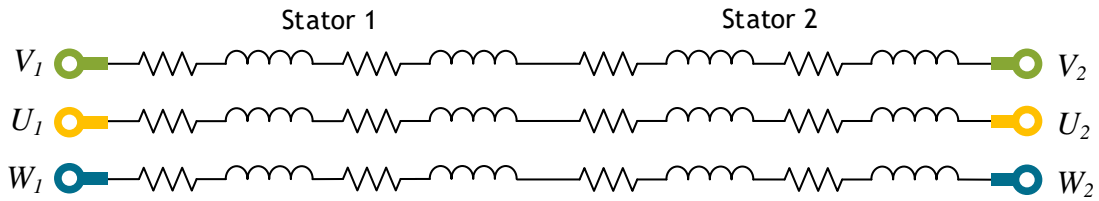


Figure 4.3 – Modified configuration of the stator windings and accessible terminals implemented in the BLDC machine *HPM-20KW*, for maximizing the values of its inductances.

According to [112], the total equivalent inductance of two inductances L_1 and L_2 connected in series, with magnetic coupling, is defined in (4.1), where M is the mutual inductance. The mutual inductance M is defined according to (4.2), where k_c is the coefficient of coupling, and results from the magnetic field interaction between the coils of the two windings. Its value and signal is dependent on the distance and orientation between them.

$$L_{eq} = L_1 + L_2 \pm 2M \quad (4.1)$$

$$M = k_c \sqrt{L_1 L_2} \quad (4.2)$$

Considering L_1 and L_2 two inductances of the same phase, a positive influence, a total coupling between the windings of the same phase (i.e., $k_c = 1$), and the same value of inductance for the windings of the same phase (i.e., $L_1 = L_2$), the proposed winding

arrangement (with the inductances of the same phase connected in series) can, at best, quadruple the value of the equivalent inductance per phase.

After concluding the proposed modifications, the measurements of the resultant values of the equivalent resistance and inductance of the windings per each phase were performed using, respectively, a multimeter (37XR-A from *Amprobe*), and a RLC-bridge (3532-50 LCR HiTESTERa from *HIOKI*). The obtained values are presented in Table 4.2.

Table 4.2 – Results of the measurements of the values of inductance and resistance of the windings of the BLDC machine used in this MSc. Thesis (with the proposed modified configuration). The values of the inductances were measured for a frequency of 20 kHz.

Measured Parameter	Value	Unit
Average value of the equivalent resistance per phase (R_s)	400	m Ω
Inductance value in the phase- <i>a</i> (L_{sa})	258	μ H
Inductance value in the phase- <i>b</i> (L_{sb})	276	μ H
Inductance value in the phase- <i>c</i> (L_{sc})	253	μ H

The obtained values for the inductances are a cause of concern. Compared with the values mentioned in the solutions discussed in Section 2.2.2, in which the stator windings have values of inductances from a few units to some dozens of mH [19], [57], [63], [74], the obtained values seem to be too low for the intended purpose.

The software *PSIM* already has a motor drive module consisting of a BLDC machine. However, the information presented in Table 4.1 and Table 4.2 is not sufficient to fill out all the required parameters to use this module in the simulation software. The value of the peak line-to-line back Electromotive Force (EMF) constant, in V/krpm units, is required, as well as the Root Mean Square (RMS) line-to-line back EMF constant, also in expressed in V/krpm. These values were obtained through laboratory experiments by configuring the BLDC machine to operate as a generator, placing an induction machine coupled to it, as presented in Figure 4.4, and using a variable speed drive to set the rotational speed of the induction machine to 1000 rpm.

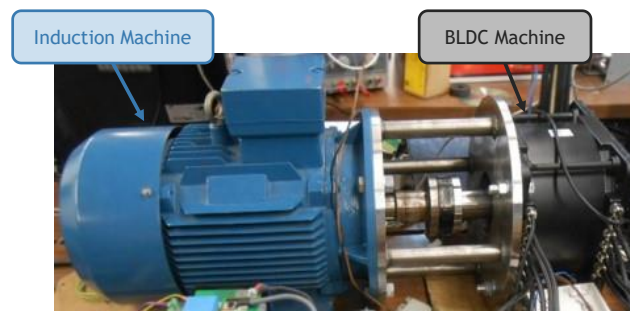


Figure 4.4 – Setup of the experimental tests performed for obtain the parameters V_{pk} / krpm and V_{RMS} / krpm of the BLDC machine used in this MSc. Thesis.

The obtained waveforms of the voltages are presented in Figure 4.5, in which it was obtained an average peak value of 73.20 V and an average RMS value of 52.84 V.

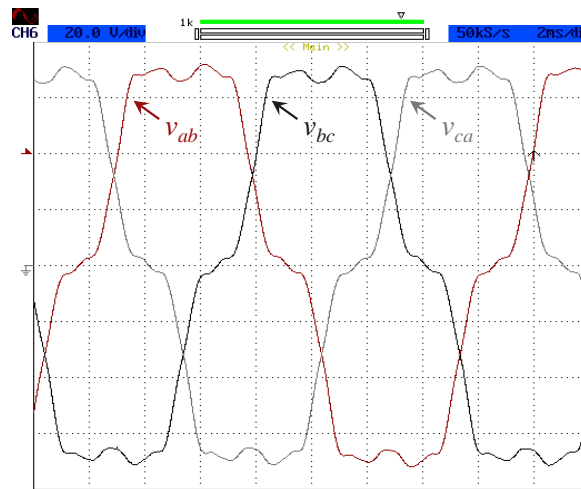


Figure 4.5 – Experimental results of the voltages v_{ab} , v_{bc} and v_{ca} (20 V/div) at the terminals of the BLDC machine, operating as a generator with a rotor speed of 1000 rpm.

The parameters used in the module of the BLDC machine available in the software *PSIM* are presented in Table 4.3. Since the values used for the moment of inertia (J) and the shaft time constant (λ_{shaft}) were not supplied by the manufacturer, the values considered are based on the information available for other electrical machines with similar characteristics. The estimated value for the stator mutual inductance (L_m), corresponds to 40% of stator self-inductance (L_s), according to the recommendations suggested by the simulation software, since its real value is not known.

Table 4.3 – Values of the parameters used in the module of the BLDC machine provided by the software *PSIM*, for the simulations of the proposed topology.

Stator resistance (R_s)	400 m Ω
Stator self-inductance (L_s)	262 μ H
Stator mutual inductance (L_m)	104.8 μ H ¹
Peak line-to-line back EMF constant ($V_{pk} / krpm$)	73.20 V/krpm
RMS line-to-line back EMF constant ($V_{RMS} / krpm$)	52.84 V/krpm
Moment of inertia (J)	0.00586 kg m ²
Shaft time constant (λ_{shaft})	0.1 s

¹ - According to the indications of the software *PSIM*, this value has to be entered as negative in the parameters of the block of the BLDC machine.

One important restriction is that the block of the model of the BLDC machine available in the software *PSIM* does not allow accessing to all the terminals of its stator windings. Thus, this block cannot be used to simulate the electrical machine operating as an input inductor filter during the battery charging operation. Therefore, in the simulations performed it was not possible to evaluate the occurrence of rotor vibrations or eventually other effects in the electrical machine, during the battery charging operation.

4.3. Dynamical Model of a Li-Ion (LiFePO₄) Battery

To validate the control algorithms described in Sections 3.4.1 and 3.4.2, applied to the bidirectional DC-DC converter, a dynamical model of a battery capable of being implemented in the simulation software *PSIM* was studied.

Different types of models of batteries are analyzed by *Mousavi et al.* in [113]. The most basic electric circuit-based model of battery consists of an ideal voltage source (V_{OC} , representing the open circuit voltage), in series with a resistance (R_{bat} , representing the internal resistance). However, this model is very limited, since the voltage supplied remains constant, without considering the State of Charge (SOC) of the battery or its typical dynamic characteristics [113].

Tremblay et al. propose in [114], [115] a dynamical model of a battery for Electric Vehicle (EV) applications. According to [113] this model has an high degree of complexity, comparatively to the most reported models, but it has the advantage of being the one for which it is easier to obtain the parameters for the simulation of a real battery, without requiring experimental tests.

As presented in Figure 4.6, the proposed model of battery is composed by two different parts: an electric circuit, consisting of a controlled voltage source in series with a resistance, and a dynamical model, responsible for setting the value of the open circuit voltage V_{OC} .

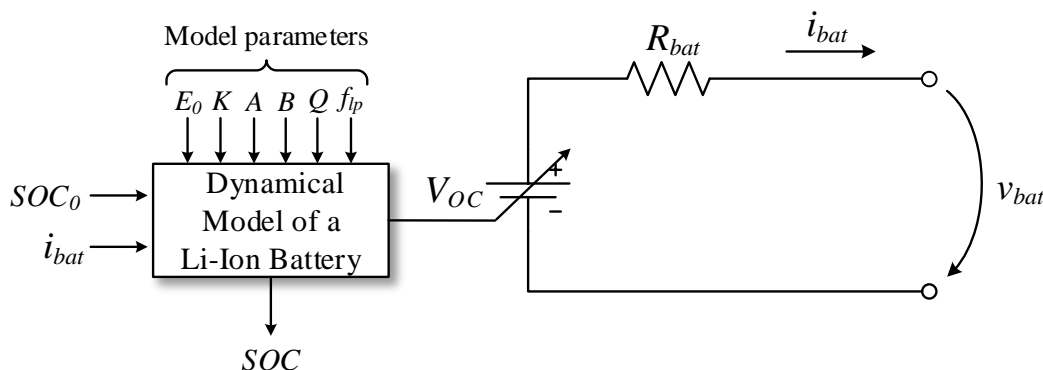


Figure 4.6 – Dynamical model of a li-ion (LiFePO₄) battery, proposed by *Tremblay et al.* in [115].

All the variables and parameters of the proposed model are described in Table 4.4.

It is important to note that this model could be easily adapted to different battery technologies, by modifying the charging and discharging expressions. In this case, the model of a li-ion battery was chosen since, according to the information provided in [23], it is one of the most used battery technologies in the commercially available EVs.

Table 4.4 – Variables and parameters of the proposed dynamical model of a li-ion (LiFePO₄) battery.

Variables			Parameters		
	Meaning	Units		Meaning	Units
v_{bat}	Instantaneous battery voltage	V	E_0	Battery constant voltage	V
i_{bat}	Instantaneous battery current	A	K_{pol}	Polarization resistance or Polarization constant	Ω or V/Ah
it	Actual battery charge $it = \int i(t) \cdot dt$	Ah	Q	Battery capacity	Ah
			A	Exponential zone amplitude	V
i_{bat}^*	Filtered current	A	B	Exponential zone time constant inverse	Ah ⁻¹
SOC	State-Of-Charge	%	R_{bat}	Internal resistance	Ω
			SOC_0	Initial State-Of-Charge	%
			f_{lp}	Low-pass filter frequency for the filtered current	Hz

According to [115], the open-circuit voltage (V_{OC}) of a li-ion (LiFePO₄) battery is defined by (4.3), where f_{charge} and $f_{discharge}$ are defined, respectively, according to (4.4) and (4.5).

$$V_{OC}(i^*, it) = E_0 - K_{pol} \frac{Q}{Q - it} it + A e^{-B it} + f_{charge}(i^*, it) + f_{discharge}(i^*, it) \quad (4.3)$$

$$f_{charge}(i^*, it) = -u_{charge}(i^*) K_{pol} \frac{Q}{it - 0.1 Q} i^* \quad (4.4)$$

$$f_{discharge}(i^*, it) = -u_{discharge}(i^*) K_{pol} \frac{Q}{Q - it} i^* \quad (4.5)$$

The decision of considering whether the battery is charging or discharging is established by the u_{charge} and $u_{discharge}$ functions, defined according to (4.6).

$$u_{charge}(i^*) = \begin{cases} 0 & \text{if } i^* \geq 0 \\ 1 & \text{if } i^* < 0 \end{cases} \quad u_{discharge}(i^*) = \begin{cases} 0 & \text{if } i^* \leq 0 \\ 1 & \text{if } i^* > 0 \end{cases} \quad (4.6)$$

In Figure 4.7 all the components of the simulation model developed in the software *PSIM* are presented, while its block representation is presented in Figure 4.8.

In the model developed, the calculations are considered to be performed with a time step of 1 second. This condition can be ensured by setting the value of the time step used

in the simulation software to the parameter $PSIM_time_step$ (Figure 4.8). On the other hand, this parameter also provides flexibility in order to speed up the response of the model.

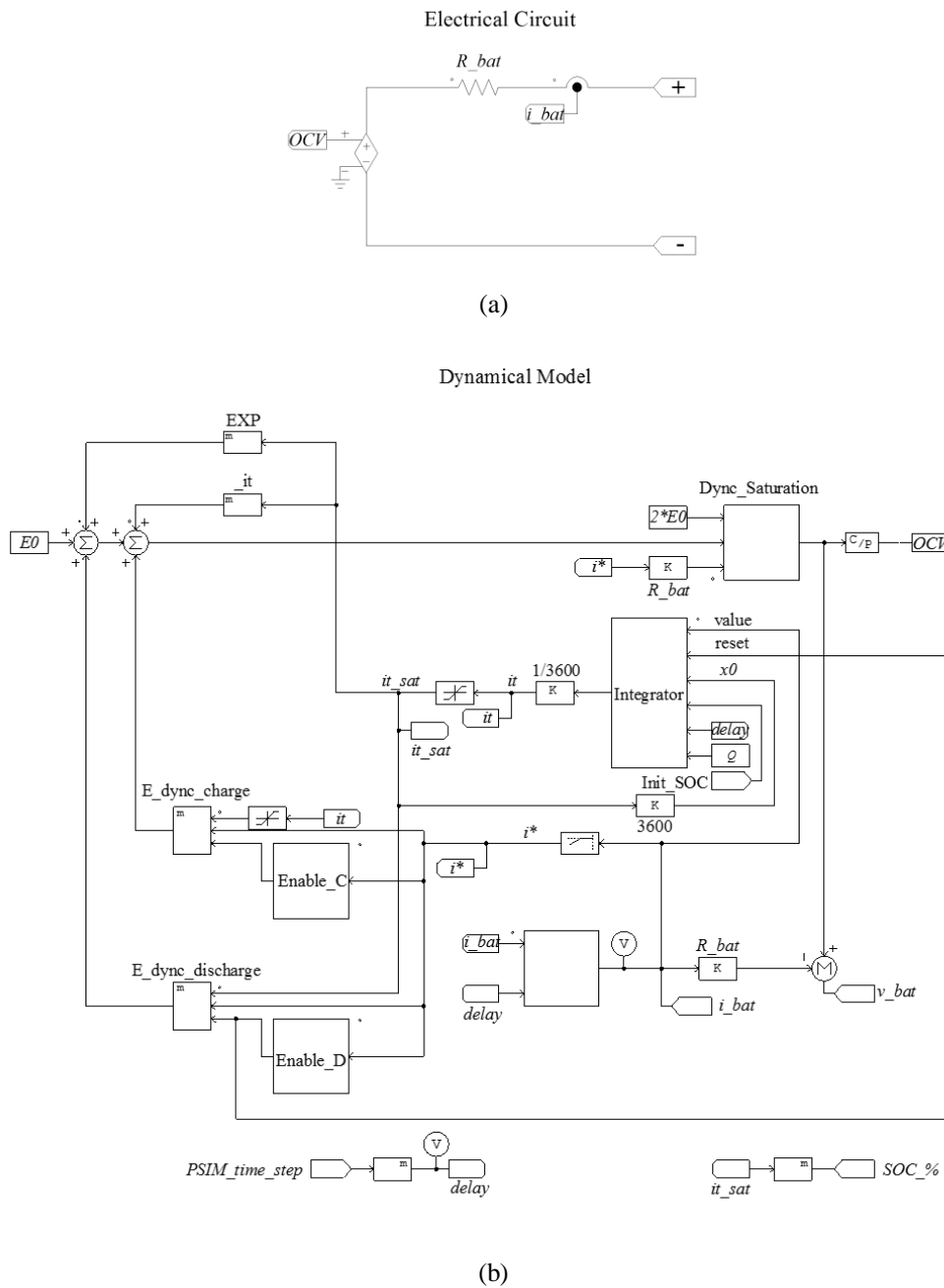


Figure 4.7 – Simulation model of the model of the battery, developed in the software *PSIM*: (a) Electrical circuit; (b) Dynamical Model.

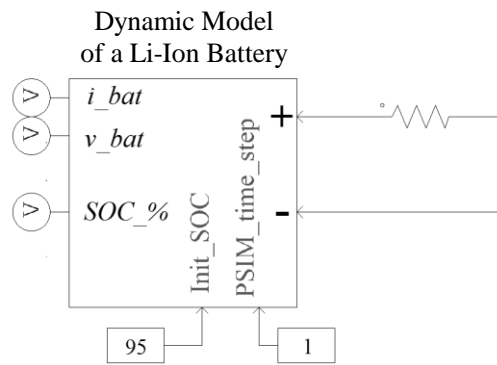


Figure 4.8 – Block representation of the dynamical model of the battery developed in the software *PSIM*.

The parameters of the model of the battery used in the simulations of the bidirectional DC-DC converter analyzed in this chapter are presented in Table 4.5.

Table 4.5 – Parameters of the model of the li-ion battery developed in the software *PSIM*, used in the simulations of the bidirectional DC-DC converter.

Battery constant voltage (E_0)	100 V
Internal resistance (R_{bat})	52.5 m Ω
Polarization resistance (K)	0.030 Ω
Exponential zone amplitude (A)	8.27 V
Exponential zone time constant inverse (B)	1.91 Ah ⁻¹
Battery capacity (Q)	100 Ah

The methodology for extracting the parameters for the model from a real battery is described in [114], being based on the discharge curve supplied by the battery manufacturer.

In this case, for simplification purposes, it is considered that the battery model represents the whole battery pack rather than each individual battery.

It is important to note that in this model the minimum battery voltage is 0 V, while the maximum voltage is $2 E_0$. On the other hand, the minimum capacity of the battery is 0 Ah and the maximum capacity cannot be greater than 100% of the SOC [114].

A simple simulation test was performed, connecting the block of the battery to a pure resistive load of 2 Ω and defining an initial SOC of 100%. The obtained waveform of the voltage at the terminals of the battery pack is presented in Figure 4.9. It is important to note that, in a real implementation it is not supposed allow that the voltage of the battery pack decreases up to zero, since typically the manufacturer defines a minimum value of voltage for ensuring its working operation.

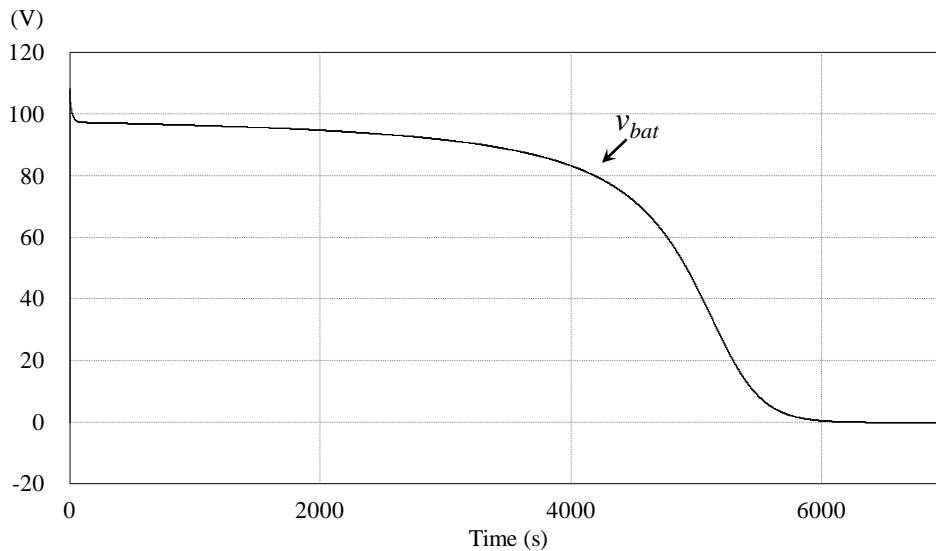


Figure 4.9 – Simulation results of the voltage at the terminals of the battery pack, connecting the dynamic model of the battery developed to a pure resistive load of 2Ω , considering that the battery pack is initially full charged.

4.4. Simulations in Motor Drive Mode

The main simulation results obtained for the motor drive mode of the first stage of the proposed unified topology, comprising the electrical machine and the three-phase Voltage Source Inverter (VSI) are presented and discussed in this section.

The control algorithm chosen for this operation mode was the Field-Oriented Control (FOC), which, according to the analysis presented in Chapter 3, is adequate for EV applications.

The simulation results described in this section were performed for a motor drive operation in two different modes: without any load coupled to the shaft of the electrical machine and with nominal load.

4.4.1. Proposed Control Algorithm

The FOC proposed in this MSc. Thesis is described in Figure 4.10. It consists of the control algorithm described by *Pedrosa et al.* in [69] that was discussed in Section 3.2.1.

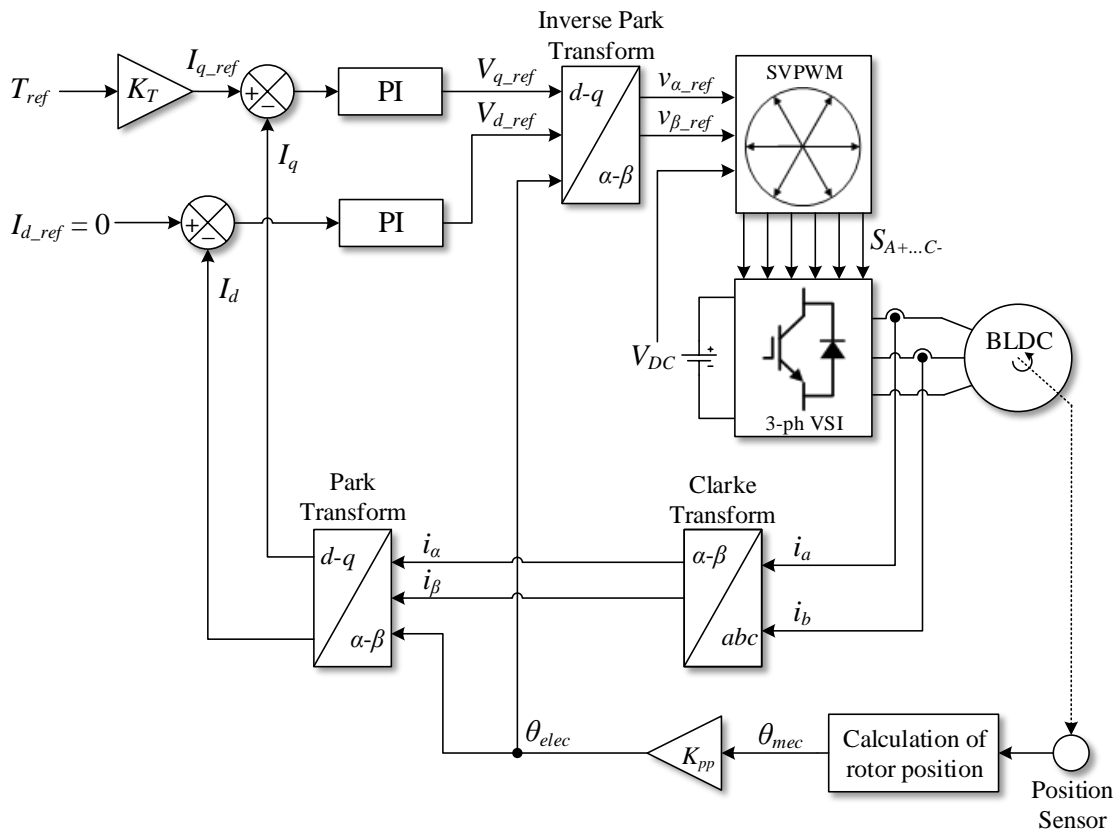


Figure 4.10 – Block diagram of the FOC proposed in this MSc. Thesis.

The simulation models of the power electronics circuit and the control system, developed in the software *PSIM* for the simulations of the motor drive mode are presented, respectively, in Figure 4.11 and Figure 4.12.

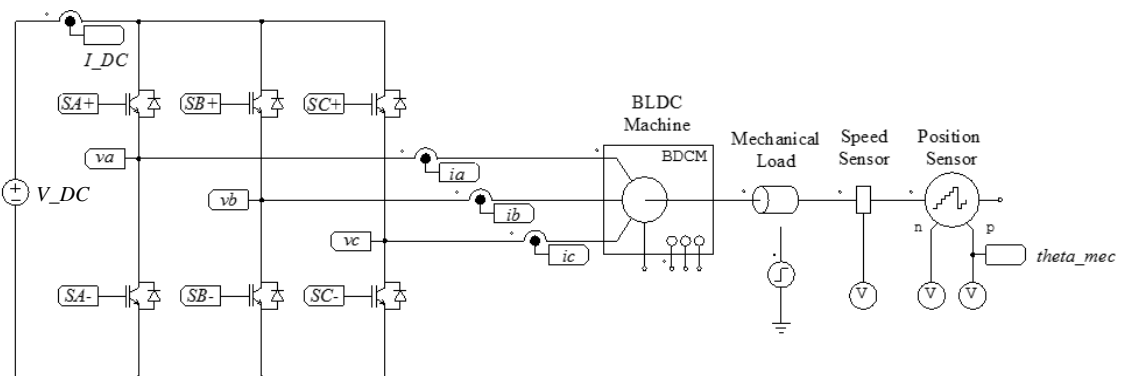


Figure 4.11 – Simulation model of the power electronics circuit, including the mechanical components and the sensor blocks, developed in the software *PSIM*, for the motor drive mode.

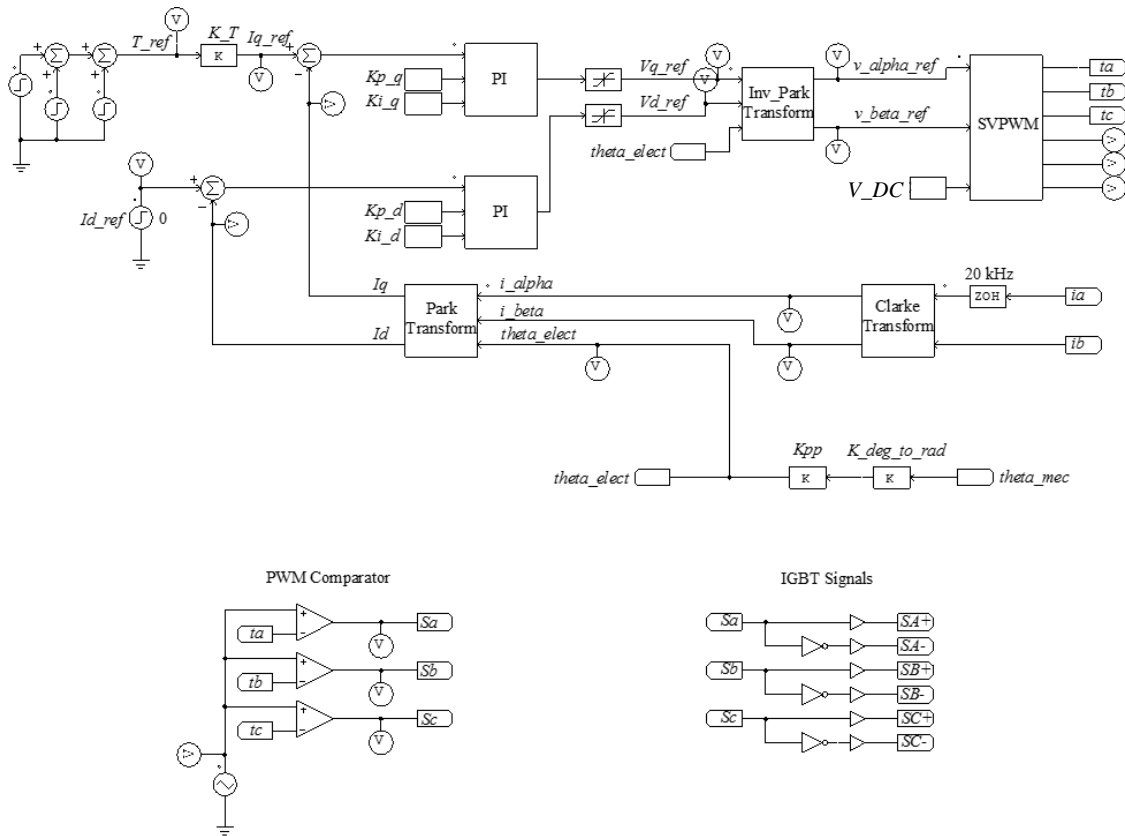


Figure 4.12 – Simulation model of the control system responsible for implementing the FOC, developed in the software *PSIM*, for the motor drive mode.

According to [116], the developed torque of the BLDC machine is defined by (4.7), where T_{load} is the load torque, ω_m the mechanical speed (in rad/s), and B the friction coefficient, which is defined according to (4.8).

$$T = T_{load} + B \omega_m + J \frac{d\omega_m}{dt} \quad (4.7)$$

$$B = \frac{J}{\tau_{shaft}} \quad (4.8)$$

4.4.2. Operating without Load

The first simulations were performed using a mechanical load with a resistant torque of 0 Nm, coupled to the shaft of the BLDC machine, corresponding to simulating the electrical machine operating without load.

In the FOC, the reference torque (T_{ref}) is set to 10 Nm at $t = 0.05$ s. This value was chosen to overcome the inertia, during the startup of the BLDC machine. At $t = 0.5$ s, the electrical machine should have reached its stationary state, and thus the torque (T_{ref}) is set to 0 Nm, to stop the engine.

The obtained waveforms of the torque reference (T_{ref}) and the torque (T) produced by the BLDC machine are presented in Figure 4.13.

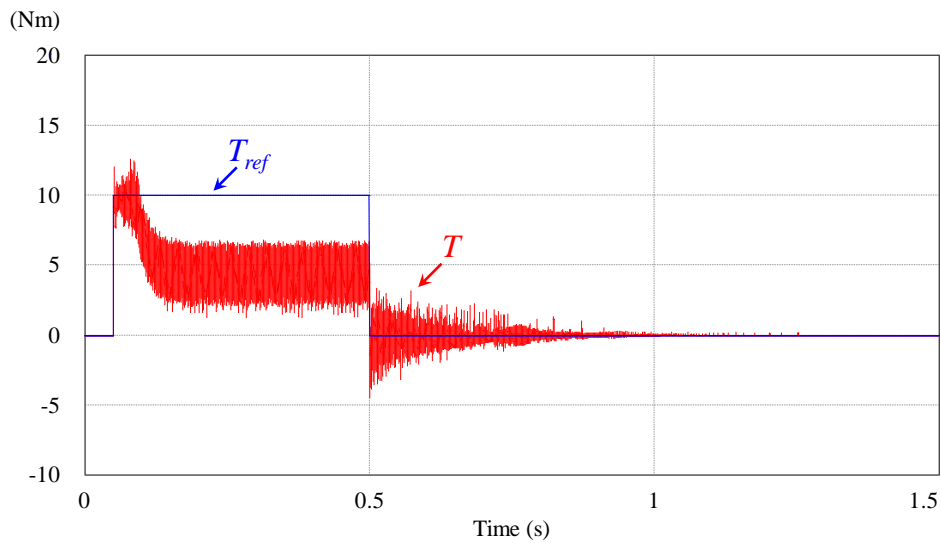


Figure 4.13 – Simulation results of the torque reference (T_{ref}) and torque (T) produced by the BLDC machine, during the motor drive mode operating without mechanical load.

The obtained results demonstrate that the torque (T) produced by the BLDC machine follows the torque reference (T_{ref}) during a certain time interval. After that, T decreases to an average value of approximately 4.35 Nm. This occurs due to the fact that, at the instant when the transition occurs, the angular acceleration of the BLDC machine begins to decrease up to zero and, as result, the system enters into the stationary regime [69]. Hence, the angular momentum will be null and the produced torque will only depend on the frictional forces of the system, considered in (4.7). After $t = 0.5$ s, T falls abruptly and varies around the reference value until approximately the instant $t = 1.26$ s, when the electrical machine stops.

As was mentioned in Chapter 3, in the FOC the q -axis current (I_q) is directly related with the torque adjustment. The obtained waveform of the instantaneous current i_q is presented in Figure 4.14. Contrary to the results obtained in [69], using a Permanent Magnet Synchronous Machine (PMSM), the obtained waveform, is the inverse of the waveform of the produced torque (T).

The obtained speed curve of the BLDC machine is presented in Figure 4.15, in which it is possible to conclude that the system reaches the steady state at $t = 0.17$ s.

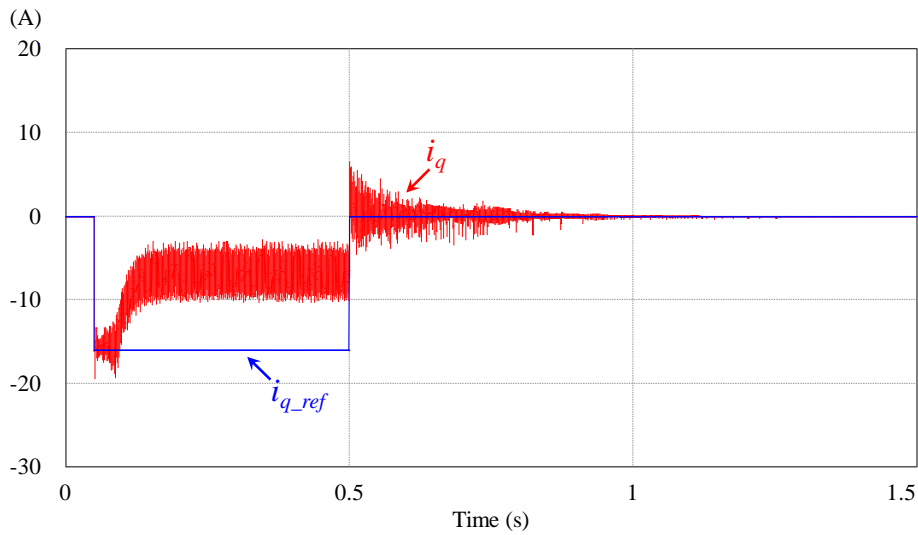


Figure 4.14 – Simulation results of the stator d - q axis reference current i_{q_ref} and the current i_q , during the motor drive mode operating without mechanical load.

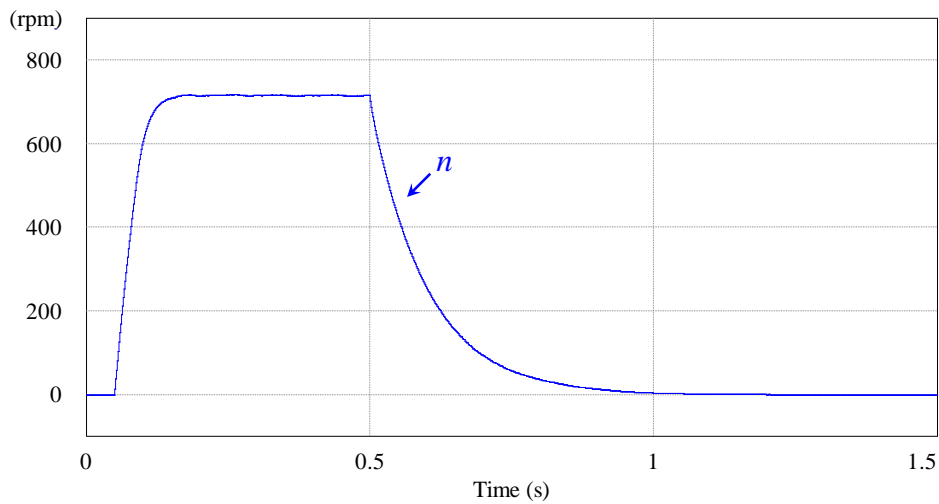


Figure 4.15 – Simulation results of the speed curve, during the motor drive mode operating without mechanical load.

The obtained waveforms of the voltages v_{ab} , v_{bc} and v_{ca} , and currents i_a , i_b and i_c when the electrical machine is operating in the steady state are presented in Figure 4.16.

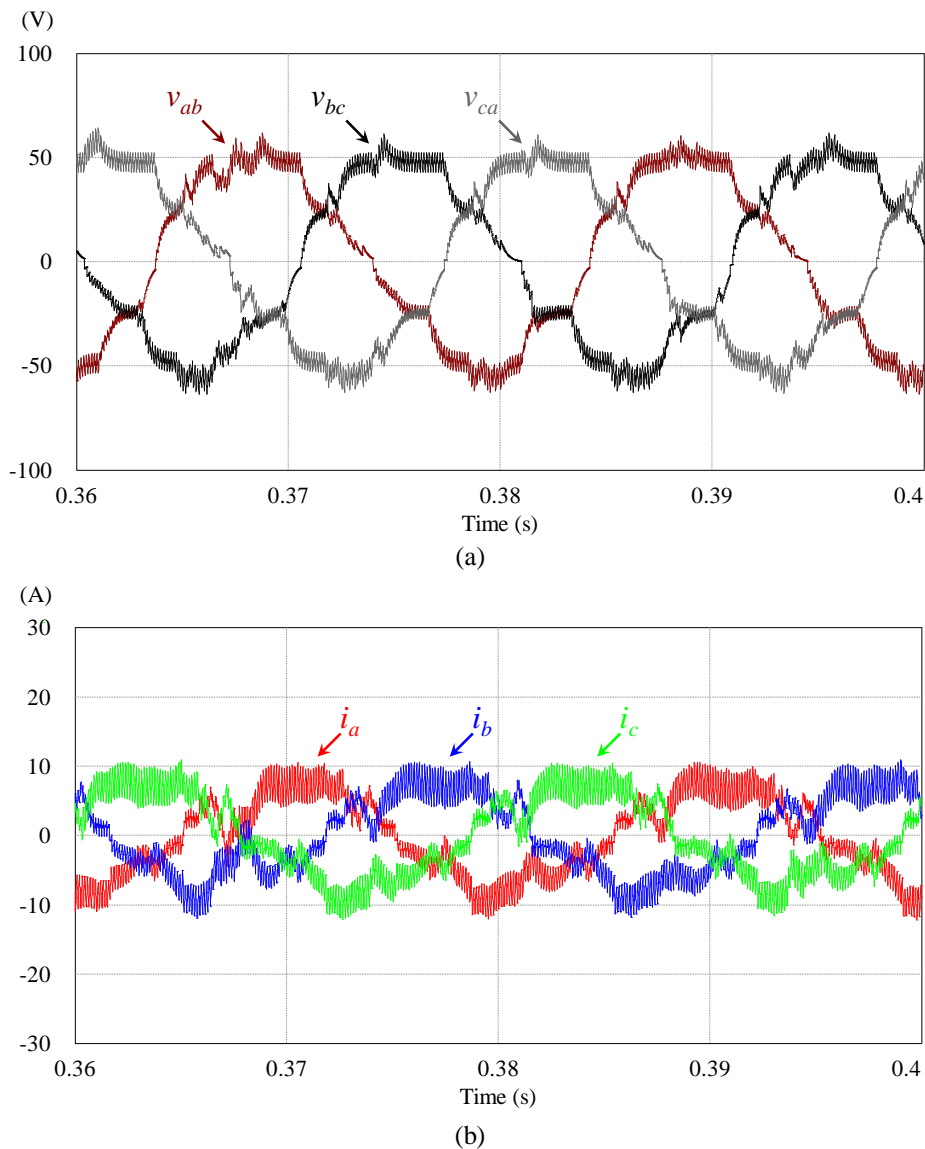


Figure 4.16 – Simulation results of the voltages and currents on the BLDC machine, during the motor drive mode operating without mechanical load: (a) v_{ab} , v_{bc} and v_{ca} ; (b) i_a , i_b and i_c . (The voltages were filtered through a low-pass filter with a cut-off frequency of 500 Hz).

The obtained waveform of the voltages presents high distortion. The voltages are shifted between each other 120° and have an average RMS value of 63.27 V. The currents present also a highly-distorted waveform and have an average RMS value of 5.59 A.

4.4.3. Operating with Nominal Load (80 Nm)

In this section are described the simulation results of the motor drive operating with a mechanical load, with a resistant torque of 80 Nm coupled to the shaft of the BLDC machine, corresponding to simulating the system with the electrical machine operating with its nominal load.

In the FOC, the reference torque (T_{ref}) is set to 100 Nm at $t = 0.05$ s and to 0 Nm at $t = 0.5$ s. The value of 100 Nm was chosen in order to evaluate the behavior of system, during the transitory regime, when a value of torque greater than the one of the

mechanical load is established for the reference of the control system. The obtained waveforms of the torque reference (T_{ref}) and the torque (T) produced by the BLDC machine are presented in Figure 4.17.

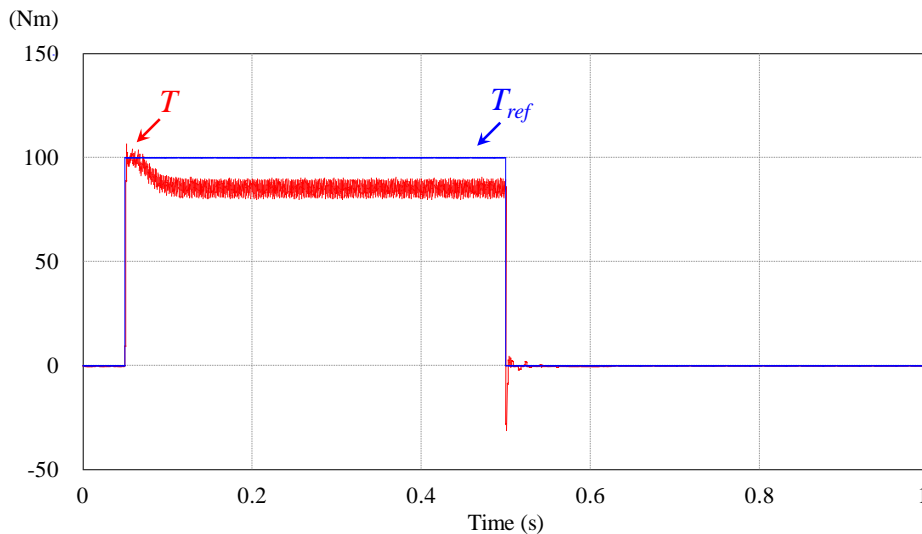


Figure 4.17 – Simulation results of the torque reference (T_{ref}) and torque (T) produced by the BLDC machine, during the motor drive mode operating with nominal load.

The obtained results demonstrate that the torque (T) produced by the BLDC machine follows the reference torque (T_{ref}) up to the instant $t = 0.07$ s. Such as it was observed in the simulation without load, from that instant T corresponds to the sum of the acceleration torque, due to the motor inertia, and, in this case, also the resistant mechanical torque of the system. Thus, once the steady state is achieved, the torque produced by the machine decreases to approximately 80 Nm, which corresponds to the value established for the mechanical load. Once again, when T_{ref} is set to zero, at $t = 0.5$ s, T falls abruptly and varies around the reference value until the machine stops rotating.

The obtained waveform of the instantaneous current i_q , presented in Figure 4.18, is once again very similar to the inverted waveform of the produced torque (T).

The obtained speed curve of the BLDC machine is presented in Figure 4.19, in which it is possible to verify that, in steady-state, the system is able to reach an average speed of 886.76 rpm in only 0.08 s (already discounting the initial 0.05 s during which T_{ref} remains null), with a ripple of 1.20%. The value of the speed achieved in steady state is related to the voltage level of the DC-bus and the distortion obtained in the waveforms of the voltages applied, resulting in low RMS voltage values.

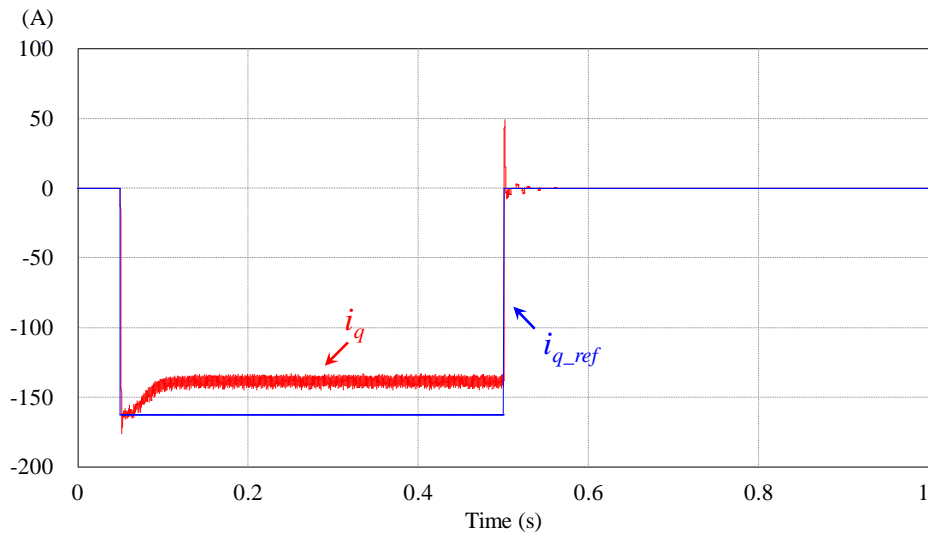


Figure 4.18 – Simulation results of the stator d - q axis reference current i_{q_ref} and the current i_q , during the motor drive mode operating with nominal load.

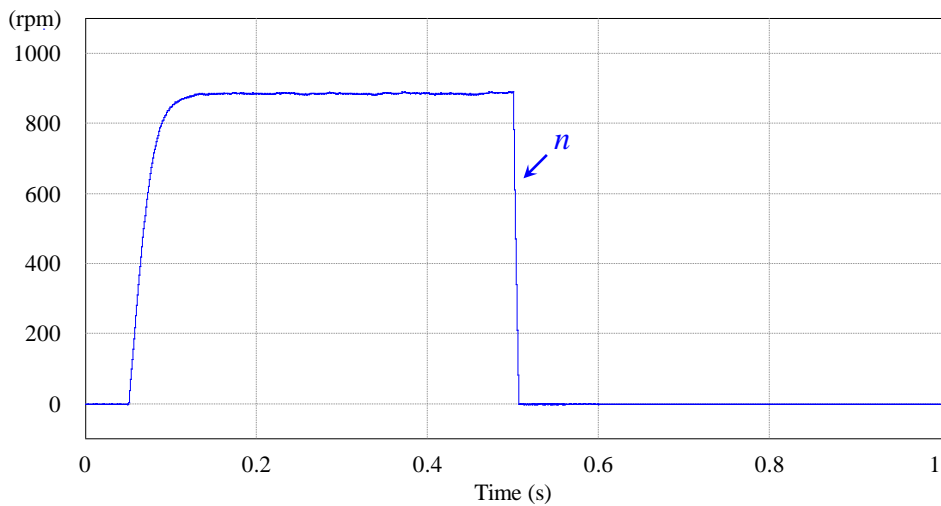


Figure 4.19 – Simulation results of the speed curve, during the motor drive mode operating with nominal load.

The obtained waveforms of the voltages v_{ab} , v_{bc} and v_{ca} , and currents i_a , i_b and i_c obtained when the electrical machine operates in steady state are presented in Figure 4.20.

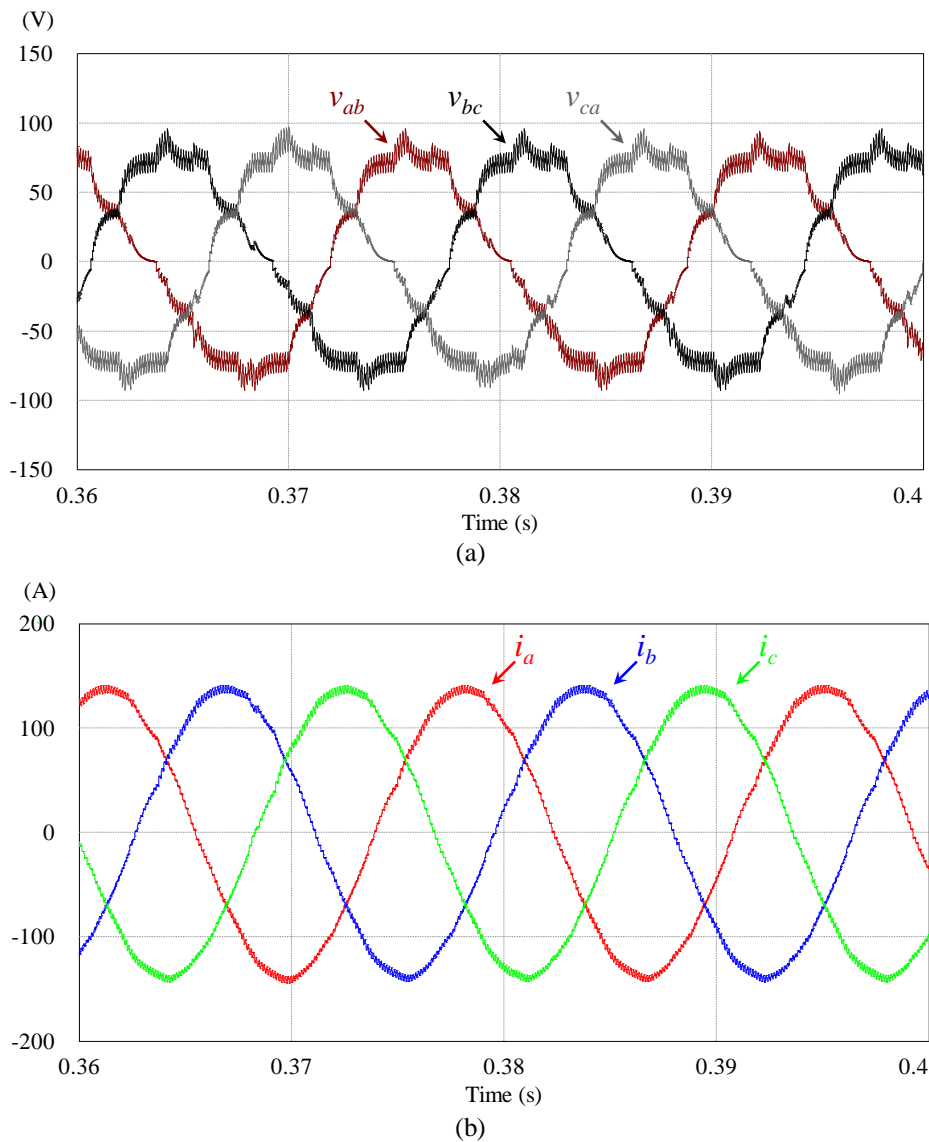


Figure 4.20 – Simulation results of the voltages and currents on the BLDC machine, during the motor drive mode operating with nominal load: (a) v_{ab} , v_{bc} and v_{ca} ; (b) i_a , i_b and i_c . (The voltages were filtered through a low-pass filter at 500 Hz).

Similar to the case of operating without a mechanical load coupled to the electrical machine, the obtained waveform of the voltages has high ripple. Their average RMS value is 95.52 V. The main difference observed is the waveform of the currents, which have much less distortion and are now practically sinusoidal, with an average RMS value of 97.68 A. Some ripple can still be noticed due to the low switching frequency of 8 kHz used.

4.5. Simulations in the Fast Charging Mode

The main simulation results obtained for the fast charging operation mode of the first stage of the proposed unified solution, comprising the three-phase VSI and the windings of the electrical machine, are presented and discussed in this section.

The control algorithm chosen for this mode is an adapted version of the Direct Power Control based on Model Predictive Control (DPC-MPC) presented in Section 3.3.2. This control algorithm was chosen since, besides its functionality, it offers flexibility to perform modifications in order to correct its performance, due to possible disturbances associated with the use of the windings of the electrical machine. In this case, the modifications were introduced in order to add more functionalities to the charging operation and to reduce the computational effort required.

One of the major concerns in the battery charging operation is its impact on the power quality of the electrical grid. This requirements are translated in terms of reactive power consumed, which should result in a power factor close to the unity, and distortion of the waveform of the currents consumed, which should be the lowest possible. In the simulations presented in this section, the harmonic content of the currents consumed, which leads to the distortion of their waveform, is evaluated considering the Total Harmonic Distortion (THD) and the standard for low-frequency Electromagnetic Compatibility (EMC) IEC 61000-3-4.

The THD is defined according to (4.9), resulting in a percentage value, where I_{RMS} is the total RMS value and I_1 the RMS value considering only the fundamental component.

$$THD = \frac{\sqrt{I_{RMS}^2 - I_1^2}}{I_1} 100 \quad (4.9)$$

The limits for the harmonic content established by the standard IEC 61000-3-4 are presented in the Table 4.6. These values should be considered for a battery charging operation (either through a single-phase or three-phase grid source), when consuming currents with RMS values (per phase) greater than 16 A.

Table 4.6 – Limits for harmonic content emissions for equipment with RMS input current greater than 16 A (per phase) (source: IEC 61000-3-4, for simplified connection of equipment [stage 1]).

Harmonic order n	Maximum admissible harmonic current ($I_n/I_1 \cdot 100\%$)	Harmonic order n	Maximum admissible harmonic current ($I_n/I_1 \cdot 100\%$)
3	21.6	21	≤ 0.6
5	10.7	23	0.9
7	7.2	25	0.8
9	3.8	27	≤ 0.6
11	3.1	29	0.7
13	2	31	0.7
15	0.7	≥ 33	≤ 0.6
17	1.2	Even	$\leq 8/n$ or ≤ 0.6
19	1.1		

4.5.1. Proposed Control Algorithm

One of the drawbacks of the Direct Power Control based on Model Predictive Control (DPC-MPC), analyzed in Section 3.3.2, is its high complexity level, since it requires calculations using complex numbers and, hence, a significant computational effort is required. This aspect is considered as an advantage by *Cortes et al.* in [109], since, as result, the control algorithm does not require using coordinate transformations. However, the coordinate transformations are required for implementing the FOC, in the motor drive mode. Thus, in this case, it was chosen to develop a modified version of this DPC-MPC, using the Clarke transform and removing the mathematical operations involving complex numbers. The configuration of the proposed modified DPC-MPC is presented in Figure 4.21.

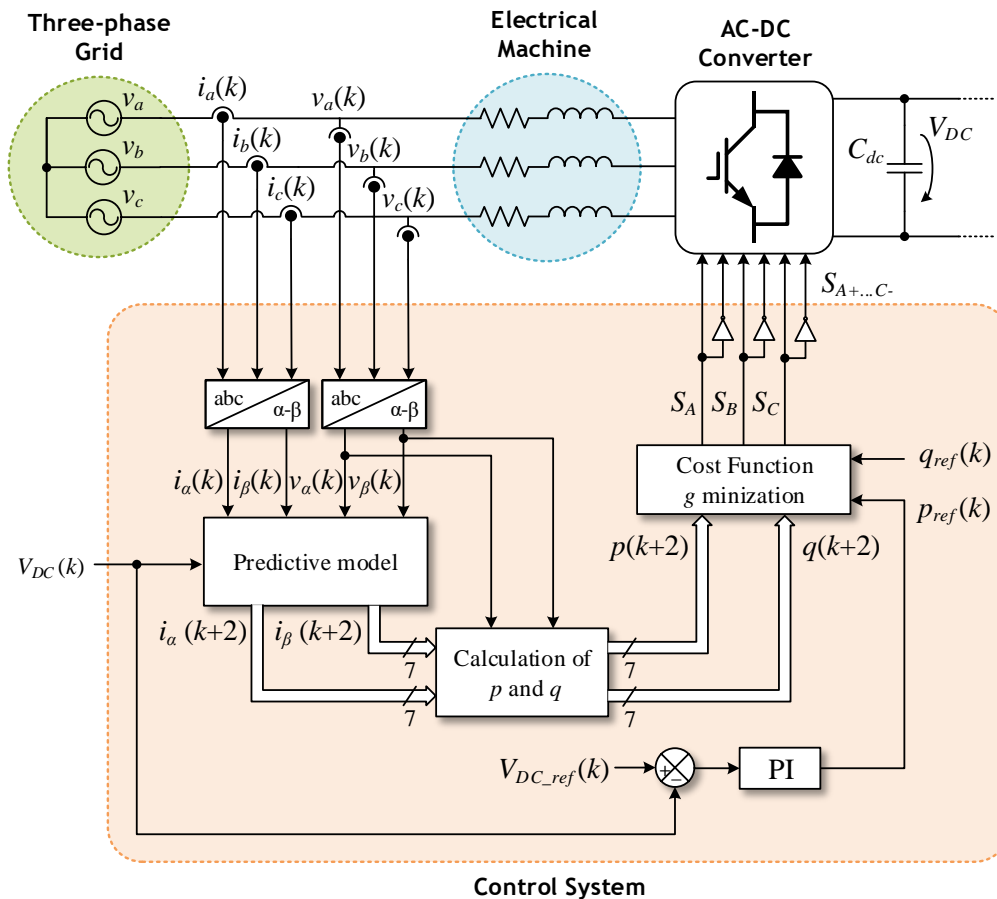


Figure 4.21 – Block diagram of the modified DPC-MPC proposed in this MSc. Thesis, for the fast charging mode.

The predictive model of the proposed modified DPC-MPC is also based on the expression that defines the input predicted current i_s presented in (4.10). However, the system variables are now defined as vectors that contain each α and β components, and thus the system variables are defined according to (4.11).

$$\vec{i}_s(k+2) = \left(1 - \frac{R_s T_s}{L_s}\right) \vec{i}_s(k+1) + \frac{T_s}{L_s} \left[\vec{v}_s(k+1) - \vec{v}_{in}(k+1) \right] \quad (4.10)$$

$$\vec{i}_s(k) = \begin{bmatrix} i_\alpha(k) \\ i_\beta(k) \end{bmatrix} \quad \vec{v}_s(k) = \begin{bmatrix} v_\alpha(k) \\ v_\beta(k) \end{bmatrix} \quad \vec{v}_{in}(k) = \begin{bmatrix} v_{\alpha,in}(k) \\ v_{\beta,in}(k) \end{bmatrix} \quad (4.11)$$

According to [117], the voltage v_{in} per phase of a three-phase VSI is defined by (4.12).

$$\begin{cases} v_{a,in} = \frac{2p_a - p_b - p_c}{6} V_{DC} \\ v_{b,in} = \frac{-p_a + 2p_b - p_c}{6} V_{DC} \\ v_{c,in} = \frac{-p_a - p_b + 2p_c}{6} V_{DC} \end{cases}, \text{ where } \begin{cases} p_x = -1 & \text{if } S_x = 0 \\ p_x = 1 & \text{if } S_x = 1 \end{cases} \text{ and } x \in \{A, B, C\} \quad (4.12)$$

Replacing the Clarke transform defined by (4.13) in (4.12), it results in (4.14), which defines the voltage v_{in} in the α - β coordinates.

$$\begin{bmatrix} v_{\alpha,in} \\ v_{\beta,in} \end{bmatrix} = \frac{2}{3} \begin{bmatrix} 1 & -\frac{1}{2} & -\frac{1}{2} \\ 0 & \frac{\sqrt{3}}{2} & -\frac{\sqrt{3}}{2} \end{bmatrix} \begin{bmatrix} v_{a,in} \\ v_{b,in} \\ v_{c,in} \end{bmatrix} \quad (4.13)$$

$$\begin{cases} v_{\alpha,in} = \frac{1}{3} \left(p_a - \frac{p_b}{2} - \frac{p_c}{2} \right) V_{DC} \\ v_{\beta,in} = \frac{1}{2\sqrt{3}} (p_b - p_c) V_{DC} \end{cases}, \text{ where } \begin{cases} p_x = -1 & \text{if } S_x = 0 \\ p_x = 1 & \text{if } S_x = 1 \end{cases} \text{ and } x \in \{A, B, C\} \quad (4.14)$$

The cost function of the DPC-MPC is also modified, resulting in (4.15).

$$g = |q_{ref} - q(k+2)| + |p_{ref} - p(k+2)| + \lambda C \quad (4.15)$$

The possibility of establishing a reference value for the instantaneous imaginary power (q_{ref}) different from zero, allows for the battery charger to also operate as an active power filter, since the control system has access to the harmonic and reactive content emitted by the loads of the electrical installation [58]. This feature offers an interesting opportunity for companies, considering a high probability of having at least one EV parked, as suggested in Figure 4.22. One important constrain is that operating, for instance, as a reactive power compensator, the power available for the battery charging operation is more limited. However, this issue can be overcome by considering that a fleet

of EVs could be connected to a control system responsible for distributing the needs of reactive power compensation per each vehicle parked.

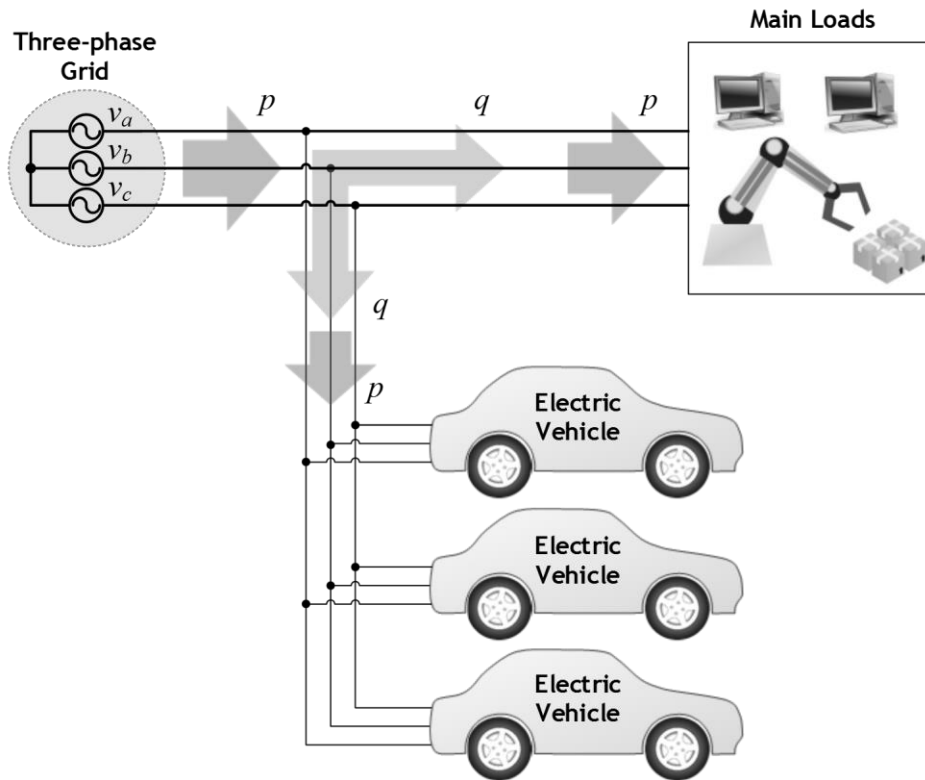


Figure 4.22 – Exchange of the p - q powers in an installation where the chargers of the EVs are used as reactive power compensators, a feature provided by the control algorithm of the fast charging mode proposed in this MSc. Thesis.

Another relevant aspect considered in Section 3.3.2 is the variable switching frequency implicit in the DPC-MPC, which makes it unfeasible the use of extra current filters to improve the waveform of the currents consumed by eliminating the high frequency components around the commutation frequency. The proposed modified cost function includes a third component, with the purpose of overcoming this issue. Before computing the cost function result, the control system checks if the switching state under analysis is equal to the last selected switching state. If it is equal, the value of C in (4.15) is set to 1, otherwise the value of C is set to 0. The parameter λ defines the weight of this component in the cost function. Thus, the higher the value of λ , the more it is ensured that the last selected switching state is avoided, since the obtained cost function result tends to be the highest one. In this case, this feature is not analyzed since one of the requirements of the proposed unified solution is to optimize the space and weigh on-board the vehicle and thus the adding of extra-equipment is not considered.

In Figure 4.23 a flowchart is presented, describing the steps required for implementing the proposed modified control algorithm.

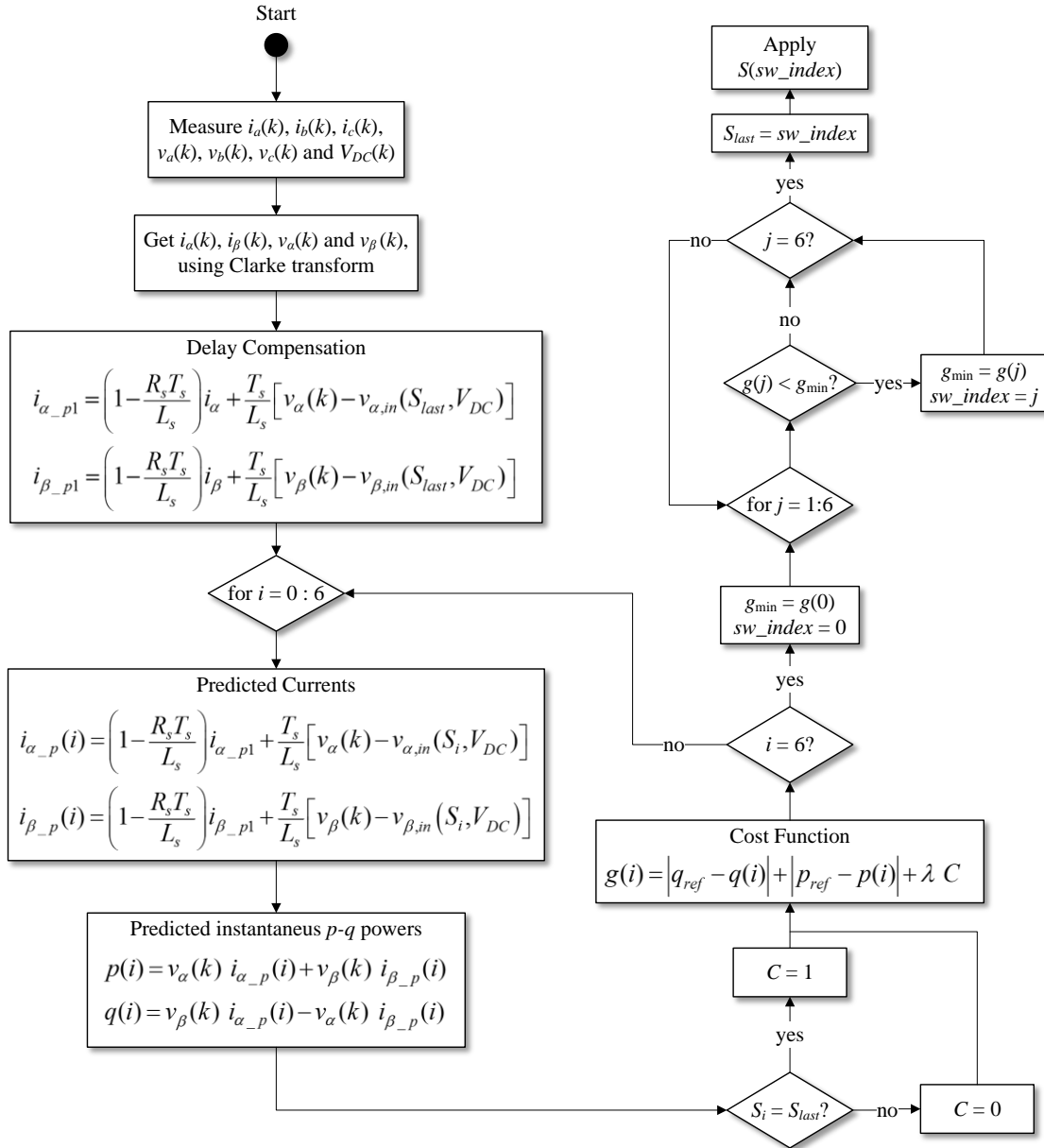


Figure 4.23 – Flowchart of the proposed modified DPC-MPC, for the fast charging mode.

4.5.2. Grid-to-Vehicle Operation

The simulation models of the power electronics circuit and the control system, developed in the software *PSIM* for the simulations in this mode are presented, respectively, in Figure 4.24 and Figure 4.25.

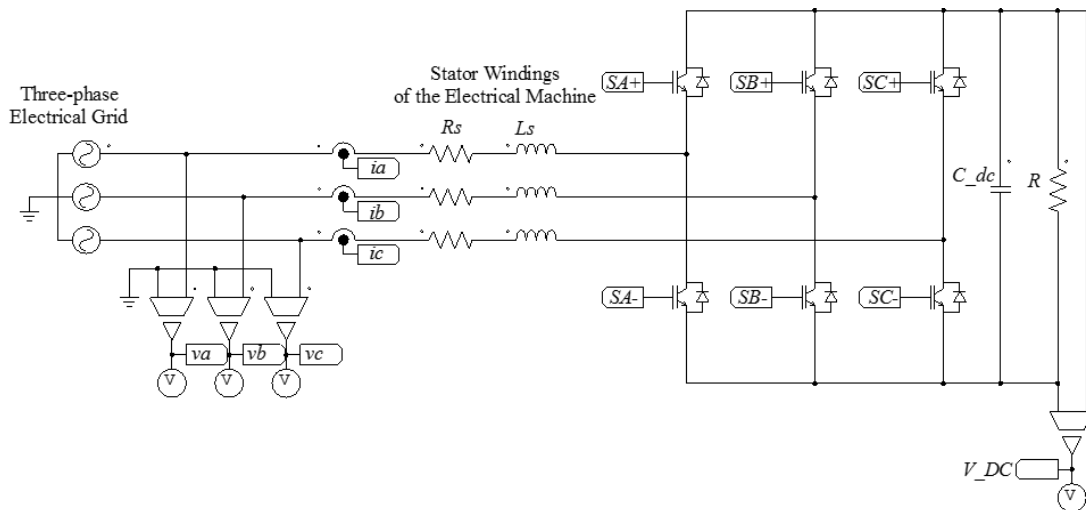


Figure 4.24 – Simulation model of the power electronics circuit, developed in the software *PSIM*, for the fast charging mode.

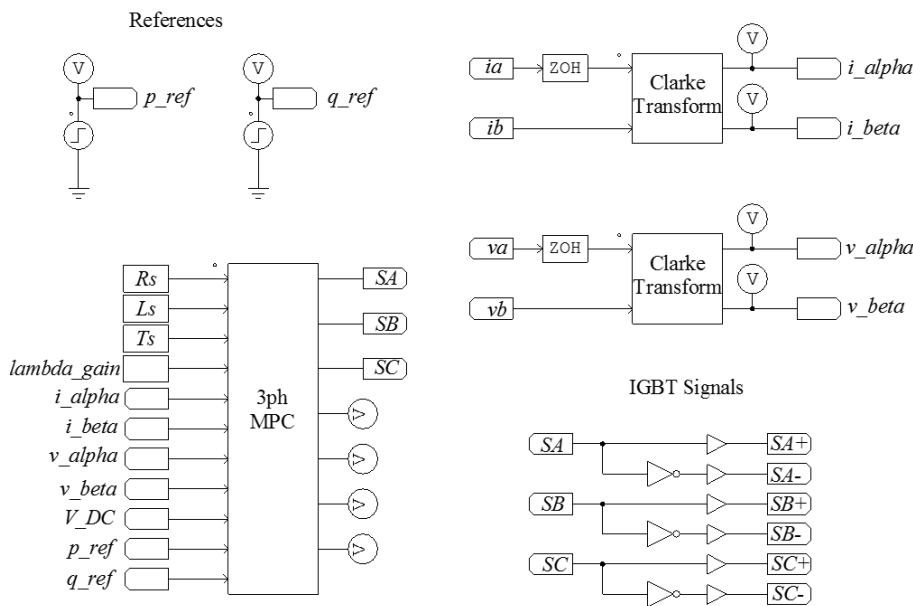


Figure 4.25 – Simulation model of the control system responsible for implementing the DPC-MPC, developed in the software *PSIM*, for the fast charging mode.

Such as in [109], in the simulations for the fast charging mode presented in this MSc. Thesis it was chosen to set the value of the instantaneous real power reference (p_{ref}) directly, instead of using the outer-loop control of the voltage at the terminals of the DC-bus.

The simulations described in this section were performed for the Grid-to-Vehicle (G2V) mode. In the control system, the instantaneous real power reference (p_{ref}) is set to 15 kVA, while the instantaneous imaginary power reference (q_{ref}) is set to 0 kVA. The main parameters used in this simulation are presented in Table 4.7. For evaluate the performance of the control system in the presence of variations in the values of the inductances, the values experimental measurements presented in Section 4.2 were used.

The obtained waveforms for the instantaneous real power (p) and the instantaneous imaginary power (q) and their respective references (p_{ref} and q_{ref}), during the steady-state, are presented in Figure 4.26.

Table 4.7 – Parameters used in the simulation of the fast charging operation in the G2V mode.

Line-to-line RMS grid voltage V_{LL}	400 V
Grid voltage frequency f_g	50 Hz
Resistance of the windings of the same phase R_s	400 m Ω
Inductance of the windings of phase a L_{sa}	258 μ H
Inductance of the windings of phase b L_{sb}	276 μ H
Inductance of the windings of phase c L_{sc}	253 μ H
Inductance per phase, considered by the MPC L_s	262 μ H
DC-bus capacitor C_{dc}	500 μ F
Load Resistance R	100 Ω
Sampling frequency f_s	20 kHz

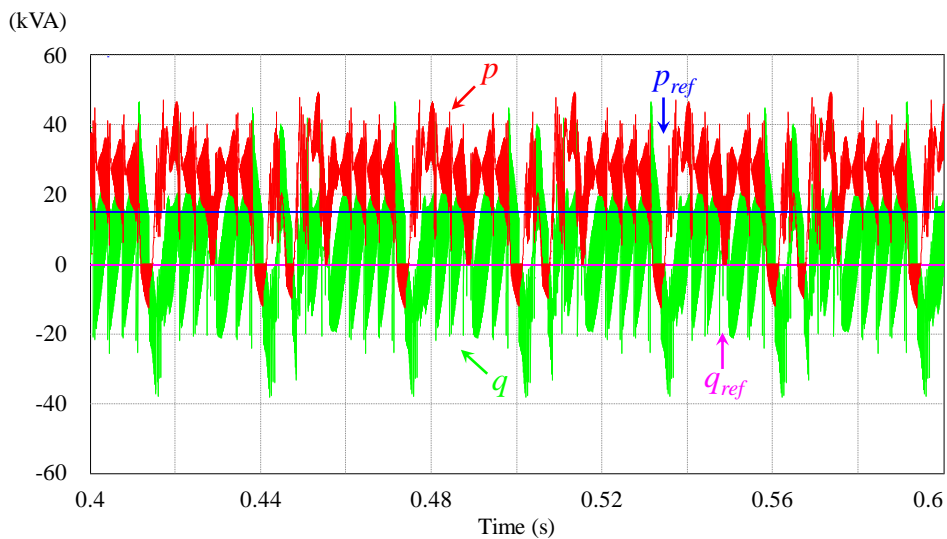


Figure 4.26 – Simulation results of the instantaneous p - q powers (in steady-state), during the fast charging mode (G2V operation).

The obtained results show that despite the references p_{ref} and q_{ref} being set as constant values, their respective real values obtained present high ripple. The value of p ranges from -12.31 kVA to 49.32 kVA, while the value of q ranges from -37.94 kVA to 46.57 kVA.

The obtained waveforms of the voltages v_a , v_b and v_c , and currents i_a , i_b and i_c in the steady-state are presented in Figure 4.27. The main relevant characteristics of the obtained currents are presented in Table 4.8.

Table 4.8 – Main relevant characteristics of the currents obtained in the simulation of the fast charging operation in the G2V mode.

	RMS	THD	Power Factor
i_a	63.33 A	102.88%	0.71 (with respect to v_a)
i_b	65.82 A	109.34%	0.73 (with respect to v_b)
i_c	65.95 A	52.54%	0.71 (with respect to v_c)

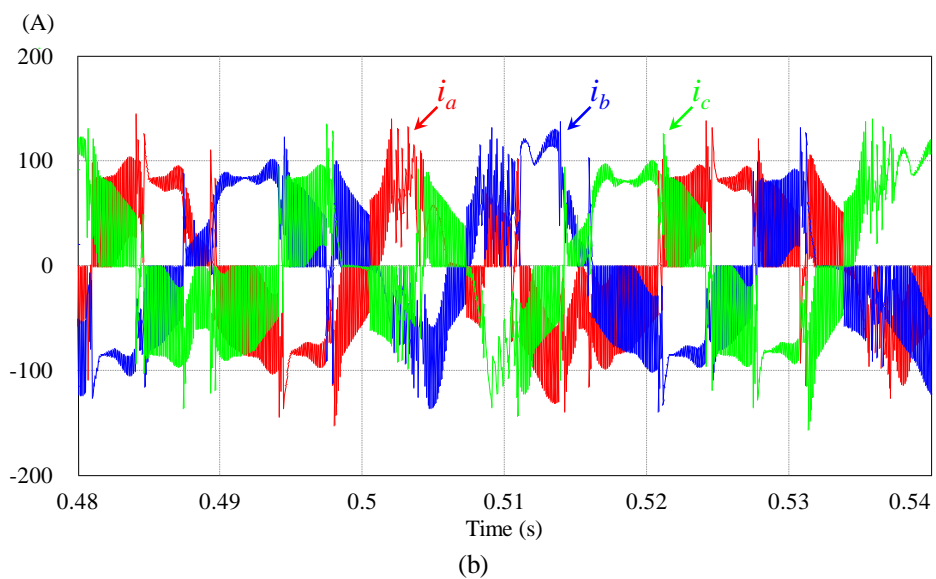
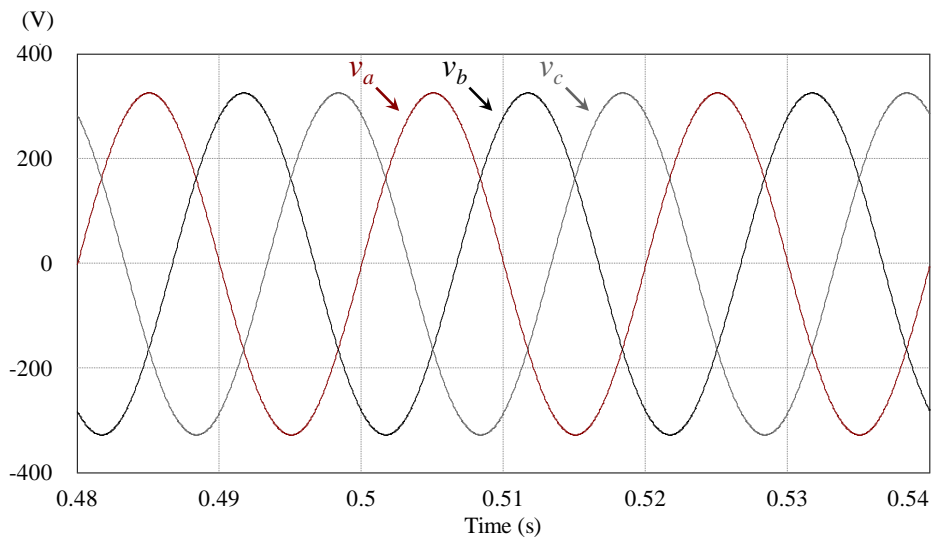


Figure 4.27 – Simulation results of the input voltages and currents, during the fast charging mode (G2V operation): (a) v_a , v_b and v_c ; (b) i_a , i_b and i_c .

Hence, the obtained results confirm that despite the modifications performed in the electrical machine (described in Section 4.2), the values of the inductances of the stator are too low for a proper battery charging operation, as a result of the obtained highly-distorted currents consumed.

As discussed in Section 2.2.2, the alternative for improve the obtained results is to increase the value of the switching frequency of the power semiconductors or increase the value of the inductances, by adding an extra inductor filter.

It is known in advance that the hardware available in our laboratory for implementing the proposed solution, limits the switching frequency of the power semiconductors to a maximum of 20 kHz, which is the value already considered. Hence, for improving the obtained results it was chosen to add an extra input inductor filter, composed by three inductors, each one with an inductance of 3 mH and a residual resistance of 10 mΩ. According to (4.16), this extra value of inductance would produce the same results if the option were to increase the switching frequency to 229 kHz.

$$X_L = 2\pi f_s \tag{4.16}$$

The value of 3 mH for the inductance of the extra filter was chosen based on the compromise between the weight and size requirements on-board of an EV and the achieved results. The extra inductors are not installed inside the electrical machine and so no magnetic interaction between the inductor filter and the windings of the electrical machine is considered. Thus, the total equivalent inductance per phase considered in the predictive model corresponds the sum of the inductance values.

The modified simulation model of the power electronics circuit is presented in Figure 4.28, while the parameters modified and included are presented in Table 4.9.

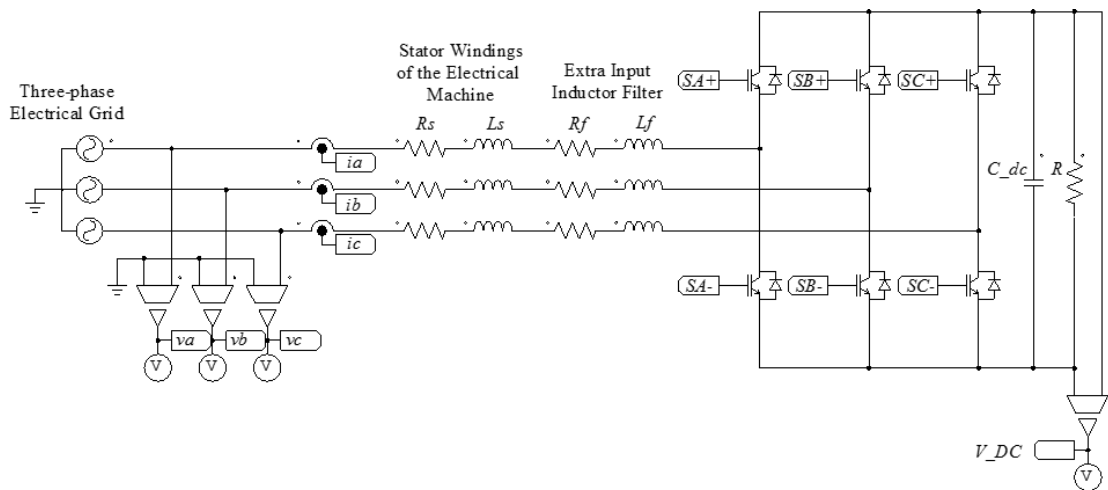


Figure 4.28 – Modified simulation model of the power electronics circuit, developed in the software *PSIM*, for the fast charging mode with an extra input filter.

Table 4.9 – Additional parameters of the simulations for the fast charging mode in the G2V mode with an extra inductor filter.

Inductance per phase, considered by the MPC L_s	3.262 mH
Resistance per phase, considered by the MPC R_s	410 mH
Resistance of the filter R_f	10 m Ω
Inductance of the filter L_f	3 mH

For a proper comparison with the last presented simulation results the same references for the p - q powers ($p_{ref} = 15$ kVA and $q_{ref} = 0$ kVA), were used.

The obtained waveforms for the instantaneous real power (p) and the instantaneous imaginary power (q) and their respective references (p_{ref} and q_{ref}), during the steady-state, are presented in Figure 4.29.

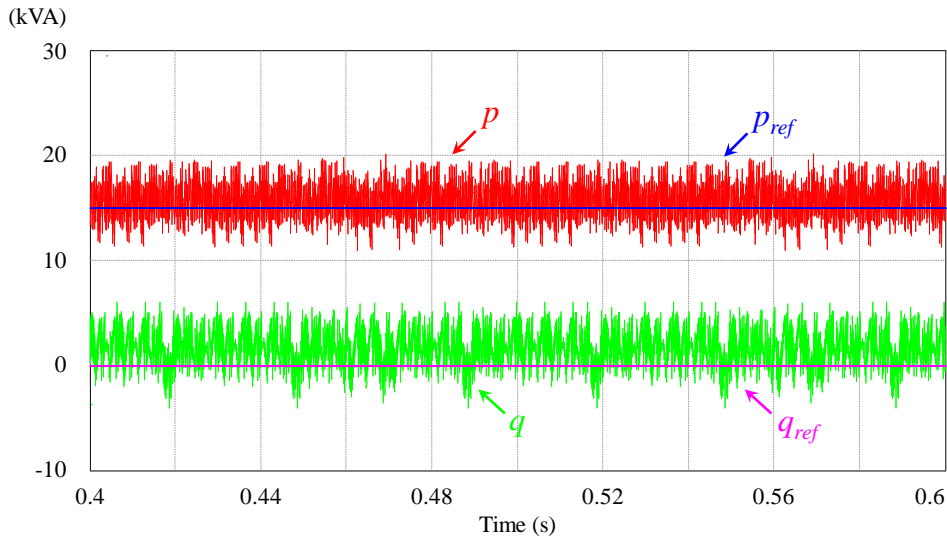


Figure 4.29 – Simulation results of the instantaneous p - q powers (in steady-state), during the fast charging mode (G2V operation) with an extra inductor filter.

In this case, the value of p ranges from 11.00 kVA to 20.17 kVA, while the value of q ranges from -3.97 kVA to 6.14 kVA. Thus, the obtained results demonstrate that the inclusion of the extra filter inductor improved significantly the performance of the control system in tracking the references of the p - q powers.

The obtained waveforms of the voltages v_a , v_b and v_c , and currents i_a , i_b and i_c in the steady-state are presented in Figure 4.30, while the main relevant characteristics of the obtained currents are presented in Table 4.10, demonstrating the improved results obtained.

The harmonic spectrum of the current i_c , in comparison with the limits established by the standard IEC 61000-3-4 is presented in Figure 4.31. This current was chosen for the harmonic spectrum analysis since, according to the information presented in Table

4.10, it is the one that has the higher percentage of THD. The harmonic spectrum shows that the harmonics of order 14, 15 and 21 exceed the limits established by the standard.

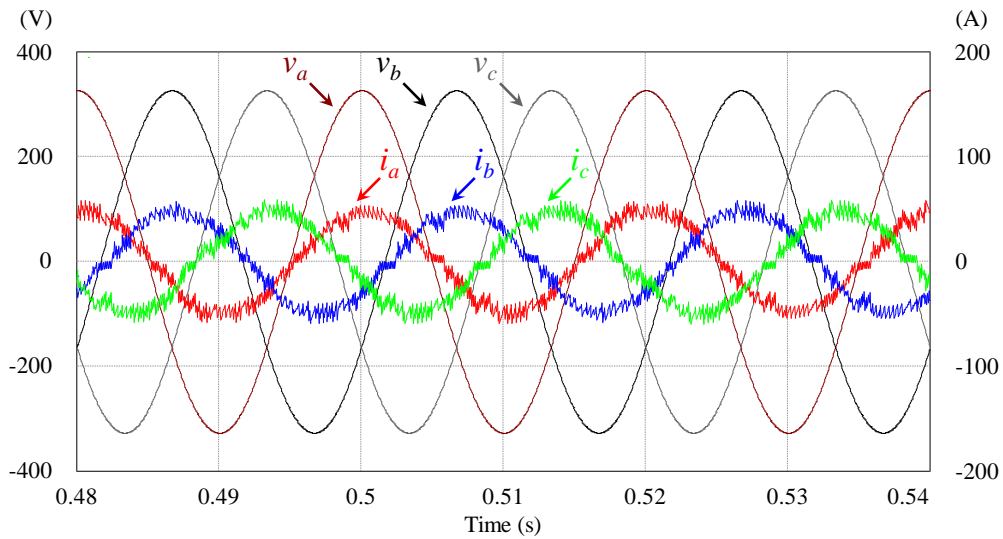


Figure 4.30 – Simulation results of the input voltages and currents, during the fast charging mode (G2V operation), with an extra inductor filter.

Table 4.10 – Main relevant characteristics of the currents obtained in the simulations of the fast charging operation in the G2V mode, with an extra inductor filter.

	RMS	THD	Power Factor
i_a	34.97 A	15.42%	0.98 (with respect to v_a)
i_b	34.85 A	15.09%	0.98 (with respect to v_b)
i_c	34.92 A	16.20%	0.98 (with respect to v_c)

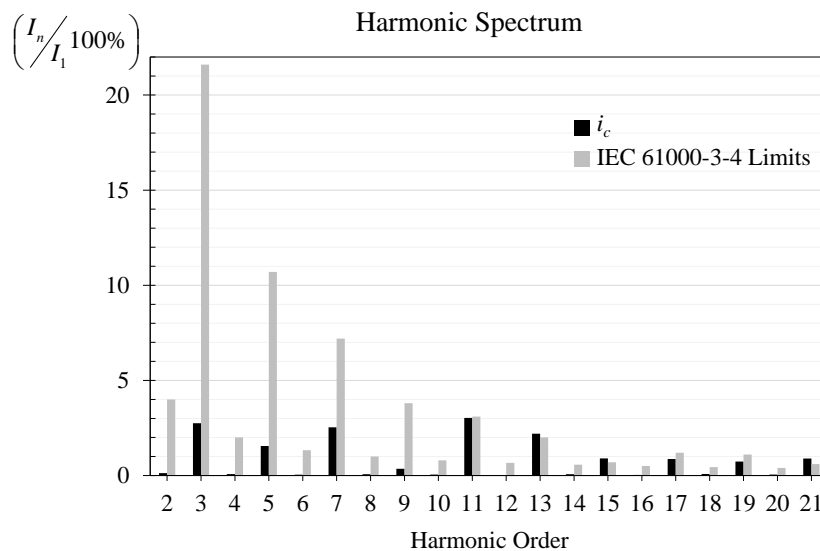


Figure 4.31 – Harmonic spectrum of the waveform of the current i_a , obtained in the simulations of the fast charging mode (G2V operation), with an extra inductor filter, in comparison with the limits established by the standard IEC 61000-3-4.

The obtained waveform of the voltage at the terminals of the DC-bus is presented in Figure 4.32. The obtained waveform has an average value of 1368.36 V, with a ripple of 1.35%.

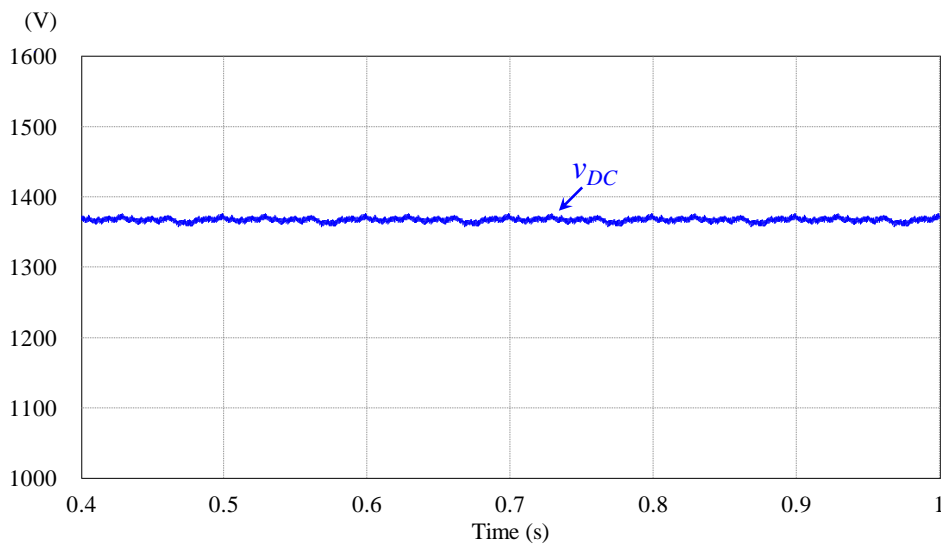


Figure 4.32 – Simulation results of the voltage at the terminals of the DC-bus, during the fast charging mode (G2V operation), with an extra inductor filter.

It is important to note that, in the G2V operation, the simulation results show that during the transitory regime it is possible for high levels of currents consumed to appear, depending on the state of the output filter capacitor. In this case, the obtained waveforms of the currents consumed, during the transitory regime, considering that the capacitor is initially fully discharged, are presented in Figure 4.33.

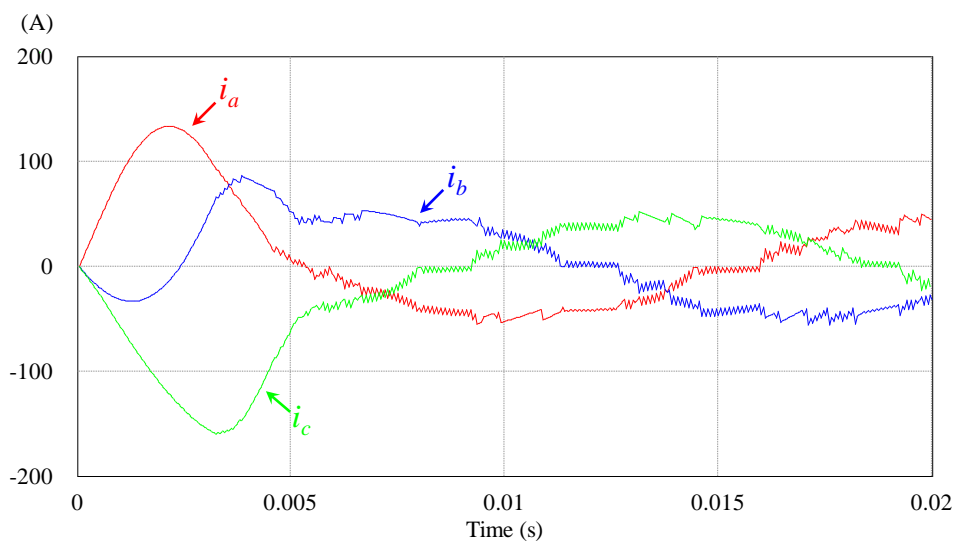


Figure 4.33 – Simulation results of the input currents (during the transitory regime), during the fast charging mode (G2V operation), considering that the output filter capacitor is fully discharged.

The obtained results show that, during the transitory regime, the current i_a reaches to a maximum value of 134.07 A, which represents more than 200% of the maximum

value reached during the steady state (58.71 A). This occurs due to the fact that when the system is turned on, the voltage V_{DC} has to grow abruptly, leading to the consumption of high current levels. In a real implementation, the integrity of the power electronics components of the proposed solution, especially of the power semiconductors, could be compromised.

To overcome this issue, in the next section the simulation results obtained through the use of a pre-charge circuit are presented.

4.5.3. Grid-to-Vehicle Operation with a Pre-Charge Circuit

In order to attenuate the issue detected during the transitory regime of the system, when the output capacitor is initially fully discharged, it was chosen to add a pre-charge circuit, modifying the power electronics circuit according to Figure 4.34. This circuit is composed by three resistances. If the voltage at the terminals of the DC-bus is too low, first the control system is disconnected and the input current forced to flow through the pre-charge resistances, so that the capacitor is charged by means of the anti-parallel diodes of the power semiconductors. Once the voltage of the DC-bus reaches a sufficiently high value, the control system is activated and the resistances of the pre-charge circuit are bypassed, in order to prevent significant power losses during the steady-state operation. Hence, the inclusion of the pre-charge circuit also required the modification of the control system, whose simulation model is presented in Figure 4.35.

The simulation results presented in this section were performed using a pre-charge resistance of $50\ \Omega$. In this case, the pre-charge is configured to remain activated until the voltage of the DC-bus reaches to 250 V.

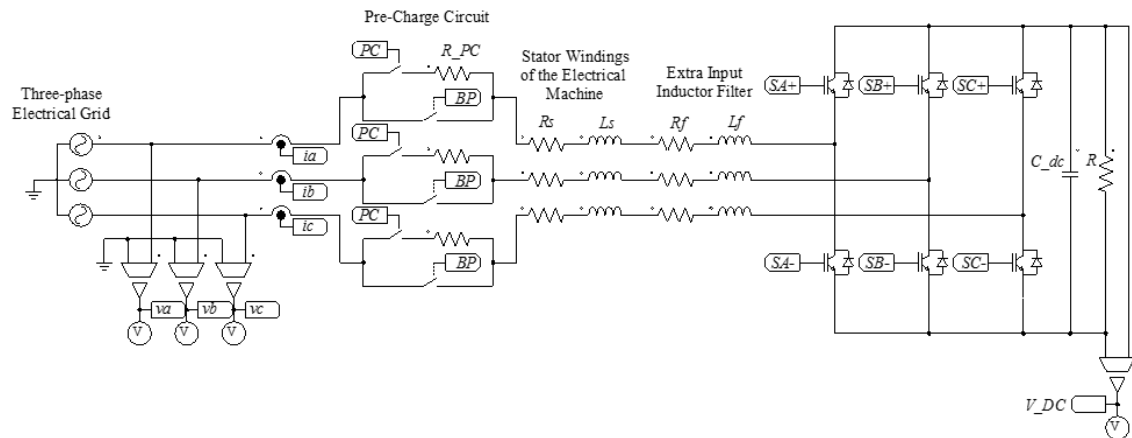


Figure 4.34 – Modified simulation model of the power electronics circuit, developed in the software *PSIM*, for the fast charging mode with an extra input filter and a pre-charge circuit.

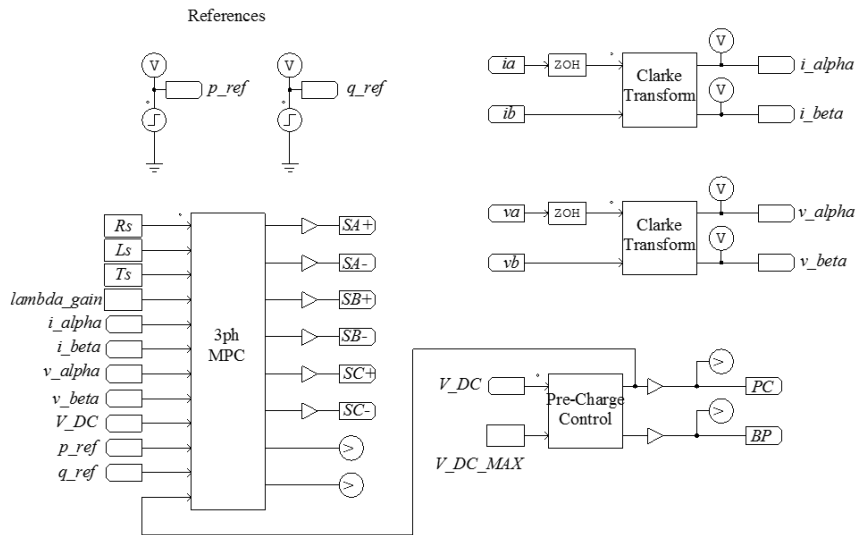


Figure 4.35 – Modified simulation model of the control system responsible for implementing the DPC-MPC, developed in the software *PSIM*, for the fast charging mode with a pre-charge circuit.

The obtained waveforms for the currents consumed, during the transitory regime, are presented in Figure 4.36, showing that the maximum reached values were significantly reduced. The respective obtained waveform of the voltage V_{DC} is presented in Figure 4.37.

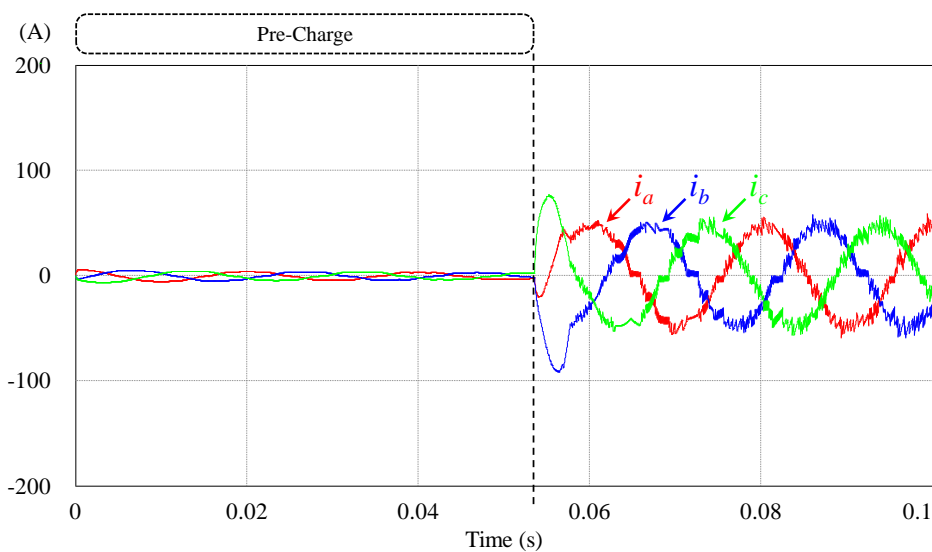


Figure 4.36 – Simulation results of the input currents, during the fast charging mode (G2V operation), with a pre-charge circuit.

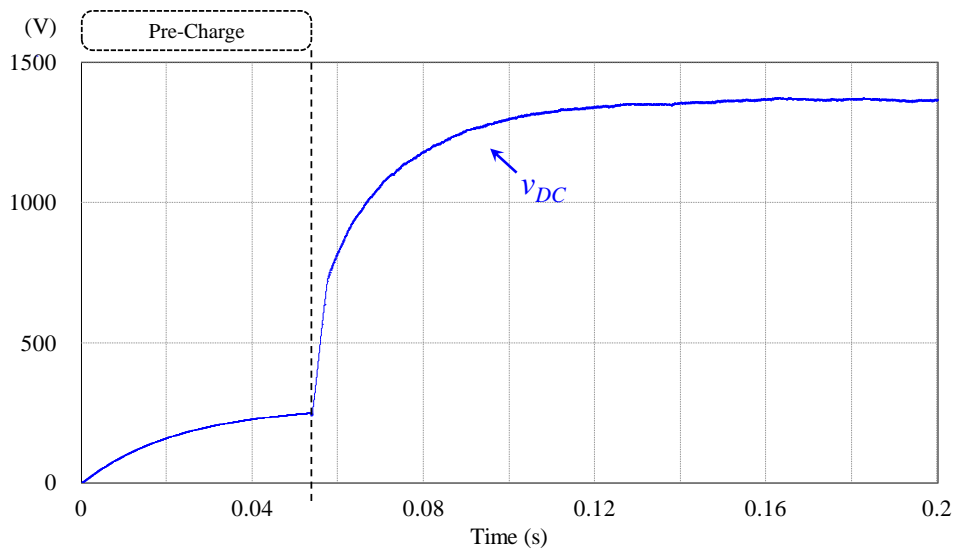


Figure 4.37 – Simulation results of the voltage at the terminals of the DC-bus, during the fast charging mode (G2V operation), with a pre-charge circuit.

Hence, the pre-charge circuit as well as the extra inductor filter are required for a proper working of the proposed solution and thus, both are considered in the afterwards presented simulations.

4.5.4. Grid-to-Vehicle Operation with Reactive Power Compensation

The main simulation results performed with a reference instantaneous imaginary power (q_{ref}) different from 0, i.e., operating as a reactive power compensator, are presented in this section.

The reference instantaneous real power (p_{ref}) is set to 15 kVA. To evaluate the dynamic response of the charging system in this mode, the reference instantaneous imaginary power (q_{ref}) is defined to be -10 kVA from the instant $t = 0$ s and 10 kVA from the instant $t = 0.5$ s.

The obtained waveforms for the instantaneous real power (p) and the instantaneous imaginary power (q) and their respective references (p_{ref} and q_{ref}), are presented in Figure 4.38, while the obtained waveforms of the voltage v_a and current i_a are presented in Figure 4.39. The obtained results allow for the demonstration of the fast dynamic response of the system.

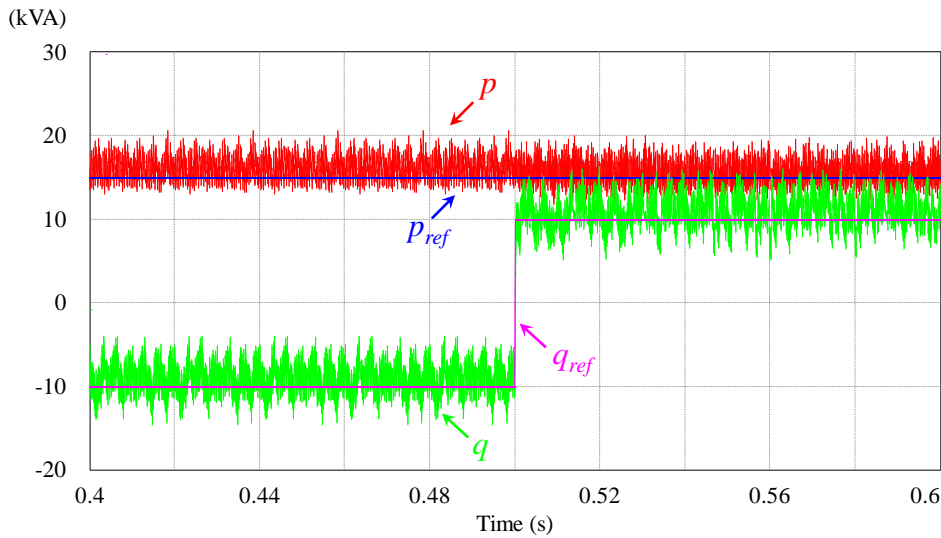


Figure 4.38 – Simulation results of the instantaneous p - q powers (in steady-state), during the fast charging mode (G2V operation with reactive power compensation).

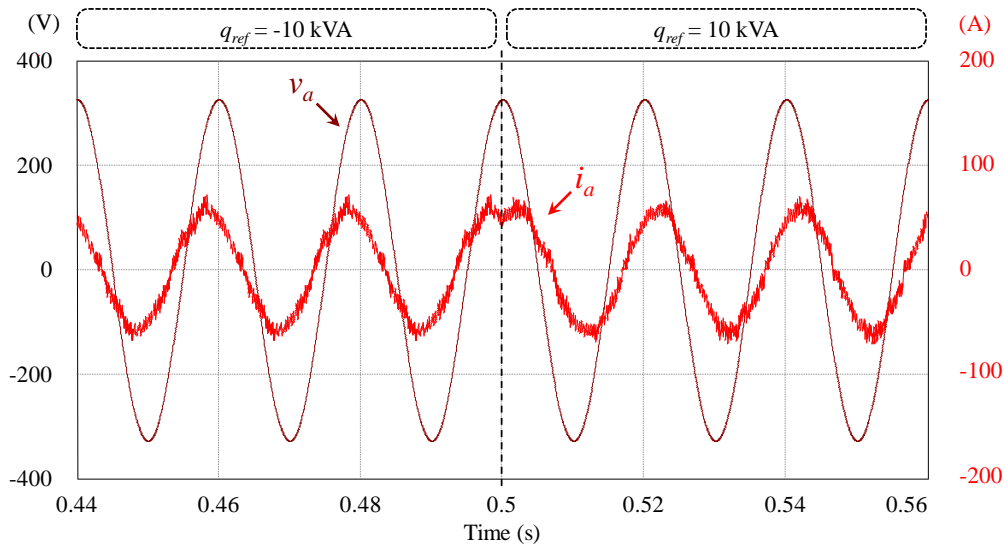


Figure 4.39 – Simulation results of the input voltage v_a and current i_a , during the fast charging mode (G2V operation with reactive power compensation).

4.5.5. Vehicle-to-Grid Operation

The last simulation presented in this chapter for the fast charging was performed for the Vehicle-to-Grid (V2G) mode. Hence, the resistor load R (presented in Figure 4.34), was replaced by an ideal voltage source of 1500 V. The instantaneous real power reference (p_{ref}) is set to -15 kVA, while the instantaneous imaginary power reference (q_{ref}) is set to 0 kVA.

The obtained waveforms for the instantaneous real power (p) and the instantaneous imaginary power (q) and their respective references (p_{ref} and q_{ref}), during the steady-state are presented in Figure 4.40, while the obtained waveforms of the voltage v_a and current i_a are presented in Figure 4.41. The current i_a is the one that has the higher THD (19.84%), and its harmonic spectrum is presented in Figure 4.42.

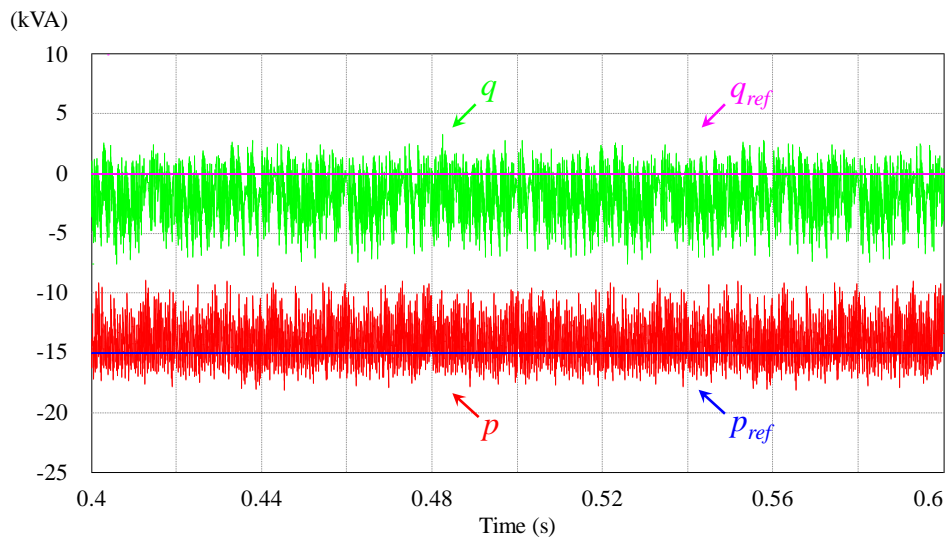


Figure 4.40 – Simulation results of the instantaneous p - q powers (in steady-state), during the fast charging mode (V2G operation).

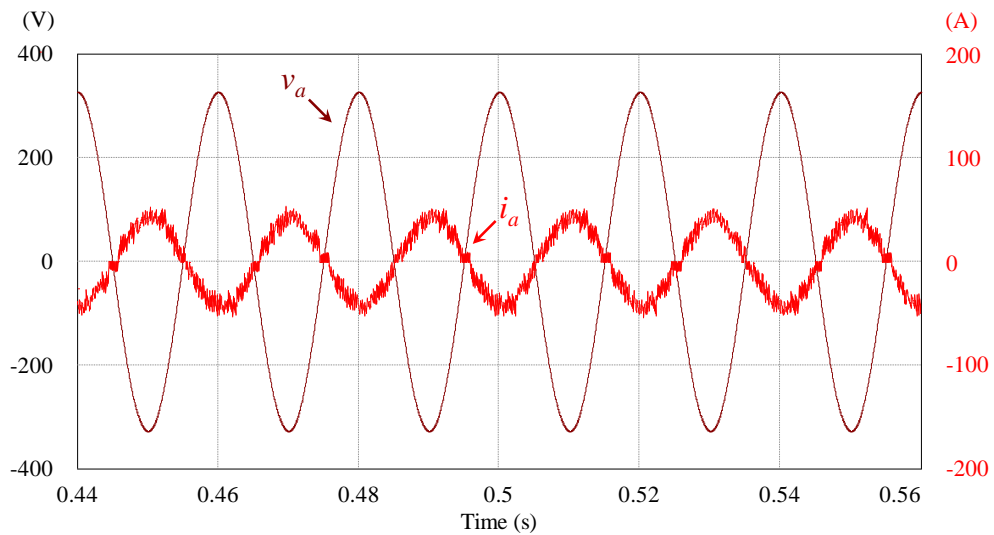


Figure 4.41 – Simulation results of the input voltage v_a and current i_a , during the fast charging mode (V2G operation).

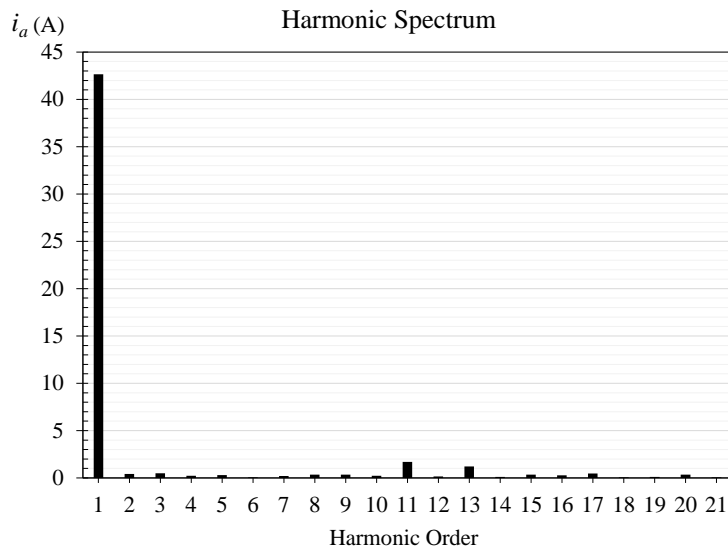


Figure 4.42 – Harmonic spectrum of the waveform of the injected current i_a , obtained in the simulations of the fast charging mode (V2G operation), with an extra inductor filter.

4.6. Simulations in the Slow Charging Mode

The main simulation results obtained for the slow charging mode of the first stage of the proposed unified solution, comprising the three-phase VSI and the windings of the electrical machine are presented and discussed in this section.

The control algorithm chosen is the adapted single-phase version of the Direct Power Control based on Model Predictive Control (DPC-MPC), discussed in Section 3.3.2.

Such as for the fast charging mode, the major concern in the battery charging operation is its impact on the power quality of the electrical grid. Thus, the same criteria mentioned in Section 4.5 are considered, with the exception of the harmonic content limits, since in this case the limits established by the standard IEC 61000-3-2 are considered.

The standard IEC 61000-3-2 establish the limits for the emissions of harmonic current of equipment having an input current with a RMS value less or equal to 16 A (per phase). The limits established by this standard are defined according to a classification of the equipment used. Such as in [50], in this MSc. Thesis the battery charger is considered an equipment of class A. Thus, the maximum admissible harmonic currents, for slow charging with input currents with a RMS value lower than 16 A, are presented in Table 4.11.

Table 4.11 – Limits for emissions of harmonic content for class A equipment with input RMS currents less than 16 A per phase (source: IEC 61000-3-2).

Harmonic order n	Maximum admissible harmonic current (A)	Harmonic order n	Maximum admissible harmonic current (A)
Odd harmonics		Even harmonics	
3	2.30	2	1.08
5	1.14	4	0.43
7	0.77	6	0.30
9	0.40	$8 \leq n \leq 40$	$0.23 \cdot 8/n$
11	0.33		
13	0.21		
$15 \leq n \leq 39$	$0.15 \cdot 15/n$		

4.6.1. Proposed Control Algorithm

The control algorithm proposed in this MSc. Thesis to perform the battery charging operation through a single-phase connection to the electrical grid is described in Figure 4.43. It consists in the Model Predictive Control (MPC) proposed in the Section 3.3.2 for the slow charging mode.

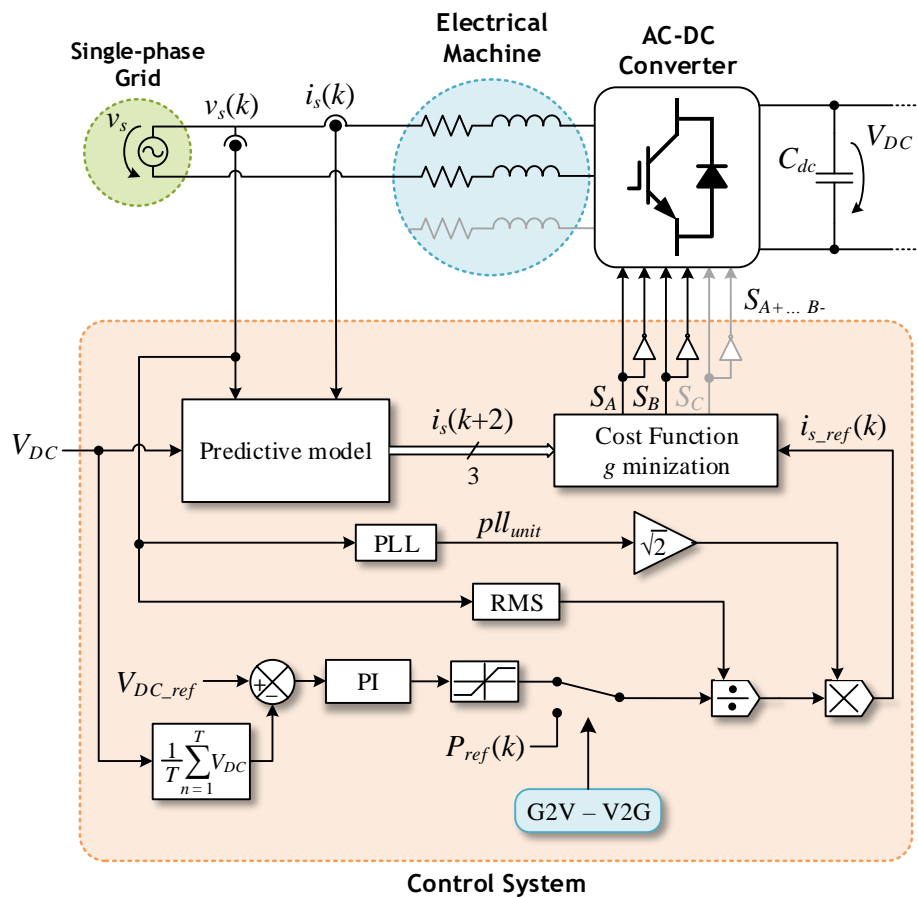


Figure 4.43 – Block diagram of the Direct Current Control based on Model Predictive Control (DCC-MPC) proposed in this MSc. Thesis, for the slow battery charge mode.

The RMS value of the source voltage v_s is obtained through the discretization of the expression that defines the RMS value, presented in (4.17), resulting in (4.18) [95], where N is the number of samples that are considered per each sampling period T_s . Thus, for a proper determination of the RMS value, N should be established according to (4.19), where f_s is the sampling frequency of the system and f_g the fundamental frequency of the voltage grid.

$$V_s = \sqrt{\frac{1}{T_s} \int_0^T v_s^2 dt} \quad (4.17)$$

$$V_s = \sqrt{\frac{1}{T_s} \sum_{k=1}^{k=N} v_s^2(k)} \quad (4.18)$$

$$N = \frac{f_s}{f_g}, \quad \forall f_s = k f_g, \quad k > 0 \wedge k \in \mathbb{N} \quad (4.19)$$

The proposed MPC for the slow charging mode requires the use of a Phase-Locked Loop (PLL) system, for generating the reference for the current consumed. In this MSc. Thesis it was chosen to use the PLL system described in Figure 4.44. This system results from the adaptation of the Enhanced PLL (EPLL) system proposed by *Karimi-Ghartemani et al.* in [92], [94], in which the component that estimates the amplitude was removed, since it is not required.

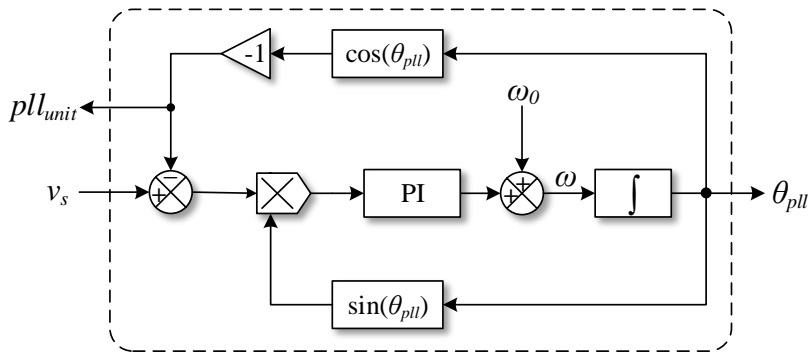


Figure 4.44 – PLL system proposed in this MSc. Thesis, for the slow charging mode.

4.6.2. Phase-Locked Loop System

The performance of the PLL system has high influence on the obtained results. Thus, the first simulations were done for evaluate the performance of the PLL system and to tune its parameters.

In this case, the simulation results presented in this section consider that the voltage source v_s is polluted with harmonics of order 3 (with 15% of the amplitude of the fundamental component), and 7 (with 10% of the amplitude of the fundamental

component). The obtained waveform of the PLL system in comparison with v_s is presented in Figure 4.45. The THD obtained for v_s is 17.83%, while the THD of pll_{unit} is 2.91%, demonstrating the good performance of the proposed PLL system.

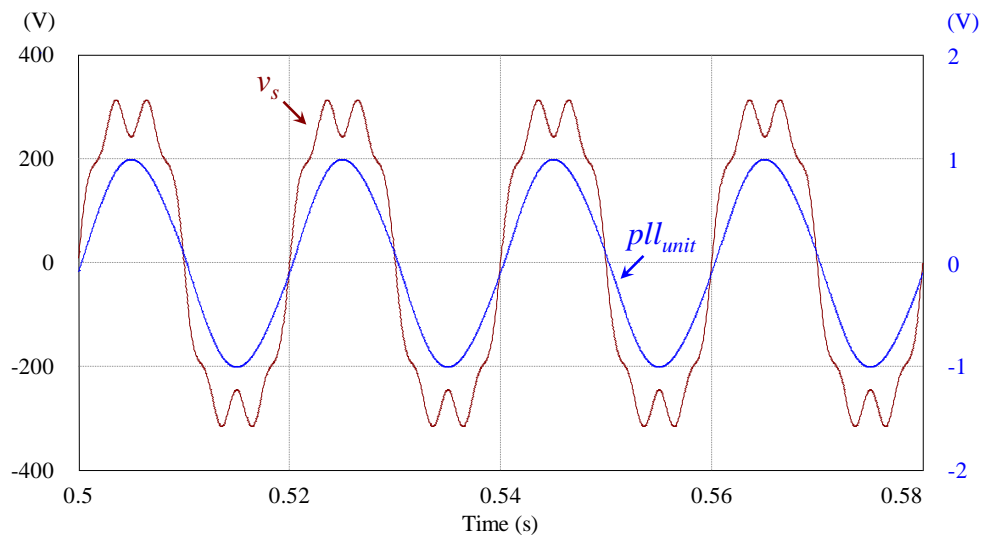


Figure 4.45 – Simulation results of the input voltage v_s and respective pll_{unit} signal, obtained by the PLL system.

The harmonic spectrum of the voltage v_s , in comparison with pll_{unit} amplified by a factor of 325 (which is the peak value of the fundamental voltage of the electrical grid), is presented in Figure 4.46. The obtained results show that the PLL system was capable of reducing significantly the harmonic components added to the source voltage.

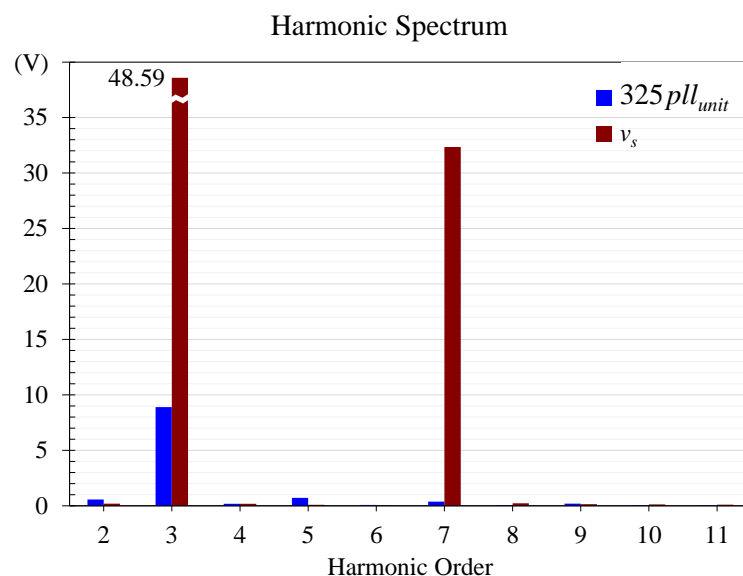


Figure 4.46 – Harmonic spectrum of the waveform of the pll_{unit} signal, obtained in the simulations of the PLL system, in comparison with the voltage v_s .

It is important to note that the results achieved by the PLL system could be improved by readjusting the gains of the PI controller. However, as a result, the

improvement on the quality of the synchronized signal would lead to an increase in the time required for the PLL system to synchronize with the source voltage.

4.6.3. Grid-to-Vehicle Operation

The simulation models of the power electronics circuit and the MPC, developed in the software *PSIM* for the simulations of the slow charging mode are presented, respectively, in Figure 4.47 and Figure 4.48. The main parameters used are presented in Table 4.12.

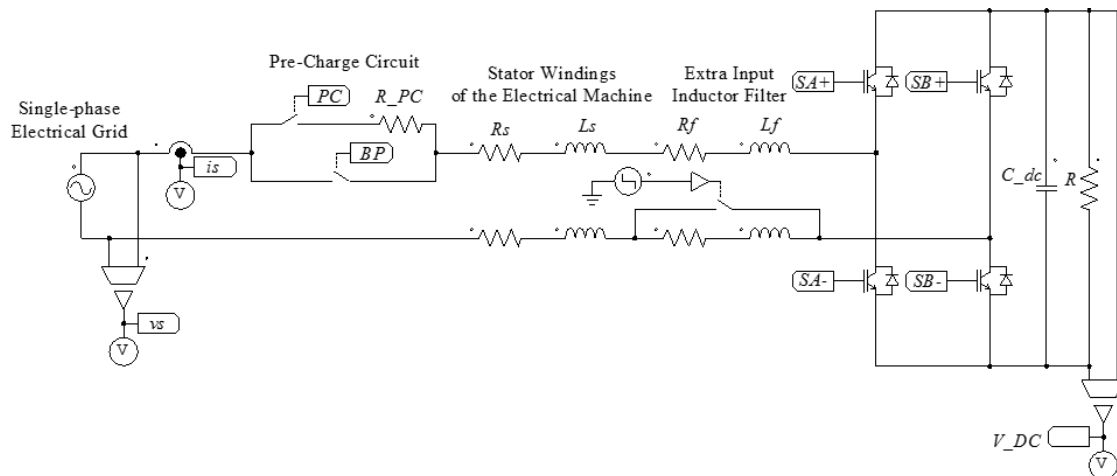


Figure 4.47 – Simulation model of the power electronics circuit, developed in the software *PSIM*, for the slow charging mode.

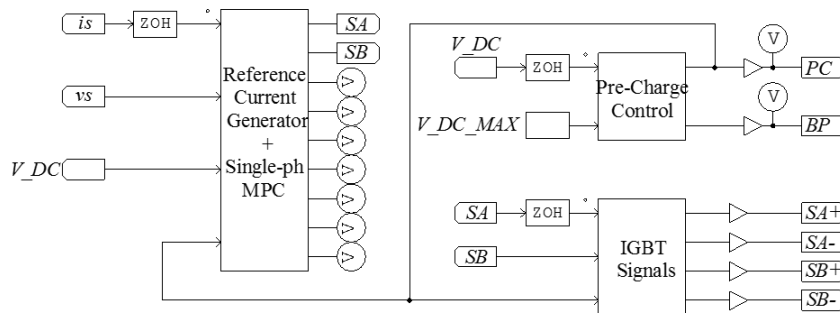


Figure 4.48 – Simulation model of the control system responsible for implementing the DCC-MPC, developed in the software *PSIM*, for the slow charging mode.

For evaluate the performance of the control system in the presence of variations in the values of the inductances, the most-dispersed values obtained in the experimental measurements presented in Section 4.2 were used.

Table 4.12 – Parameters used in the simulation of the fast charging operation in the G2V mode.

RMS of the grid voltage V_s	230 V
Grid voltage frequency f_g	50 Hz
Resistance of the windings of the same phase R_s	400 m Ω
Inductance of the windings of the phase L_{sa}	253 μ H
Inductance of the windings of the neutral L_{sb}	276 μ H
Inductance per phase, considered by the MPC L_s	262 μ H
DC-bus capacitor C_{dc}	500 μ F
Load Resistance R	100 Ω
Sampling frequency f_s	20 kHz

Despite the low value of the inductances of the extra inductor filter proposed (3 mH), for the fast charging mode, high values of consumed currents were obtained. Hence, high-current inductors are required, which might compromise its inclusion on-board the EV. Thus, for the slow charging mode, the power electronics circuit proposed (Figure 4.47) considers using the windings of two phases of the electrical machine (for maximizing its value), but the extra inductor filter only includes one inductor (instead of two, in which the other inductor is bypassed), for evaluate the results achieved considering installing only one extra inductor on-board the vehicle.

The simulation presented in this section was performed for the G2V mode, establishing a reference value for the DC-bus voltage (V_{DC_ref}) of 550 V. This value was chosen in order to ensure that the RMS value of the obtained current consumed is less than 16 A, allowing for the analysis of the obtained results according to the limits defined in the standard IEC 61000-3-2.

The obtained waveforms of the voltage v_s and current i_s , in the steady-state, are presented in Figure 4.49. The obtained waveform for the current i_s has a RMS value of 15.36 A and a THD of 21.27%, with a power factor of 0.97, with respect to the source voltage v_s .

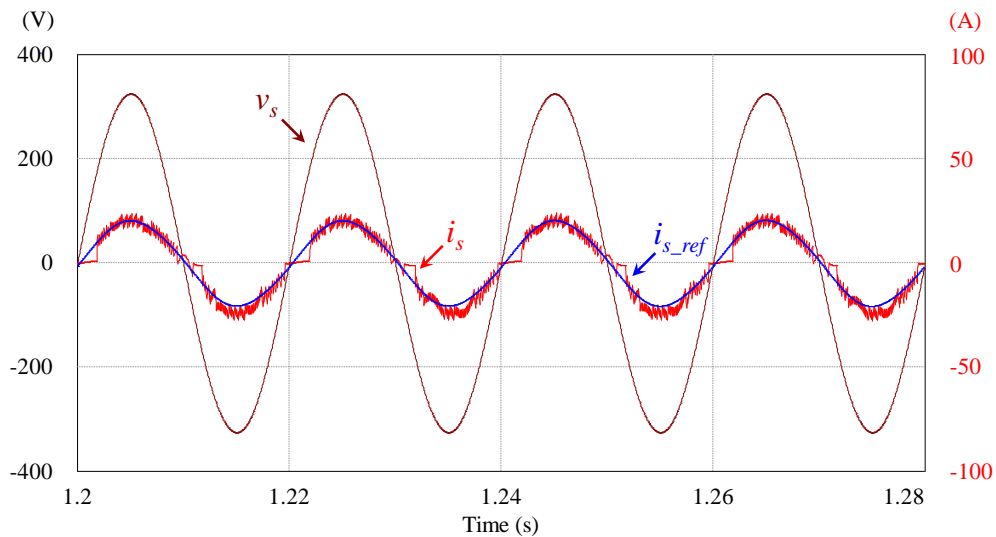


Figure 4.49 – Simulation results of the input voltage v_s and current i_s , during the slow charging mode (G2V operation), with an extra inductor filter.

The harmonic spectrum of the current i_s , in comparison with the limits established by the standard IEC 61000-3-2 is presented in Figure 4.50.

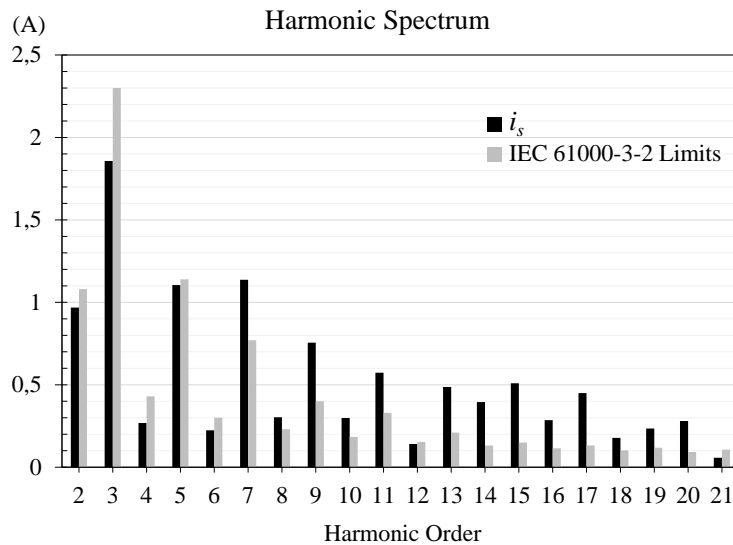


Figure 4.50 – Harmonic spectrum of the waveform of the current i_s , obtained in the simulations of the slow charging mode (G2V operation), with an extra inductor filter, in comparison with the limits established by the standard IEC 61000-3-2.

The harmonic spectrum obtained shows that for a reference value for the voltage of the DC-bus of 550 V, the obtained consumed current has some difficulties in accomplish with the limits established by the standard.

The waveform of the voltage at the terminals of the DC-bus, following the established reference of 550 V with a ripple of 9.40%, is presented in Figure 4.51.

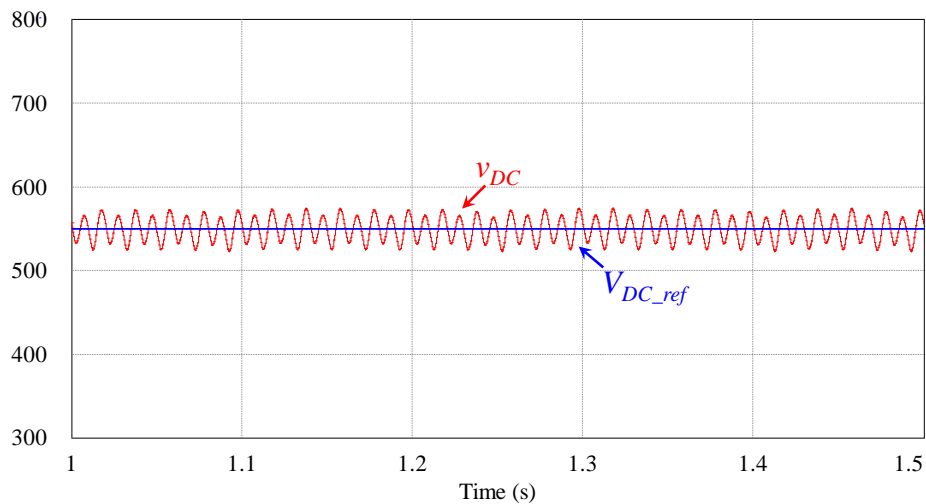


Figure 4.51 – Simulation results of the voltage of the DC-bus V_{DC} , during the slow charging mode (G2V operation), with an extra inductor filter.

4.6.4. Vehicle-to-Grid Operation

The last simulation presented in this chapter for the slow charging mode was performed for the V2G mode. Hence, the resistor load R (Figure 4.47), was replaced by an ideal voltage source of 600 V. In this mode, the control variable is the active power reference (P_{ref}) which, in this case, is set to -3.3 kW.

The obtained waveforms of the voltage v_s and current i_s , in the steady-state, are presented in Figure 4.52. The obtained waveform for the current i_s has a RMS value of 13.46 A and a THD of 21.95%. The harmonic spectrum of the current consumed is presented in Figure 4.53.

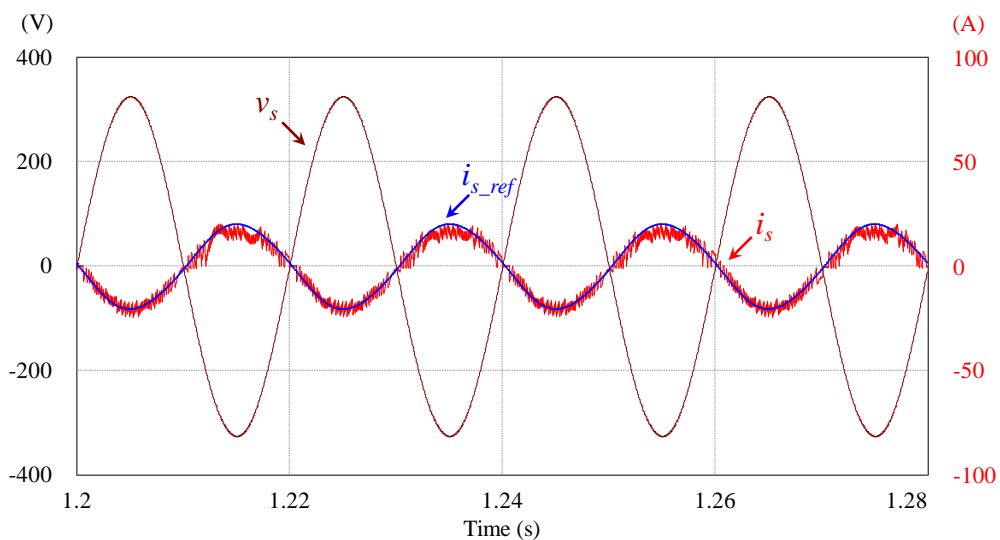


Figure 4.52 – Simulation results of the input voltage v_s and current i_s , during the slow charging mode (V2G operation), with an extra inductor filter.

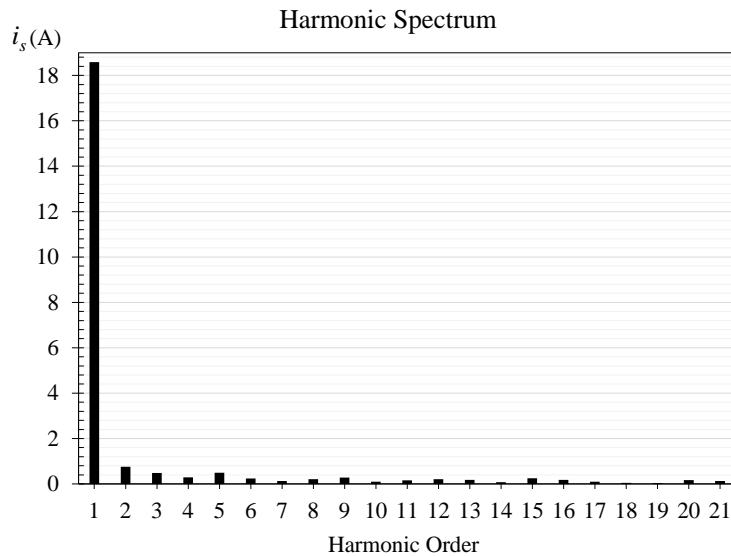


Figure 4.53 – Harmonic spectrum of the waveform of the injected current i_s , obtained in the simulations of the slow charging mode (V2G operation), with an extra inductor filter.

4.7. Simulations of the Bidirectional DC-DC Converter

The simulation results obtained for the motor drive and battery charging modes of the second stage of the proposed unified topology, comprising the bidirectional DC-DC converter and the battery pack, are presented in this section.

4.7.1. Motor Drive and Battery Charging (Vehicle-to-Grid) Modes

For the motor drive and battery charging (V2G) modes, it is proposed in this MSc. Thesis to use the control algorithm described in Section 3.4.1.

The simulation model of the power electronics circuit, developed in the software *PSIM* for the simulation presented in this section is presented in Figure 4.54.

The parameters used for the circuit of the DC-DC converter are presented in Table 4.13.

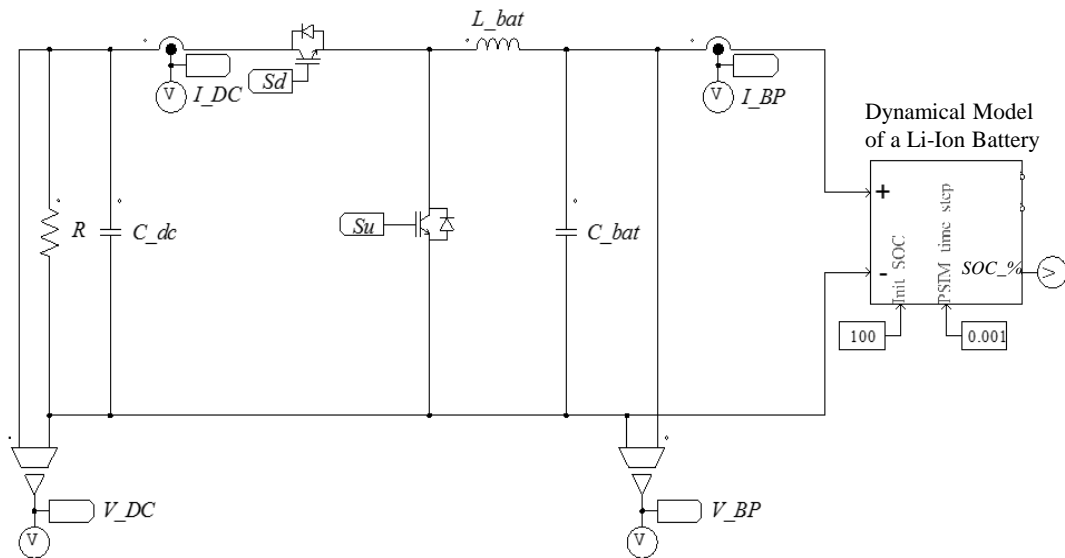


Figure 4.54 – Simulation model of the power electronics circuit, developed in the software *PSIM*, for the motor drive mode of the bidirectional DC-DC converter of the proposed unified topology.

Table 4.13 – Parameters of the circuit used in the simulations of the DC-DC converter for the motor drive mode.

Capacitance of the DC-bus C_{dc}	500 μF
Resistance of the DC-bus R	100 Ω
Inductance of the DC-DC converter L_{bat}	5 mH
Capacitance of the DC-DC converter C_{bat}	100 μF

In Figure 4.55 is presented the obtained waveform of the DC-bus voltage, for a reference value of 180 V, resulting in a ripple of 13.5%, while in Figure 4.56 the respective waveform of voltage at the terminals of the battery pack is presented.

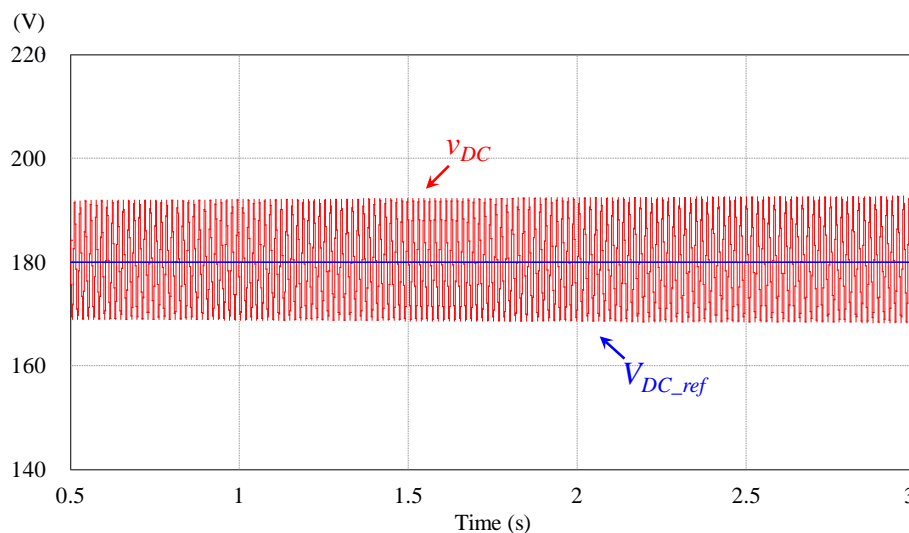


Figure 4.55 – Simulation results of the DC-bus voltage, during the motor drive mode.

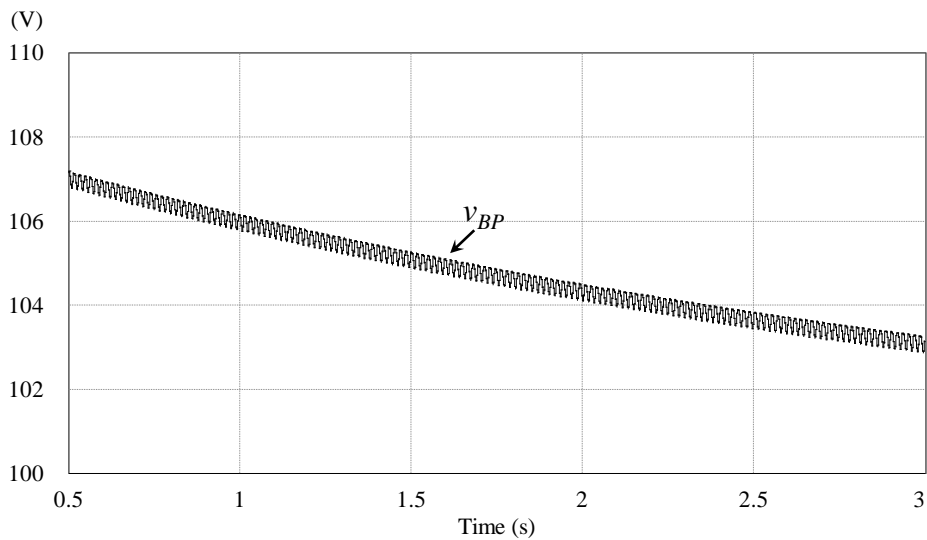


Figure 4.56 – Simulation results of the voltage of the battery pack, during the motor drive mode (the *PSIM_time_step* parameter was adjusted for providing a fast dynamic behavior of the battery pack).

4.7.2. Battery Charging Mode (Grid-to Vehicle Operation)

For the battery charging (G2V) mode, it is proposed in this MSc. Thesis to use the control algorithm described in Section 3.4.2.

In the simulation model of the power electronics circuit presented in Figure 4.54, the resistance R was replaced by an ideal voltage source of 500 V.

The obtained waveforms of the current flowing through the battery pack and its respective reference value (defined to be 10 A) are presented in Figure 4.57, while the respective voltage at the terminals of the battery pack is presented in Figure 4.58.

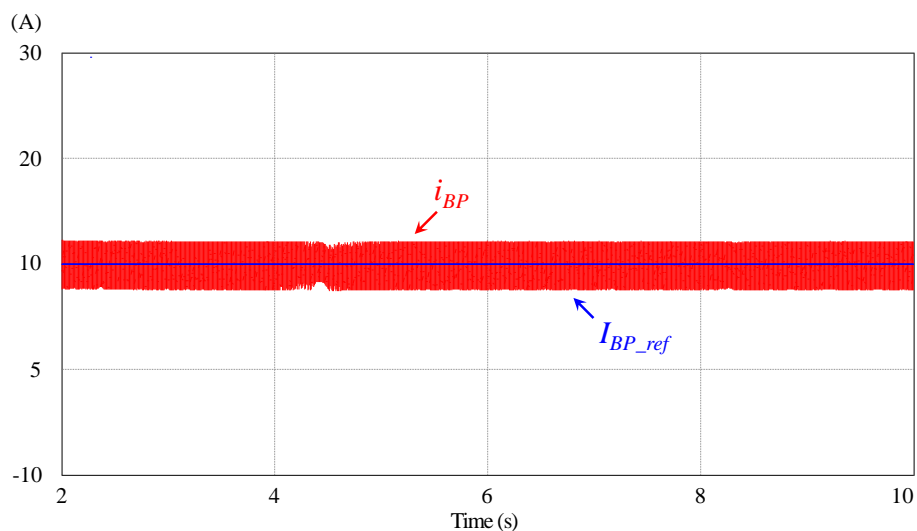


Figure 4.57 – Simulation results of the current flowing through the battery pack, during the constant-current mode of the battery charging.

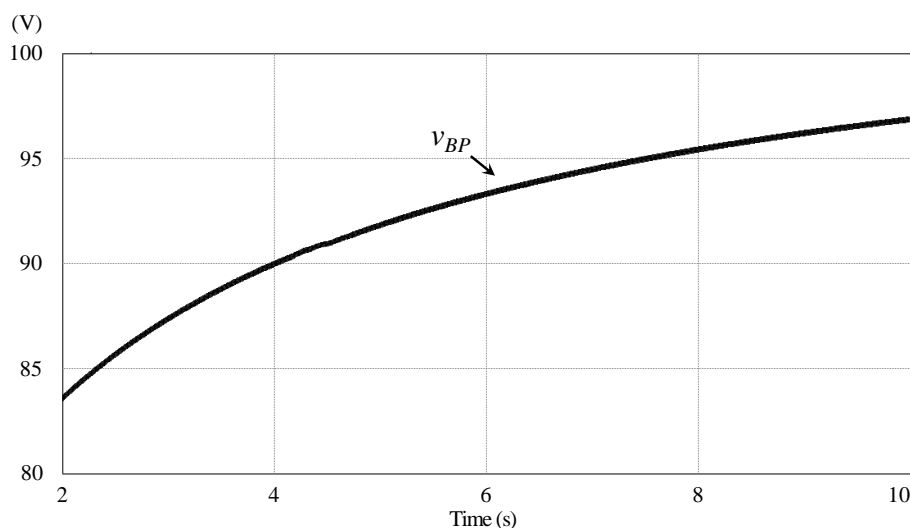


Figure 4.58 – Simulation results of the voltage at the terminals of the battery pack, during the constant-current mode of the battery charging (the *PSIM_time_step* parameter was adjusted for providing a fast dynamic behavior of the battery pack).

4.8. Conclusions

In this chapter, the obtained simulation results that allow for the validation of the control algorithms chosen for the unified topology are presented.

Initially the main characteristics of the electrical machine and the battery dynamical model proposed in the MSc. Thesis are presented.

The first simulations presented in this chapter are referred to the operation in the motor drive mode. The obtained results allowed for the validation of the compatibility of the proposed control algorithm with the electrical machine and the unified topology proposed.

Then, the simulations performed for the battery charging mode, separated into fast charging (through a three-phase grid connection), and slow charging (through a single-phase grid connection), are presented. The obtained results allowed concluding that some modification are required in the proposed topology. The electrical machine used to test the proposed topology has too low values of inductances on its windings. Thus, it is necessary to add an extra filter inductor, since the hardware available in the laboratory does not allow for increase the switching frequency (which is the preferable option). On the other hand, the obtained results during the transitory regime allow concluding the need of using a pre-charge circuit in order to ensure the integrity of the power electronics components, when the output filter capacitor is initially fully discharged, due to the high currents generated.

Despite the low value of inductances considered for the extra inductor filter proposed (3 mH), for the fast charging mode high values of currents are consumed,

requiring high-current inductors, which compromise its inclusion on-board the EV. Thus, for the slow charging mode only one inductor for the extra filter is considered.

The obtained results for the battery charging mode allow for the validation of the compatibility of the proposed control algorithm with the unified topology proposed, even when disturbances in the individual values of the inductances of the electrical machine are considered. However, it is important to note that, in this case, the obtained results should be analyzed not just considering the immunity of the control algorithm, but also the fact that the stator windings of the electrical machine considered only represents about 8% of the total filter inductance.

Finally, the main simulation results obtained for the bidirectional DC-DC converter of the proposed unified topology are presented. The obtained results allowed for the validation of the proposed control algorithms. These results allowed also for conclude that for the fast charging mode, a high-power DC-DC converter might be required, depending on the characteristics of the battery pack. For instance, if a small value of current is required for charging the battery pack, in the fast charging mode the power electronics components of the DC-DC converter have to handle high values of voltages.

Chapter 5

Implementation of the Control System and the Power Stage of a Proof-of-Concept Prototype

5.1. Introduction

The implementation of a proof-of-concept prototype of the proposed unified solution is described in this chapter. The topology of this prototype is presented in Figure 5.1.

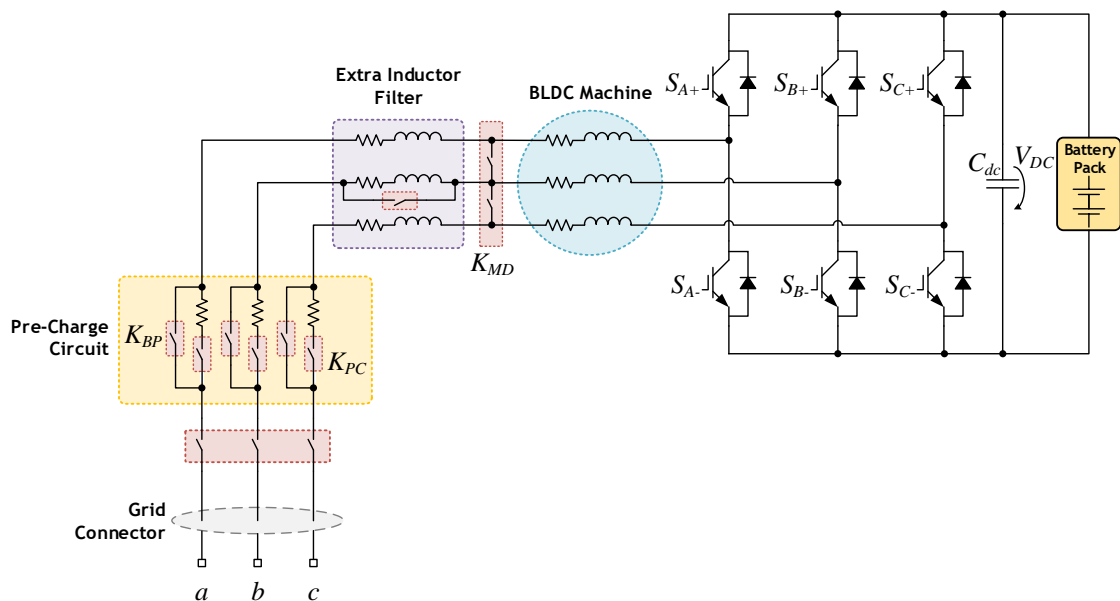


Figure 5.1 – Topology of the proof-of-concept prototype implemented in this MSc. Thesis.

This prototype has the purpose of validate the first stage of the unified motor drive and battery charger proposed in this MSc. Thesis, in order to demonstrate its operation capability.

In this case, due to the low values of the inductances of the electrical machine used, it is also considered the use of an extra inductor filter, as discussed in Section 4.5.2. Also a pre-charge circuit was added in order to ensure the integrity of the power electronics components, when the output filter capacitor is full discharged, as discussed also in Section 4.5.2.

This prototype does not include the second stage of the proposed solution, comprising the bidirectional DC-DC converter since this converter is used typically in the same way for the majority of the topologies of battery chargers, either unified or separated from the motor drive system, not properly representing an added value in the unification process.

Initially in this chapter, the implementation of the control system is described. The flowchart of the finite-state machine that describes the software implemented on the Digital Signal Controller (DSC), is presented as well as the main hardware implemented.

Afterwards, the implementation of the power stage is described, in which the components used are presented.

Finally, the obtained final result of the proof-of-concept prototype developed is presented.

All the components presented in this chapter were selected according the requirements established for this prototype.

5.2. Control System

The control system implemented in this MSc. Thesis is based on the finite-state machine presented in Figure 5.2. The first task is the configuration and initialization of the control system. Then the control system stays in idle state, waiting for some Interrupt Service Routine (ISR) be triggered or that the values of the system variables (currents and voltages of the power electronics system) be signed as updated, for apply the control algorithm according to the operation mode selected.

In this case, the control system is configured with three ISRs: the ISR of timer 0, an external ISR and the ISR of the Serial Peripheral Interface (SPI). The ISR of timer 0 is responsible for sending a periodic signal to the external Analog-to-Digital Converter (ADC), used for measuring the required current and voltage variables, and the position sensor, in order to start the conversion processes. The external ISR is triggered when the conversion process of the external ADC is finished, in order to update the values of the system variables. On the other hand, the ISR of the SPI is triggered when a new value is received in the buffer of the SPI unit, allowing update the value of the position of the rotor of the electrical machine.

As presented in Figure 5.2, the transition between states is done according to the state of certain flags, whose meaning is described in Table 5.1.

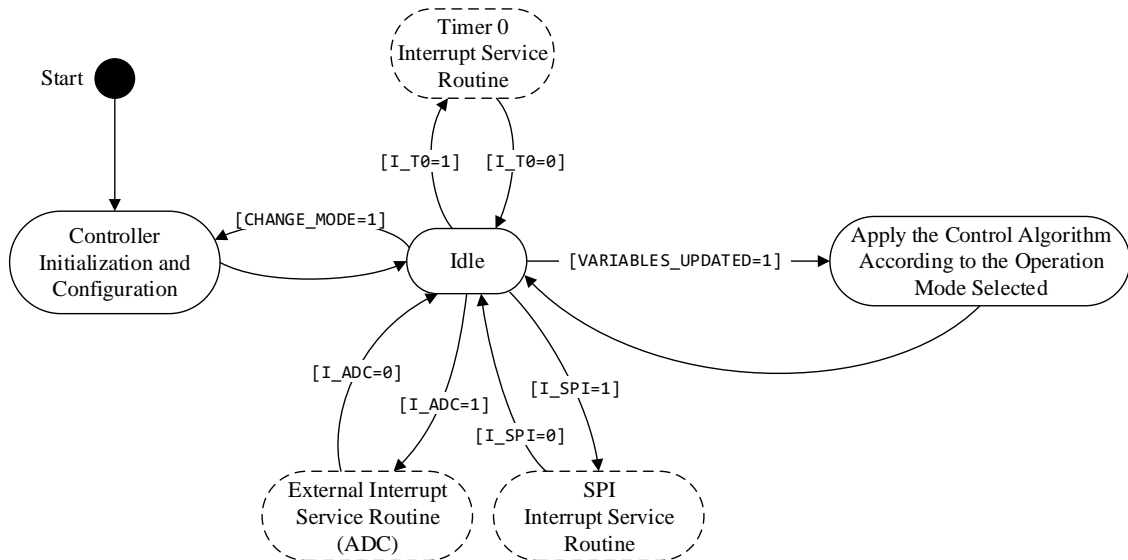


Figure 5.2 – Finite-state machine of the control system implemented in this MSc. Thesis.

Table 5.1 – Flags responsible for the transition of states in the finite-state machine of the control system implemented in this MSc. Thesis.

Flag	Its meaning when activated (i.e., has the value '1')
I_T0	Timer 0 overflow
I_ADC	Finished the conversion process in the external ADC
CHANGE_MODE	The operation mode was changed
I_SPI	The buffer of the SPI unit was updated
VARIABLES_UPDATED	The system variables were successfully updated

When the operation mode is changed the control system has to be reconfigured, since different amount of system variables are required (for instance, for the motor drive mode the values of the source voltages are not required, while for the slow charging mode only the values of the current and voltage of the phase a are required), and the relays contactors have to change their state.

A diagram describing the proof-of concept prototype and its main components for the implementation of the digital control system proposed is presented in Figure 5.3.

In this case, since the three-phase system is considered a balanced system, the conditions (5.1) and (5.2) are verified and thus only five sensors (2 current sensors and 3 voltage sensors), are used for measuring the currents and voltages required for the control system.

$$v_a(t) + v_b(t) + v_c(t) = 0, \forall t \in \mathbb{R}_0^+ \quad (5.1)$$

$$i_a(t) + i_b(t) + i_c(t) = 0, \forall t \in \mathbb{R}_0^+ \quad (5.2)$$

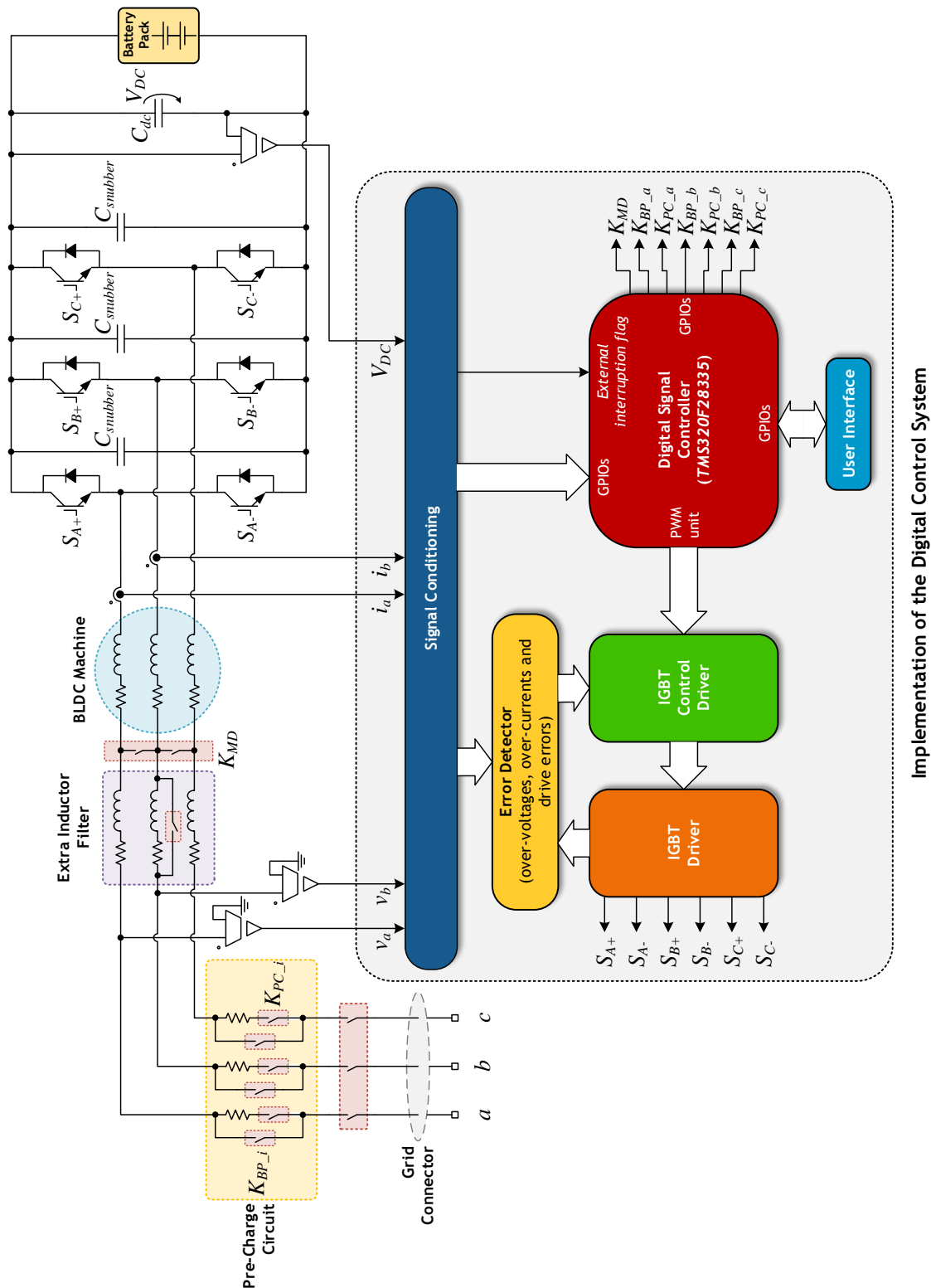


Figure 5.3 – Diagram describing the proof-of concept prototype and its main components for the implementation of the digital control system proposed in this MSc. Thesis.

The snubber capacitors were added in the proposed topology, since in an inductive circuit, these capacitors allow for attenuate the rise of the voltage across the collector and the emitter of each Insulated-Gate Bipolar Transistor (IGBT), when the current is suddenly interrupted [59].

In the following sections the main components used for the implementation of the control system are described.

5.2.1. Voltage Sensors

For measuring the voltages (v_a , v_b and V_{DC}), required for the control system, it was chosen to use three *Hall-effect* voltage sensors *CYHVS5-25A* from *ChenYang*. Each sensor allows measuring a maximum voltage of 1000 V and its input is represented in terms of a current, with a conversion ratio of 2500:1000 and a limited input range of ± 10 mA (RMS) and output range of ± 25 mA (RMS). This sensor has an accuracy of $\pm 0.8\%$, a linearity error less than 0.2% and a response time lower than 40 μ s [118].

Each one of the three sensors was implemented through the circuit presented in Figure 5.4, resulting in the Printed Circuit Board (PCB) presented in Figure 5.5.

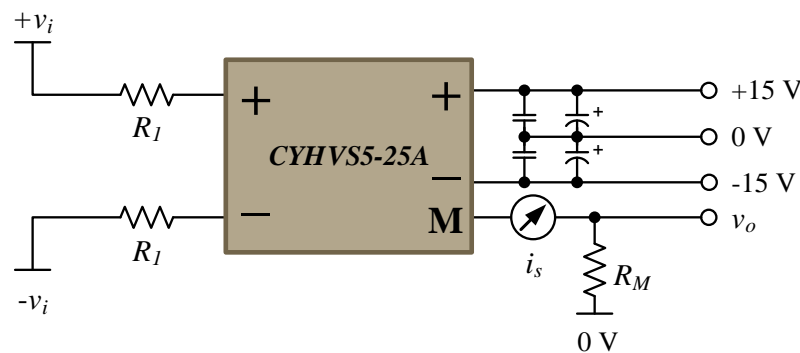


Figure 5.4 – Implemented circuit for the measuring the voltage, using the sensor *CYHVS5-25A* (adapted from [118]).

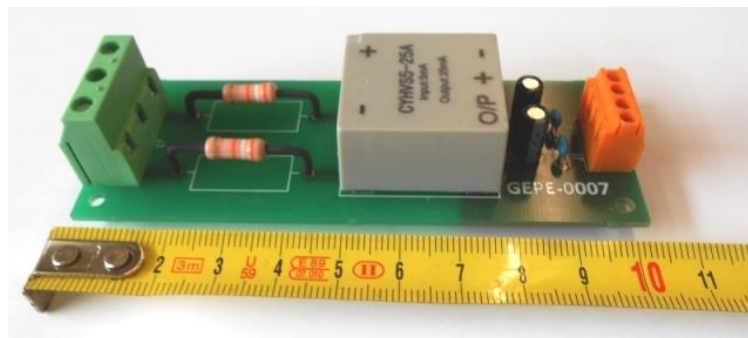


Figure 5.5 – Printed Circuit Board (PCB) developed in the GEPE for the measuring the voltage, using the sensor *CYHVS5-25A*.

The value R_I of the two input resistances (Figure 5.4), was established according to the expected rated voltage level and considering the recommendations of the manufacturer that the input rated current should be 10 mA, for an optimal measure accuracy [118]. Thus, R_I was determined using (5.3), where V_{i_rated} and I_{i_rated} are, respectively, the rated input voltage and current. The nominal power of each resistance is established according to (5.4).

$$R_1 = \frac{V_{i_rated}}{2 I_{i_rated}} = \frac{V_{i_rated}}{2 \times 0.01} = 50 V_{i_rated} \quad (5.3)$$

$$P_{R_1} = R_1 I_{i_rate}^2 \quad (5.4)$$

When the rated voltage is measured, the obtained output current will be equal to 25 mA, according to the conversion ratio of the sensor (2500:1000). Since the input range of the ADC used is ± 5 V, the value of R_M is determined considering that, under those circumstances, the obtained output voltage should be equal to 2.5 V. Thus, it results in a value of resistance of 100 Ω , with a nominal power of 6.25 mW, according to (5.5) and (5.6), respectively.

$$R_M = \frac{V_{o_rated}}{I_{o_rated}} = \frac{V_{o_rated}}{\frac{2500}{1000} I_{i_rated}} = \frac{2.5}{0.025} = 100 \Omega \quad (5.5)$$

$$P_{R_M} = R_M I_{o_rated}^2 = 6.25 \text{ mW} \quad (5.6)$$

In this case, the resistance R_M is installed in the signal conditioning board, instead of being installed in the sensor board presented in Figure 5.5. This was done so that the output signal of the sensor board is transmitted as a current, which is less sensitive to electromagnetic noise, ensuring less degradation of the transmitted signal.

5.2.2. Current Sensors

For measuring the currents (i_a and i_b), required for the control system, it was chosen to use two *Hall*-effect current sensors *LA 200-P* from *LEM*. Each sensor allows measuring currents of a range between -300 A and 300 A. The conversion ratio is 1:2000, which results that for an input current of 200 A, the obtained output current will be 100 mA. This sensor has an accuracy of $\pm 0.4\%$, a linearity error less than 0.15% and a reaction time lower than 500 ns [119].

Each one of the two sensors was implemented through the circuit presented in Figure 5.6, resulting in the PCB presented in Figure 5.7.

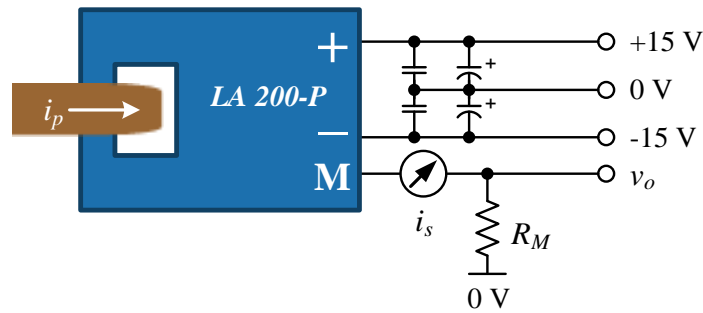


Figure 5.6 – Implemented circuit for the measuring the current, using the sensor *LA 200-P* (adapted from [119]).

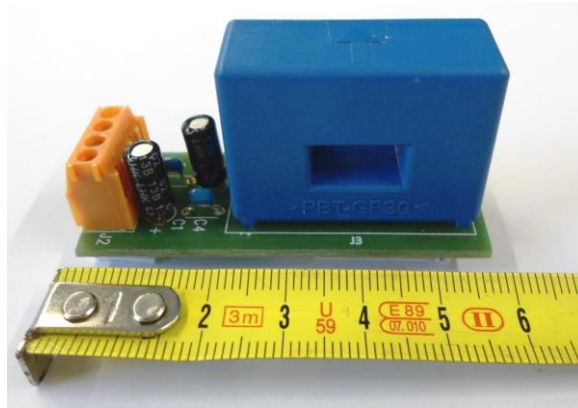


Figure 5.7 – PCB developed in the GEPE for the measuring of the current, using the sensor *LA 200-P*.

Once again, the resistance R_M was not installed in the sensor board and its value was established considering the desired output voltage level for the expected rated current. In this case, it was defined that when the current sensor is measuring a current of 200 A, the output value of the voltage should be 2.5 V. Hence, the value of R_M is obtained using (5.7), resulting in the value of 25 Ω , while the respective nominal power dissipated is obtained using (5.8), resulting in a value of 0.25 W.

$$R_M = \frac{V_{o_rated}}{I_{o_rated}} = \frac{V_{o_rated}}{\frac{1}{2000} I_{i_rated}} = \frac{2.5}{\frac{1}{2000} \times 200} = \frac{2.5}{0.1} = 25 \Omega \quad (5.7)$$

$$P_{R_M} = R_M I_S^2 = 0.25 \text{ W} \quad (5.8)$$

5.2.3. Signal Conditioning

The values of the system variables (the voltages v_a , v_b and V_{DC} and the currents i_a and i_b), are transmitted to the DSC, through an external ADC. It was chosen to use an external ADC due to the limitations on the characteristics of the ADC included in the DSC used for this implementation.

The external ADC chosen was the *MAX1320* from *Maxim*. This ADC has a resolution of 14 bits and 8 conversion channels, with an input range of ± 5 V. In this case four channels of the ADC are used, which allow for a maximum transmission speed of 357 000 samples per second [120].

For the signal acquisition the PCB presented in Figure 5.8 is used. In this board are included the resistances R_M , previously considered, an inverting amplifier circuit for conditioning the input signals obtained and the ADC.



Figure 5.8 – PCB developed in the GEPE for the signal conditioning.

5.2.4. Digital Signal Controller

For implementing the algorithms of the proposed control system it was chosen to use the 32-bit floating-point Digital Signal Controller (DSC) *TMS320F28335* from *Texas Instruments*, whose main characteristics are summarized in Table 5.2.

Table 5.2 – Main characteristics of the *TMS320F28335* (source: [121])

Operating Frequency	150 Mhz
RAM	68 kB
Flash Memory	512 kB
No. of PWM channels	18
Timers	3x 32 bits
General Purpose Inputs/Outputs (GPIOs)	88
Communication modules	SPI, I2C, UART, CAN

This DSC was used embedded in a *controlCARD*, presented in Figure 5.9. For programming and debug the implemented code, *Texas Instruments* provides a *docking station*. In the research lab of the GEPE the PCB presented in Figure 5.10 was developed, consisting of a *docking station* that provides an easier and more robust interface with the

peripherals of the DSC, through male headers and DB9 sockets. However, despite the features provided, only the *docking station* provided by *Texas Instruments* allows for the debug operation.



Figure 5.9 – *ControlCARD* provided by *Texas Instruments* to interface with the DSC *TMS320F28335*.

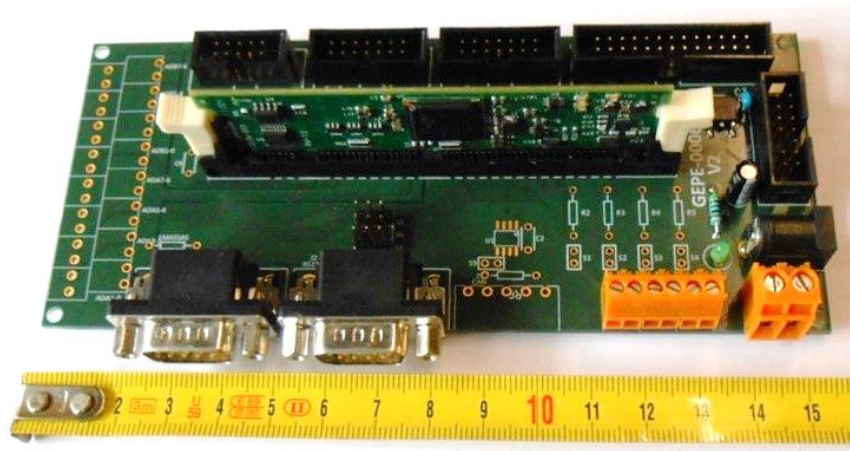


Figure 5.10 – *Docking station* developed in the GEPE providing an easier and more robust interface with the peripherals of the DSC.

The proposed control system was codified in C language and programmed using the software *Code Composer Studio 6*, an Integrated Development Environment (IDE), provided by *Texas Instruments*. This software allows optimizing the developed source code for the DSCs of *Texas Instruments*, while providing a high abstraction level.

5.2.5. Control Driver of the Insulated Gate Bipolar Transistors

For interface the six PWM signals, obtained from the DSC, with the driver module of the IGBTs the PCB presented in Figure 5.11 is used. This board is composed by an error module, responsible for detecting errors coming from the DSC. It also has an external error module, which in this MSc. Thesis is used to receive an external signal, triggered when over-voltages on the DC-bus are detected.

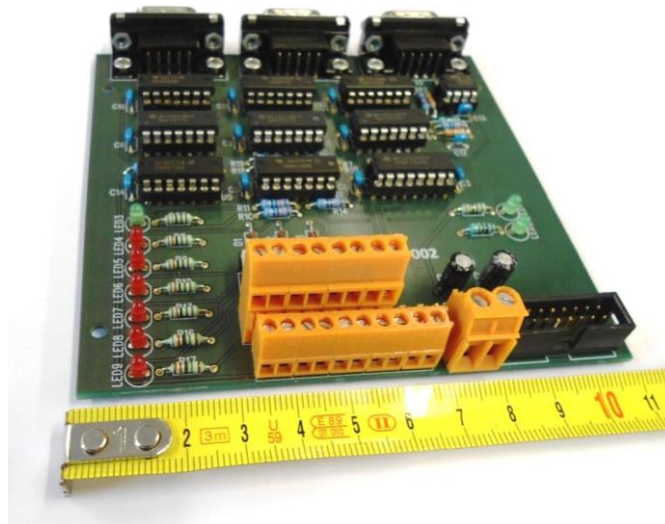


Figure 5.11 – PCB developed in the GEPE for the control of the drive of the IGBTs.

5.2.6. Control Board for the Pre-Charge Circuit

As discussed in Section 4.5.3, a pre-charge circuit is required for ensuring the integrity of the power electronics components, especially the power semiconductors, during the battery charging operation, when the capacitor of the DC-bus is initially fully discharged.

The implemented control circuit responsible for actuate or bypass the pre-charge resistances in the circuit is presented in Figure 5.12.



Figure 5.12 – PCB developed in the GEPE for control the actuation of the pre-charge circuit.

5.2.7. Position Sensor

The Field-Oriented Control (FOC) algorithm proposed for the motor drive mode requires the mechanical angle corresponding to the position of the rotor of the electrical machine. In this case, it was chosen to use the magnetic *Hall*-effect position sensor *RMB28SC* from *RLS*. In Figure 5.13 is presented the position sensor mounted on the surface of the electrical machine. This sensor is configured for a resolution of 11 bits,

which allows supporting a maximum speed 10 000 rpm. The measured value is obtained communicating through the Synchronous Serial Interface (SSI) protocol.

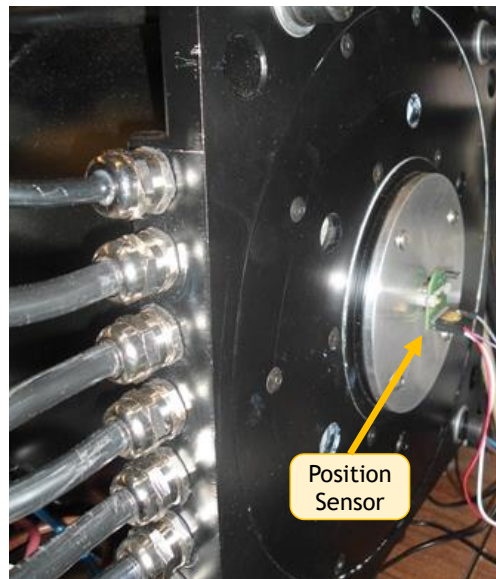


Figure 5.13 – Position sensor (*RMB28SC* from *RLS*), mounted on the electrical machine.

5.2.8. Interface Board for the Position Sensor

The DSC used in this implementation does not provide communication using the SSI protocol. To overcome this issue it was used the SPI protocol, whose signals are compatible with the SSI through the use of the interface board presented in Figure 5.14.



Figure 5.14 – PCB developed in the GEPE for interface between the position sensor with the DSC.

5.2.9. Torque Reference

For emulate the torque reference established by the user of an Electric Vehicle (EV), during the motor drive mode, it is used the electronic accelerator pedal presented in Figure 5.15, which is based on a linear potentiometer.



Figure 5.15 – Electronic accelerator pedal used for setting the torque reference in the motor drive mode.

5.2.10. Human–Machine Interface

For an easier interface with the control system, it is used the Human-Machine Interface (HMI), presented in Figure 5.16.



Figure 5.16 – Human-Machine Interface (HMI), developed in the GEPE, used to provide an easier interface with the control system.

For the motor drive mode, this interface allows emulating the position of the gearbox between “Forward” (F), “Neutral” (N) and “Reverse” (R). It also provides useful information such as the rotational speed of the electrical machine.

For the battery charging mode, this interface allows control the start of the operation and it is also prepared for provide useful information such as the State of Charge (SOC) of the battery pack, through a progress bar.

5.3. Power Stage

In this section the main components used for the implementation of the power stage of the proof-of-concept prototype are described. The electrical machine used is not

considered in this section, since its main characteristics were already presented in Section 4.2.

5.3.1. Three-Phase Voltage Source Inverter

Three modules *SKM100GB125DN* from *Semikron*, presented in Figure 5.17 (a), are used for implementing the three-phase Voltage Source Inverter (VSI) of the proposed topology. Each module is composed by two IGBTs and its respective pinout is presented in Figure 5.17 (b).

Each IGBT handles a maximum collector-to-emitter voltage (V_{CES}) of 1200 V, a maximum current of 100 A and a short-circuit current six times greater than its nominal current (75 A) [122].

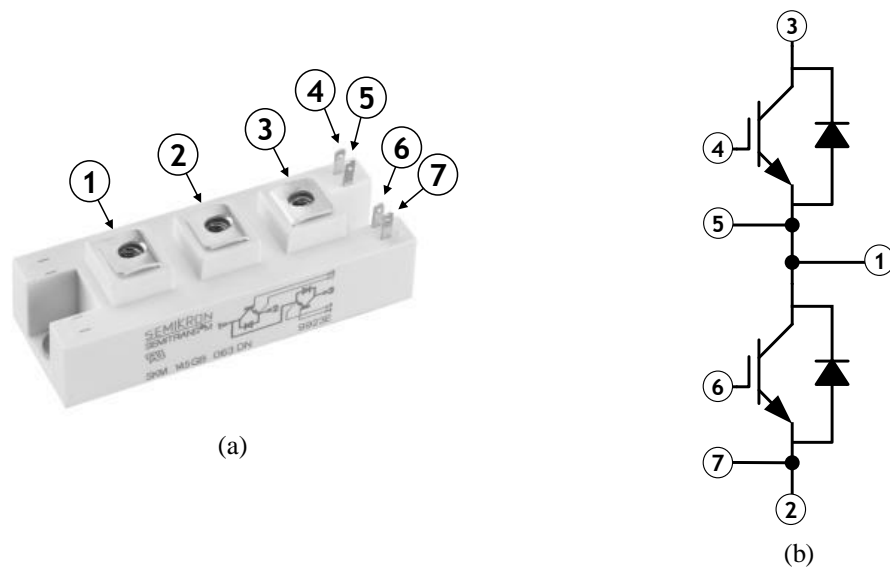


Figure 5.17 – IGBT module *SKM300GB126D* from *Semikron* (adapted from [122]): (a) Module; (b) Respective pinout.

Each IGBT has a rise time (t_r) of 40 ns and a fall time (t_f) of 20 ns. With respect to the thermal characteristics, each one has a thermal resistance junction-to-case [$R_{th(j-c)}$] of 0.18 K/W, while each antiparallel diode has a thermal resistance of 0.5 K/W [122].

For protecting the gate terminals of each module of IGBTs it is used the PCB presented in Figure 5.18.

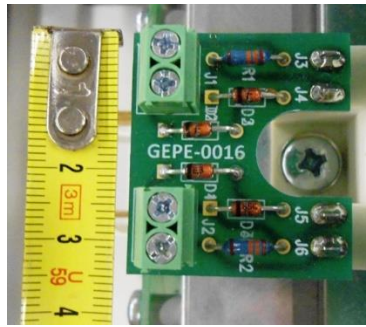


Figure 5.18 – PCB developed in the GEPE for the protection of the gates of each module of IGBTs.

The three modules of IGBTs are controlled using the six-pack IGBT driver *SKHI 61 R* from *Semikron*. This driver has a galvanic isolation capable of handling a maximum voltage, between the primary and the secondary side, of 2500 V (RMS), during 2 seconds. The turn-on gate voltage output is 14.9 V while the turn-off gate voltage output is -6.5 V [123].

This module allows configuring a deadtime for its output signals. However, in this case, the deadtime is already considered in the PWM signals generated by the DSC, configuring the “dead band” module of the PWM unit to a deadtime of 5 μ s. Another interesting feature of this driver module is the external error signal input, which is used to turn-off the drive module, when errors are detected.

The implemented PCB, containing the driver circuit is presented in Figure 5.19.



Figure 5.19 – PCB developed in the GEPE for the driver circuit of the IGBTs.

5.3.2. DC-Bus

The DC-bus was implemented using a pack of capacitors composed by 10 capacitors *B43456A5108-M* from *EPCOS*. Each capacitor has a capacity of 1000 μ F, with a tolerance of 20%, handles a voltage of 400 V across its terminals and has an Equivalent Series Resistance (ESR) of 180 m Ω [59].

In this case, a capacitor pack was developed so that the resultant equivalent capacitor has a total capacity of 10 mF, handling a maximum voltage of 450 V.



Figure 5.20 – DC-bus implemented, composed by a pack of capacitors resulting in a total capacity of 10 mF and a maximum voltage of 450 V.

For security purposes, the protection circuit for the DC-bus presented in Figure 5.21 it was developed. This circuit limits the voltage V_{DC} to a maximum value of 350 V, since the implementation tests performed in this MSc. These are of low-power. Thus, if a voltage higher than 350 V is detected, a power semiconductor is actuated in order to dissipate the power in excess to a resistive load.

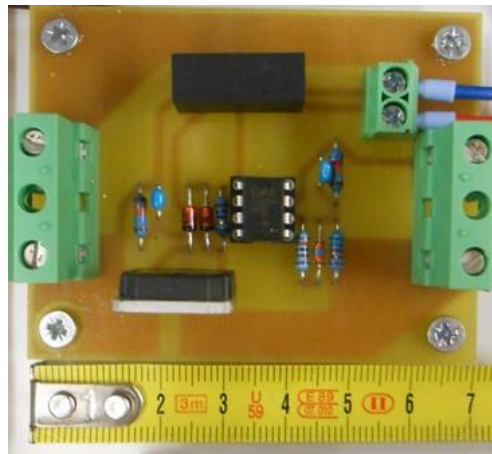


Figure 5.21 – PCB developed in the GEPE for the protection of the DC-bus.

5.3.3. Sources and Auxiliary Loads

For testing the motor drive mode, the DC-bus is feed using DC voltage sources, providing a voltage of 120 V.

For testing the battery charging mode under a low-power level the voltages of the electrical grid are connected to the transformers presented in Figure 5.22. In this mode, a resistive load of 75 Ω is connected in parallel with the capacitor of the DC-bus.



Figure 5.22 – Transformers used to reduce the levels of the voltages supplied by the electrical grid.

5.3.4. Extra Inductor Filter

For implement the extra inductor filter required, a set composed by three inductors is used. Each inductor, presented in Figure 5.23, has a value of inductance of approximately 3 mH.



Figure 5.23 – Inductor used to implement the extra input filter of proof-of-concept prototype.

5.3.5. Resistances of the Pre-Charge Circuit

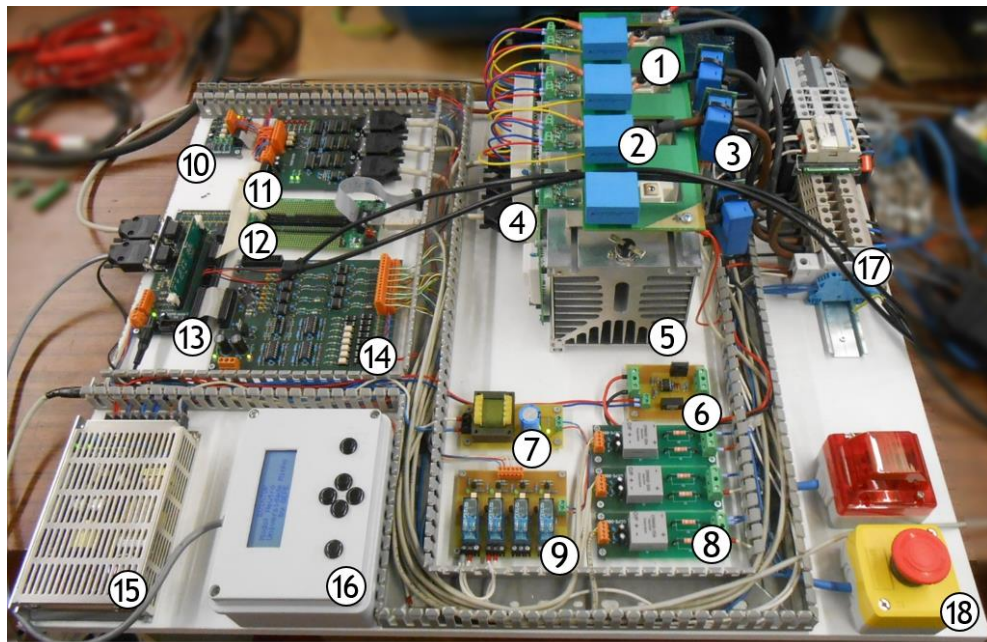
For the pre-charge circuit the three resistances presented in Figure 5.24 are used. Each one has a resistance value of 100 Ω , with a tolerance of 5% and a rated power of 50 W.



Figure 5.24 – Resistances used for the pre-charge circuit (each one with a resistance value of $100\ \Omega \pm 5\%$, 50 W).

5.4. Final Result

The obtained final result of the implemented control system and power stage described in this chapter, is presented in Figure 5.25.



- | | | |
|----------------------|--|-----------------------------|
| ① IGBTs | ⑦ Auxiliar supply for the pre-charge control circuit | ⑬ DSC Board |
| ② Snubber capacitors | ⑧ Voltage sensors | ⑭ Signal conditioning board |
| ③ Current sensors | ⑨ Control board of the pre-charge circuit | ⑮ Auxiliar voltage source |
| ④ IGBT driver | ⑩ Auxiliar control board for error detection | ⑯ HMI |
| ⑤ Heat sink | ⑪ Control board of the IGBT driver | ⑰ Circuit breakers |
| ⑥ DC-bus protection | ⑫ Docking station from Texas (for debug) | ⑱ Emergency stop button |

Figure 5.25 – Final result of the implementation of the proof-of-concept prototype.

During the operation of the three-phase VSI it is possible the presence of high levels of currents flowing. Therefore the VSI was installed upon a heat sink, as presented in

Figure 5.25, which also has a fan attached, providing an easier dissipation of the power losses produced in the form of heat.

There are four modules of IGBTs presented in Figure 5.25. There is one module that appears disconnected in Figure 5.25, this one was installed considering the future implementation of the second stage of the unified topology proposed in this MSc. Thesis, comprising the bidirectional DC-DC converter.

5.5. Conclusions

In this chapter the implementation stage of a proof-of-concept prototype of the proposed unified solution is described.

Initially, the control system implementation is described. It is presented the flowchart describing the control system implemented as a finite-states machine and presented a diagram describing the main components required for the implementation of the digital control system. Then the main hardware components used for the implementation of the control system are presented, containing: (i) Voltage sensors; (ii) Current sensors; (iii) Signal conditioning; (iv) Digital Signal Controller (DSC); (v) Control driver of the Insulated Gate Bipolar Transistors (IGBTs); (vi) Control board for the pre-charge circuit; (vii) Position sensor; (viii) Interface board for the position sensor; (ix) Torque reference; (x) Human-Machine-Interface (HMI).

Afterwards, the power stage implementation is described, in which the following hardware is presented: (i) Three-phase Voltage Source Inverter (VSI); (ii) DC-bus; (iii) Sources and auxiliary loads; (iv) Extra inductor filter; (v) Resistances of the pre-charge circuit.

Finally, the obtained final result of the proof-of-concept topology implemented is presented.

Chapter 6

Experimental Results

6.1. Introduction

In this chapter the main experimental results obtained from the proof-of-concept prototype, whose implementation was described in the previous chapter, are presented and discussed.

The experimental setup developed for the laboratory tests of the proof-of-concept prototype is presented in Figure 6.1.

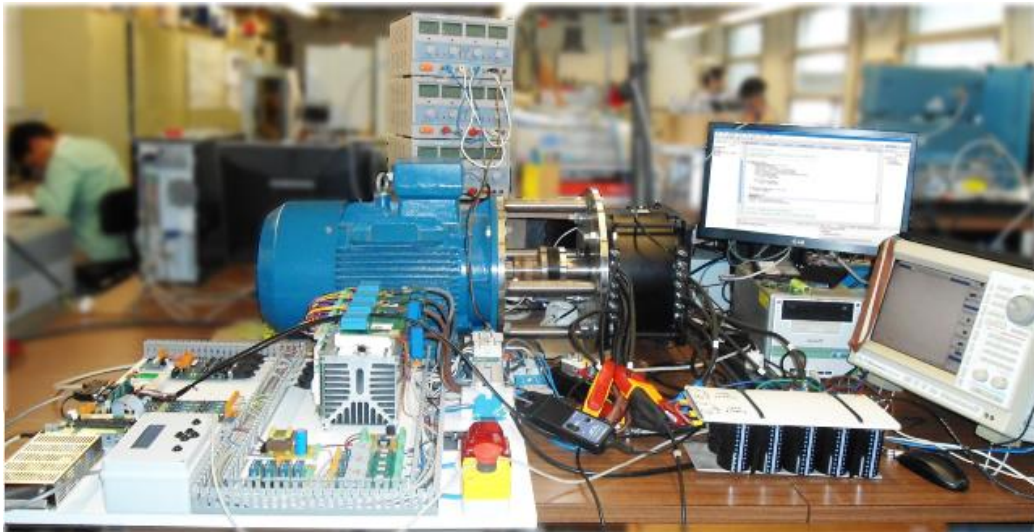


Figure 6.1 – Experimental setup of the proof-of-concept prototype implemented in this MSc. Thesis (for the motor drive mode).

Due to time restrictions it was not possible to test in time all the operation modes proposed. In this chapter the obtained results for the motor drive mode (without mechanical load) and for the slow charging mode (Grid-to-Vehicle operation) are presented.

6.2. Motor Drive Mode

In this section, the main results obtained for the motor drive mode without mechanical load are presented.

The experimental results obtained for the voltages and the currents of the Brushless DC (BLDC) machine are presented in Figure 6.2, for a rotational speed of 220 rpm. These

signals obtained were firstly filtered using a low-pass filter with a cut-off frequency of 500 Hz. The respective waveforms of the voltage at the terminals of the DC-bus and the current flowing are presented in Figure 6.3.

As expected, under these conditions the obtained waveforms of the currents flowing through the electrical machine are highly distorted.

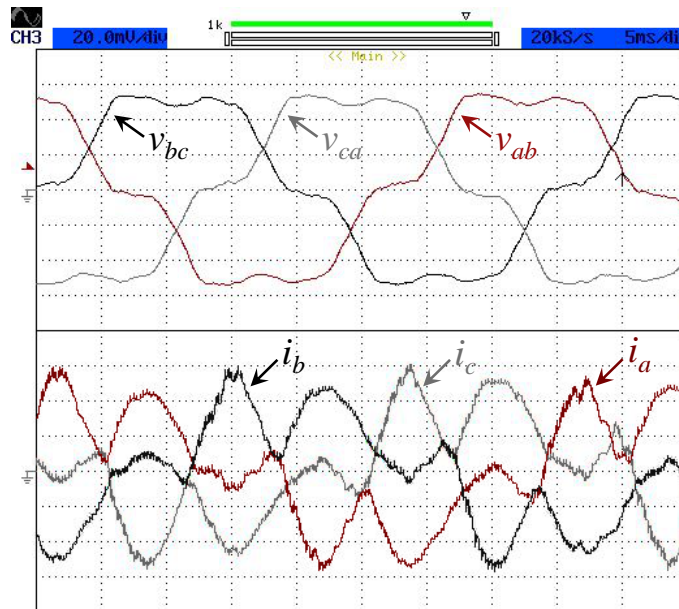


Figure 6.2 – Experimental results of the voltages (20 V/div) and currents (2 A/div) of the BLDC machine, during the motor drive mode, operating without mechanical load.

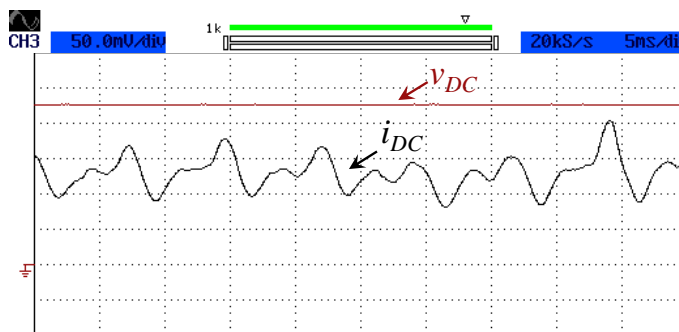


Figure 6.3 – Experimental results of the voltage (20 V/div) and current (5 A/div) of the DC-bus, during the motor drive mode, operating without mechanical load.

6.3. Slow Charging Mode

In this section, the main results obtained for the slow charging mode are presented.

The experimental tests described in this section were performed for a voltage source v_s with a peak value of approximately 45 V and a frequency of 50 Hz.

Such as it was mentioned in Section 4.6.2, the performance of the PLL system has high influence on the obtained results in this mode. Thus, the first experiments were done for evaluate the performance of the PLL system and to tune its parameters. The obtained results during the transitory regime are presented in Figure 6.4, in which is possible to

verify that the PLL system is capable of locking with the source voltage v_s after three cycles, even with a voltage source v_s with some distortions due to the use of the transformers.

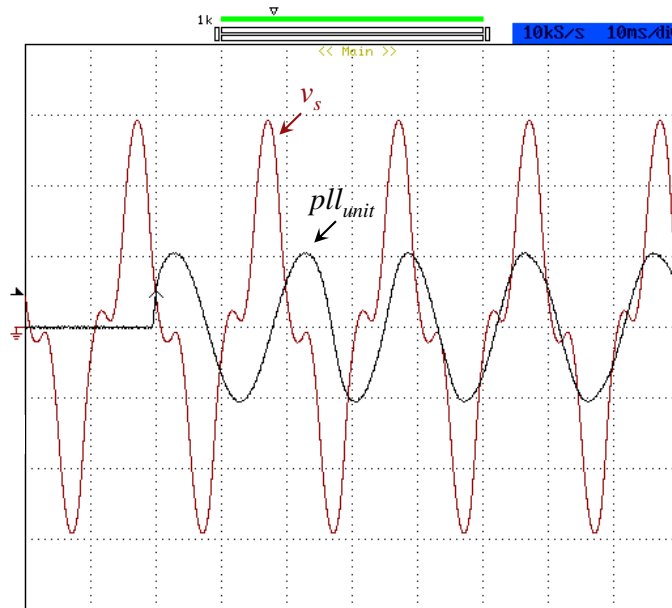


Figure 6.4 – Experimental results of the source voltage v_s (20 V/div) and respective obtained PLL signal (1 V/div), obtained during the transitory regime in the slow charging mode.

After validating the PLL system, the first experiments were performed setting V_{DC_ref} to 80 V. The obtained waveforms of the voltage source v_s , the respective PLL signal pll_{unit} , the current consumed i_s and its reference i_{s_ref} as well as the voltage at the terminals of the DC-bus are presented in Figure 6.5. The harmonic spectrum of i_s as well as its main characteristics are described in Figure 6.6.

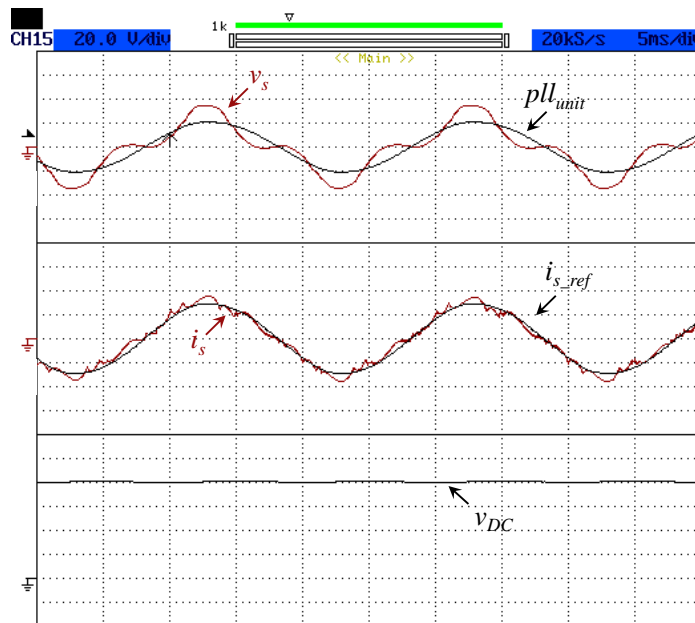


Figure 6.5 – Experimental results of the source voltage v_s (40 V/div) and respective obtained PLL signal (1 V/div), the current consumed i_s (1 A/div) and its respective reference i_{s_ref} (1 A/div) and the voltage at the terminals of the DC-bus (20 V/div), during the slow charging mode with $V_{DC_ref} = 80$ V.

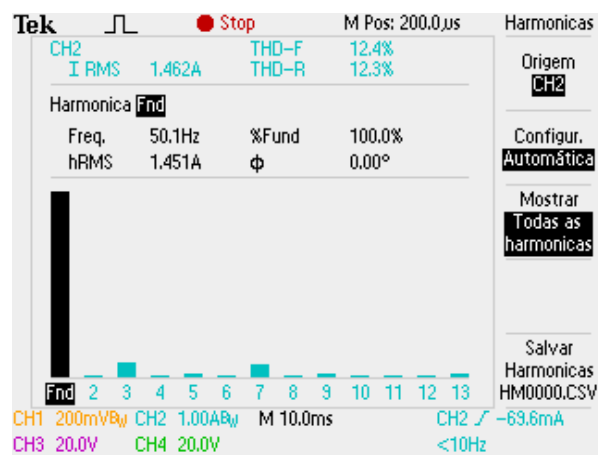


Figure 6.6 – Harmonic spectrum of the current consumed for the slow charging mode with $V_{DC_ref} = 80$ V.

Then, experimental tests setting V_{DC_ref} to 110 V were performed. The obtained waveforms of the system variables are presented in Figure 6.7. The harmonic spectrum as well as the main characteristics obtained for i_s are described in Figure 6.8.

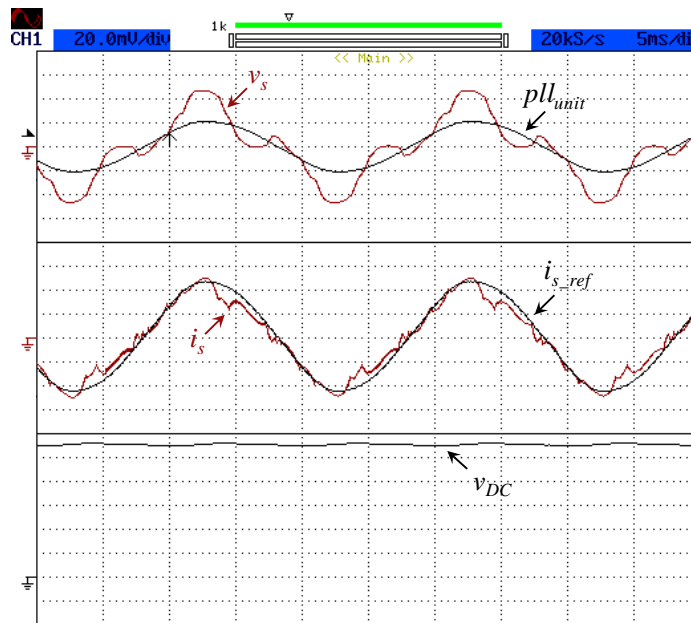


Figure 6.7 – Experimental results of the source voltage v_s (20 V/div) and respective obtained PLL signal (1 V/div), the current consumed i_s (2 A/div) and its respective reference i_{s_ref} (2 A/div) and the voltage at the terminals of the DC-bus (20 V/div), during the slow charging mode with $V_{DC_ref} = 110$ V.

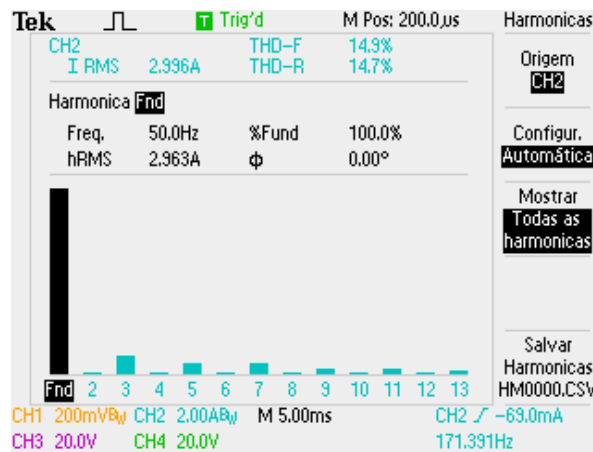


Figure 6.8 – Harmonic spectrum of the current consumed for the slow charging mode with $V_{DC_ref} = 110$ V.

6.4. Conclusions

In this chapter some experimental results obtained from the implemented proof-of-concept prototype of the proposed unified solution are presented.

First the obtained results for the motor drive mode, operating without mechanical load coupled, are presented. The results demonstrate the highly distortion of the waveform of the currents flowing through the electrical machine under those conditions.

Then the obtained results for the slow charging mode are presented. There are some disturbances of the current consumed on tracking its reference due to the low values of the inductances of the inductor filter, as verified in the simulations performed.

The model of the BLDC machine used in the software *PSIM* during the simulations, does not allowed accessing to all the terminals of the stator windings of the machine.

Thus, it was not possible to evaluate the possible physical effects, such as rotor vibrations that could occur due to its use during the battery charging mode.

During the experimental tests performed for the battery charging mode there were no vibrations noticeable on the electrical machine, even being with practically no load coupled. However, it should be noted that this result might also be caused due to the low power of the tests performed and by the fact that for the slow charging mode not all the windings of the electrical machine are used.

The obtained experimental results, despite not being completed yet, allows for validate experimentally some of the operation modes of the solution proposed in this MSc. Thesis.

Chapter 7

Conclusions

7.1. Main achievements

This MSc. Thesis had the purpose of develop a unified motor drive and battery charger applied to Electric Vehicles (EVs), in order to contribute to optimize the space, weight and cost of the power electronics components on-board the vehicle, while also providing a faster charging operation.

First, the main unified solutions proposed by the scientific community were studied, based on the use of the power electronics components of the motor drive system during the battery charging operation.

The majority of the unified solutions reported does not provide battery charging with galvanic isolation, due to the space and weight restrictions on-board the vehicle. In this MSc. Thesis two kinds of topologies were distinguished: the ones that use the power electronics converters of the motor drive system (defined as level-1 solutions) and the ones that, besides the power electronics converters, also employ the electrical machine of the motor drive system (defined as level-2 solutions).

The level-2 solutions allow maximizing the unification process. However, the implementation of this kind of solutions must consider the type of electrical machine used as well as its inductances' values. An electrical machine capable of operate asynchronously or with low values of inductances on its windings, might compromise the requirements of the unification.

Hence, the level-1 solutions despite the lower integration, are the ones that have typically a higher potentiality of application, since its effectiveness for the battery charging mode is not dependent on the characteristics of the electrical machine used. However, typically for the fast charging mode these solutions require high-current inductors, compromising the space optimization required.

Unified solutions providing battery charging with galvanic isolation are typically based on using a special type of electrical machine. Typically, the electrical machine is used as transformer and its effectiveness is compromised by its air gap. However, the solution of using a split-windings Permanent Magnet Synchronous Machine (PMSM), discussed in Section 2.3, seems to overcome those restrictions and allow the effectiveness

of the operation. However, it is important to note the limitations that this solution might impose in the range of the EV.

In this MSc. Thesis a level-2 solution was chosen, based on the use of the three-phase Voltage Source Inverter (VSI), typically installed for the motor drive system of EVs, as well as the windings of the electrical machine, during the battery charging mode, operating the set as a boost active AC-DC converter.

The respective control algorithms that allow manage the proposed solution in each operation mode were studied. For the motor drive mode the Field-Oriented Control (FOC) was chosen, while for the battery charging mode two control algorithms were chosen based on the Model Predictive Control (MPC).

Afterwards, there were performed simulation tests of the proposed solution and implemented a proof-of-concept prototype.

The obtained results demonstrated that the performance of the solution chosen for the battery charging mode is highly dependent on the characteristics of the electrical machine used, especially in what is referred to the values of the inductances of its windings. In this case, the inductances of the windings of the electrical machine used were not sufficiently high for a proper battery charging operation. Hence, it was necessary to add an extra input inductor filter, which compromises the space optimization intended. The preferable alternative would it be increase the switching frequency and, eventually, use Metal Oxide Semiconductor Field Effect Transistors (MOSFETs). However, in this case, the option of adding an extra input inductor filter was chosen due to the restrictions of the hardware available in our laboratory.

Despite the low value of the inductances of the extra inductor filter proposed (3 mH), for the fast charging mode high values of currents are obtained, requiring high-current inductors.

The obtained experimental results, despite not being completed yet, allowed validating experimentally some of the operation modes of the unified solution proposed in this MSc. Thesis.

One important result achieved in this MSc. Thesis is that the control algorithm chosen for the fast charging mode resulted in a unified topology for EVs, providing the additional feature of operating as a reactive power compensator. Despite this feature was not initially defined as a requirement for this MSc. Thesis, it represents an important contribute, increasing the capabilities of the EVs and their potential role in order to contribute to improve the power quality of the electrical grid.

In addition to a unified hardware system, it would also be possible to develop a unified control system since the FOC and the Direct Current Control based on Synchronous Reference Frame (DCC-SRF), described in Section 3.3.1, have very similarities. However, in this case for the battery charging mode it was chosen to use a different control algorithm, having more robustness and capable of being more easily modified to accommodate possible disturbances, related to the use of the electrical machine during the battery charging operation.

7.2. Future Work

First of all it is proposed to continue with the experimental tests, in order to validate the proposed solution and respective control algorithms for all the operation modes considered in the proof-of-concept prototype implemented in this MSc. Thesis.

Additionally, some other activities are proposed for a more complete analysis of the unified solution proposed in this MSc. Thesis, such as:

- Study the impact on the behavior of the electrical machine, when it is used during the battery charging, considering the use of specialized software, such as the *ANSYS*, for evaluate aspects such as the magnetic flux distribution and the thermal characteristics.
- Evaluate the possibility of use the position sensor of the motor drive system in the battery charging system, to attenuate disturbances caused by the variation of the inductances of the windings, considering the use of electrical machines projected with high values of inductances. One solution might be the modification of the control system for the battery charging, so that the predictive model considers the individual values of the inductances per phase (instead of considering all the inductances as having the same value). These values would be attributed at the beginning of the battery charging operation, through the measurement of the rotor angle and using a look-up table containing the inductance values previously measured for a range of rotor angles or the mathematical expressions studied in Section 2.2.2.

The achieved results demonstrate that, despite the potentialities of the proposed unified solution, the electrical machine used in this MSc. Thesis does allow achieving totally the intended results. Thus, since the electrical machine has two stators, it is proposed evaluate the possibility of using this feature to achieve isolated battery charging.

Considering that the Brushless DC (BLDC) machine used in this MSc. Thesis is intended to be implemented in a real EV and under the hardware limits of the maximum switching frequency, it is proposed the solution presented in Figure 7.1. For allowing optimize the size and weight of the power electronics components on-board the vehicle only one high-current inductor of the filter would it be included on-board the vehicle, providing slow charging, through an AC single-phase grid supply. The two other inductors required for the fast charging would it be installed in a dedicated supply equipment connected to a three-phase electrical grid.

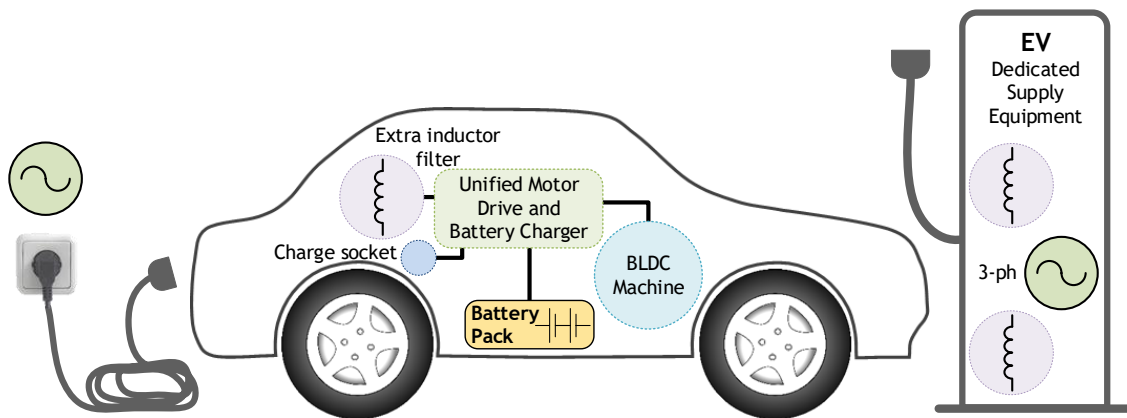


Figure 7.1 – Proposed solution for a unified motor drive and battery charger, considering an EV with the BLDC machine used in this MSc. Thesis.

References

- [1] “World Population Prospects: The 2012 Revision,” *United Nations, Department of Economic and Social Affairs, Population Division*, 2013. [Online]. Available: <http://esa.un.org/unpd/wpp/Excel-Data/population.htm>. [Accessed: 30-Oct-2014].
- [2] OECD/IEA, “Transport,” 2015. [Online]. Available: <https://www.iea.org/aboutus/faqs/transport/>. [Accessed: 01-Nov-2014].
- [3] C. C. Chan, “The State of the Art of Electric and Hybrid Vehicles,” *Proc. IEEE*, vol. 90, no. 2, pp. 247–275, 2002, ISSN: 00189219, doi: 10.1109/5.989873.
- [4] M. Tran, D. Banister, J. D. K. Bishop, and M. D. McCulloch, “Simulating early adoption of alternative fuel vehicles for sustainability,” *Technol. Forecast. Soc. Change*, vol. 80, no. 5, pp. 865–875, Jun. 2013, ISSN: 00401625, doi: 10.1016/j.techfore.2012.09.009.
- [5] M. Ehsani, Y. Gao, S. E. Gay, and A. Emadi, “Environmental Impact and History of Modern Transportation,” in *Modern Electric, Hybrid Electric, and Fuel Cell Vehicles: Fundamentals, Theory, and Design*, CRC Press LLC, Ed. 2005, ISBN: 0-8493-3154-4.
- [6] L. Wang, J. Liang, G. Xu, K. Xu, and Z. Song, “A Novel Battery Charger for Plug-in Hybrid Electric Vehicles,” in *2012 IEEE International Conference on Information and Automation*, 2012, no. June, pp. 168–173, ISBN: 978-1-4673-2237-9, doi: 10.1109/ICInfA.2012.6246802.
- [7] J. Larminie and J. Lowry, “Developments Towards the End of the 20th Century,” in *Electric Vehicle Technology Explained*, J. W. & S. Ltd, Ed. 2003, ISBN: 0-470-85163-5.
- [8] S. E. de Lucena, “A Survey on Electric and Hybrid Electric Vehicle Technology,” in *Electric Vehicles - The Benefits and Barriers*, InTech, 2011, pp. 1–18, ISBN: 9789533072876, doi: 10.5772/18046.
- [9] C. C. Chan and K. T. Chau, “An Overview of Power Electronics in Electric Vehicles,” *IEEE Trans. Ind. Electron.*, vol. 44, no. 1, pp. 3–13, 1997, ISSN: 02780046, doi: 10.1109/41.557493.
- [10] C. E. Sandy Thomas, “How green are electric vehicles?,” *Int. J. Hydrogen Energy*, vol. 37, no. 7, pp. 6053–6062, Apr. 2012, ISSN: 03603199, doi: 10.1016/j.ijhydene.2011.12.118.
- [11] R. T. Doucette and M. D. McCulloch, “Modeling the CO₂ emissions from battery electric vehicles given the power generation mixes of different countries,” *Energy Policy*, vol. 39, no. 2, pp. 803–811, Feb. 2011, ISSN: 03014215, doi: 10.1016/j.enpol.2010.10.054.

- [12] M. Yilmaz and P. T. Krein, "Review of Battery Charger Topologies, Charging Power Levels, and Infrastructure for Plug-In Electric and Hybrid Vehicles," *IEEE Trans. Power Electron.*, vol. 28, no. 5, pp. 2151–2169, May 2013, ISSN: 0885-8993, doi: 10.1109/TPEL.2012.2212917.
- [13] Y. J. Lee, A. Khaligh, and A. Emadi, "Advanced Integrated Bidirectional AC/DC and DC/DC Converter for Plug-In Hybrid Electric Vehicles," *IEEE Trans. Veh. Technol.*, vol. 58, no. 8, pp. 3970–3980, 2009, ISSN: 00189545, doi: 10.1109/TVT.2009.2028070.
- [14] V. Monteiro, J. C. Ferreira, G. Pinto, D. Pedrosa, and J. L. Afonso, "iV2G Charging Platform," *13th Int. IEEE Conf. Intell. Transp. Syst.*, pp. 409–414, Sep. 2010, doi: 10.1109/ITSC.2010.5625255.
- [15] D. M. Bellur and M. K. Kazimierczuk, "DC-DC Converters for Electric Vehicle Applications," in *2007 Electrical Insulation Conference and Electrical Manufacturing Expo*, 2007, pp. 286–293, doi: 10.1109/EEIC.2007.4562633.
- [16] J. Larminie and J. Lowry, "The Relative Decline of Electric Vehicles after 1910," in *Electric Vehicle Technology Explained*, John Wiley & Sons Ltd, Ed. 2003, ISBN: 0-470-85163-5.
- [17] C. C. Chan, "The State of the Art of Electric, Hybrid, and Fuel Cell Vehicles," *Proc. IEEE*, vol. 95, no. 4, 2007, ISSN: 0018-9219, doi: 10.1109/JPROC.2007.892489.
- [18] M. Dijk, R. J. Orsato, and R. Kemp, "The emergence of an electric mobility trajectory," *Energy Policy*, vol. 52, pp. 135–145, Jan. 2013, ISSN: 03014215, doi: 10.1016/j.enpol.2012.04.024.
- [19] M. Zaja, M. Oprea, C. Gomez Suarez, and L. Mathe, "Electric Vehicle Battery Charging Algorithm Using PMSM Windings and an Inverter as an Active Rectifier," in *2014 IEEE Vehicle Power and Propulsion Conference (VPPC)*, 2014, pp. 1–6, doi: 10.1109/VPPC.2014.7007057.
- [20] L. De Sousa, B. Silvestre, and B. Bouchez, "A Combined Multiphase Electric Drive and Fast Battery Charger for Electric Vehicles," in *2010 IEEE Vehicle Power and Propulsion Conference*, 2010, pp. 1–6, ISBN: 978-1-4244-8220-7, doi: 10.1109/VPPC.2010.5729057.
- [21] H. Ye, Y. Yang, and A. Emadi, "Traction Inverters in Hybrid Electric Vehicles," *2012 IEEE Transp. Electrification Conf. Expo, ITEC 2012*, ISBN: 9781467314077, doi: 10.1109/ITEC.2012.6243442.
- [22] M. Werber, M. Fischer, and P. V. Schwartz, "Batteries: Lower cost than gasoline?," *Energy Policy*, vol. 37, no. 7, pp. 2465–2468, Jul. 2009, ISSN: 03014215, doi: 10.1016/j.enpol.2009.02.045.
- [23] K. Young, C. Wang, L. Y. Wang, and K. Strunz, "Electric Vehicle Battery Technologies," in *Electric Vehicle Integration into Modern Power Networks*, New York, NY: Springer New York, 2013, ISBN: 978-1-4614-0133-9,

- doi: 10.1007/978-1-4614-0134-6.
- [24] J. Larminie and J. Lowry, “Batteries,” in *Electric Vehicle Technology Explained*, John Wiley & Sons Inc, Ed. 2003, ISBN: 0-470-85163-5.
- [25] K. T. Chau, C. C. Chan, and Chunhua Liu, “Overview of Permanent-Magnet Brushless Drives for Electric and Hybrid Electric Vehicles,” *IEEE Trans. Ind. Electron.*, vol. 55, no. 6, pp. 2246–2257, Jun. 2008, ISSN: 0278-0046, doi: 10.1109/TIE.2008.918403.
- [26] W. Lhomme, P. Delarue, X. Kestelyn, P. Sandulescu, and A. Bruyere, “Control of a Combined Multiphase Electric Drive and Battery Charger for Electric Vehicle,” in *2013 15th European Conference on Power Electronics and Applications (EPE)*, 2013, pp. 1–10, ISBN: 978-1-4799-0116-6, doi: 10.1109/EPE.2013.6631890.
- [27] R. Surada and A. Khaligh, “A Novel Approach towards Integration of Propulsion Machine Inverter with Energy Storage Charger in Plug-In Hybrid Electric Vehicles,” in *IECON 2010 - 36th Annual Conference on IEEE Industrial Electronics Society*, 2010, pp. 2493–2498, ISBN: 978-1-4244-5225-5, doi: 10.1109/IECON.2010.5675358.
- [28] S. Haghbin, “Integrated Motor Drives and Battery Chargers for Electric or Plug-in Hybrid Electric Vehicles,” Ph.D. dissertation, Dept. of Energy and Environment, Chalmers University of Technology, Gothenburg, Sweden, 2013.
- [29] S. Ketsingsoi and Y. Kumsuwan, “An Off-line Battery Charger Based on Buck-Boost Power Factor Correction Converter for Plug-in Electric Vehicles,” *Energy Procedia*, vol. 56, pp. 659–666, 2014, ISSN: 18766102, doi: 10.1016/j.egypro.2014.07.205.
- [30] S. Haghbin, K. Khan, S. Lundmark, M. Alakula, O. Carlson, M. Leks, and O. Wallmark, “Integrated Chargers for EV’s and PHEV’s: Examples and New Solutions,” in *The XIX International Conference on Electrical Machines - ICEM 2010*, 2010, pp. 1–6, ISBN: 978-1-4244-4174-7, doi: 10.1109/ICELMACH.2010.5608152.
- [31] S. Dusmez and A. Khaligh, “A Charge-Nonlinear-Carrier-Controlled Reduced-Part Single-Stage Integrated Power Electronics Interface for Automotive Applications,” *IEEE Trans. Veh. Technol.*, vol. 63, no. 3, pp. 1091–1103, Mar. 2014, ISSN: 0018-9545, doi: 10.1109/TVT.2013.2284592.
- [32] R. Maia, M. Silva, R. Ara, and U. Nunes, “Electric Vehicle Simulator for Energy Consumption Studies in Electric Mobility Systems,” 2011, ISBN: 9781457709920.
- [33] M. K. Yoong, Y. H. Gan, G. D. Gan, C. K. Leong, Z. Y. Phuan, B. K. Cheah, and K. W. Chew, “Studies of Regenerative Braking in Electric Vehicle,” *IEEE Conf. Sustain. Util. Dev. Eng. Technol. 2010, STUDENT 2010 - Conf. Bookl.*, no. November, pp. 40–45, 2010, ISBN: 9781424475032, doi: 10.1109/STUDENT.2010.5686984.
- [34] Binggang Cao, Zhifeng Bai, and Wei Zhang, “Research on Control for

- Regenerative Braking of Electric Vehicle,” in *IEEE International Conference on Vehicular Electronics and Safety*, 2005, pp. 92–97, doi: 10.1109/ICVES.2005.1563620.
- [35] D. Pedrosa, V. Monteiro, H. Gonçalves, B. Exposto, J. G. Pinto, and J. L. Afonso, “Conversion of an Internal Combustion Engine Vehicle into an Electric Vehicle,” in *Seminário Anual de Automação, Eletrônica Industrial e Instrumentação 2012*, 2012, pp. 446–451.
- [36] V. Monteiro, D. Pedrosa, and B. Exposto, “Smart Charging System of the Electric Vehicle CEPIUM,” in *Annual Seminar on Automation, Industrial Electronics and Instrumentation 2012 - SAAEI’12*, 2012, pp. 500–505.
- [37] M. Ehsani, Y. Gao, and A. Emadi, “Electric Propulsion Systems,” in *Modern Electric, Hybrid Electric, and Fuel Cell Vehicles: Fundamentals, Theory, and Design*, 2nd ed., C. Press, Ed. p. 152, ISBN: 978-1-4200-5398-2.
- [38] M. Ehsani, Y. Gao, and A. Emadi, “Vehicle Fundamentals,” in *Modern Electric, Hybrid Electric, and Fuel Cell Vehicles: Fundamentals, Theory, and Design*, 2005, p. 395, ISBN: 978-1-4200-5398-2.
- [39] L. Shi, H. Xu, D. Li, and Z. Yuan, “A Novel High Power Factor PWM Rectifier Inverter for Electric Vehicle Charging Station,” in *2011 International Conference on Electrical Machines and Systems*, 2011, pp. 1–6, ISBN: 978-1-4577-1044-5, doi: 10.1109/ICEMS.2011.6073790.
- [40] M. Yilmaz and P. T. Krein, “Review of Integrated Charging Methods for Plug-In Electric and Hybrid Vehicles,” in *2012 IEEE International Conference on Vehicular Electronics and Safety (ICVES 2012)*, 2012, pp. 346–351, ISBN: 978-1-4673-0993-6, doi: 10.1109/ICVES.2012.6294276.
- [41] S. Haghbin, K. Khan, S. Zhao, M. Alaküla, S. Lundmark, and O. Carlson, “An Integrated 20-kW Motor Drive and Isolated Battery Charger for Plug-In Vehicles,” *IEEE Trans. Power Electron.*, vol. 28, no. 8, pp. 4013–4029, 2013, ISSN: 08858993, doi: 10.1109/TPEL.2012.2230274.
- [42] O. Hegazy, J. Van Mierlo, and P. Lataire, “Design and Control of Bidirectional DC/AC and DC/DC Converters for Plug-In Hybrid Electric Vehicles,” in *2011 International Conference on Power Engineering, Energy and Electrical Drives*, 2011, no. May, pp. 1–7, ISBN: 978-1-4244-9845-1, ISSN: 2155-5516, doi: 10.1109/PowerEng.2011.6036530.
- [43] S. Haghbin, S. Lundmark, O. Carlson, and M. Alakula, “A Combined Motor/Drive/Battery Charger Based on a Split-Windings PMSM,” in *2011 IEEE Vehicle Power and Propulsion Conference*, 2011, pp. 1–6, ISBN: 978-1-61284-248-6, doi: 10.1109/VPPC.2011.6043000.
- [44] M. Yilmaz and P. T. Krein, “Review of Charging Power Levels and Infrastructure for Plug-In Electric and Hybrid Vehicles,” *2012 IEEE Int. Electr. Veh. Conf.*, pp. 1–8, Mar. 2012, ISBN: 978-1-4673-1561-6, doi: 10.1109/IEVC.2012.6183208,

- [45] L. Solero, "Nonconventional On-Board Charger for Electric Vehicle Propulsion Batteries," *IEEE Trans. Veh. Technol.*, vol. 50, no. 1, pp. 144–149, 2001, ISSN: 00189545, doi: 10.1109/25.917904.
- [46] S. Dusmez and A. Khaligh, "Cost Effective Solutions to Level 3 On-board Battery Chargers," in *2012 Twenty-Seventh Annual IEEE Applied Power Electronics Conference and Exposition (APEC)*, 2012, pp. 2121–2127, ISBN: 978-1-4577-1216-6, doi: 10.1109/APEC.2012.6166114.
- [47] N. Sakr, D. Sadarnac, and A. Gascher, "A Review Of On-board Integrated Chargers For Electric Vehicles," in *2014 16th European Conference on Power Electronics and Applications*, 2014, pp. 1–10, ISBN: 978-1-4799-3015-9, doi: 10.1109/EPE.2014.6910865.
- [48] V. Monteiro, H. Goncalves, and J. L. Afonso, "Impact of Electric Vehicles on Power Quality in a Smart Grid Context," in *11th International Conference on Electrical Power Quality and Utilisation*, 2011, pp. 1–6, ISBN: 978-1-4673-0378-1, ISSN: 21506647, doi: 10.1109/EPQU.2011.6128861.
- [49] Mobi.E and SGORME, "Postos de Carregamento da Rede Pública Mobi.E," *Associação Portuguesa de Veículos Eléctricos*. [Online]. Available: http://www.apve.pt/upload/docs/lista_postos.pdf. [Accessed: 05-Nov-2014].
- [50] S. Lacroix, "Modélisation et commande d'une chaîne de conversion pour véhicule électrique intégrant la fonction de charge des batteries," Ph.D. dissertation, Université Paris Sud, Paris, France, 2013.
- [51] G. Glanzer, T. Sivaraman, J. I. Buffalo, M. Kohl, and H. Berger, "Cost-efficient Integration of Electric Vehicles with the Power Grid by Means of Smart Charging Strategies and Integrated On-board Chargers," in *2011 10th International Conference on Environment and Electrical Engineering*, 2011, vol. 100205, no. 100205, pp. 1–4, ISBN: 978-1-4244-8779-0, doi: 10.1109/EEEIC.2011.5874709.
- [52] J. G. Pinto, V. Monteiro, H. Goncalves, B. Exposto, D. Pedrosa, C. Couto, and J. L. Afonso, "Bidirectional Battery Charger with Grid-to-Vehicle, Vehicle-to-Grid and Vehicle-to-Home Technologies," in *IECON Proceedings (Industrial Electronics Conference)*, 2013, pp. 5934–5939, ISBN: 9781479902248, ISSN: 1553-572X, doi: 10.1109/IECON.2013.6700108.
- [53] V. Monteiro, H. Goncalves, J. C., and J. L., "Batteries Charging Systems for Electric and Plug-In Hybrid Electric Vehicles," in *New Advances in Vehicular Technology and Automotive Engineering*, InTech, 2012, pp. 149–168, ISBN: 9789535106982, doi: 10.5772/45791.
- [54] S. Haghbin, S. Lundmark, M. Alakula, and O. Carlson, "Grid-Connected Integrated Battery Chargers in Vehicle Applications: Review and New Solution," *IEEE Trans. Ind. Electron.*, vol. 60, no. 2, pp. 459–473, Feb. 2013, ISBN: 0278-0046 VO - 60, ISSN: 0278-0046, doi: 10.1109/TIE.2012.2187414.
- [55] K. Khan, S. Haghbin, M. Leksell, and O. Wallmark, "Design and Performance Analysis of a Permanent-Magnet Assisted Synchronous Reluctance Machine for an Integrated Charger Application," in *The XIX International Conference on*

- Electrical Machines - ICEM 2010*, 2010, pp. 1–6, ISBN: 978-1-4244-4174-7, doi: 10.1109/ICELMACH.2010.5607905.
- [56] A. Bruyere, L. De Sousa, B. Bouchez, P. Sandulescu, X. Kestelyn, and E. Semail, “A Multiphase Traction/Fast-Battery-Charger Drive for Electric or Plug-in Hybrid Vehicles: Solutions for Control in Traction Mode,” in *2010 IEEE Vehicle Power and Propulsion Conference*, 2010, pp. 1–7, ISBN: 978-1-4244-8220-7, doi: 10.1109/VPPC.2010.5729220.
- [57] S. Haghbin and I. S. Guillen, “Integrated Motor Drive and Non-Isolated Battery Charger Based on the Torque Cancellation in the Motor,” in *2013 IEEE 10th International Conference on Power Electronics and Drive Systems (PEDS)*, 2013, pp. 824–829, ISBN: 978-1-4673-1792-4, doi: 10.1109/PEDS.2013.6527131.
- [58] M. C. B. P. Rodrigues, I. D. N. Souza, A. A. Ferreira, P. G. Barbosa, and H. A. C. Braga, “Simultaneous Active Power Filter and G2V (or V2G) Operation of EV On-Board Power Electronics,” in *IECON 2013 - 39th Annual Conference of the IEEE Industrial Electronics Society*, 2013, pp. 4684–4689, ISBN: 978-1-4799-0224-8, doi: 10.1109/IECON.2013.6699891.
- [59] J. D. V. de Carvalho, “Desenvolvimento de um Controlador com DSP para um Motor CA de 30 kW para o CEPIUM,” M.S. thesis, Dept. Industrial. Electronics, University of Minho, Guimarães, Portugal, 2013.
- [60] B. Singh, B. N. Singh, A. Chandra, K. Al-Haddad, A. Pandey, and D. P. Kothari, “A Review of Three-Phase Improved Power Quality AC-DC Converters,” *IEEE Trans. Ind. Electron.*, vol. 51, no. 3, pp. 641–660, Jun. 2004, ISSN: 0278-0046, doi: 10.1109/TIE.2004.825341.
- [61] F. Lacressonniere and B. Cassoret, “Converter used as a battery charger and a motor speed controller in an industrial truck,” in *2005 European Conference on Power Electronics and Applications*, 2005, vol. 9, p. 7 pp.–P.7, ISBN: 90-75815-09-3, doi: 10.1109/EPE.2005.219286.
- [62] S. Dusmez, C. Chen, and A. Khaligh, “A Reduced-Part Single Stage Direct AC/DC On-board Charger for Automotive Applications,” in *2013 Twenty-Eighth Annual IEEE Applied Power Electronics Conference and Exposition (APEC)*, 2013, pp. 1791–1797, ISBN: 978-1-4673-4355-8, doi: 10.1109/APEC.2013.6520538.
- [63] S. Lacroix, E. Laboure, and M. Hilairet, “An Integrated Fast Battery Charger for Electric Vehicle,” in *2010 IEEE Vehicle Power and Propulsion Conference*, 2010, pp. 1–6, ISBN: 978-1-4244-8220-7, doi: 10.1109/VPPC.2010.5729063.
- [64] A. E. Fitzgerald, C. Jr. Kingsley, and D. S. Umans, “C.2 Basic Synchronous-Machine Relations in dq0 Variables,” in *Electric Machinery*, Sixth Edit., McGraw-Hill, ISBN: 0-07-112193-5.
- [65] G.-J. Su and L. Tang, “A New Integrated Onboard Charger and Accessory Power Converter for Plug-in Electric Vehicles,” in *2014 IEEE Energy Conversion Congress and Exposition (ECCE)*, 2014, pp. 4790–4796, ISBN: 978-1-4799-5776-7, doi: 10.1109/ECCE.2014.6954057.

- [66] A. G. Cocconi, “Combined Motor Drive and Battery Recharge System,” U.S. Patent 5 341 075, Aug. 23, 1994.
- [67] S. Ozcira, N. Bekiroglu, and E. Aycicek, “Speed Control of Permanent Magnet Synchronous Motor Based on Direct Torque Control Method,” in *2008 International Symposium on Power Electronics, Electrical Drives, Automation and Motion*, 2008, pp. 268–272, ISBN: 978-1-4244-1663-9, doi: 10.1109/SPEEDHAM.2008.4581072.
- [68] D. Pedrosa, H. Goncalves, B. Exposto, J. S. Martins, and J. L. Afonso, “A Simplified Methodology for Parameters Measurement of an Axial Flux Permanent Magnet Motor Without Neutral Point,” in *IECON Proceedings (Industrial Electronics Conference)*, 2012, pp. 1637–1642, ISBN: 9781467324212, doi: 10.1109/IECON.2012.6388730.
- [69] D. Pedrosa, J. Carvalho, H. Goncalves, V. Monteiro, A. Fernandes, and J. L. Afonso, “Field Oriented Control of an Axial Flux Permanent Magnet Synchronous Motor for Traction Solutions,” in *IECON 2014 - 40th Annual Conference of the IEEE Industrial Electronics Society*, 2014, pp. 1466–1472, ISBN: 978-1-4799-4032-5, doi: 10.1109/IECON.2014.7048695.
- [70] G.-Y. Choe, J.-S. Kim, and B.-K. Lee, “Comparison of Integrated Battery Chargers for Plug-In Hybrid Electric Vehicles: Topology and Control,” *2011 IEEE Int. Electr. Mach. Drives Conf.*, pp. 1294–1299, May 2011, ISBN: 978-1-4577-0060-6, doi: 10.1109/IEMDC.2011.5994791.
- [71] G. Pellegrino, E. Armando, and P. Guglielmi, “Integrated Battery Charger for Electric Scooter,” *2009 13th Eur. Conf. Power Electron. Appl.*, 2009, ISBN: 978-1-4244-4432-8.
- [72] N. Mohan, T. M. Undeland, and W. P. Robbins, “Step-Up (Boost) Converter,” in *Power Electronics: Converters, Applications, and Design*, Wiley, 1995, ISBN: 978-0471584087.
- [73] W. E. Rippel and A. G. Cocconi, “Integrated Motor Drive and Recharge System,” U.S. Patent 5 009 186, Mar. 24, 1992.
- [74] S. Haghbin, T. Thiringer, and O. Carlson, “An Integrated Split-Phase Dual-Inverter Permanent Magnet Motor Drive and Battery Charger for Grid-Connected Electric or Hybrid Vehicles,” in *2012 XXth International Conference on Electrical Machines*, 2012, pp. 1941–1947, ISBN: 978-1-4673-0142-8, doi: 10.1109/ICEIMach.2012.6350147.
- [75] S. Haghbin, M. Alakula, K. Khan, S. Lundmark, M. Leksell, O. Wallmark, and O. Carlson, “An Integrated Charger for Plug-in Hybrid Electric Vehicles Based on a Special Interior Permanent Magnet Motor,” in *2010 IEEE Vehicle Power and Propulsion Conference*, 2010, pp. 1–6, ISBN: 978-1-4244-8220-7, doi: 10.1109/VPPC.2010.5729071.
- [76] R. Carrow S., *Electrician’s Technical Reference: Variable frequency drives*. Delmar Cengage Learning, 2001, ISBN: 978-0766819238.

- [77] X. del T. Garcia, B. Zigmund, A. A. Terlizzi, R. Pavlanin, and L. Salvatore, "Comparison between FOC and DTC Strategies for Permanent Magnet Synchronous Motors," *Adv. Electr. Electron. Eng.*, vol. 5, no. 1, pp. 76–81, 2006, doi: 10.15598/aeec.v5i1-2.179.
- [78] K. H. Harib, E. A. Khousa, and A. Ismail, "Field oriented motion control of a 3-phase permanent magnet synchronous motor," in *2011 2nd International Conference on Electric Power and Energy Conversion Systems (EPECS)*, 2011, vol. 17555, pp. 1–7, ISBN: 978-1-4577-0806-0, doi: 10.1109/EPECS.2011.6126797.
- [79] J. Khodabakhsh, "DTC in Contrast to FOC on Power train of Hybrid Electrical Vehicle," no. 1, pp. 2–5, 2012, ISBN: 9891262022.
- [80] E. Simon, "Implementation of a Speed Field Oriented Control of 3-phase PMSM Motor using TMS320F240," 1999. [Online]. Available: <http://www.ti.com/lit/an/spra588/spra588.pdf>. [Accessed: 10-Dec-2014].
- [81] A. Faiz, N. Azam, A. Jidin, M. A. Said, H. Jopri, and M. Manap, "High Performance Torque Control of BLDC Motor," pp. 1093–1098, 2013, ISBN: 9781479914470.
- [82] Texas Instruments, "Field Orientated Control of 3-Phase AC-Motors," 1998. [Online]. Available: <http://www.ti.com/lit/an/bpra073/bpra073.pdf>. [Accessed: 10-Dec-2014].
- [83] A. Gupta, T. Kim, T. Park, and C. Lee, "Intelligent Direct Torque Control of Brushless DC Motors for Hybrid Electric Vehicles," pp. 116–120, 2009, ISBN: 9781424426010.
- [84] C. Bian, S. Ren, and L. Ma, "Sensorless DTC of Super High-speed PMSM," in *2007 IEEE International Conference on Automation and Logistics*, 2007, pp. 3060–3064, ISBN: 978-1-4244-1530-4, doi: 10.1109/ICAL.2007.4339107.
- [85] S. B. Ozturk and H. a. Toliyat, "Direct Torque Control of Brushless DC Motor with Non-sinusoidal Back-EMF," *2007 IEEE Int. Electr. Mach. Drives Conf.*, pp. 165–171, 2007, ISBN: 1-4244-0742-7, doi: 10.1109/IEMDC.2007.383571.
- [86] Wang Xu, Huang Kaizheng, Yan Shijie, and Xu Bin, "Simulation of three-phase voltage source PWM rectifier based on the Space Vector Modulation," in *2008 Chinese Control and Decision Conference*, 2008, pp. 1881–1884, ISBN: 978-1-4244-1733-9, doi: 10.1109/CCDC.2008.4597650.
- [87] Y. Ye, M. Kazerani, and V. H. Quintana, "A novel modeling and control method for three-phase PWM converters," in *2001 IEEE 32nd Annual Power Electronics Specialists Conference (IEEE Cat. No.01CH37230)*, 2001, vol. 1, pp. 102–107, ISBN: 0-7803-7067-8, ISSN: 0275-9306, doi: 10.1109/PESC.2001.954002.
- [88] M. P. Kazmierkowski and L. Malesani, "Current control techniques for three-phase voltage-source PWM converters: a survey," *IEEE Trans. Ind. Electron.*, vol. 45, no. 5, pp. 691–703, 1998, ISSN: 02780046, doi: 10.1109/41.720325.

- [89] C. Fitzer, V. K. Ramachandaramurthy, A. Arulampalam, M. Barnes, and N. Jenkins, "Software phase-locked loop applied to dynamic voltage restorer (DVR)," *2001 IEEE Power Eng. Soc. Winter Meet. Conf. Proc. (Cat. No.01CH37194)*, vol. 3, no. C, pp. 1033–1038, 2001, ISBN: 0-7803-6672-7, doi: 10.1109/PESW.2001.917210.
- [90] S. a O. Da Silva, E. Tomizaki, R. Novochadlo, and E. A. A. Coelho, "PLL structures for utility connected systems under distorted utility conditions," *IECON Proc. (Industrial Electron. Conf.)*, pp. 2636–2641, 2006, ISBN: 1424401364, ISSN: 1553-572X, doi: 10.1109/IECON.2006.347416.
- [91] L. G. B. Rolim, D. R. Da Costa, and M. Aredes, "Analysis and software implementation of a robust synchronizing PLL circuit based on the pq theory," *IEEE Trans. Ind. Electron.*, vol. 53, no. 6, pp. 1919–1926, 2006, ISSN: 02780046, doi: 10.1109/TIE.2006.885483.
- [92] M. Karimi-Ghartemani and M. R. Iravani, "A new phase-locked loop (PLL) system," *Proc. 44th IEEE 2001 Midwest Symp. Circuits Syst. MWSCAS 2001 (Cat. No.01CH37257)*, vol. 1, pp. 5–8, 2001, ISBN: 0-7803-7150-X, doi: 10.1109/MWSCAS.2001.986202.
- [93] H. Zhang, C. Dai, and S. Wu, "Research on Single-Phase PLL for the Synchronization of Thyristor Controlled Series Capacitor," in *2012 Asia-Pacific Power and Energy Engineering Conference*, 2012, pp. 1–5, ISBN: 978-1-4577-0547-2, ISSN: 2157-4839, doi: 10.1109/APPEEC.2012.6307295.
- [94] M. Karimi-Ghartemani and M. R. Iravani, "A nonlinear adaptive filter for online signal analysis in power systems: Applications," *IEEE Trans. Power Deliv.*, vol. 17, no. 2, pp. 617–622, 2002, ISSN: 08858977, doi: 10.1109/61.997949.
- [95] V. Monteiro, J. G. Pinto, B. Exposto, J. C. Ferreira, and J. L. Afonso, "Smart Charging Management for Electric Vehicle Battery Chargers," in *2014 IEEE Vehicle Power and Propulsion Conference (VPPC)*, 2014, pp. 1–5, ISBN: 978-1-4799-6783-4, doi: 10.1109/VPPC.2014.7007133.
- [96] M. Karimi-Ghartemani and A. K. Ziarani, "Periodic orbit analysis of two dynamical systems for electrical engineering applications," *J. Eng. Math.*, vol. 45, no. 2, pp. 135–154, 2003, ISBN: 00220833, doi: 10.1023/A:1022124027718.
- [97] E. M. Sasso, G. G. Sotelo, a a Ferreira, E. H. Watanabe, M. Aredes, and P. G. Barbosa, "Investigaçao dos modelos de circuitos de sincronismo trifásicos baseados na teoria das potências real e imaginária instantâneas (p-pll e q-pll)," *An. do CBA*, no. 1, pp. 480–485, 2002, doi: 10.13140/2.1.2663.5203.
- [98] H. Akagi, Y. Kanazawa, and A. Nabae, "Instantaneous Reactive Power Compensators Comprising Switching Devices without Energy Storage Components," *IEEE Trans. Ind. Appl.*, vol. IA-20, no. 3, pp. 625–630, 1984, ISSN: 0093-9994, doi: 10.1109/TIA.1984.4504460.
- [99] E. Wantanabe, R. Stephan, and M. Aredes, "New concepts of instantaneous active and reactive powers in electrical systems with generic loads," *IEEE Trans. Power Deliv.*, vol. 8, no. 2, pp. 697–703, 1993, ISSN: 0885-8977,

- doi: 10.1109/61.216877.
- [100] F. D. Freijedo, J. Doval-Gandoy, Ó. López, D. Piñeiro, C. M. Peñalver, and A. a. Nogueiras, “Real-time implementation of a SPLL for FACTS,” *IECON Proc. (Industrial Electron. Conf.)*, pp. 2390–2395, 2006, ISBN: 1424401364, ISSN: 1553-572X, doi: 10.1109/IECON.2006.347484.
- [101] P. Rodríguez, J. Pou, J. Bergas, J. I. Candela, R. P. Burgos, and D. Boroyevich, “Decoupled Double Synchronous Reference Frame PLL for Power Converters Control,” *IEEE Trans. Power Electron.*, vol. 22, no. 2, pp. 584–592, 2007, ISBN: 0780390334, ISSN: 08858993, doi: 10.1109/TPEL.2006.890000.
- [102] M. Bhardwaj, “Software Phased-Locked Loop Design Using C2000™ Microcontrollers for Single Phase Grid Connected Inverter,” *Application Report*, 2013. [Online]. Available: <http://www.ti.com/lit/an/sprabt3/sprabt3.pdf>. [Accessed: 05-Apr-2015].
- [103] L. R. Limongi, R. Bojoi, C. Pica, F. Profumo, and A. Tenconi, “Analysis and Comparison of Phase Locked Loop Techniques for Grid Utility Applications,” *Fourth Power Convers. Conf. PCC-NAGOYA 2007 - Conf. Proc.*, pp. 674–681, 2007, ISBN: 142440844X, doi: 10.1109/PCCON.2007.373038.
- [104] J. Rodriguez, P. Cortes, R. Kennel, and M. P. Kazmierkowski, “Model Predictive Control - A Simple and Powerful Method to Control Power Converters,” *2009 IEEE 6th Int. Power Electron. Motion Control Conf.*, vol. 56, no. 6, pp. 1826–1838, 2009, ISBN: 978-1-4244-3556-2, doi: 10.1109/IPEMC.2009.5289335.
- [105] M. Parvez, S. Mekhilef, N. M. L. Tan, and H. Akagi, “Model Predictive Control of a Bidirectional AC-DC Converter for V2G and G2V Applications in Electric Vehicle Battery Charger,” *2014 IEEE Transp. Electrification Conf. Expo*, pp. 1–6, 2014, ISBN: 978-1-4799-2262-8, doi: 10.1109/ITEC.2014.6861795.
- [106] J. Rodriguez, M. P. Kazmierkowski, J. R. Espinoza, P. Zanchetta, H. Abu-Rub, H. a Young, and C. a Rojas, “State of the Art of Finite Control Set Model Predictive Control in Power Electronics,” *Ind. Informatics, IEEE Trans.*, vol. 9, no. 2, pp. 1003–1016, 2013, ISSN: 1551-3203, doi: 10.1109/TII.2012.2221469.
- [107] A. Bouafia, J.-P. Gaubert, and F. Krim, “Design and implementation of predictive current control of three-phase PWM rectifier using space-vector modulation (SVM),” *Energy Convers. Manag.*, vol. 51, no. 12, pp. 2473–2481, 2010, ISSN: 01968904, doi: 10.1016/j.enconman.2010.05.010.
- [108] J. Wang, H. Nademi, and L. Norum, “Control of Input Current Harmonics and Output Voltage of Three-phase Voltage Source PWM Rectifier Using Model Predictive Control,” in *2013 IEEE International Symposium on Industrial Electronics*, 2013, pp. 1–6, ISBN: 978-1-4673-5193-5, doi: 10.1109/ISIE.2013.6563634.
- [109] P. Cortes, J. Rodriguez, P. Antoniewicz, and M. Kazmierkowski, “Direct Power Control of an AFE Using Predictive Control,” *IEEE Trans. Power Electron.*, vol. 23, no. 5, pp. 2516–2523, 2008, ISSN: 0885-8993, doi: 10.1109/TPEL.2008.2002065.

- [110] S. A. Middlebrooks and J. B. Rawlings, "Model Predictive Control of Single Phase Grid-connected Inverter," *IEEE Trans. Semicond. Manuf.*, vol. 20, no. 2, pp. 114–125, May 2007, ISBN: 0780374908, doi: 10.1109/TSM.2007.895203.
- [111] J. S. Moon, J. H. Lee, I. Y. Ha, T. K. Lee, and C. Y. Won, "An Efficient Battery Charging Algorithm based on State-of-Charge Estimation for Electric Vehicle," *2011 Int. Conf. Electr. Mach. Syst. ICEMS 2011*, 2011, ISBN: 9781457710445, doi: 10.1109/ICEMS.2011.6073783.
- [112] D. Patrick, R. and S. Fardo, W., "Resistance, Inductance, and Capacitance in AC Circuits," in *Understanding AC Circuits*, Newnes, 2000, ISBN: 978-0750671033.
- [113] S. M. Mousavi G. and M. Nikdel, "Various battery models for various simulation studies and applications," *Renew. Sustain. Energy Rev.*, vol. 32, pp. 477–485, 2014, ISSN: 13640321, doi: 10.1016/j.rser.2014.01.048.
- [114] O. Tremblay, L.-A. Dessaint, and A.-I. Dekkiche, "A Generic Battery Model for the Dynamic Simulation of Hybrid Electric Vehicles," *2007 IEEE Veh. Power Propuls. Conf.*, no. V, pp. 284–289, 2007, ISBN: 978-0-7803-9760-6, doi: 10.1109/VPPC.2007.4544139.
- [115] O. Tremblay and L. a. Dessaint, "Experimental validation of a battery dynamic model for EV applications," *World Electr. Veh. J.*, vol. 3, no. 1, pp. 1–10, 2009, ISSN: 2032-6653.
- [116] Powersim Inc., "PSIM - User's Guide," 2014. [Online]. Available: <http://powersimtech.com/wp-content/uploads/2015/05/PSIM-User-Manual.pdf>. [Accessed: 05-Feb-2015].
- [117] J. S. Lim and Y. Il Lee, "Model Predictive Control of Current and Voltage for Li-Ion Battery Charger using 3-Phase AC / DC Converter," *SICE Annu. Conf. 2010, Proc.*, pp. 215–218, 2010.
- [118] ChenYang, "Hall-Effect Voltage Sensor CYHVS5-25A." [Online]. Available: <http://www.hallsensors.de/CYHVS5-25A.pdf>. [Accessed: 03-Aug-2015].
- [119] LEM, "Current Transducer LA 200-P." [Online]. Available: http://www.lem.com/docs/products/la_200-p.pdf. [Accessed: 03-Aug-2015].
- [120] Maxim Integrated, "MAX1320." [Online]. Available: <https://datasheets.maximintegrated.com/en/ds/MAX1316-MAX1326.pdf>. [Accessed: 03-Aug-2015].
- [121] Texas Instruments, "TMS320F28335 | Delfino F2833x/F2837x | Realtime Control | Description & parametrics," 2015. [Online]. Available: <http://www.ti.com/product/tms320f28335>. [Accessed: 01-Sep-2015].
- [122] Semikron, "SKM 100GB125DN." [Online]. Available: <http://www.semikron.com/dl/service-support/downloads/download/semikron-datasheet-skm100gb125dn-21915390>. [Accessed: 03-Aug-2015].

- [123] Semikron, “SKHI 61 R.” [Online]. Available: <http://www.semikron.com/dl/service-support/downloads/download/semikron-datasheet-skhi-61-r-l6100061>. [Accessed: 03-Aug-2015].

Appendix A

Estimative of the Maximum Distortion Value of the Stator Inductances in a Synchronous Machine with Salient Poles

In this appendix the mathematical operations required for obtain the expression, presented in Section 2.2.2, that defines the maximum distortion of the stator inductances in a synchronous machine with salient poles and buried magnets are described.

Based on [19], the inductance mean and the inductance variation, using the d -axis and q -axis stator inductances are defined according to (A1.1) and (A1.2) respectively.

$$\bar{L} = \frac{L_d + L_q}{2} \quad (\text{A1.1})$$

$$\tilde{L} = \frac{L_d - L_q}{2} \quad (\text{A1.2})$$

Such as discussed in Section 2.2.2, in a simplified method [19] each inductance value per phase can be described according to (A1.3), (A1.4) and (A1.5), where p represents the number of poles of the electrical machine and θ_r the rotor angle (in radians).

$$L_a = \bar{L} + \tilde{L} \cos(p \theta_r) \quad (\text{A1.3})$$

$$L_b = \bar{L} + \tilde{L} \cos\left(p \theta_r - \frac{2\pi}{3}\right) \quad (\text{A1.4})$$

$$L_c = \bar{L} + \tilde{L} \cos\left(p \theta_r + \frac{2\pi}{3}\right) \quad (\text{A1.5})$$

For the battery charging operation of an EV, the rotor of the electrical machine can be stopped at any position. For analyze the worst possible scenario, *Zaja et al.* propose to use a vector \vec{L}_0 , defined according to (A1.6).

$$\vec{L}_0 = L_a + L_b e^{j\frac{2\pi}{3}} + L_c e^{-j\frac{2\pi}{3}} \quad (\text{A1.6})$$

Using the definition expressed in (A1.7), the vector \vec{L}_0 is now defined according to (A1.8).

$$e^{j\theta} = \cos(\theta) + j \sin(\theta) \quad (\text{A1.7})$$

$$\begin{aligned} \vec{L}_0 &= L_a + L_b \left[\cos\left(\frac{2\pi}{3}\right) + j \sin\left(\frac{2\pi}{3}\right) \right] + L_c \left[\cos\left(-\frac{2\pi}{3}\right) + j \sin\left(-\frac{2\pi}{3}\right) \right] \\ &= L_a + L_b \cos\left(\frac{2\pi}{3}\right) + L_c \cos\left(-\frac{2\pi}{3}\right) + j \left[L_b \sin\left(\frac{2\pi}{3}\right) + L_c \sin\left(-\frac{2\pi}{3}\right) \right] \end{aligned} \quad (\text{A1.8})$$

For simplifying the calculus, the analysis of the vector \vec{L}_0 is divided it terms of its real and imaginary components defined in (A1.9) and (A1.10), respectively.

$$\Re\{\vec{L}_0\} = L_a + L_b \cos\left(\frac{2\pi}{3}\right) + L_c \cos\left(-\frac{2\pi}{3}\right) \quad (\text{A1.9})$$

$$\Im\{\vec{L}_0\} = L_b \sin\left(\frac{2\pi}{3}\right) + L_c \sin\left(-\frac{2\pi}{3}\right) \quad (\text{A1.10})$$

The real component of vector \vec{L}_0 can be described considering (A1.11) and (A1.12), resulting in (A1.13).

$$\cos\left(\frac{2\pi}{3}\right) = \cos\left(\frac{\pi}{6} + \frac{\pi}{2}\right) = -\sin\left(\frac{\pi}{6}\right) = -\frac{1}{2}, \quad \cos\left(\alpha + \frac{\pi}{2}\right) = -\sin(\alpha) \quad (\text{A1.11})$$

$$\cos(-\alpha) = \cos(\alpha) \Rightarrow \cos\left(-\frac{2\pi}{3}\right) = \cos\left(\frac{2\pi}{3}\right) \quad (\text{A1.12})$$

$$\Re\{\vec{L}_0\} = L_a - \frac{1}{2}(L_b + L_c) \quad (\text{A1.13})$$

Replacing the expressions that define the inductances per phase, described in (A1.3), (A1.4) and (A1.5) in (A1.13), results in (A1.14).

$$\begin{aligned} \Re\{\vec{L}_0\} &= \bar{L} + \tilde{L} \cos(p \theta_r) - \frac{1}{2} \left[\bar{L} + \tilde{L} \cos\left(p \theta_r - \frac{2\pi}{3}\right) + \bar{L} + \tilde{L} \cos\left(p \theta_r + \frac{2\pi}{3}\right) \right] \\ &= \bar{L} + \tilde{L} \cos(p \theta_r) - \frac{1}{2} \left[2\bar{L} + \tilde{L} \left(\cos\left(p \theta_r - \frac{2\pi}{3}\right) + \cos\left(p \theta_r + \frac{2\pi}{3}\right) \right) \right] \end{aligned} \quad (\text{A1.14})$$

Taking into account the relation presented in (A1.15), the real component of vector \vec{L}_0 is now established according to (A1.16).

$$\cos(\alpha - \beta) + \cos(\alpha + \beta) = 2 \cos(\alpha) \cos(\beta) \quad (\text{A1.15})$$

$$\begin{aligned} \Re\{\vec{L}_0\} &= \bar{L} + \tilde{L} \cos(p \theta_r) - \frac{1}{2} \left[2\bar{L} + \tilde{L} \left(2 \cos(p \theta_r) \cos\left(\frac{2\pi}{3}\right) \right) \right] \\ &= \bar{L} + \tilde{L} \cos(p \theta_r) - \frac{1}{2} \left[2\bar{L} + \tilde{L} (-1 \cos(p \theta_r)) \right] \\ &= \tilde{L} \cos(p \theta_r) + \frac{1}{2} \left[\tilde{L} \cos(p \theta_r) \right] \\ &= \frac{3}{2} \tilde{L} \cos(p \theta_r) \end{aligned} \quad (\text{A1.16})$$

Finally, replacing the inductance variation defined in (A1.2), the resultant expression that defines the real component of the vector \vec{L}_0 is described (A1.17).

$$\begin{aligned} \Re\{\vec{L}_0\} &= \frac{3}{2} \left(\frac{L_d - L_q}{2} \right) \cos(p \theta_r) = \\ &= \frac{3}{4} (L_d - L_q) \cos(p \theta_r) \end{aligned} \quad (\text{A1.17})$$

The imaginary component of vector \vec{L}_0 can be simplified considering (A1.18) and (A1.19), resulting in (A1.20).

$$\sin\left(\frac{2\pi}{3}\right) = \sin\left(\frac{\pi}{6} + \frac{\pi}{2}\right) = \cos\left(\frac{\pi}{6}\right) = \frac{\sqrt{3}}{2}, \quad \sin\left(\alpha + \frac{\pi}{2}\right) = \cos(\alpha) \quad (\text{A1.18})$$

$$\sin(-\alpha) = -\sin(\alpha) \Rightarrow \sin\left(-\frac{2\pi}{3}\right) = -\sin\left(\frac{2\pi}{3}\right) \quad (\text{A1.19})$$

$$\begin{aligned} \Im\{\vec{L}_0\} &= L_b \sin\left(\frac{2\pi}{3}\right) + L_c \sin\left(-\frac{2\pi}{3}\right) \\ &= L_b \left(\frac{\sqrt{3}}{2}\right) + L_c \left(-\frac{\sqrt{3}}{2}\right) \\ &= \frac{\sqrt{3}}{2} (L_b - L_c) \end{aligned} \quad (\text{A1.20})$$

Replacing the expressions that define the inductances per phase, described in (A1.3), (A1.4) and (A1.5) in (A1.20), results in (A1.21).

$$\begin{aligned}\Im\{\vec{L}_0\} &= \frac{\sqrt{3}}{2} \left[\bar{L} + \tilde{L} \cos\left(p \theta_r - \frac{2\pi}{3}\right) - \bar{L} - \tilde{L} \cos\left(p \theta_r + \frac{2\pi}{3}\right) \right] \\ &= \frac{\sqrt{3}}{2} \tilde{L} \left[\cos\left(p \theta_r - \frac{2\pi}{3}\right) - \cos\left(p \theta_r + \frac{2\pi}{3}\right) \right]\end{aligned}\quad (\text{A1.21})$$

Taking into account the relation presented in (A1.22), the imaginary component of vector \vec{L}_0 is now established according to (A1.23).

$$\cos(\alpha - \beta) - \cos(\alpha + \beta) = 2 \sin(\alpha) \sin(\beta) \quad (\text{A1.22})$$

$$\begin{aligned}\Im\{\vec{L}_0\} &= \frac{\sqrt{3}}{2} \tilde{L} \left(2 \left[\sin(p \theta_r) \sin\left(\frac{2\pi}{3}\right) \right] \right) \\ &= \frac{\sqrt{3}}{2} \tilde{L} \left(2 \left[\frac{\sqrt{3}}{2} \sin(p \theta_r) \right] \right) = \frac{(\sqrt{3})^2}{2} \tilde{L} \sin(p \theta_r) \\ &= \frac{3}{2} \tilde{L} \sin(p \theta_r)\end{aligned}\quad (\text{A1.23})$$

Finally, replacing the inductance variation defined in (A1.2), the resultant expression that defines the imaginary component of the vector \vec{L}_0 is described in (A1.24).

$$\begin{aligned}\Im\{\vec{L}_0\} &= \frac{3}{2} \left(\frac{L_d - L_q}{2} \right) \sin(p \theta_r) \\ &= \frac{3}{4} (L_d - L_q) \sin(p \theta_r)\end{aligned}\quad (\text{A1.24})$$

The rotor position that results in the highest difference on the inductances values is obtained calculating the absolute value of \vec{L}_0 , which represent the amount of system unbalance [19]. Since the vector \vec{L}_0 is defined in terms of a real and an imaginary component, according to (A1.25), its absolute value is determined using (A1.26).

$$\vec{L}_0 = \Re\{\vec{L}_0\} + j \Im\{\vec{L}_0\} \quad (\text{A1.25})$$

$$|\vec{L}_0| = \sqrt{(\Re\{\vec{L}_0\})^2 + (\Im\{\vec{L}_0\})^2} \quad (\text{A1.26})$$

Thus, the absolute value of the vector \vec{L}_0 is obtained replacing the simplified expressions obtained for the real and imaginary components that are described in (A1.17) and (A1.24), respectively, in (A1.26) resulting in (A1.27).

$$\begin{aligned} |\vec{L}_0| &= \sqrt{\left[\frac{3}{4}(L_d - L_q)\cos(p\theta_r)\right]^2 + \left[\frac{3}{4}(L_d - L_q)\sin(p\theta_r)\right]^2} \\ &= \sqrt{\left[\frac{3}{4}(L_d - L_q)\right]^2 [\cos^2(p\theta_r) + \sin^2(p\theta_r)]} \end{aligned} \quad (\text{A1.27})$$

Taking into account the Pythagorean trigonometric identity, presented in (A1.28), the expression that defines the absolute value of the vector \vec{L}_0 can be simplified, resulting in (A1.29).

$$\cos^2(\alpha) + \sin^2(\alpha) = 1 \quad (\text{A1.28})$$

$$|\vec{L}_0| = \sqrt{\left[\frac{3}{4}(L_d - L_q)\right]^2} = \frac{3}{4}(L_d - L_q) \quad (\text{A1.29})$$

Thus, despite the stator inductances value be dependent on the rotor position, the obtained result demonstrates that the amplitude of the distortion of the inductances is not dependent on the rotor position but remains the same, according to the L_q and L_d values.